DWDM source with precise channel spacing and good reliability

Yiming Sun

A Thesis submitted to

School of Engineering

University of Glasgow

In fulfilment of the requirements for the degree of

Doctor of Philosophy (Ph.D.)

March 2025

Abstract

This thesis discusses advancements in photonic integrated circuits, focusing on monolithic semiconductor laser arrays and narrow linewidth laser designs around 1550 nm. The research proposes efficient solutions to the challenges of laser fabrication and integration, contributing to high-capacity optical communication systems.

Four major innovations are presented. First, a four-channel laser array based on four-phase-shifted distributed feedback (DFB) lasers was demonstrated. The array achieves a uniform 100 GHz channel spacing, with each laser exhibiting a single-mode suppression ratio (SMSR) exceeding 50 dB. The integration of a semiconductor optical amplifier enables an output power of 33 mW, making the array suitable for dense wavelength-division multiplexing (DWDM) applications. Second, a DFB laser with a distributed phase shift region at the cavity centre was developed to achieve narrow linewidth operation. Compared to conventional π-phase-shifted DFB lasers, the optimised DPS design enables stable single-longitudinal-mode operation over a broader current range, with lower threshold current, higher slope efficiency, and improved SMSR. The minimum linewidth was reduced from 1.3 MHz to 220 kHz, demonstrating potential for high-precision applications such as LiDAR and coherent optical communications. Third, a novel grating modulation technique was proposed to enhance wavelength control in DFB laser arrays. By introducing an arithmetic phase progression, this method enables channel spacings of 0.493 nm, 0.949 nm, and 1.956 nm while maintaining a strong coupling coefficient and improving fabrication tolerance. Finally, asymmetric twin waveguide integration was implemented, demonstrating an integrated four-phase-shifted DFB laser array with 0.873 nm channel spacing, an SMSR exceeding 45 dB, and an electro-absorption modulator extinction ratio over 10 dB. These advancements enable scalable, precise, and efficient photonic integration.

Collectively, this work advances semiconductor laser technology, offering new solutions for linewidth narrowing, wavelength control, and integration, with applications in telecommunications, metrology, and quantum technologies.

Declaration

I declare that the thesis does not include work forming part of a thesis presented successfully for another degree.

I declare that the thesis represents my own work except where acknowledged to others.

I declare that this thesis is my own work and has not been submitted for any other degree. Unless otherwise stated, all results and content reflect original research conducted during my PhD at the University of Glasgow. Contributions from collaborators or prior group work are duly acknowledged and referenced where applicable.

List of Publications

Journal Papers

1. M. Al-Rubaiee, X. Sun, B. Yuan, Y. Fan, S. Zhu, **Y. Sun**, J. H. Marsh, S. J. Sweeney, and L. Hou, "Simultaneous multi-wavelength mode-locked DFB laser based on waveguide Bragg grating microcavities," Opt. Express 33, 22222-22234, 2025.
2. Y. Fan, M. Al-Rubaiee, S. Zhu, B. Yuan, X. Sun, **Y. Sun**, A. E. Kelly, J. H. Marsh, L. Hou, "Mode-locked DBR and DFB lasers with multiple phase-shifted gratings for THz generation," in Journal of Lightwave Technology, 2025.
3. X. Sun, Z. Li, **Y. Sun**, Y. Wang, J. Wang, J. H. Marsh, S. J. Sweeney, A. E. Kelly, L. Hou, "Narrow Linewidth Laser Based on Extended Topological Interface States in 1D Photonic Crystals," Laser & Photonics Reviews, 2025
4. **Y. Sun**, B. Yuan, X. Sun, S. Zhu, Y. Fan, M. Al- Rubaiee, J. H. Marsh, S. Sweeney, L. Hou, "Narrow Linewidth Distributed Feedback Lasers Utilizing Distributed Phase Shift, " Optics Letters, vol.50, no.1, pp.1-4, 2025.
5. **Y. Sun**, S. Zhu, B. Yuan, Y. Fan, M. Al- Rubaiee, X. Sun, J. H. Marsh, S. Sweeney, L. Hou, "Continuous Phase Modulation Technology Based on Grating Period Interval for High Grating Coupling Coefficiency and Precise Wavelength Control, " Optics Letters, vol.50, no.3, pp.750-753, 2025.
6. S. Zhu, B. Yuan, M. Al-Rubaiee, **Y. Sun,** Y. Fan, H. A. Seckin, S. Sweeney, J. H. Marsh, L. Hou, "Widely Tunable Photonic Filter Based on Equivalent Chirped Four-Phase-Shifted Sampled Bragg Gratings, " in ACS Photonics, vol.12, no.2, 2025, doi: 10.1021/acsphotonics.4c01899.
7. S. Zhu, B. Yuan, W. Cheng, Y. Fan, **Y. Sun**, M. Al-Rubaiee, J. Akbar, J. Marsh, L. Hou, "Dual-band Photonic Filters with Wide Tunable Range Using Chirped Sampled Gratings," IEEE Photonics Technology Letters, vol. 37, no. 3, pp. 169-172, 2025.
8. L. Hou, B. Yuan, Y. Fan, X. Sun, **Y. Sun**, S. Zhu, S. J. Sweeney, J. H. Marsh, "Monolithic Dual Wavelength DFB Lasers Based on Sidewall Gratings for THz/MMW Signal Generation," IEEE Journal of Selected Topics in Quantum Electronics, doi: 10.1109/JSTQE.2024.3427770.
9. Y. Fan, B. Yuan, M. Al-Rubaiee, **Y. Sun**, S. Zhu, J. H. Marsh, and L. Hou, "Dual-wavelength distributed feedback laser array based on four-phase-shifted sampled Bragg grating for terahertz generation," Optics Letters, vol. 49, no.12, pp.3472-3475, 2024.
10. Y. Fan, B. Yuan, M. Al-Rubaiee, **Y. Sun**, S. Zhu, J. Akbar, J. Marsh, L. Hou, "Millimeter-Wave Generation Based on Four Phase-Shifted Sampled Moiré Grating Dual-Wavelength DFB Laser," IEEE Photonics Technology Letters, vol. 36, no. 4, pp. 282-285, 2024.
11. B. Yuan, Y. Fan, S. Ye, Y. Zhang, **Y. Sun**, X. Sun, W. Cheng, S. Liang, Y. Huang, R. Zhang, J. Wang, J. H. Marsh, L. Hou, "Dual-wavelength DFB Laser Array Based on Sidewall Grating and Lateral Modulation of the Grating Coupling

Coefficient," Journal of Lightwave Technology, vol. 41, no. 9, pp. 2775-2784, 2023.

12. X. Sun, S. Liang, W. Cheng, S. Ye, **Y. Sun**, Y. Huang, R. Zhang, J. Xiong, X. Liu, J. H. Marsh, L. Hou, "Regrowth-free AlGaInAs MQW polarization controller integrated with sidewall grating DFB laser," Photonics Research, vol.11, no.4, pp.622-630, 2023.
13. W. Cheng, X. Sun, S. Ye, B. Yuan, **Y. Sun**, J. H. Marsh, and L. Hou, "Sidewall grating slot waveguide microring resonator biochemical sensor," Optics Letters, vol. 48, pp.5113-5116, 2023.
14. W. Cheng, X. Sun, S. Ye, B. Yuan, J. Xiong, X. Liu, **Y. Sun**, J. H. Marsh, and L. Hou, "Double slot micro ring resonators with inner wall angular gratings as ultra-sensitive biochemical sensors," Opt. Express Vol. 31, no.12, pp. 20034-20048, 2023.
15. X. Sun, W. Cheng, **Y. Sun**, S. Ye, A. Al-Moathin, Y. Huang, R. Zhang, S. Liang, B. Qiu, J. Xiong, X. Liu, J. H. Marsh and L. Hou, "Simulation of an AlGaInAs/InP Electro-Absorption Modulator Monolithically Integrated with Sidewall Grating Distributed Feedback Laser by Quantum Well Intermixing," Photonics, vol.9, no.8, 564, 2022.
16. **Y. Sun**, B. Yuan, X. Sun, S. Liang, Y. Huang, R. Zhang, S. Ye, Y. Fan, W. Cheng, J. H. Marsh, L. Hou, "DFB laser array based on four phase-shifted sampled Bragg grating with precise wavelength control, " Optics Letters, vol.47, no.23, pp.6237-6240, 2022.

Conference Papers

1. S. Zhu, M. Al-Rubaiee, B. Yuan, Y. Fan, **Y. Sun**, J. H. Marsh, L. Hou, "Dual-band microwave photonic filter utilizing equivalent chirped four-phase-shifted sampled Bragg grating for 52.1 GHz–439.5 GHz range," in Optical Components and Materials XXII, 2025, vol. 13362, pp. 68-71: SPIE.
2. **Y. Sun**, M. Al-Rubaiee, B. Yuan, A. S. Hezarfen, X. Sun, S. Zhu, Y. Fan, J. H. Marsh, and L. Hou, "DWDM Source Utilizing a 4PS-SBG DFB Laser Array with Monolithic ATG Technology," in *CLEO 2025*, Long Beach, California, USA, May 2025.
3. Al-Rubaiee, Y. Fan, B. Yuan, S. Zhu, **Y. Sun**, A. S. Hezarfen, J. H. Marsh, S. J. Sweeney and L. Hou, "Four-Wavelength Mode-Locked DFB Laser with Four Phase-Shifted Chirped Sampled Bragg Grating" *in CLEO* 2025, Long Beach, California, USA, May 2025.
4. Z. Wang, Y. Fan, X. Sun, B. Yuan, **Y. Sun**, M. Al-Rubaiee, A. S. Hezarfen, S. Zhu, J. H. Marsh, A. Kelly and L. Hou, "Linewidth-Reduced Optical Injection-Locked Laser Utilizing Four-Phase-Shifted Sampled Bragg Grating" *in CLEO 2025*, Long Beach, California, USA, May 2025.
5. S. Zhu, M. Al-Rubaiee, B. Yuan, Y. Fan, **Y. Sun**, J. H. Marsh, and L. Hou, "Broadband Tunable Microwave Photonic Filter Utilizing Equivalent Chirped

Sampled Bragg Gratings for Optical Frequency Division," in Optical Fiber Communication Conference (OFC) 2025, Technical Digest Series, 2025

6. **Y. Sun**, B. Yuan, X. Sun, J. H. Marsh and L. Hou, “Eight-Channel DFB Laser Array Based on Four Phase-Shifted Sampled Bragg Gratings,” *46th European Semiconductor Laser Workshop (ESLW 2023)*, Glasgow, UK, 30 Sept 2023.
7. Y. Fan, Y. Zhang, **Y. Sun**, B. Yuan, J. H. Marsh, and L. Hou, "Monolithic Optical Injection Locking DFB Lasers Based on Four Phase-Shifts Sampling Sections," in *Conference on Lasers and Electro-Optics/Europe (CLEO/Europe 2023)* and *European Quantum Electronics Conference (EQEC 2023)*, Technical Digest Series (Optica Publishing Group, 2023).
8. X. Sun, **Y. Sun**, S. Ye, W. Cheng, S. Liang, Y. Huang, J. Xiong, X. Liu, J. H. Marsh, and L. Hou, "Eight-channel EML array based on four phase-shifted sampled Bragg gratings," in CLEO 2023, Technical Digest Series (Optica Publishing Group, 2023), paper SF2Q.3.
9. X. Sun, W. Cheng, S. Liang, S. Ye, Y. Huang, **Y. Sun**, R. Zhang, J. Xiong, X. Liu, J. H. Marsh, and L. Hou, "Monolithic MQW Polarization Mode Controller Integrated with Sidewall Grating DFB Laser," in CLEO 2023, Technical Digest Series (Optica Publishing Group, 2023), paper STu3P.5.
10. X. Sun, Z. Li, **Y. Sun**, W. S. Wright, C. G. Leburn, A. E. Kelly, L. Hou, "780 nm Distributed Feedback Lasers with a Lateral Modulated Four-Phase-Shifted Sampling Grating," *2024 IEEE Photonics Conference (IPC)*, Rome, Italy, 2024, pp. 1-2, doi: 10.1109/IPC60965.2024.10799906.
11. X. Sun, W. Cheng, S. Ye, **Y. Sun**, J. H. Marsh, and L. Hou, "AlGaInAs/InP EML with Sidewall Grating Distributed Feedback Laser and Quantum Well Intermixing Technology." *2022 IEEE Photonics Conference (IPC)*, Vancouver, BC, Canada, 13-17 Nov 2022. doi: 10.1109/IPC53466.2022.9975652.
12. **Y. Sun**, X. Sun, B. Yuan, Y. Fan, J. H. Marsh, and L. Hou, "DFB Laser Array Based on Four Phase-Shifted Sampled Bragg Gratings," *2022 IEEE Photonics Conference (IPC)*, Vancouver, BC, Canada, 13-17 Nov 2022, doi: 10.1109/IPC53466.2022.9975710.

Acknowledgements

As I conclude my PhD journey, I extend my heartfelt gratitude to those who have supported me along the way. Your guidance, encouragement, and companionship have made this challenging yet rewarding experience possible.

First and foremost, I am deeply grateful to my supervisor, Dr. Lianping Hou, for his invaluable guidance, encouragement, and unwavering support throughout my PhD. His deep expertise and insightful advice have been instrumental in shaping my research. Whenever I encountered difficulties, his valuable advice and technical insights always pointed me in the right direction. I am also immensely thankful to my second supervisor, Prof. John Marsh, whose mentorship in wafer design, fabrication, and characterisation has been instrumental in my work.

I sincerely appreciate my seniors, Dr. Shengwei Ye, Dr. Xiao Sun, and Dr. Bocheng Yuan. They have been more than just seniors, they have been mentors, friends, and constant sources of support. Their willingness to share their knowledge and experience has greatly helped me throughout my research, and I have learned so much from our discussions.

Special thanks to the staff at the James Watt Nanofabrication Centre (JWNC) for their dedication to maintaining the facilities essential for my experimental work. Their efforts have been crucial to the success of my research.

Beyond that, I am grateful to Yizhe Fan, Simeng Zhu, momos and all my friends, who have been part of this journey. Your companionship, discussions, and shared experiences, whether in the office or over coffee, have provided motivation and balance.

Finally, to my family, no words can truly express my gratitude for your unconditional love and support. Your belief in me has been my greatest strength, making this PhD not just my achievement but a reflection of your unwavering encouragement.

Contents

List of Figures

List of Tables

Acronyms

2D	Two-Dimensional
2PS-SBG	Two Phase-Shifted Sampled Bragg Grating
3PS-SBG	Three Phase-Shifted Sampled Bragg Grating
4PS-SBG	Four Phase-Shifted Sampled Bragg Grating
Al	Aluminum
Al_2O_3	Alumina
AOM	Acousto-Optic Modulator
AR	Antireflection
As	Arsenic
ATT	Attenuator
ATG	Asymmetric Twin Waveguide
BPM	Beam Propagation Method
CAD	Computer-Aided Design
CB	Conduction Band
CH_3COCH_3	Acetone
CMP	Chemical Mechanical Polishing
CMT	Coupled Mode Theory
CPSG	Continuous-Phase-Shift-Grating
C-SBG	Conventional SBG
DFB	Distributed Feedback
DHS	Double Heterostructure
DPS	Distributed Phase Shift
DWDM	Dense Wavelength Division Multiplexing
EA	Electro-Absorption
EAM	Electro-Absorption Modulator
EBL	Electron Beam Lithography
EMLs	Electro-Absorption Modulated Lasers
EO	Electro-Optic
ER	Extinction Ratio
ESA	Electrical Spectrum Analyzer
FDTD	Finite-Difference Time-Domain
FP	Fabry-Pérot
FRL	Far-field Reduction Layer
FWHM	Full Width at Half Maximum
Ga	Gallium
GPIB	General-Purpose Interface Bus
GRINSCH	Graded-Index Separate Confinement Heterostructure
HSQ	Hydrogen Silsesquioxane
ICP	Inductively Coupled Plasma
In	Indium

InP	Indium Phosphide
IoT	Internet of Thing
IPA	Alcohol
ISO	Optical Isolator
JWNC	James Watt Nanofabrication Centre
MBE	Molecular Beam Epitaxy
MMI	Multimode Interferometer
MOCVD	Metal-Organic Chemical Vapour Deposition
MPS-DFB	Multiple-Phase-Shift DFB
MQW	Multiple Quantum Well
OC	Optical Coupler
P	Phosphorus
PC	Polarisation controller
PD	Photodetector
PICs	Photonic Integrated Circuits
PMMA	Polymethyl Methacrylate
Pt	Platinum
QCSE	Quantum-Confined Stark Effect
QW	Quantum Well
RBW	Resolution Bandwidth
REC	Reconstruction Equivalent Chirp
RF	Radio Frequency
RIE	Reactive Ion Etching
RO	Reverse Osmosis
RTA	Rapid thermal annealing
SBG	Sampled Bragg Grating
SHB	Spatial Hole Burning
Si	Silicon
S.I.	semi-insulating
SiO_2	Silica
SLM	Single-Longitudinal-Mode
SMSR	Side-Mode Suppression Ratio
SOA	Semiconductor Optical Amplifier
TE	Transverse Electric
TEC	Thermoelectric Cooler
Ti	Titanium
TIR	Total Internal Reflection
TMM	Transfer Matrix Method
VB	Valence Band
VBW	Video Bandwidth
WDM	Wavelength Division Multiplexing

Chapter 1

Introduction

1.1 Motivation

The exponential growth of global data traffic has driven an unprecedented demand for high-capacity, energy-efficient, and scalable optical communication systems [1]. As the backbone of modern information infrastructure, optical networks facilitate the transmission of vast data volumes with minimal loss over long distances [2]. Emerging technologies such as 5G, data centres, and the Internet of Things (IoT) further amplify the need for higher bandwidth utilisation, cost reduction, and enhanced integration [3, 4]. Meeting these demands necessitates innovative laser designs and advanced photonic integration strategies.

One of the most effective strategies for enhancing spectral efficiency in optical communication is Dense Wavelength Division Multiplexing (DWDM), which enables multiple data channels to be transmitted simultaneously over distinct wavelengths within a single optical fibre [5]. By enabling narrower channel spacing, such as 100 GHz, DWDM significantly increases network capacity [6]. However, achieving such dense spectral packing without performance degradation imposes strict requirements on laser stability, single-mode operation, and spectral purity to mitigate crosstalk and interference.

For optical communications, the spectral purity of the optical source is crucial and is typically quantified by its linewidth. In coherent optical communication, narrow linewidth lasers are essential, as phase noise and coherence directly affect signal quality [7]. Beyond telecommunications, lasers with linewidths in the sub-megahertz range are indispensable in precision applications such as spectroscopy, metrology, and quantum technologies, where high coherence ensures accuracy and sensitivity [8-10]. Despite these demands, the simultaneous realisation of narrow linewidth, high output power, and scalable manufacturability remains a formidable challenge.

Beyond individual laser performance, monolithic photonic integration offers a transformative approach to advancing photonic technologies. Integrating active and passive components, including lasers, modulators, detectors, and waveguides, on a single chip reduces optical losses, device footprint, and manufacturing costs [11, 12]. However, achieving integration requires overcoming major challenges, such as low loss coupling between active and passive devices and ensuring high fabrication tolerance.

This research aims to address these interconnected challenges by advancing semiconductor laser technology and photonic integration. By focusing on narrow channel spacing, narrow linewidths, and monolithic integration, this work contributes solutions that are academically significant and practically impactful for next generation optical communication and photonic technologies.

1.2 Optical Communications System

Optical communication systems form the foundation of modern data transmission, enabling the efficient transport of information over vast distances with exceptional speed and reliability. These systems utilise light as the carrier of information, transmitted after being modulated through optical fibres, which is a type of wired communication. Since the 1980s, fibre-optic communication systems have revolutionised the telecommunications industry and played a very important role in the digital age [13, 14]. Although optical systems are not yet as mature as electronic systems in terms of electrical integration, their superior scalability makes them the preferred choice for data centres, telecommunication networks, and emerging fields such as quantum communication and precision sensing [15, 16].

A typical optical communication system consists of three key components: the optical transmitter, the optical fibre transmission medium, and the optical receiver. As illustrated in Figure 1.1, the system operates by first converting the transmitted information into an electrical signal as input, which then modulates a semiconductor laser to generate an optical signal. The modulated light intensity varies according to the amplitude of the electrical signal and is transmitted through the optical fibre via total internal reflection (TIR). At the receiving end, a photodetector converts the incoming optical signal back into an electrical signal, which is subsequently demodulated to restore the original information [17, 18]. Therefore, the performance of the light source is critical to overall system efficiency, as it directly influences signal quality, transmission reliability, and data integrity, particularly in high-capacity optical networks like DWDM systems.

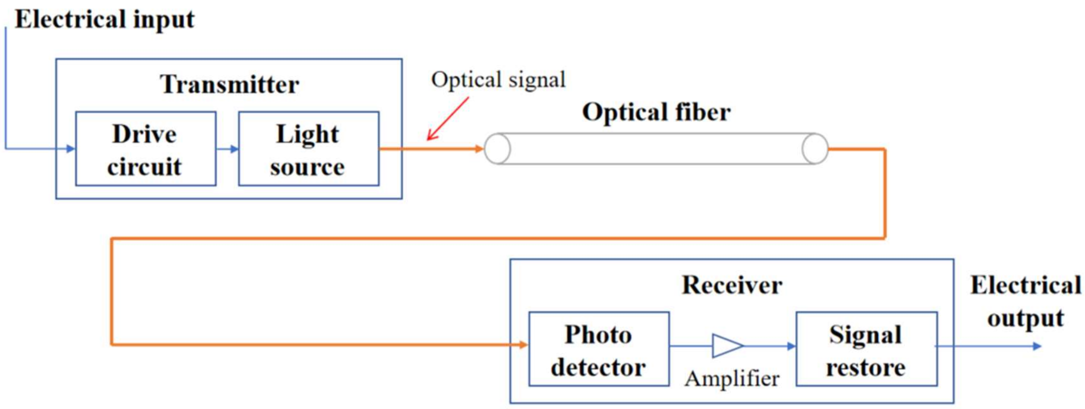

Figure 1.1: A typical structure of an optical fibre communication system.

Among the various semiconductor lasers used in optical communication, distributed feedback (DFB) lasers have emerged as the preferred choice due to their compact size, high efficiency, and well-defined spectral properties. Their ability to maintain stable single-mode operation makes them particularly suitable for applications requiring high spectral purity and precise wavelength control [19]. However, as optical networks grow increasingly complex, the performance demands on these lasers continue to escalate. To ensure optimal system operation, a laser must exhibit exceptional wavelength stability, minimal spectral linewidth, and sufficient output power. Any instability or spectral impurity can lead to signal distortion, data loss, and increased error rates, particularly in high-capacity and long-haul communication networks [20, 21].

For example, in wavelength division multiplexing (WDM) systems or densely configured optical networks, even slight wavelength fluctuations can cause wavelength drift and inter channel crosstalk, degrading signal integrity and reducing data transmission efficiency [22]. In addition, excess phase noise or spectral broadening in the laser source can introduce errors, signal fading, and decreased detection accuracy, particularly in coherent communication systems [23]. To mitigate these effects, laser sources must sustain single-mode operation and minimize phase and intensity noise across a wide range of operating conditions (e.g., current, temperature, and external perturbations), ensuring crosstalk suppression and signal coherence. Among these performance factors, laser linewidth, a key indicator of spectral purity, directly impacts system stability, particularly in phase-sensitive applications such as coherent optical communication and precision metrology [24].

Addressing these challenges requires continuous innovation in semiconductor laser technology. Advances in grating structures, cavity design, epitaxial layer engineering, and fabrication techniques are essential for achieving high output power, narrow linewidths, and stable operation in lasers with narrow wavelength spacing. Moreover, as optical communication systems advance toward higher levels of integration, the seamless incorporation of lasers with passive photonic components on a single chip is becoming increasingly critical. This integration not only enhances system compactness and efficiency but also reduces manufacturing complexity and overall costs, paving the way for next-generation photonic technologies.

1.3 Wavelength Division Multiplexing System

WDM is a fundamental technology in modern optical communication that significantly enhances fibre transmission capacity. By dividing the available optical spectrum into multiple discrete wavelengths, WDM enables the simultaneous transmission of independent data streams through a single fibre, maximising spectral efficiency and fully utilizing the vast bandwidth potential of optical networks. Figure 1.2 illustrates a typical WDM link in telecom applications [25].

In WDM system, multiple semiconductor lasers generate independent wavelengths, each modulated by an electrical signal. These signals are then combined using a wavelength multiplexer and transmitted through a single-mode fibre. After propagation, the signals are demultiplexed at the receiver, separating the wavelengths and directing each to its respective detector. WDM technology is widely employed in both short reach interconnects and long-haul optical communication systems, providing scalability and efficiency for high-capacity networks [26].

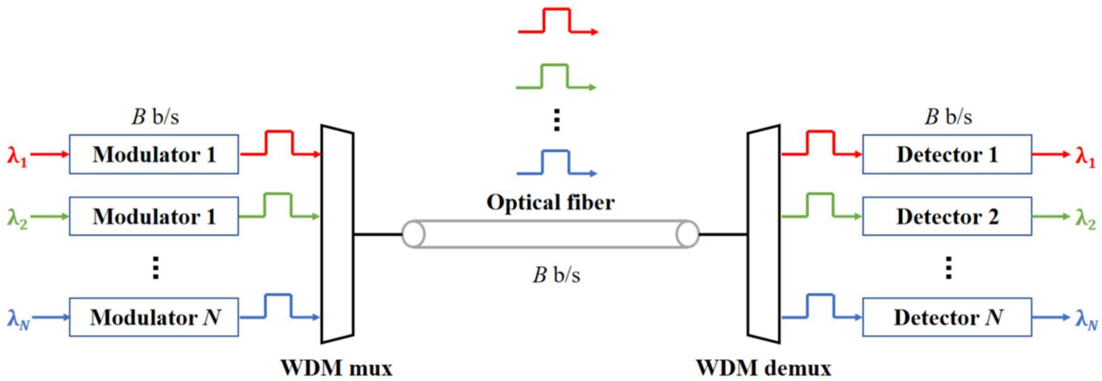

Figure 1.2: The diagram of a typical WDM link.

Early implementations of WDM, known as coarse wavelength division multiplexing (CWDM), utilised relatively wide channel spacing, typically several nanometers, and had fewer than eight active wavelengths per fibre to reduce system complexity and lower component costs [27]. CWDM's wide spacing also relaxed the wavelength stability requirements of laser sources, making it a cost-effective solution for short-reach applications. However, while suitable for moderate-capacity networks, CWDM's coarse spacing inherently limited the number of channels that could be accommodated within the optical spectrum. As data traffic demands escalated, the need for higher spectral efficiency and increased channel density became evident, driving the development of DWDM.

DWDM systems enhance WDM technology by employing significantly narrower channel spacing, typically measured in gigahertz. Depending on the wavelength channel spacing, the International Telecommunication Union (ITU) classifies dense wavelength-division multiplexing into four types: 12.5 GHz, 25 GHz, 50 GHz, and 100 GHz DWDM. The different wavelength spacing of these 4 DWDM wavelength grids is as the table below [28]. DWDM dices spectrum finely, multiplexes many signals onto a single fibre, which enhanced spectral utilization effectively multiplies the data-carrying capacity of the fibre and enables a substantial increase in channel count within the same spectral range. However, as channel spacing narrows, even slight wavelength drift can cause overlapping spectra, leading to severe signal degradation and data loss. To prevent this, DWDM systems impose stringent performance requirements on the laser sources [29].

Table 1.1 The different wavelength spacing of 4 DWDM wavelength grids

Comparison	12.5 GHz	25 GHz	50 GHz	100 GHz
Wavelength Spacing	0.1 nm	0.2 nm	0.4 nm	0.8 nm

To mitigate the impact of frequency offset on system performance, the ITU-T Recommendation specifies that centre frequency deviation, the difference between the standard and actual centre frequencies, should generally remain below 10% of the designated channel frequency [30]. It means that, in a 100 GHz DWDM system, the maximum allowable wavelength error of 0.08 nm between adjacent channels. This imposes stringent performance requirements on DWDM laser sources, demanding exceptional wavelength stability to ensure each channel remains within its allocated spectral slot. Additionally, high output power and narrow linewidth lasers are critical to reducing spectral broadening, minimising crosstalk, and preserving signal integrity in high-density optical networks.

The evolution from CWDM to DWDM has revolutionised optical communication, enabling high-capacity and scalable networks. In modern DWDM systems, commercial optical communication networks now support up to 400 Gb/s per channel on a 50 GHz grid, achieving a total transmission capacity of approximately 76 Tb/s for long-haul applications [31, 32]. In the research domain, single-wavelength data rates have exceeded 1 Tb/s, and the total WDM capacity in a single-mode fibre has reached up to 56.51 Tb/s. Additionally, recent experiments have demonstrated ultra-high data transmission rates of 402.2 Tb/s using a commercial standard optical fibre spanning the O to U bands [33].

These advances in transmission capacity have intensified the demand for laser sources with narrow linewidth, high output power, and excellent wavelength stability. In response, significant efforts have been made to develop semiconductor laser technologies that meet these stringent requirements. Quantum dot DFB lasers have achieved intrinsic linewidths as low as 30 kHz, attributed to their low α-factors and atom-like gain spectra [34]. Discrete-mode lasers, such as those developed by Eblana Photonics, enable reliable single-mode operation with linewidths around 100 kHz. Meanwhile, frequency comb lasers offer a broadband alternative, generating evenly spaced, phase-coherent spectral lines. Recent demonstrations have achieved sub-50 fs timing jitter and high power per line [35].

1.4 The Emergence of the Laser

Laser, an acronym for Light Amplification by Stimulated Emission of Radiation, which has been first proposed by Charles Townes and Arthur Schawlow in 1958 [36]. From the inception of the initial laser to the contemporary advent of the first general-purpose programmable photonic processor, the evolution over six decades has rendered the generation and application of lasers indispensable entities within our lives [37]. Nowadays, lasers have been widely used in manufacturing (such as ultrafast laser processing) [38], life sciences (like spectrometry bioimaging) [39], electronics (like laser printers) and scientific research (including photon energy transfer and physical random bit generation) [40-42]. Additionally, lasers serve as essential light sources for data transmission, making them integral to modern telecommunications networks.

In optical communication, lasers serve as the primary light source for transmitting data over optical fibres. Their key function is to generate a stable and coherent light beam that can be modulated to encode information [43]. Depending on the system requirements, modulation techniques such as amplitude, frequency, or phase modulation are used to enable long-distance data transmission with minimal loss and distortion. For DWDM systems, where multiple data channels are transmitted on different wavelengths, lasers must provide precise and stable wavelength control to ensure minimal interference and crosstalk. Similarly, in coherent communication systems, which rely on phase-sensitive detection, narrow linewidth lasers are essential to reduce phase noise and improve signal fidelity. High-power lasers compensate for fibre losses in long-haul networks, improving signal quality and system stability.

The unique properties of lasers make them indispensable for optical communication. Their ability to generate coherent, stable, and high-quality light underpins the high capacity, efficiency, and reliability of modern optical networks. However, as the demand for higher data rates, greater spectral efficiency, and integrated photonic solutions grows, so too do the performance requirements for laser sources. Achieving narrow linewidths, higher power levels, and integration with passive components remains a key challenge for the next generation of optical networks, necessitating continuous advancements in laser design and fabrication.

1.5 Photonic Integrated Circuits

As discussed earlier, DWDM systems rely on various optical and electrical components for signal processing, modulation, and amplification. However, implementing these functionalities using discrete, independent devices significantly increases system complexity, cost, and alignment difficulties. Traditional optical systems, which interconnect separately packaged components via fibre or free-space optics, face inherent scalability challenges, high deployment costs, and precise alignment requirements.

Photonic Integrated Circuits (PICs) address these limitations by consolidating multiple optical functions onto a single chip, reducing system footprint while improving performance, efficiency, and reliability. Similar to how electronic integrated circuits revolutionised electronics by integrating transistors, diodes, and other elements onto a semiconductor substrate, PICs achieve the same for optical components—such as lasers, modulators, waveguides, semiconductor optical amplifiers (SOA), and photodetectors. This integration enables the development of compact, highly functional optical systems, making PICs a cornerstone technology for applications ranging from high-speed optical communication and interconnects to advanced sensing and quantum technologies [44].

One of the most significant advantages of PICs lies in their ability to seamlessly integrate both active and passive photonic devices. Active components, including lasers, modulators, and photodetectors, are responsible for generating and processing optical signals, while passive elements such as waveguides, filters, and splitters facilitate signal routing and manipulation. This monolithic integration offers several benefits. The confinement of light within the chip reduces coupling inefficiencies typically found in discrete systems, minimising optical losses at interfaces. The elimination of external optical connections enhances reliability by reducing susceptibility to misalignment and environmental variations. The compact nature of PICs makes them particularly suitable for space-constrained environments, such as data centres and mobile devices. Additionally, integrating multiple functions into a single substrate simplifies packaging and enables mass production, lowering overall system costs [45].

Despite these advantages, the development and deployment of PICs present several technical challenges. Achieving efficient optical coupling between active and passive components is crucial, as even minor mismatches in optical mode profiles can lead to significant transmission losses. Precise fabrication processes are necessary to ensure alignment between different components, requiring advanced lithography techniques and meticulous process control. The stringent fabrication tolerances in PICs further complicate manufacturing. Unlike electronic circuits, where small variations in feature size often have minimal impact, PIC performance is highly sensitive to dimensional deviations [46]. Waveguide width variations or errors in grating structures can cause wavelength shifts or optical mode distortion, significantly degrading system performance.

Material integration presents another significant challenge. Active devices, such as lasers, typically require III-V semiconductors like InP or GaAs for efficient light generation, whereas passive components are often fabricated from low-loss materials such as silicon or silicon nitride [47]. Integrating these materials on a single platform necessitates hybrid or heterogeneous integration techniques, which introduce additional fabrication complexity and alignment difficulties.

PICs represent a fundamental advancement in optical technology, offering unparalleled advantages in size, efficiency, and functionality. As the demand for higher-capacity, more integrated optical systems grows, PICs will play a crucial role in next-generation telecommunications and photonic applications. However, realising their full potential requires overcoming challenges in coupling efficiency, fabrication tolerances, and material integration. Continued innovations in device design, manufacturing processes, and integration techniques will be key to enabling scalable, high-performance PIC-based optical systems.

1.6 The Aim of This Research

This research aims to advance semiconductor laser design and photonic integration strategies to overcome key challenges in wavelength stability, narrow linewidth, and integration efficiency for next generation DWDM and coherent communication systems. The research focuses on developing three novel semiconductor devices: (1) a multi-channel laser array designed with high power and precise wavelength control, (2) a DFB laser for narrow linewidth and (3) a laser array integrating with active and passive devices for DWDM applications. These devices leverage optimised grating structures, cavity configurations, and fabrication techniques to enhance performance in PICs.

By designing the grating structure, phase modulation has been introduced to control the output wavelength or to smooth the optical field distribution within the cavity. This optimisation enables the realisation of narrow channel spacing and narrow linewidth laser performance. The experiment successfully demonstrated the channel spacings as 100 GHz and linewidth narrowing from 1.3 MHz to 220 kHz. Furthermore, this study confirms that continuous phase shift modulation technology not only overcomes the manufacturing limitations of traditional gratings but also maintains high coupling efficiency and precise wavelength control, making it a promising approach for next-generation photonic integration.

In addition to advancing laser technology, this research contributes to the evolution of PICs by developing innovative designs and fabrication strategies based on asymmetric twin waveguide (ATG) technology. By leveraging ATG integration, the research enhances the integration of active and passive photonic devices, enabling more efficient, compact, and scalable optical communication systems. These advancements support high spectral efficiency and increased channel capacity, addressing the growing demands of next-generation DWDM and coherent communication networks.

1.7 Thesis Overview

The thesis is organised as follows. Chapter 2 provides an overview of the fundamental wafer structures and ridge waveguide designs used in simulations. It then reviews the theoretical foundations and design principles of different grating structures, including Bragg grating reflection theory and the transfer matrix method for simulation analysis. The chapter also introduces key innovations in grating design for both narrow linewidth DFB lasers and laser arrays, along with their corresponding simulation results.

Chapter 3 details the design and fabrication of three new DFB lasers: four phase-shifted sampled Bragg gratings (4PS-SBG), distributed phase shift (DPS) DFB lasers and continuous phase shift gratings (CPSG). It describes the fabrication processes and testing methodologies for each laser type, with a particular focus on the key fabrication steps and experimental validation of their performance. The 4PS-SBG DFB array achieves a uniform 0.8 nm channel spacing, with each laser exhibiting an SMSR exceeding 50 dB. The integration of a semiconductor optical amplifier further enhances its performance, enabling a maximum output power of 33 mW. The DPS device demonstrates low threshold current, high slope efficiency, and improved SMSR, with the linewidth reduced from 1.3 MHz to 220 kHz. The CPSG device achieves precisely controlled channel spacings of 0.493 nm, 0.949 nm, and 1.956 nm, maintaining a strong coupling coefficient while significantly improving fabrication tolerance. This chapter provides a comprehensive analysis of the fabrication techniques and performance enhancements introduced by these novel DFB lasers, demonstrating their potential for high-performance photonic integration.

Chapter 4 presents the design and implementation of PIC devices based on ATG technology, covering their operating principles, design methodologies, fabrication processes, and experimental validation. By integrating the 4PS-SBG DFB array with the ATG platform, the resulting device demonstrates stable single-mode operation in each channel with an SMSR exceeding 45 dB. ATG device achieves a precise wavelength spacing of 0.873 nm, and with electro-absorption modulator (EAM) modulation, an extinction ratio of -12 dB is achieved, making it highly suitable for DWDM applications.

Chapter 5 concludes the thesis by summarising the key innovations and contributions of this work. It reviews the main achievements and discusses the remaining challenges, providing insights and suggestions for future research directions in semiconductor lasers and PIC technology.

Chapter 2

Theory and Design

The development of high-performance photonic devices follows a structured approach to ensure optimal functionality, efficiency, and manufacturability. This process involves several critical stages, as outlined in Figure 2.1, including requirements analysis, material selection, device design, fabrication, testing, and application. Each stage plays a crucial role in defining and refining device performance, ensuring that the final photonic system meets the stringent demands of optical communication applications.

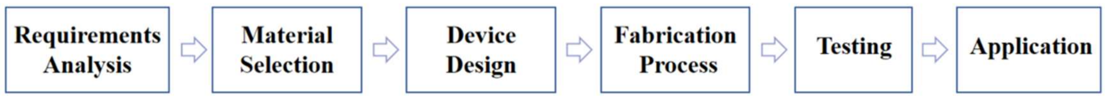

Figure 2.1: Workflow of Semiconductor Laser Design and Development

In this chapter, we introduce the theoretical foundations of laser design, with a particular focus on material selection and grating design. By optimising these aspects, we aim to improve wavelength stability, achieve narrow linewidths, and enhance overall device efficiency, all of which are essential for DWDM and coherent optical communication systems.

2.1 Material Selection and Wafer Structure

2.1.1 Materials Selection

The choice of materials is a fundamental aspect in the design of photonic devices, as the intrinsic properties of the materials directly impact the optical, thermal, and electronic performance of the system. Among these considerations, the choice of material is closely related to the requirements of the operating wavelength, as different wavelengths require materials with specific bandgap energies and optical properties [48]. For this work, the operating wavelength of 1550 nm was chosen due to its critical role in optical communications. The 1550 nm wavelength falls within the C-band, where low loss pure silica core fibres can achieve the lowest transmission loss (0.16 dB/km) shown in Figure 2.2, and dispersion-shifted fibres are engineered to exhibit minimal chromatic dispersion at this wavelength [49, 50]. This makes it the ideal wavelength for long-distance, high-speed communication networks.

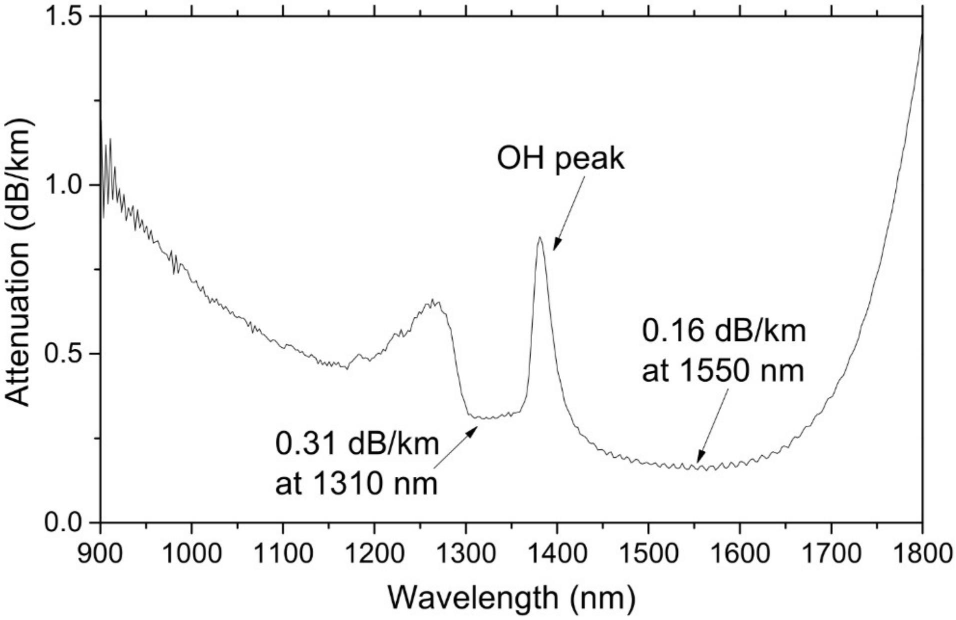

Figure 2.2. Spectral attenuation of the tested ultra-low loss pure silica core fibre [49].

For devices operating in the telecommunications wavelength range around 1550 nm, indium phosphide (InP) has long been the substrate material of choice due to its excellent lattice matching with a range of III-V compound semiconductors and its optical transparency in the target wavelength range [51]. As a substrate, InP also provides the foundation for growing active and passive layers with high crystalline quality, enabling the fabrication of efficient photonic devices [52].

InP-based photonic devices often employ quaternary alloys like InGaAsP as the active region material, taking advantage of its tunable bandgap and compatibility with the InP lattice. By adjusting the composition of Indium (In), Gallium (Ga), Arsenic (As), and Phosphorus (P), InGaAsP can be engineered to emit or absorb light within the telecommunications bands [53]. This material system has been widely used in DFB lasers, electro-absorption modulators, and other active photonic components due to its ability to achieve efficient light generation and modulation.

2.1.2 Energy Band Comparison to InGaAsP/InP and AlGaInAs/InP

However, as optical communication systems demand increasingly higher performance, the limitations of InGaAsP, particularly under high-temperature and high-power operation, have become apparent. One of the major problems associated with InGaAsP is its relatively low conduction band (CB) offset, which can lead to carrier leakage from the active region into the cladding layers, especially at elevated temperatures [54].

In a semiconductor material system, the conduction band represents the energy levels where free electrons can move and contribute to electrical conduction, while the valence band (VB) corresponds to the lower energy states where holes reside. In a heterostructure, the bandgap difference ΔE_g between two materials determines the conduction and valence band offsets (ΔE_c and ΔE_v). As shown in Figure 2.3(a), the conduction band offset in InGaAsP/InP is only $0.4\Delta E_g$, meaning that only 40% of the total bandgap energy contributes to electron confinement. This relatively small CB offset weakens carrier confinement, allowing greater electron leakage from the active region into the cladding layers, which not only reduces the optical gain but also increases the threshold current and degrades the overall efficiency of the device [55].

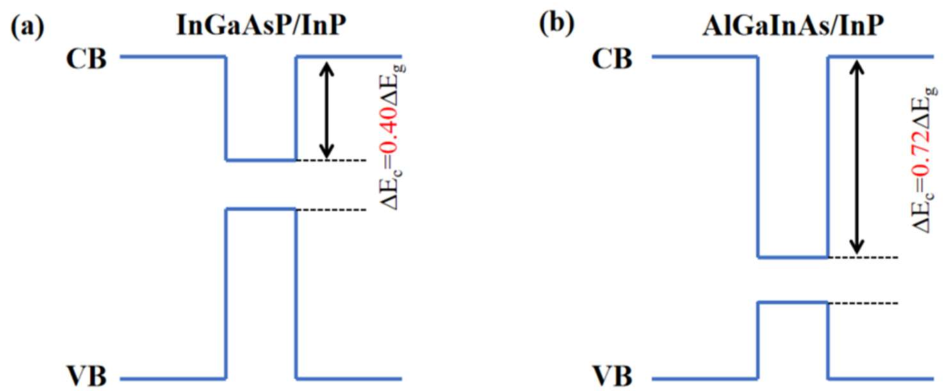

Figure 2.3. Comparison of the band discontinuities between (a) InGaAsP/InP and (b) AlGaInAs/InP material systems.

To overcome these limitations, AlGaInAs has emerged as a promising alternative active region material for InP-based photonic devices. The introduction of aluminium (Al) into the alloy composition offers several key advantages over InGaAsP. As illustrated in Figure 2.3(b), AlGaInAs provides a larger conduction band offset of $0.72\Delta E_g$, meaning that 72% of the total bandgap energy contributes to electron confinement. This enhanced carrier confinement in the quantum wells significantly reduces leakage, particularly at high temperatures [56].

Furthermore, AlGaInAs offers a higher differential gain than InGaAsP, which results in a steeper dependence of optical gain on carrier density. This enhances the relaxation oscillation frequency and thus increases the modulation bandwidth. As a result, AlGaInAs enables faster carrier-to-photon conversion dynamics, supporting higher modulation speeds, which is crucial for achieving data rates beyond 100 Gb/s in DWDM systems. Its improved carrier confinement not only enhances modulation efficiency but also contributes to superior thermal stability by reducing carrier leakage at high temperatures, thereby supporting higher output power and more stable lasing performance. These advantages collectively lead to reduced linewidth broadening and lower intensity noise during operation.

Although the inclusion of aluminium increases susceptibility to oxidation during fabrication, this challenge can be effectively mitigated through optimised metal-organic chemical vapour deposition (MOCVD) and molecular beam epitaxy (MBE) growth techniques and protective encapsulation [57]. In this work, AlGaInAs is employed as the active material for DFB lasers, where its superior carrier confinement and thermal stability enable high power, narrow linewidth, and low noise operation.

2.1.3 Lasing Principle and Quantum Well

The discussion on the energy band comparison between InGaAsP and AlGaInAs highlights the importance of strong carrier confinement for efficient laser operation.

While material composition plays a crucial role, the active region design further determines the performance, efficiency, and reliability of semiconductor lasers.

Figure 2.4 illustrates the main structure and operation of a semiconductor laser, which consists of an active region embedded within a waveguide structure. The active region, typically a Multiple Quantum Well (MQW) structure, serves as the gain medium where electron-hole recombination generates photons. This region is positioned within a waveguide core, which confines the optical mode and ensures efficient light propagation. The waveguide core is surrounded by upper and lower cladding layers with a lower refractive index, creating a high-contrast refractive index profile that enables strong optical confinement [58]. To sustain laser oscillation, the cavity is enclosed by two partially reflecting mirrors, denoted as R_1 and R_2, at each end, forming a Fabry-Pérot (FP) resonator. These mirrors provide the necessary optical feedback, allowing photons to undergo multiple reflections and interact with the gain medium. Through stimulated emission, each passing photon induces additional recombination, generating phase-matched, coherent photons, thereby amplifying light within the cavity. A fraction of this amplified light escapes through the partially reflecting mirrors, forming the laser output (Light 1 & Light 2).

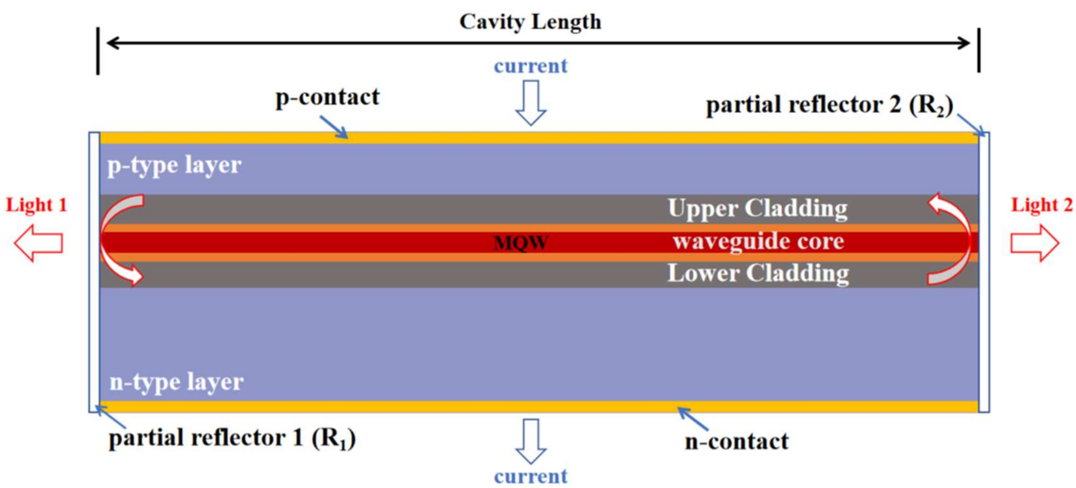

Figure 2.4: Simple side view schematic of semiconductor laser diode.

From an electrical perspective, a semiconductor laser operates as a P-I-N structure, where current injection occurs via the p-contact (top) and n-contact (bottom). When a forward bias is applied, electrons from the n-type region and holes from the p-type region are injected into the active region, where they recombine radiatively, emitting photons. As shown in Figure 2.5, electrons and photons interact in three distinct ways: absorption, spontaneous emission, and stimulated emission [59]. Initially, light is generated through spontaneous emission, in which photons are emitted with random phases and directions. However, for sustained laser action, stimulated emission must dominate. In this process, an incoming photon with the same energy and phase as an excited carrier triggers recombination, producing an identical, phase-matched photon, leading to optical amplification.

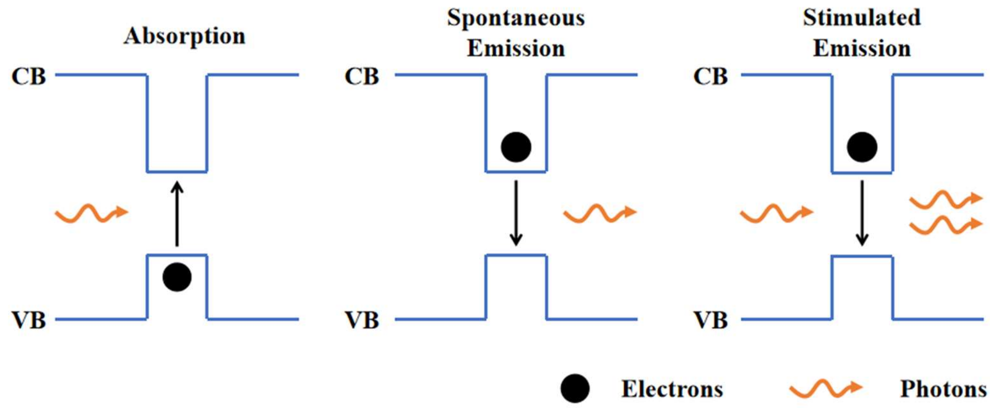

Figure 2.5: Three ways that an electron interacts with a photon: absorption, spontaneous emission and stimulated emission.

Unlike a standard P-I-N structure, where light emission is weak and inefficient, a semiconductor laser incorporates a double heterostructure (DHS) or quantum well (QW) design to significantly enhance carrier confinement and optical efficiency [60, 61]. In a DHS, the active region is sandwiched between two materials with a higher bandgap energy, effectively confining both electrons and holes, leading to a higher probability of recombination. This confinement also improves optical feedback, ensuring that emitted photons remain within the active region for efficient amplification. Quantum well structures further enhance this effect by restricting carriers to nanometer-thin layers, improving gain, modulation speed, and thermal stability.

Further improvements were achieved with MQW structures, where carriers are distributed across several wells [62]. Compared to single quantum wells, MQWs offer stronger carrier confinement, reduced threshold currents and greater design flexibility. In an MQW design, the total carrier density required to achieve a given optical gain is spread over multiple wells, rather than being concentrated in a single active region. This spatial distribution reduces the carrier density in each well, which in turn lowers the probability of nonradiative recombination mechanisms such as Auger recombination, known to scale superlinearly with carrier density [63].

By suppressing nonradiative loss mechanisms, MQW designs help to improve internal quantum efficiency and enhance the thermal stability of the laser, while also supporting lower threshold currents due to improved carrier confinement and reduced recombination losses [64, 65]. Furthermore, strain engineering using alternating compressively and tensile strained layers optimises electronic and optical properties while ensuring structural integrity.

Given these advantages, MQW structures are widely used in high-performance 1550 nm photonic devices, such as DFB lasers, tunable lasers, and high-speed modulators. In this work, AlGaInAs/InP MQW wafer structures serve as the foundation for high-power, narrow-linewidth, and low-noise semiconductor lasers.

2.1.4 MQW Wafer Structures

The AlGaInAs/InP MQW wafer structures used in this work serve as the foundation for designing and developing high-performance 1550 nm photonic devices. The basic wafer structure is shown in Figure 2.6. These wafers were grown using MOCVD on n-doped InP substrates to ensure high-quality epitaxial growth and compatibility with the InP-based material system. The basic structure features five compressively strained QWs, each 6 nm thick with a strain level of +1.2%, made of $Al_{0.07}Ga_{0.22}In_{0.71}As$. These QWs are separated by six tensile strained barriers, each 10 nm thick with a strain level of -0.3%, composed of $Al_{0.224}Ga_{0.286}In_{0.49}As$. The strain-balanced configuration ensures structural stability while enhancing the optical and electronic properties of the active region.

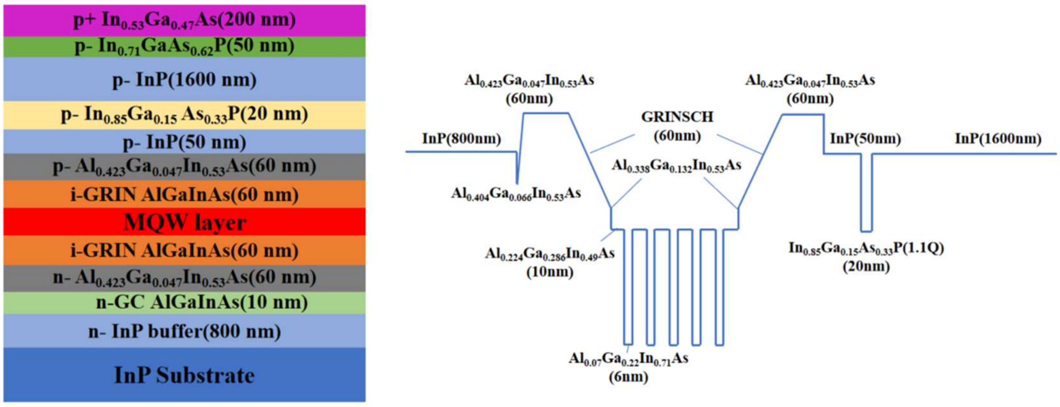

Figure 2.6: IQE five quantum well wafer structure.

To achieve effective carrier and optical mode confinement, the QWs and barriers are embedded within two 60 nm AlGaInAs graded-index separate confinement heterostructure (GRINSCH) layers. This design reduces the carrier population in the optical core layer at threshold compared to standard SCH structures, thereby lowering the threshold current density and enhancing the differential gain. Additionally, the lower cladding, upper cladding, and contact layers complete the structure, with the lower cladding consisting of an 800 nm thick n-doped InP layer, the upper cladding comprising a 1600 nm thick p-doped InP layer, 50 nm 1.3Q ($In_{0.71}GaAs_{0.62}P$) layer, and the contact layer being a 200 nm thick highly doped InGaAs layer with a doping concentration of 1.5×10^{19} cm^{-3}.

This baseline structure serves as a fundamental platform, the specific wafer structures were modified to meet the requirements of different device designs. Adjustments were made to parameters such as the number of quantum wells and barriers, as well as the doping levels and thicknesses of the cladding layers. These variations were introduced to optimise performance metrics such as output power, linewidth, and thermal stability. The exact details of these tailored configurations and their impact on device performance will be presented in subsequent chapters.

2.2 Laser Design and Parameter Optimisation

With the wafer structures established as the foundational platform, the next step in the development of photonic devices is the design of the laser itself. The wafer provides the active region and the necessary confinement layers, but the performance and functionality of the device are ultimately determined by the laser cavity design and its associated parameters. In November 1957, Gordon Gould sketched the concept of an FP laser resonator in his notebook, laying the foundation for understanding more complex laser architectures [66].

2.2.1 Fabry-Pérot Laser

The FP laser represents the simplest structure in semiconductor lasers, consisting of a single waveguide that acts as both the optical cavity and the light propagation path. The design relies on the natural reflection at the cleaved facets of the waveguide to provide optical feedback, eliminating the need for additional complex structures. This simplicity not only makes FP lasers easy to fabricate but also establishes them as a foundational design for understanding more advanced laser architectures.

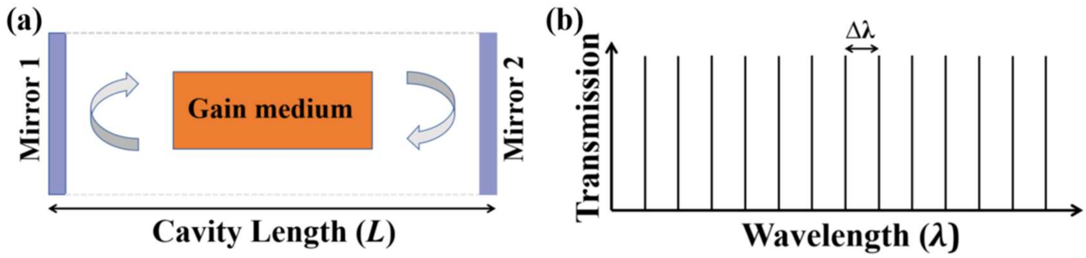

Figure 2.7: (a) Schematic illustration of light transmission in an FP resonator. (b) The longitudinal modes supported by the resonator.

Figure 2.7 (a) illustrates the schematic of an FP cavity laser. The FP cavity consists of a gain section sandwiched between two reflective mirrors, which form a resonant cavity. Photons generated within the gain region bounce incessantly between the two mirrors while experiencing optical gain from the active medium and losses primarily through transmission at the mirrors. As light reflects and forth, it undergoes constructive or destructive interference, depending on the wavelength, leading to the formation of multiple longitudinal modes within the gain spectrum as shown in Fig. 2.7 (b). For an FP cavity of length L and free-space wavelength λ, the longitudinal modes satisfy the resonance condition [67]:

$$m\lambda = 2n_{eff}L \tag{2.1}$$

m is the optical mode number, n_{eff} is the refractive index of the cavity. The wavelength separation between adjacent modes is $\Delta\lambda = \lambda_m - \lambda_{m+1}$; therefore:

$$\Delta\lambda = \frac{2n_{eff}L}{m} - \frac{2n_{eff}L}{m+1} \approx \frac{2n_{eff}L}{m^2} \tag{2.2}$$

By combining Equations 2.1 and 2.2:

$$\Delta\lambda = \frac{\lambda_0^2}{2n_{eff}L} \tag{2.3}$$

In Equation 2.3, λ_0 is the dominant or peak laser resonant wavelength.

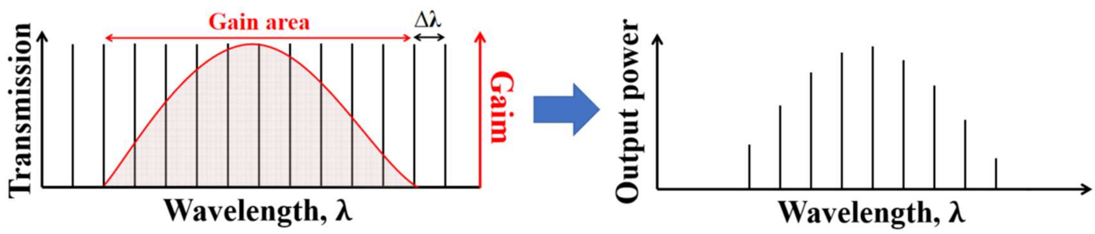

Figure 2.8: Schematic illustration of the resonant modes overlapping with the optical gain curve (in red) and its lasing longitudinal modes of the FP laser.

The calculation above of wavelength spacing for FP lasers assumes an idealised scenario where the gain bandwidth is infinitely wide. However, in practical semiconductor lasers, the gain bandwidth of the active region imposes a significant constraint on the number and intensity of lasing wavelengths [68]. In semiconductor lasers, the gain distribution can be described by a Gaussian distribution, where the gain is highest near the centre of the spectrum and decreases toward the edges and typically ranges from 20 nm to 40 nm, depending on factors such as the QW composition, strain, and operating temperature [69]. This means that longitudinal modes closer to the gain peak experience stronger amplification, while those further away are less likely to reach the threshold gain required for lasing, as shown in Figure 2.8.

Figure 2.9 illustrates the simplified schematic of an FP laser in semiconductors. In typical manufactured FP lasers, the cavity is formed by cleaving the ridge waveguide structure to a specific length, with the cleaved facets acting as reflective surfaces that provide the optical feedback necessary for lasing. From its cross-sectional view, the waveguide structure is built on a layered semiconductor material system, where a p-n junction is formed by the p-doped and n-doped cladding layers. The intrinsic quantum well layers, positioned between these cladding layers, serve as the active region, facilitating efficient carrier recombination and lasing action.

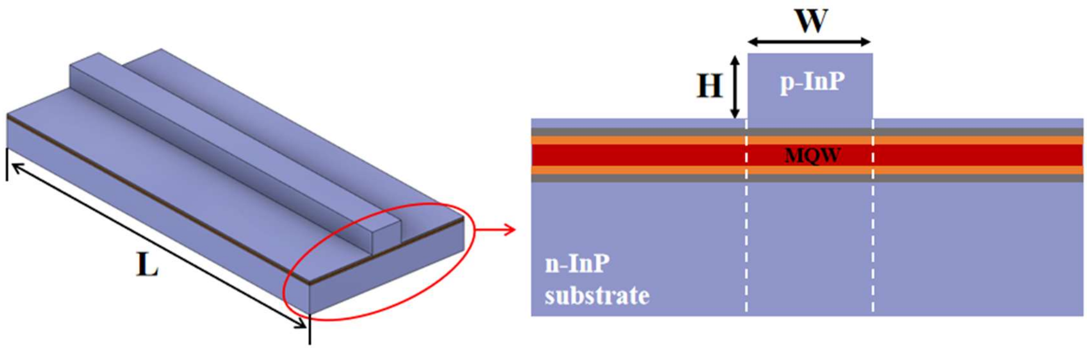

Figure 2.9: The typical manufactured FP laser in semiconductors(left) and its cross-section(right).

Electrical contacts will be formed during the later fabrication process by depositing a metal layer on the top of the FP ridge to create the p-contact and another metal layer on the backside to serve as the n-contact. When a current is applied across the p-n junction, carriers are injected into the active region, providing the optical gain required to drive the laser. Once the threshold current is reached, stimulated emission occurs, generating lasing light that is confined and amplified within the waveguide cavity. The lasing emission exits through one or both facets of the cleaved cavity.

Despite its straightforward configuration, the performance of FP lasers is highly dependent on key design parameters. The waveguide depth H, which influences vertical confinement and coupling efficiency; the waveguide width W, which controls lateral confinement, beam quality, and mode selection; additionally, the waveguide length L directly influences the cavity's longitudinal mode spacing, threshold current, and output power. By carefully optimising these parameters, FP lasers can be designed to meet specific performance requirements.

2.2.2 Waveguide Design

In a basic FP laser structure, laser performance is strongly influenced by the waveguide design, which governs optical confinement and propagation within the cavity. This confinement is achieved by creating a refractive index contrast between the ridge and the surrounding etched regions, ensuring efficient mode guidance and forming the basis of many semiconductor laser designs.

2.2.2.1 Effect of Waveguide Depth

In a semiconductor laser, the etched ridge structure defines the lateral optical confinement, while the vertical confinement is dictated by the refractive index contrast between the waveguide core and cladding layers. Figure 2.10 (a) and (b) show the two primary types of ridge waveguides based on shallow etched and deep etched, respectively. In shallow etched waveguides, the etching extends only to a depth between the original surface and the upper edge of the active region, resulting in a weaker refractive index contrast. This design offers smoother mode profiles and lower scattering losses, making it suitable for applications requiring high beam quality [70].

Conversely, deep etched waveguides are etched pass through the active region, creating a stronger refractive index contrast. This provides more robust lateral confinement, enabling single mode operation even in wider waveguides. However, the increased etching depth may introduce defects into QWs when etching and cause higher scattering losses and fabrication complexity. In this thesis, all the fabricated semiconductor lasers are based on shallow-etch waveguides.

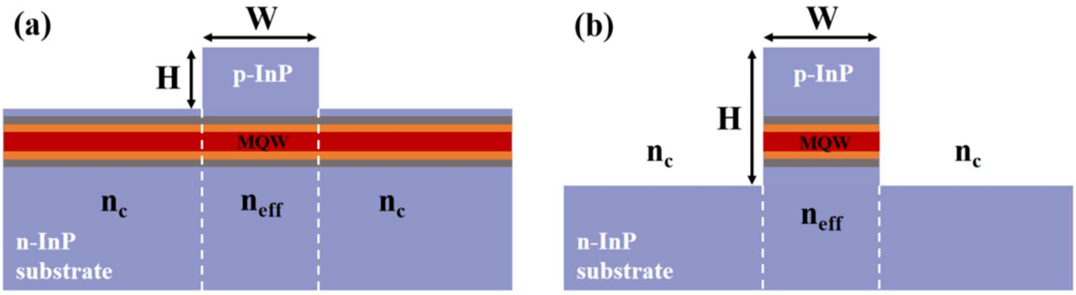

Figure 2.10: Cross-sectional schematics of (a) a shallow-etched waveguide and (b) a deep-etched waveguide, where n_{eff} represents the effective refractive index of the optical mode, and n_c denotes the refractive index of the surrounding cladding layer.

2.2.2.2 Effect of Waveguide Width

The width of the ridge waveguide determines the lateral optical mode size and strongly influences the beam quality and coupling efficiency. Similarly, Figure 2.11 shows the two primary types of ridge waveguides based on the waveguide width: narrower waveguides and wider waveguides.

Narrower waveguides generally support single mode operation by suppressing higher-order modes, making them ideal for applications requiring high spatial coherence. However, overly narrow waveguides can result in increased propagation losses due to enhanced mode overlap with the etched sidewalls.

In contrast, wider waveguides allow for higher optical power by supporting larger optical modes, but they may also permit higher-order mode propagation, leading to reduced spatial coherence. To achieve optimal performance, the waveguide width is typically designed within a range that balances single-mode operation and acceptable power levels.

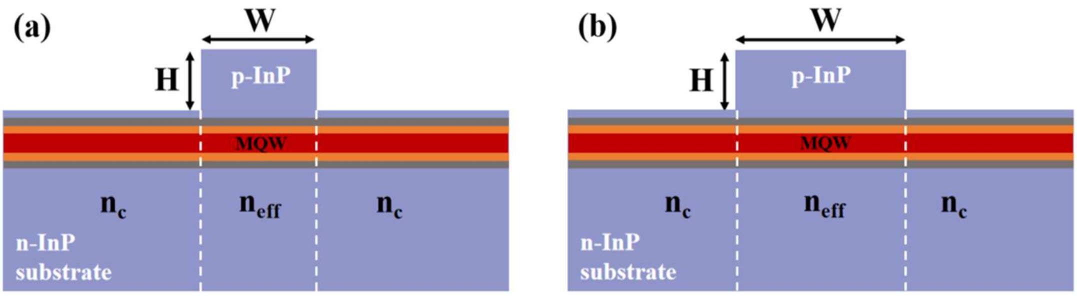

Figure 2.11: Cross-sectional schematics of ridge waveguides with (a) a narrower waveguide; and (b) a wider waveguide. n_{eff} denotes the effective refractive index of the middle waveguide, and n_c represents the refractive index of the left and right waveguides.

The design and performance of shallow-etched waveguides were simulated using *RSoft BeamPROP*, a 3D Beam Propagation Method (BPM) simulator, to calculate the mode field profile and effective refractive index. For this material system, simulations indicate that an effective index contrast Δn is achieved when the ridge waveguide is shallow etched down to the top of the optical core layer, corresponding to an etch depth of 1920 nm. This depth aligns with the first Al-containing layer, which serves as a dry etch stop layer. At this etch depth, the simulations yield ridge and cladding effective indices of n_{eff}=3.201 and n_c=3.166, respectively, resulting in an index contrast of Δn=0.035. This contrast provides sufficient optical confinement while ensuring manufacturability and robustness during fabrication.

Based on this optimised waveguide design, simulations were performed to analyse the modal behaviour for a DFB laser with a compressively strained QW structure. At a lasing wavelength of 1550 nm, the effective refractive index was simulated as a function of ridge width for the fundamental, first-order, and second-order transverse electric (TE) modes, as shown in Figure 2.12. The results indicate that the modal effective index increases with ridge width for a specific TE mode. For a fixed ridge width, higher-order modes exhibit a lower effective index than the fundamental mode.

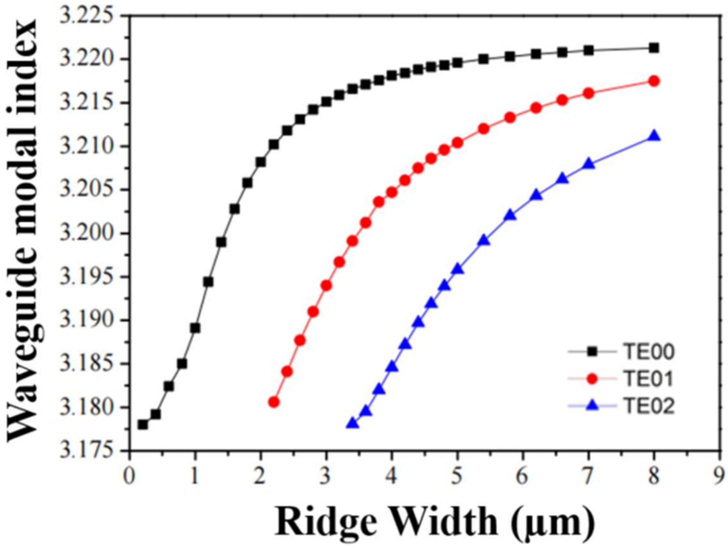

Figure 2.12: Waveguide modal effective index versus ridge width for the fundamental, 1st- and 2nd-order TE modes at a wavelength of 1550 nm.

From the simulation results, it is observed that only the fundamental TE mode is supported when the ridge width is 2 μm or less. Considering fabrication tolerances and single-mode operation requirements, a ridge width of 2.5 μm was chosen for the semiconductor lasers in this work.

Figure 2.13 illustrates the simulated fundamental optical mode for a shallow etched ridge waveguide, based on the wafer structure presented in Fig. 2.6, with a ridge width W of 2.5 μm and an etch depth H of 1920 nm. The results confirm that the optical mode is effectively confined within the shallow etched ridge, ensuring stable single-mode operation. The modal effective index for this configuration is simulated to be 3.206, which is significantly higher than the cladding refractive index ($n_{cladding}$=3.166). This result demonstrates that most of the optical field is well confined within the waveguide core. At this ridge width, only the fundamental TE mode supports lasing, effectively suppressing the propagation of higher-order modes. This ensures efficient light confinement, robust single-mode operation, and stable optical guidance within the waveguide.

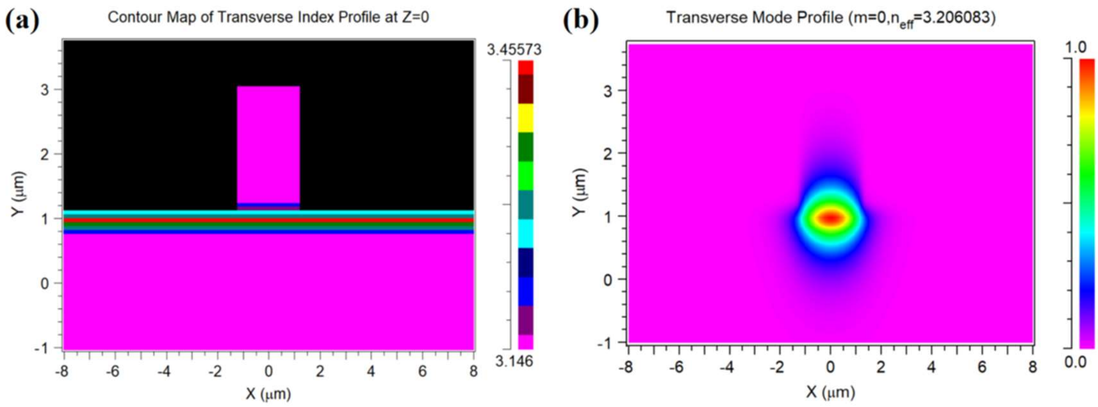

Figure 2.13: (a) Cross-sectional schematics and (b) its simulated fundamental optical mode for a shallow-etched ridge waveguide with a 2.5 μm wide, 1920 nm deep ridge.

2.2.2.3 Effect of Waveguide Length

In FP lasers, longitudinal modes are spaced according to the cavity length, with the mode spacing Δv given in Equation 2.2. Shorter cavities lead to wider mode spacing, which helps suppress multiple longitudinal modes and increases the likelihood of single-mode operation.

In contrast, longer cavities have narrower mode spacing, allowing more longitudinal modes to oscillate within the gain bandwidth. While shorter cavities are advantageous for single mode operation and applications requiring high spectral purity, longer cavities are preferred in high power applications where minimising the threshold current is crucial [71].

FP lasers can be optimised by carefully designing the waveguide width, depth, and cavity length to achieve efficient optical confinement and stable lasing operation. Their structural simplicity and ease of fabrication have made them widely utilized in applications such as low-cost optical communication systems, sensing light sources, and basic photonic integration.

2.2.3 Distributed Feedback Laser

However, the inherent limitations of FP lasers make them unsuitable for applications requiring high spectral purity or precise wavelength control. Due to their cavity design, FP lasers naturally support multiple longitudinal modes, resulting in a multi-mode output spectrum. Additionally, their lasing wavelength is determined by the cavity length and material gain profile, offering limited flexibility for precise wavelength selection. These characteristics make FP lasers less ideal for advanced applications such as DWDM in optical communications or high-resolution spectroscopy, where single mode operation is critical.

To overcome these limitations, DFB lasers were developed. Unlike FP lasers, which rely on cleaved facet reflections for feedback, DFB lasers incorporate a periodic grating structure within the waveguide, enabling wavelength-selective feedback. This structure can ensure that only one longitudinal mode is amplified, providing single-mode operation with high spectral purity and wavelength stability [72].

The grating in a DFB laser is formed by a periodic variation of the refractive index along the waveguide, typically achieved by etching the semiconductor material or introducing periodic perturbations above the core layer for buried gratings. This structure enables distributed Bragg reflection, providing wavelength-selective feedback along the cavity. When light propagates through the waveguide, only wavelengths satisfying the Bragg condition experience constructive interference and are reflected into the cavity, while other wavelengths are suppressed. The Bragg condition depends on the grating period and the effective refractive index, allowing precise control over the lasing wavelength [73].

By leveraging this effect, compared to FP lasers, DFB lasers eliminate the reliance on cavity length for wavelength selection, providing superior spectral stability and tunability. To understand how the grating achieves wavelength-selective feedback, it is necessary to delve into the theory of Bragg grating reflection, which governs the fundamental operation of DFB lasers.

2.2.3.1 Theory of Bragg Grating Reflection

The fundamental principle of DFB lasers lies in the wavelength-selective feedback provided by the periodic Bragg grating embedded within the waveguide structure. The periodic refractive index modulation induces Bragg reflection, where only wavelengths satisfying the Bragg condition experience strong feedback and constructive interference, enabling single-mode operation. The precise lasing wavelength in DFB lasers is inherently governed by the grating period, coupling coefficient, and refractive index contrast, allowing fine-tuned spectral control [73].

Bragg grating is created by periodically modulating the refractive index along the waveguide, forming alternating high-index n_1 and low-index n_2 regions. This periodic structure induces distributed reflection, where the index contrast $\Delta n = n_1 - n_2$ determines the strength of the grating and its ability to reflect light.

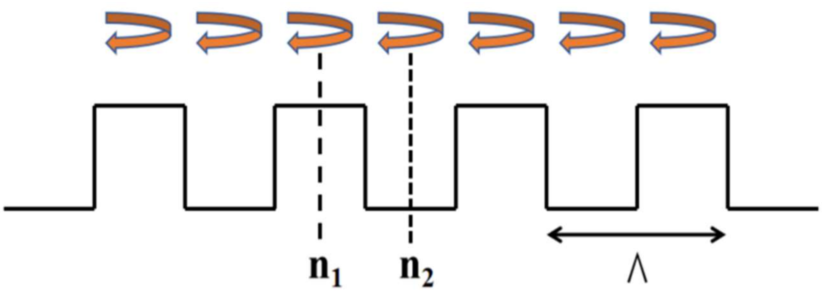

Figure 2.14: Schematic of a Bragg grating, showing periodic refractive index modulation with high index n_1 and low index n_2 regions. The grating period Λ determines the reflected wavelength based on the Bragg condition.

As illustrated in Figure 2.14, the periodic variation of the refractive index creates a series of alternating high- and low-index regions, spaced by the grating period Λ. Light propagating through the grating undergoes partial reflections at each refractive index interface. When the optical path difference between these reflections corresponds to an integer multiple of the wavelength, constructive interference occurs, reinforcing the reflected wave at that specific wavelength. This phenomenon, known as Bragg reflection, is the key mechanism that enables wavelength-selective feedback in DFB lasers, ensuring stable single mode operation [74].

The condition for constructive interference, known as the Bragg condition, is given by:

$$\lambda_B = \frac{2n_{eff}\Lambda}{m} \tag{2.4}$$

where λ_B is the Bragg wavelength, n_{eff} is the effective refractive index of the waveguide mode, Λ is the grating period, and m is the diffraction order (m is an integer, $m > 0$). For DFB semiconductor lasers, the first-order grating ($m = 1$) for wavelength resonance is often adopted, because it has the largest coupling efficiency.

2.2.3.2 Transfer Matrix Method

A Bragg grating, with its periodic refractive index variations, can be approximated as a multilayer stack of alternating high- and low-index regions. Partial reflections and phase shifts at each interface shape its optical behaviour. The transfer matrix method (TMM) efficiently models light propagation through this structure, accounting for reflections, phase shifts, and transmission at each layer.

The core idea of TMM is to mathematically describe light propagation through each layer of a periodic structure while accounting for transmission and reflection at each interface. Each layer in the grating is associated with a transfer matrix that relates the electric field components on either side of the interface [75]. By cascading these individual matrices, a global transfer matrix is obtained, allowing the overall optical properties of the grating to be determined. To further analyse light behaviour in periodic waveguides, coupled mode theory (CMT) provides an alternative yet complementary framework [73]. CMT describes how forward- and backward-propagating optical waves interact within a modulated structure and can be derived from the general electromagnetic wave equation governing the propagation of the electric field. The following derivation starts from Maxwell's equations, leading to the coupled mode equations that describe Bragg grating interactions [76]:

$$\frac{d^2E}{dz^2} + \beta_0^2 E = 0 \tag{2.5}$$

where E is the sum of the forward and backward propagating electric fields. For a free space wavelength λ_b, the free space propagation constant k_0, only considering the first order grating, m = 1, can be described as:

$$k_0 = \frac{2\pi}{\lambda_b} \tag{2.6}$$

If we use n(z) as the refractive index changing along the propagating direction z, the Bragg propagation constant β_0 can be written as:

$$\beta_0 = n(z)k_0 \tag{2.7}$$

And if we use R(z) and S(z) representing forward and backward propagating electric field magnitudes, the general solution of the electric field $E(z)$ can be given as:

$$E(z) = R(z)e^{(-j\beta_0 z)} + S(z)e^{(j\beta_0 z)} \tag{2.8}$$

For DFB semiconductor lasers, the difference between high-index n_1 and low-index n_2 is relatively small, meaning that the refractive index $n(z)$ changes gradually along the propagation direction. As a result, the optical field components, including the electric field E(z), forward-propagating wave S(z), and backward-propagating wave R(z), also vary slowly along the waveguide. To simplify analysis, it is reasonable to approximate that within small segments of the Bragg grating, the refractive index n(z) and field distribution $E(z)$ remain nearly constant. This assumption forms the basis of the TMM, allowing the grating to be treated as a series of discrete layers with uniform properties. A key parameter in this model is the coupling coefficient κ, which quantifies the strength of interaction between the Bragg grating and the propagating optical modes. The coupling coefficient depends on the grating's refractive index contrast, period, and duty cycle. When the grating has a duty cycle of 0.5, meaning that the high- and low-index regions occupy equal lengths within one period, κ can be expressed as [77]:

$$\kappa = \frac{(n_2^2 - n_1^2)\Gamma_{x,y}}{2n_{eff}^2 \Lambda_0} \tag{2.9}$$

where $\Gamma_{x,y}$ is the optical confinement factor of the mode to the grating area. Based on the coupled-mode theory, there is a set of equations known as the coupled-wave equations [76]:

$$\frac{dR}{dz} + j\Delta\beta R = -j\kappa S \tag{2.10}$$

$$\frac{dS}{dz} + j\Delta\beta S = -j\kappa R \tag{2.11}$$

where $\Delta\beta$ is the detuning around β_0, with $\Delta\beta << \beta_0$. When the coupling coefficient κ = 0, meaning there is no periodic modulation of the refractive index, the forward and backward propagating waves remain completely independent and do not exchange energy. However, in DFB structures, the periodic grating introduces coupling, allowing energy transfer between the two modes. For a uniform Bragg grating of length L, starting from z = 0, the coupled-wave equations that describe this interaction can be expressed as[78]:

$$R(L) = [\cosh(\gamma z) - \frac{j\Delta\beta}{\gamma}\sinh(\gamma z)]R(0) - \frac{j\kappa}{\gamma}\sinh(\gamma z)S(0)] \tag{2.12}$$

$$S(L) = \frac{j\kappa}{\gamma}\sinh(\gamma z)R(0) + [\cosh(\gamma z) + \frac{j\Delta\beta}{\gamma}\sinh(\gamma z)]S(0) \tag{2.13}$$

where $\gamma^2 = \kappa^2 - \Delta\beta^2$. These equations can be written in the matrix form:

$$\begin{bmatrix} R(L) \\ S(L) \end{bmatrix} = T \begin{bmatrix} R(0) \\ S(0) \end{bmatrix} \tag{2.14}$$

T is called the transfer matrix, where:

$$T=\begin{bmatrix}\cosh(\gamma z)-\dfrac{j\Delta\beta}{\gamma}\sinh(\gamma z) & -\dfrac{j\kappa}{\gamma}\sinh(\gamma z)\\ \dfrac{j\kappa}{\gamma}\sinh(\gamma z) & \cosh(\gamma z)+\dfrac{j\Delta\beta}{\gamma}\sinh(\gamma z)\end{bmatrix} \tag{2.15}$$

As an approximation, the Bragg gratings can be divided into many sections. In each section, the gratings are seen as uniform and can be represented by a typical transfer matrix.

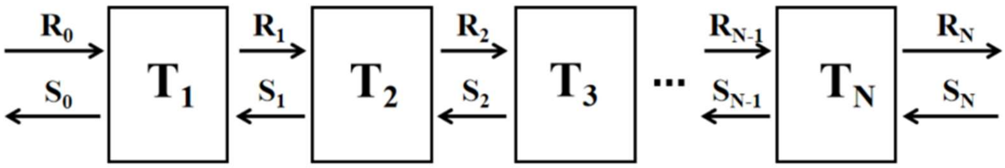

Figure 2.15: Transfer matrix representation of a Bragg grating, where the structure is divided into *N* quasi-uniform sections. Each section is modelled by a transfer matrix T_i, relating the forward R_i and backward S_i propagating waves.

Figure 2.15 illustrates the transfer matrix representation of a Bragg grating, where the entire structure is divided into N sections. Each section is assumed to be quasi-uniform, meaning that within each segment, the refractive index can be approximated as constant. This segmentation allows the grating to be analysed using the TMM, where each section is characterised by a transfer matrix T_i that relates the forward R_i and backward propagating S_i optical waves. For an individual section i, the relationship between the input and output wave amplitudes can be expressed as:

$$\begin{bmatrix}R_i\\ S_i\end{bmatrix}=T_i\begin{bmatrix}R_{i-1}\\ S_{i-1}\end{bmatrix}(i=1,2\ldots N) \tag{2.16}$$

Then, we can obtain

$$\begin{bmatrix}R_N\\ S_N\end{bmatrix}=T_1*T_2*T_3*\ldots*T_N*\begin{bmatrix}R_0\\ S_0\end{bmatrix}=T\begin{bmatrix}R_0\\ S_0\end{bmatrix} \tag{2.17}$$

where the transfer matrix $T = T_1 * T_2 * T_3 \ldots * T_N$. By cascading the transfer matrices of all sections, the overall optical response of the Bragg grating can be determined, including its reflection and transmission characteristics. The TMM serves as a powerful mathematical framework for designing and analysing Bragg gratings, enabling precise control over their reflection and transmission properties. In this thesis, the TMM will be applied to evaluate the reflection and transmission properties of Bragg gratings.

2.2.3.3 Uniform Grating

The design process begins with selecting the target Bragg wavelength, which is determined by the intended operational wavelength of the laser. This choice is critical, as it dictates the material system, which in turn influences the grating period and refractive index, both essential parameters for achieving optimal wavelength selectivity and feedback strength [79].

Once the wavelength is chosen, the next step in Bragg grating design is to define the grating structure that provides the desired wavelength selectivity and mode control. The uniform grating represents the simplest and most widely used configuration, particularly for first-order gratings with a 0.5 duty cycle, which maximise the coupling coefficient and provide strong feedback for single-mode operation. According to Equation 2.1, the Bragg wavelength λ_b of the uniform grating can be designed by adjusting the grating period Λ and the effective refractive index n_{eff}. For example, assuming the refractive index of the material is 3.201, the grating period Λ of 242 nm is chosen to target the gain peak of the semiconductor material, which is centred around 1550 nm.

Figure 2.16 presents a simplified schematic of a typical DFB laser structure, where alternating high n_1 and low n_2 refractive index regions are arranged with a fixed grating period Λ and a 0.5 duty cycle.

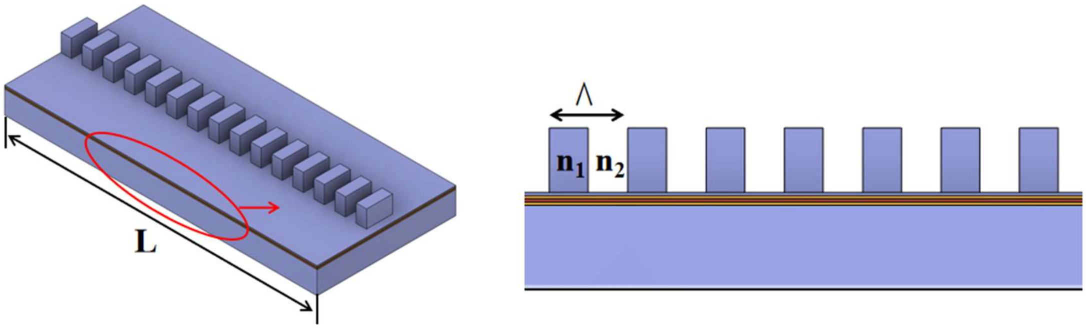

Figure 2.16: The typical structure of a uniform grating(left) and its cross-section(right).

In FP lasers, the cavity length L determines the resonant wavelengths, leading to multimode output and lower spectral stability. In contrast, DFB lasers achieve precise wavelength control by satisfying the Bragg condition [76]:

$$\lambda_B = 2n_{eff}\Lambda \tag{2.18}$$

To better illustrate the differences between FP and DFB laser structures, we can compare their reflectivity spectra. The key spectral characteristics include the width of the reflectivity spectrum (commonly referred to as the stop band of the grating) and the peak reflectivity at the Bragg wavelength. From the coupled-wave Equations 2.12 and 2.13, and considering that $\Delta\beta = \frac{2\pi n_{eff}}{\lambda} - \frac{2\pi n_{eff}}{\lambda_b}$ and $\gamma^2 = \kappa^2 - \Delta\beta^2$, the behaviour of a Bragg grating as a wavelength-dependent reflector can be described by its power reflectivity $R(\lambda)$:

$$R(\lambda) = \frac{\kappa^2 \sinh^2(\gamma L)}{\Delta\beta^2 \sinh^2(\gamma L) + \gamma^2 \cosh^2(\gamma L)} \tag{2.19}$$

At the central wavelength λ_b, reflection occurs with a path difference of 2Λ, satisfying the Bragg condition. This ensures that all reflected waves remain in phase, resulting in maximum constructive interference and the highest reflectivity. At this point, the detuning parameter becomes $\Delta\beta = 0$ and $\gamma^2 = \kappa^2$. Thus, the maximum reflectivity is given by:

$$R_{\max} = \tanh^2(\kappa L) \tag{2.20}$$

Equation 2.20 shows that the magnitude of reflection at λ_b is determined only by the κL product. This dimensionless parameter, known as normalised coupling coefficient κL, determines the overall performance of the grating. By characterising the interaction between the κ and L, it enables a generalised analysis applicable to gratings with varying coupling coefficients and lengths. Figure 2.17 illustrates the relationship between peak power reflectivity R(λ_B) as a function of κL.

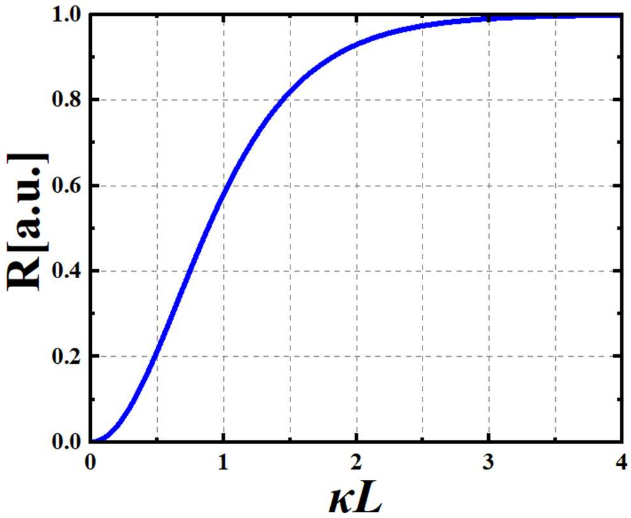

Figure 2.17: The relationship between peak power reflectivity R(λ_B) as a function of κL.

After finalizing all parameter settings, the TMM can be employed to compute the optical reflectivity spectra of uniform Bragg gratings using MATLAB simulations. In this simulation, a grating period Λ of 242 nm and an effective refractive index n_{eff} of 3.201 are used to align with a Bragg wavelength λ_B near 1550 nm. The coupling coefficient κ is set to 100 cm^{-1}, with a grating length L of 400 μm ensuring a sufficiently high κL product to achieve strong wavelength-selective feedback, and the refractive index contrast Δn is set at 0.02, ensuring a well-defined stop band in the reflectivity spectrum.

Figure 2.18 presents the reflectivity spectrum of a simulated uniform Bragg grating, featuring a main reflectivity peak at 1550 nm, demonstrating strong feedback at the designed wavelength. However, in this configuration, the reflected light does not exclusively support a single longitudinal mode. As shown in the inset plot, two symmetric modes on either side of the grating centre compete for dominance due to the uniform grating providing equal feedback for both. This mode competition arises from the lack of a mechanism to break degeneracy between these modes, leading to ambiguity in the lasing wavelength in practical operation [80, 81].

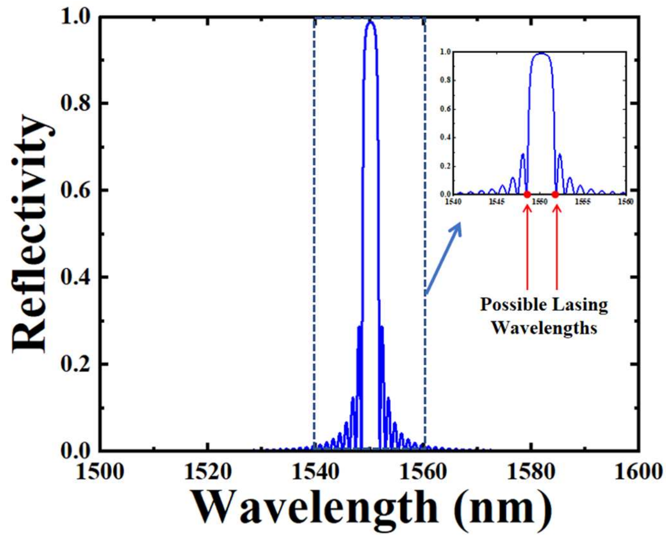

Figure 2.18: Simulated reflectivity spectrum of a uniform Bragg grating, showing the main reflectivity peak at 1550 nm. The inset highlights the presence of symmetric competing modes, leading to ambiguity in lasing wavelength.

2.2.3.4 Single Mode Lasing

To achieve stable single-mode lasing, it is necessary to introduce mechanisms that selectively enhance one longitudinal mode while suppressing others. Two common methods are shown in Figure 2.19(a) and (b). One approach involves using a nonuniform waveguide structure while keeping the grating structure unchanged. In this case, changing the waveguide width modifies the effective refractive index within the phase-adjustment region, thereby influencing mode selection conditions. The shift in effective refractive index depends on the length of the adjustment region and the difference in strip widths (W_2-W_1), where W_1 represents the original waveguide width and W_2 corresponds to the widened section. This requires precise control over the phase-adjustment region to ensure stable single-mode lasing [82, 83].

Another method introduces a phase shift at the grating centre, creating a localized phase discontinuity by modifying the periodic structure. This is typically achieved by shifting the grating pattern within a specific region, effectively altering the feedback conditions and ensuring stable single-mode operation [84]. In this work, we adopt the second method, as it allows for greater design flexibility, ease of fabrication, and precise control over the lasing wavelength in DFB lasers.

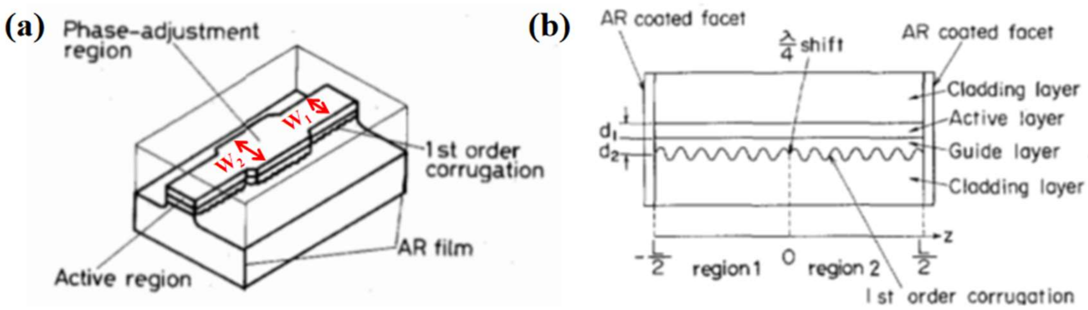

Figure 2.19: To achieve stable single mode lasing of the DFB laser by (a) uniform grating but non-uniform waveguide width [83], or (b) a phase shift at the grating cavity centre [84].

Building upon the second method approach, to achieve single-mode lasing is to introduce a π-phase shift (also called a quarter-wavelength phase shift) at the centre of the grating cavity. This phase shift can be implemented by shifting the right half of the uniform Bragg grating by half of the grating period Λ/2. By doing so, the symmetry of the feedback structure is altered, effectively suppressing unwanted modes and ensuring that only a single longitudinal mode dominates the lasing operation. The mathematical representation of this phase-shifted Bragg grating is given by the following equations:

$$\Delta n(z) = \frac{1}{2}\Delta n \begin{cases} \exp(j\dfrac{2\pi z}{\Lambda}) + c.c & (0 \le \mathrm{z} \le \mathrm{z}_0) \\ \exp(j\dfrac{2\pi(z+\Lambda/2)}{\Lambda}) + c.c & (\mathrm{z} > \mathrm{z}_0) \end{cases} \tag{2.21}$$

Which is

$$\Delta n(z) = \frac{1}{2}\Delta n \begin{cases} \exp(j\frac{2\pi z}{\Lambda}) + c.c & (0 \le z \le z_0) \\ \exp(j\frac{2\pi z}{\Lambda}) \cdot \exp(j\pi) + c.c & (z > z_0) \end{cases} \tag{2.22}$$

z_0 is the centre position of the uniform Bragg grating. By introducing a π-phase shift at this position, single mode lasing can occur at the Bragg wavelength. Different movement directions (right or left) correspond to a positive or negative π-phase change at the centre of the grating. Figure 2.20 illustrates a simplified schematic of a Bragg grating with a π-phase shift, where the grating exhibits a half-period shift at the centre of the structure.

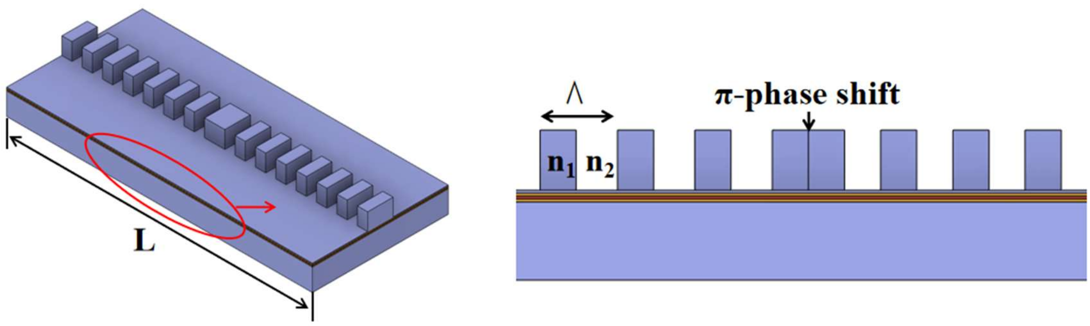

Figure 2.20: (a)The typical structure of a uniform grating with a π-phase shift, where the grating exhibits a half-period shift at the centre of the structure, and (b)its cross-section.

When the phase shift is introduced within the transmission matrix framework, the Bragg grating becomes discontinuous at the phase-shift point, leading to the incorporation of a new phase change matrix. This additional matrix accounts for the abrupt phase discontinuity, ensuring that the modified reflectivity and transmission properties are accurately captured. The single phase-shift matrix T_φ is defined as [77]:

$$T_\varphi = \begin{bmatrix} e^{-j\varphi/2} & 0 \\ 0 & e^{j\varphi/2} \end{bmatrix} \tag{2.23}$$

φ represents the phase shift introduced at a specific point in the grating, and the transmission matrix corresponding to an arbitrary phase shift can be expressed as:

$$T_1 * T_2 * \ldots * T_{\varphi} * \ldots * T_{\mathrm{N}} \tag{2.24}$$

Figure 2.21 compares the reflectivity spectra of a uniform Bragg grating and a π-phase-shift Bragg grating, both designed with the same grating period. In the π-phase-shift Bragg grating, a localised phase discontinuity in the centre of the structure significantly alters the reflectivity characteristics. Unlike the uniform Bragg grating, which exhibits a high reflectivity peak at λ_B, the π-phase shift creates a transmission peak at λ_B, resulting in zero reflectivity at the centre of the spectrum. This effect causes only a single longitudinal mode to resonate within the cavity, which is essential for stable single mode lasing.

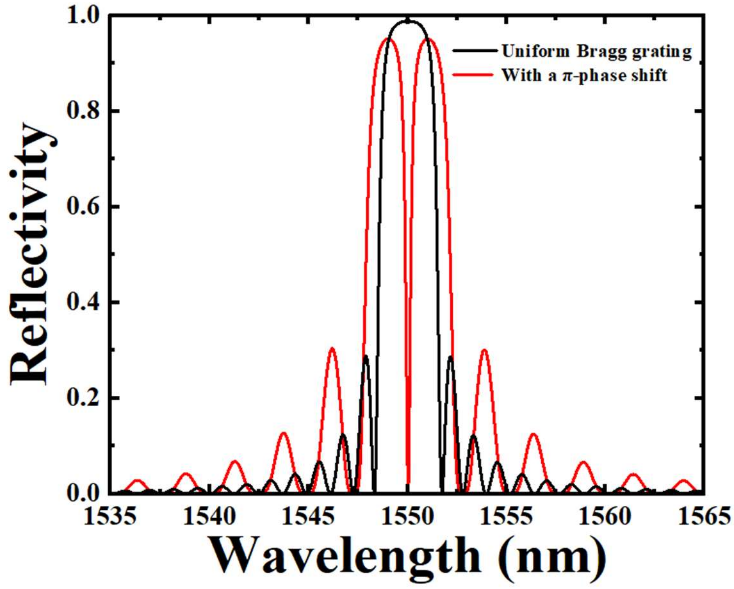

Figure 2.21: Comparison of reflectivity spectra for a uniform Bragg grating (black line) and a π-phase shift Bragg grating(red line).

With this design, the reflectivity at the central wavelength is minimised, allowing preferential lasing at this wavelength while suppressing side modes, which ensures stable, single-mode operation at the designed lasing wavelength. The resulting high spectral purity and wavelength stability are crucial for optical communication systems, where narrow linewidths and precise wavelength control are required to minimise crosstalk and phase noise.

2.2.4 DFB Laser with Narrow Channel Spacing.

After obtaining a single mode DFB laser, the next step is to use it in the DWDM system, achieving multiple signals are transmitted simultaneously over a single optical fibre with narrow channel spacing (typically is 0.8 nm).

2.2.4.1 Limitation of Uniform Grating

With current photolithography technologies, uniform gratings face inherent limitations in achieving the precise wavelength control and narrow linewidths required for DWDM. For instance, according to Equation 2.4, the difference of Bragg wavelength $\Delta\lambda_B$ can be expressed as,

$$\Delta\lambda_B = 2 \cdot \Delta\Lambda \cdot n_{eff} \tag{2.25}$$

$\Delta\Lambda$ is the difference in grating period. In a DWDM system with a channel spacing of 0.8 nm, which means $\Delta\lambda_B$ equals 0.8 nm. Suppose n_{eff} is equal to 3.2, $\Delta\Lambda$ should be 0.125 nm, where the grating period difference is often defined by electron beam lithography (EBL). However, this level of precision exceeds the resolution limits of current EBL, which can achieve a maximum accuracy of approximately 0.5 nm [85].

If a uniform grating structure is directly used to design a DWDM laser array, fabrication variations, such as fluctuations in the grating period, can introduce errors that further degrade its performance. These inaccuracies make it challenging to meet the stringent wavelength tolerances of ±0.1 nm (< 10%) typically required in DWDM systems.

2.2.4.2 Possible Solutions

To overcome the challenges associated with achieving the precise wavelength spacing required for DWDM, which cannot be solely controlled by adjusting the grating period, researchers have explored alternative optimisation strategies. Two approaches can be derived from Equation 2.25. The first involves modifying the refractive index to change the effective Bragg wavelength, while the second focuses on enhancing the resolution capability of EBL to improve fabrication precision.

The first method to controlling the lasing wavelength is by adjusting the refractive index, which can be achieved through waveguide width modulation. This technique was first reported by Bell Northern Research in 1995 [86], followed by the development of a 16-wavelength gain-coupled DFB laser array in 1996, where each laser was equipped with an integrated thin-film thermal resistor for wavelength tuning [87]. In this design, the ridge waveguide width was varied from 1.6 μm to 5.2 μm, enabling a comprehensive thermal tuning range with a wavelength spacing of 0.8 nm. The corresponding device structure and wavelength coverage of each channel are illustrated in Figure 2.22. However, this method presents several limitations. Firstly, the variation in ridge waveguide width introduces non-uniform optical confinement across the laser array, leading to inconsistencies in mode profiles, threshold currents, and output power. Secondly, precise wavelength control remains difficult, as fabrication tolerances and process variations can cause deviations from the intended refractive index modulation. Additionally, the reliance on thermal tuning for wavelength adjustment increases power consumption and may introduce long-term wavelength drift, reducing the overall stability and reliability of the laser array in DWDM applications.

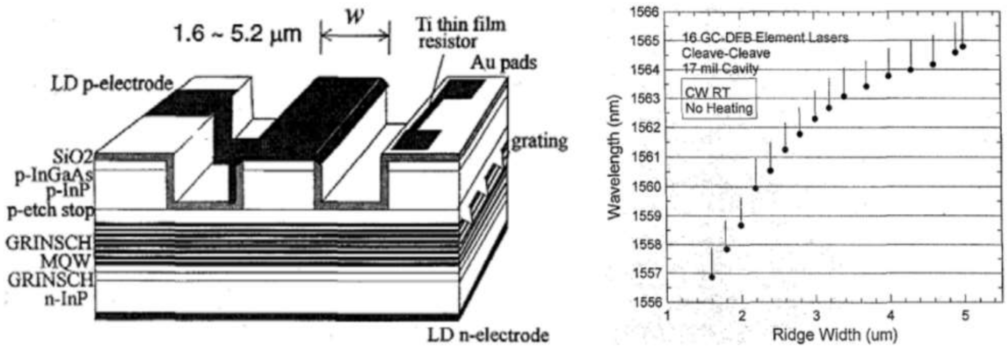

Figure 2.22: 16-wavelength gain-coupled DFB laser array [87].

Another method is to enhance the resolution of EBL. In 2000, NEC Corporation of Japan reported a monolithic 8-wavelength DFB laser array integrated with an electro-absorption (EA) modulator, fabricated using narrow strip selective epitaxy technology (Fig. 2.23) [88]. This multi-wavelength laser array was realised through direct electron beam exposure, where an improved weighted dose distribution technique enabled variable-period gratings with a resolution of 0.025 nm. This high-precision control over the grating period allowed for highly accurate wavelength selection. With additional temperature tuning, the integrated device covered the ITU wavelength range of 1552.5–1567.8 nm, supporting 40 channels with 50 GHz spacing. However, this method imposes extremely stringent requirements on electron beam exposure processing, demanding high-end EBL systems and meticulous process control. Furthermore, extensive experimental optimisation is required to achieve the ideal grating period variation, making the fabrication process complex and time-consuming.

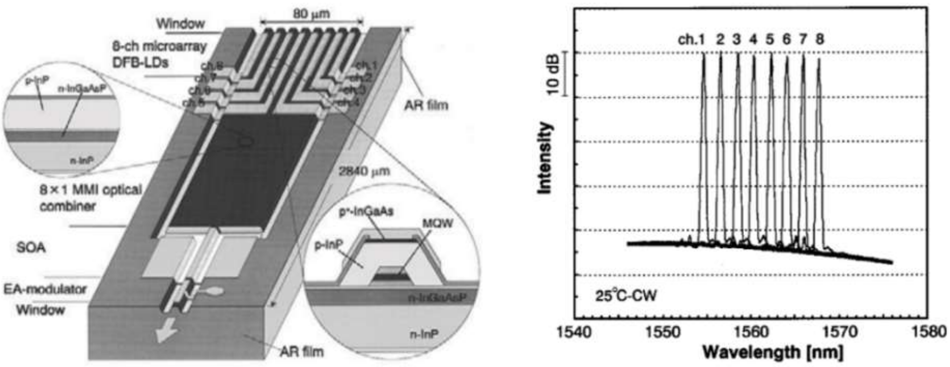

Figure 2.23: Monolithic 8-wavelength DFB laser array and EAM integrated chip [88].

Two different approaches provide potential solutions for achieving the precise wavelength spacing required in DWDM systems. However, both methods come with significant limitations. Refractive index modulation requires precise material engineering and introduces fabrication inconsistencies, making it challenging to maintain uniformity across large-scale laser arrays. On the other hand, pushing the resolution limits of EBL demands high-end lithography systems, significantly increasing manufacturing complexity and production costs, while also posing scalability challenges for mass production. Given these constraints, an alternative approach is needed to achieve precise wavelength control in a more scalable and cost-effective manner.

Another innovative approach to achieving precise wavelength control is to optimise grating structures, enabling accurate wavelength selection through structural modifications. In 2014, Nanjing University reported a 16-wavelength DFB laser array fabricated using the different grating structures called sampled Bragg grating (SBG) technique, as shown in Figure 2.24 [89]. This study demonstrated exceptional wavelength control, achieving a measured channel spacing of 0.7944 nm/channel, closely matching the designed value of 0.80 nm/channel. Moreover, most wavelength residuals were within 0.1 nm, meeting the stringent requirements of DWDM systems.

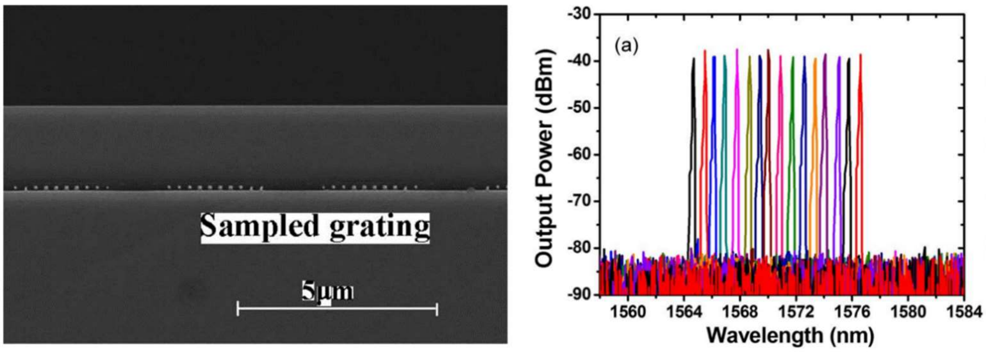

Figure 2.24: 16-Wavelength DFB Laser Array with SBGs Technique [89].

2.2.5 Sampled Bragg grating

2.2.5.1 Principle of Sampled Bragg Grating

To overcome the limitations of uniform gratings in achieving precise wavelength control, researchers have explored alternative grating structures that offer greater design flexibility. Among these, SBG is a practical solution. In DFB semiconductor lasers, first-order Bragg grating periods typically range from several hundred nanometers, making it challenging to achieve narrow wavelength spacing by simply adjusting the grating period. Sampled Bragg gratings provide an effective approach to addressing this limitation [90]. As illustrated in Fig. 2.25(a), a uniform first-order Bragg grating maintains a fixed grating period Λ, whereas Fig. 2.25(b) depicts a traditional sampled Bragg grating, which introduces an additional sampling period *P*.

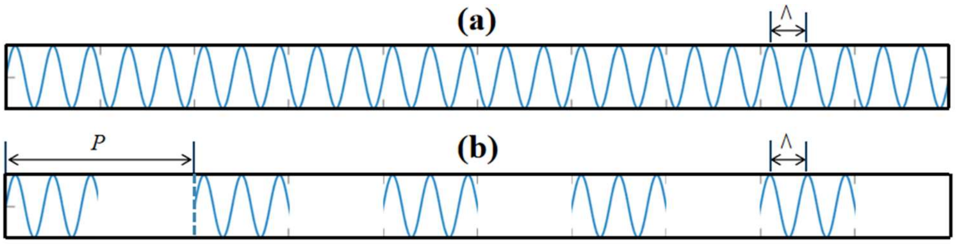

Figure 2.25: Schematics of (a) a uniform Bragg grating, with the grating period Λ, and (b) a uniformly sampled Bragg grating, with the sampling period P.

In SBG, with each sampling period P consisting of alternating sections where the Bragg grating is either present or absent. Therefore, this type of structure can be mathematically represented by describing the refractive index variation along the propagation direction. The total refractive index change $\Delta n_s(z)$ along the propagating direction can be described as [76]:

$$\Delta n_s(z) = \frac{1}{2}\Delta n \exp(j\frac{2\pi z}{\Lambda_0})s(z) + c \cdot c \cdot \tag{2.26}$$

where Δn is the refractive index difference, and $s(z)$ represents the sampling function that defines the periodic modulation of the grating. Since the sampling structure has a sampling period of P, $s(z)$ can be expanded as a Fourier series:

$$s(z) = \sum_m F_m \exp(j\frac{2m\pi z}{P}) \tag{2.27}$$

where m is the order of the Fourier series, and F_m is the corresponding Fourier coefficient. Therefore, substituting this into the expression for $\Delta n_s(z)$, the total refractive index difference variation along z can be rewritten as:

$$\Delta n_s(z) = \sum_m \frac{1}{2}\Delta n F_m \exp(j\frac{2m\pi z}{P} + j\frac{2\pi z}{\Lambda_0}) + c \cdot c \cdot \tag{2.28}$$

which can be transformed into a Fourier series:

$$\Delta n_s(z) = \sum_m \frac{1}{2}\Delta n F_m \exp(j\frac{2\pi z}{\Lambda_m}) + c \cdot c \cdot \tag{2.29}$$

where Λ_m, referred to as the mth-order Fourier sub-grating, is given by:

$$\frac{1}{\Lambda_m} = \frac{m}{p} + \frac{1}{\Lambda_0} \tag{2.30}$$

In this case, Λ_0 can be named the "seed grating".

Compared to uniform gratings, SBGs provide a more effective approach for achieving the 0.8 nm channel spacing required in DWDM applications. The lasing wavelength spacing in SBGs can be precisely controlled by adjusting the sampling period P [91]. The relationship between these parameters is given by the following equation:

$$\Delta\lambda_{ch} = \frac{\lambda_B^2}{2n_{eff}}\left(\frac{1}{P_i} - \frac{1}{P_{i+1}}\right) \tag{2.31}$$

where $\Delta\lambda_{ch}$ is the channel spacing of the DFB laser array, P_i denotes the sampling period of the i^{th} channel. According to Equation 2.31, $\Delta\lambda_{ch}$ decreases as the sampling period of the SBG increases, providing a means to finely adjust the wavelength spacing in DWDM systems. The advent of SBGs has enabled a wider tunable range of lasing wavelengths in comparison to uniform Bragg gratings. Figure 2.26 illustrates a simplified schematic of an SBG.

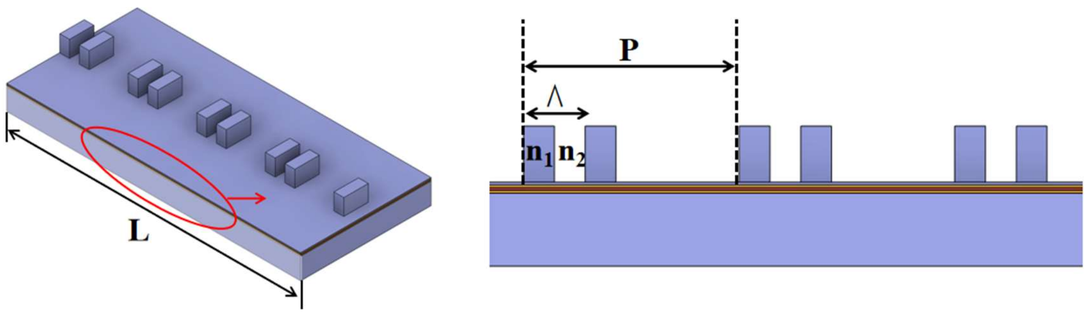

Figure 2.26: The typical structure of sampled Bragg gratings in semiconductors (left) and its cross-section (right).

By using the TMM, the simulated reflectivity spectra of SBGs can be computed using *MATLAB*. Figure 2.27(a) presents the reflectivity spectrum of a uniform Bragg grating, which exhibits a primary reflectivity peak at the Bragg wavelength (0th-order reflectivity peak). In comparison, the reflectivity spectrum of a uniformly sampled Bragg grating, shown in Figure 2.27(b), features multiple higher-order reflectivity peaks. Among these, the ±1st-order reflectivity peaks are usually selected as the operational channels for DFB lasers, as they provide well-defined and stable wavelength selection. The higher-order reflectivity peaks beyond the ±1st order are significantly weaker and can generally be disregarded in practical applications.

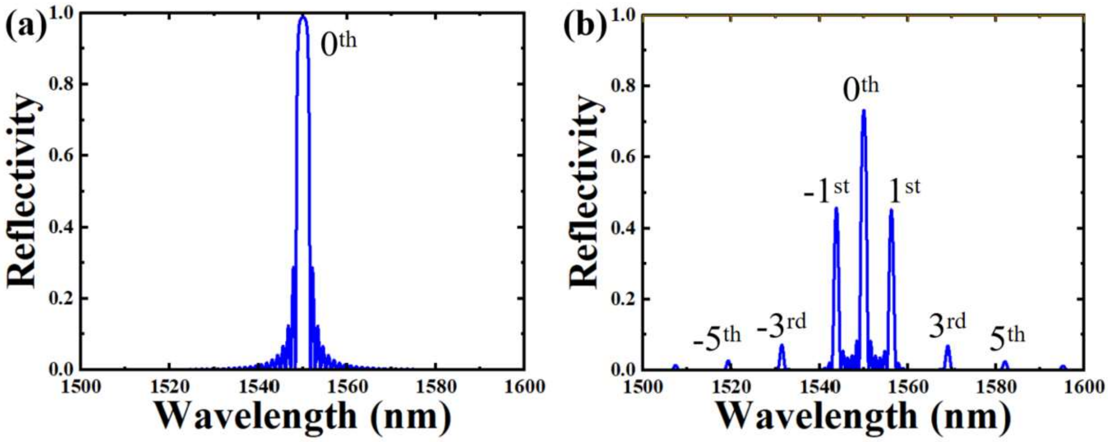

Figure 2.27: Reflectivity spectra of (a) Uniform grating. (b) SBG, where the ±1st-order peaks are used for lasing operation.

2.2.5.2 Sampled Bragg Gratings with Multiple Phase-Shifted Sections

However, as shown in Figure 2.28(b), the simulated reflection spectrum of an SBG reveals that the intensity of the ±1st-order modes is noticeably lower than 50% of the central peak intensity observed in a uniform Bragg grating. This reduction is primarily due to the absence of a grating structure in half of the sampling period. The missing grating regions weaken the effective grating strength and reduce coupling efficiency, leading to lower reflectivity and diminished optical feedback.

Moreover, the conventional SBG (C-SBG) can introduce additional challenges in maintaining a single mode, since the non-grating part of the sampling period produces additional modes in the spectrum. Therefore, while C-SBGs offer a practical solution for wavelength selectivity, their limitations must be addressed to ensure optimal device performance.

To enhance the coupling coefficient κ and reduce the impact of the non-grating part, the remaining half of the sampling period is also filled with gratings that maintain the same grating period, however, incorporate a phase shift θ relative to the original section. This novel structure is an SBG with two phase-shifted sections in one sampling period, which is named as two phase-shifted sampled Bragg grating (2PS-SBG). This design enhances the coupling efficiency and improves mode selectivity by redistributing the grating more effectively. Extending this concept further, three phase-shifted sampled

Bragg grating (3PS-SBG) and four phase-shifted sampled Bragg grating (4PS-SBG) can also be implemented. In general, these structures are referred to as n phase-shifted sampled Bragg gratings (nPS-SBGs), where n denotes the number of phase-shifted sections within a single period [92].

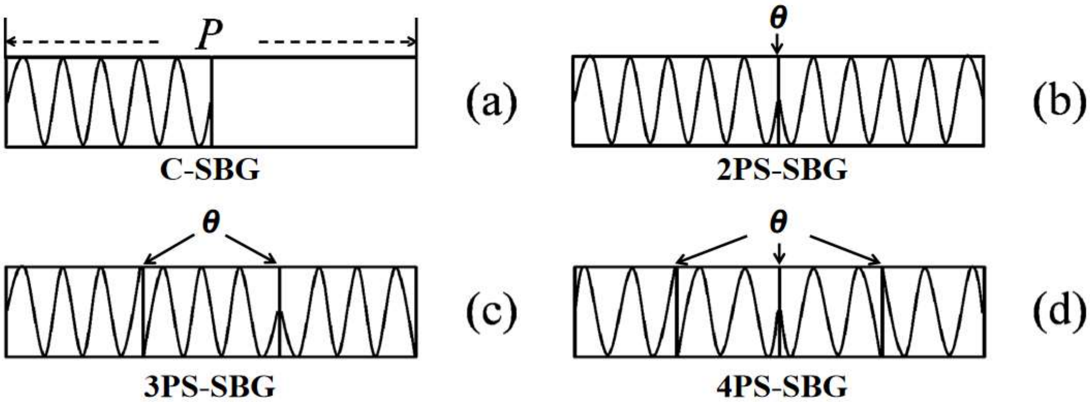

Figure 2.28: The illustration of (a) C-SBG, (b) 2PS-SBG, (c) 3PS-SBG and (d) 4PS-SBG [92].

The primary distinction among these variations lies in the number of segments per period and the relative phase shift introduced between adjacent sections. As illustrated in Figure 2.28, the configurations of C-SBG, 2PS-SBG, 3PS-SBG, and 4PS-SBG are compared, highlighting their structural differences, and the phase shift θ between adjacent sections is defined as:

$$\theta = \frac{2\pi}{n} \tag{2.32}$$

To illustrate this concept more intuitively, Figure 2.29 presents the configuration of a 4PS-SBG, where a single sampling period is divided into four equal sections. Each adjacent grating segment experiences a $\pi/2$-phase shift, effectively redistributing the optical feedback. Unlike C-SBG, which evenly distributes grating and non-grating regions within each sampling period, the nPS-SBG features a fully grating-filled sampling period, with multiple phase shifts strategically inserted and adjusted in both position and amplitude.

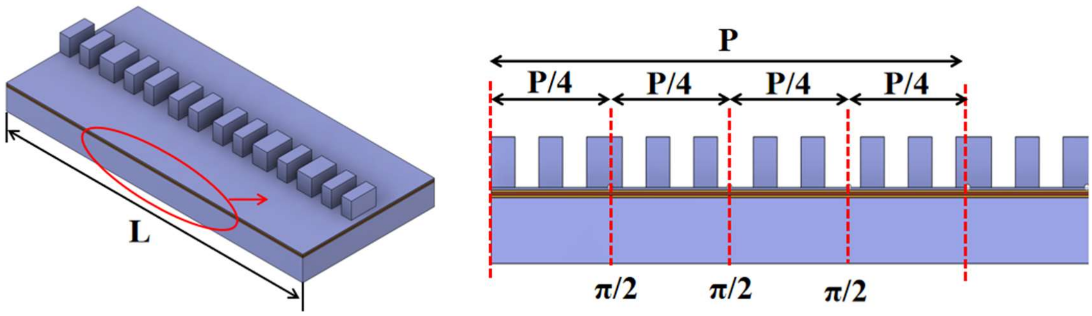

Figure 2.29: The typical structure of 4PS-SBG in semiconductors and its cross-section.

A fixed phase θ introduces at specific intervals along the grating, the phase matrix $T_{\theta,z}$ corresponding to a phase shift θ at point z can be expressed by Equation 2.23 as:

$$T_{\theta,z} = \begin{bmatrix} e^{-j\theta/2} & 0 \\ 0 & e^{j\theta/2} \end{bmatrix} \tag{2.33}$$

Using the TMM algorithm, the phase matrix is incorporated at each corresponding position to compute the reflectivity spectrum of the *n*PS-SBG. For comparison, Figure 2.30 (a) illustrates the spectrum of a C-SBG, and Figure 2.30 (b) presents the spectrum of a 2PS-SBG. In the 2PS-SBG, the 0th-order reflection is completely suppressed, and the effective coupling coefficient κ of the ±1st-order channels is doubled compared to that of the C-SBG. The simulated spectra of 3PS-SBGs and 4PS-SBGs are displayed in Figures 2.30(c) and (d), respectively. In 3PS-SBGs, the reflection of −1st-order and 2nd-order is increased, while the 1st-order and 0th-order reflection is eliminated. For 4PS-SBGs, the -1st order reflectivity grows even higher, and as with 2PS-SBGs and 3PS-SBGs, the 0th order is eliminated. Unlike 3PS-SBGs, the 2nd-order reflection in 4PS-SBG design disappears and the 3rd-order reflection increases. From the simulation results, all SBGs with multiple phase-shifted sections do not have the 0th-order reflection.

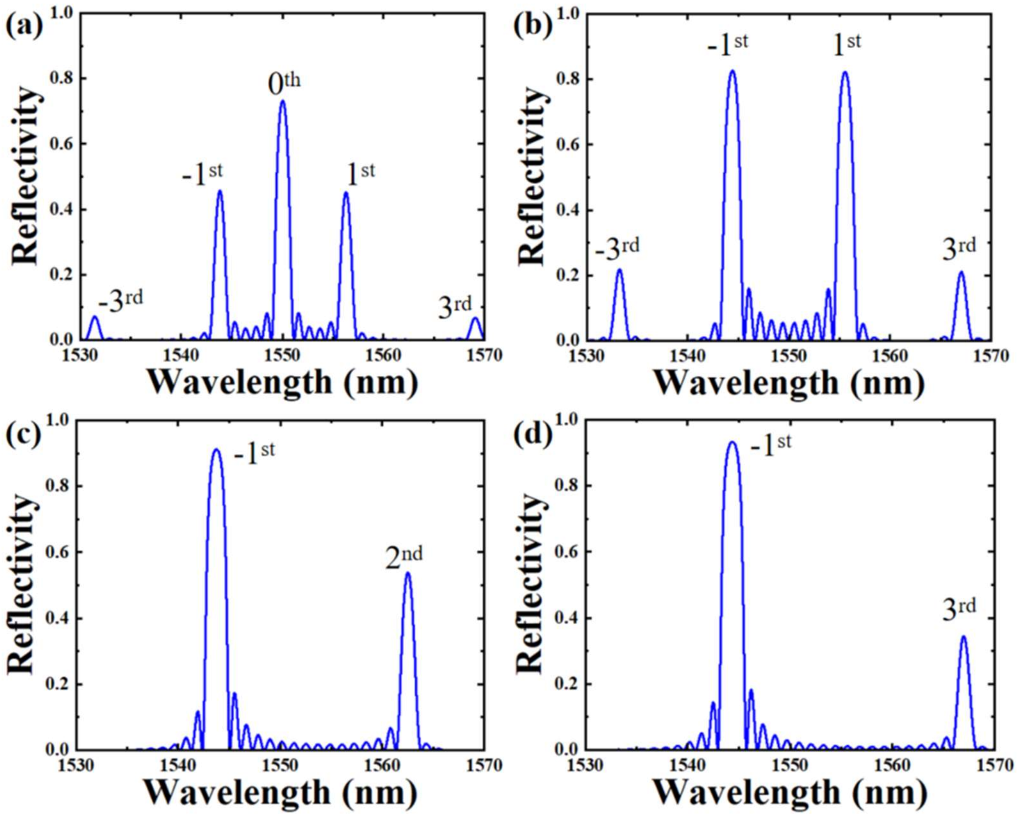

Figure 2.30: Reflectivity spectra of (a) C-SBG, (b) 2PS-SBG, (c) 3PS-SBG and (d) 4PS-SBG.

In *n*PS-SBG design, the ±1st-order reflection peaks are typically selected as the lasing wavelengths, as they offer better control over wavelength selection and stability. To further enhance the wavelength selectivity and suppress interference from undesired reflection orders, a larger seed grating is often employed. This ensures that the 0th-order is kept away from the output, ensuring that only the desired ±1st-order modes dominate lasing operation in the gain area. From Equation 2.30, the grating periods $\Lambda_{\pm1}$ for the ±1st-order subgratings can be derived as:

$$\frac{1}{\Lambda_{\pm1}} = \frac{1}{\Lambda_0} \mp \frac{1}{P} \tag{2.34}$$

which is

$$\Lambda_{\pm1} = \frac{P\Lambda_0}{P \mp \Lambda_0} \tag{2.35}$$

Therefore, by systematically adjusting the P, the lasing wavelength of the ±1st-order modes can be fine-tuned without altering the grating period. This provides a straightforward and effective method for precise wavelength control in laser arrays.

To calculate the coupling coefficient κ of nPS-SBG, the ratio between the effective κ of the mth-order channel and that of uniform gratings can be represented by the Fourier coefficient F_m, whose expression is [76],

$$F_m = \frac{1}{P}\int_0^P s(z)\cdot e^{im\pi z/(p/2)} dz \tag{2.36}$$

Using this equation, we can determine the ratio between the effective κ for SBGs with n phase-shifted sections and that of uniform gratings. Choice F_{-1} to calculate, which is conventionally used as the lasing channel in laser design and fabrication.

$$F_{-1} = \frac{1}{P}\int_0^P s(z)\cdot e^{-i\pi z/(p/2)} dz \tag{2.37}$$

The value of F_{-1} is calculated by *Matlab* for C-SBG, 2PS-SBG, 3PS-SBG and 4PS-SBG. The computed values are summarised in Table 2.1.

Table 2.1 The Effective Coupling Coefficient of Gratings

Number of phase-shifted sections	Effective κ ratio of uniform Bragg grating
C-SBG	1/π (0.32)
2PS-SBG	2/π (0.64)
3PS-SBG	0.83
4PS-SBG	0.90

The design of nPS-SBGs provides a practical approach to precisely control lasing wavelengths for DWDM applications, overcoming the limitations of conventional uniform and standard sampled gratings. With increased coupling efficiency and enhanced spectral selectivity, these structures contribute to the development of high-performance multi-wavelength laser arrays.

2.2.6 DFB Laser with Narrow Linewidth

While precise wavelength control and optimised channel spacing are essential for DWDM systems, another critical challenge is achieving narrow linewidths, as linewidth directly impacts signal quality and system transmission capabilities [93]. In DWDM systems, narrow linewidth lasers enhance signal integrity and spectral efficiency by reducing phase noise and improving coherence. Although they do not directly determine channel spacing, their low phase noise and high spectral purity help minimise inter-channel crosstalk, leading to more stable and interference-resistant transmission.

Beyond communication systems, narrow-linewidth lasers are essential in a wide range of precision applications. They are crucial in fibre-optic sensors, including strain and temperature sensing [94], as well as in interferometric measurements [95]. Additionally, narrow linewidth lasers are employed in trace gas detection using differential absorption lidar [96] and in Doppler lidar for wind speed measurements [97]. The linewidth requirements vary depending on the application; some fibre-optic sensors demand linewidths in the kilohertz range, while applications such as lidar measurement typically require linewidths around 100 kHz. More stringent applications, such as optical frequency metrology, necessitate ultra-narrow linewidths in the sub-10 kHz range [98]. As a result, extensive research has been conducted on laser linewidth reduction techniques, focusing on minimising phase noise and enhancing spectral purity to meet the stringent demands of modern optical systems [99].

2.2.6.1 Theoretical Analysis

The linewidth of a laser refers to the width of its optical spectrum, typically defined by the full width at half maximum (FWHM) [100]. In theory, laser emission is governed by stimulated emission, where light waves are generated through constructive and destructive interference of reflected light within the laser cavity. Ideally, this process should produce a perfectly monochromatic and highly coherent beam, meaning the linewidth should be zero. However, lasers exhibit a finite linewidth due to several broadening mechanisms. The most fundamental cause is spontaneous emission, which introduces random phase fluctuations into the laser cavity. These phase fluctuations couple to the stimulated emission process, introducing phase noise that broadens the laser linewidth [101].

To quantify this broadening effect, Schawlow and Townes derived a theoretical expression for laser linewidth even before the first laser was experimentally demonstrated [36]. Since then, various models have been developed to predict and refine linewidth calculations. One significant improvement came from Henry's introduction of the linewidth enhancement factor, which accounts for carrier-induced refractive index changes and their effect on phase noise. This led to the widely used Henry linewidth formula, describing the FWHM linewidth of a semiconductor laser with a Lorentzian line shape, expressed as follows [101]:

$$\Delta\nu = \frac{\pi}{\mathrm{T_{coh}}} = \frac{R_{sp}}{4\pi F}(1+\alpha_H^2) \tag{2.38}$$

In the above equation, $\Delta\nu$ represents the laser linewidth, T_{coh} denotes the coherence time of the laser, R_{sp} is the time-averaged total spontaneous emission rate that is coupled into the laser cavity, and F represents the time-averaged total photon number within the laser cavity. α_H^2 is the linewidth enhancement factor, which quantifies the coupling between carrier density fluctuations and refractive index variations, and is defined as,

$$\alpha_H = -\frac{4\pi}{\lambda}\frac{\frac{\partial n}{\partial N}}{\frac{\partial g}{\partial N}} \tag{2.39}$$

In Equation 2.39, λ represents the emission wavelength, g denotes the material gain, n is the refractive index, and N corresponds to the carrier density. For a single-frequency laser, if the photon density in the laser cavity grows exponentially, Equation 2.38 can be further expressed as [102]:

$$\Delta\nu = \frac{v_g^2 h\nu n_{sp}\alpha_m(\alpha_m+\alpha_i)(1+\alpha_H^2)k_c}{8\pi P_{out}} \tag{2.40}$$

where v_g indicates the group velocity, h represents Planck's constant, v denotes the optical frequency, n_{sp} is the population inversion factor, α_m is the mirror loss factor per unit length, α_i is the internal loss factor per unit length, and k_c is the Petermann factor. The power output from the laser P_{out} is given by [75]:

$$P_{out} = \frac{hv\eta_i(I + I_{th})}{q} \frac{\alpha_m}{\alpha_m + \alpha_i} \tag{2.41}$$

where the threshold current
$$I_{th} = \frac{qV_{act}N_{th}}{\tau_c} \tag{2.42}$$

For the above two equations, η_i is the internal quantum efficiency, I is the bias current, q is the elementary charge, V_{act} represents the active region volume, N_{th} is the threshold carrier density, and τ_c denotes the carrier lifetime.

Therefore, the linewidth of the laser can be minimised through a series of optimisations. On one hand, linewidth reduction can be achieved by decreasing the internal loss α_i and mirror loss α_m, while increasing the differential gain and injection efficiency. These improvements can be realised by optimising the wafer structure or introducing external optical injections.

On the other hand, since the laser linewidth is inversely proportional to the total power output P_{out}, and P_{out} is directly proportional to the photon density within the laser cavity, increasing the photon density effectively reduces the linewidth. This optimisation can be achieved through grating structure engineering.

It should be noted that the theoretical linewidth models presented here primarily account for intrinsic noise mechanisms, such as spontaneous emission and carrier-induced refractive index fluctuations. However, in practical measurements, the observed linewidth can also be influenced by several extrinsic factors, including current source noise, temperature fluctuations, mechanical vibrations, and unintentional optical feedback. These effects were not systematically studied in this work, but could contribute to additional broadening in the measured spectra. In the following research, the focus will be on designing optimised DFB laser gratings to enhance photon density and achieve narrow linewidth operation.

2.2.6.2 Field Intensity Distribution

To further optimise laser performance and achieve a narrow linewidth, it is essential to analyse the field intensity distribution within the laser cavity, as the photon intensity distribution and power intensity distribution are closely related to it. The field distribution within the laser cavity can be determined by considering the interaction and interference of forward and backward propagating components. The scalar wave equation governing the electric field can be expressed as [103]:

$$\frac{\partial^2}{\partial z^2} E + k^2 E = 0 \tag{2.43}$$

where

$$k = n(z)\frac{2\pi}{\lambda} \tag{2.44}$$

For the above equation, λ is the wavelength satisfying the Bragg condition, and $n(z)$ is the refractive index function, which can be obtained through couple wave solutions. Then, field intensity distribution has been simulated by *Matlab*. Figure 2.31 shows the reflectivity spectra of a uniform Bragg grating and its field distribution along the cavity.

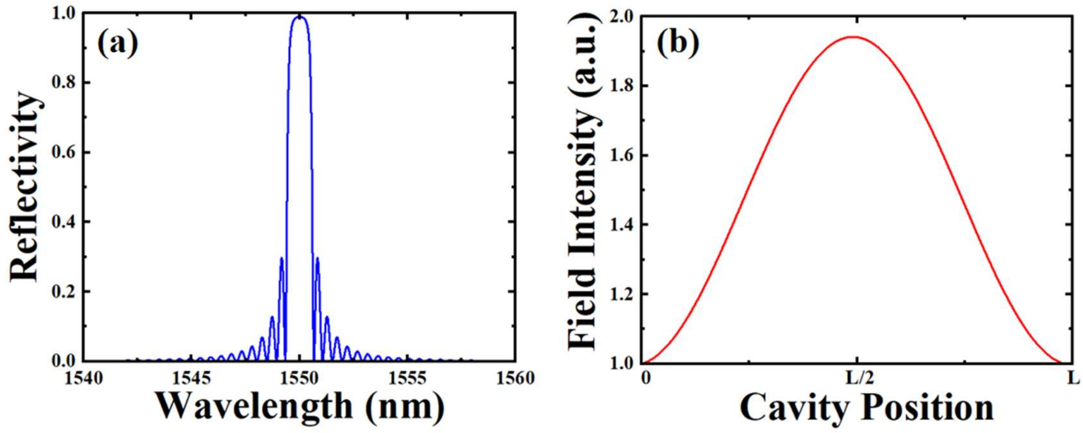

Figure 2.31: (a) The reflectivity spectra of a uniform Bragg grating and (b) its field distribution along the cavity.

However, a challenge arises when a single-mode output is required. As discussed in the previous section, DFB semiconductor lasers with uniform Bragg gratings suffer from mode competition, leading to mode instability. A widely adopted solution to enforce single-mode operation is the introduction of a π-phase shift at the centre of the cavity. For a π-phase-shifted DFB laser, the field intensity distribution becomes highly non-uniform along the cavity, leading to spatial hole burning (SHB) [83]. Figure 2.32 presents the normalised field distributions for both uniform and π-phase-shifted DFB lasers, clearly illustrating that the phase-shifted grating exhibits a significantly higher field intensity at the location of the phase-shift region.

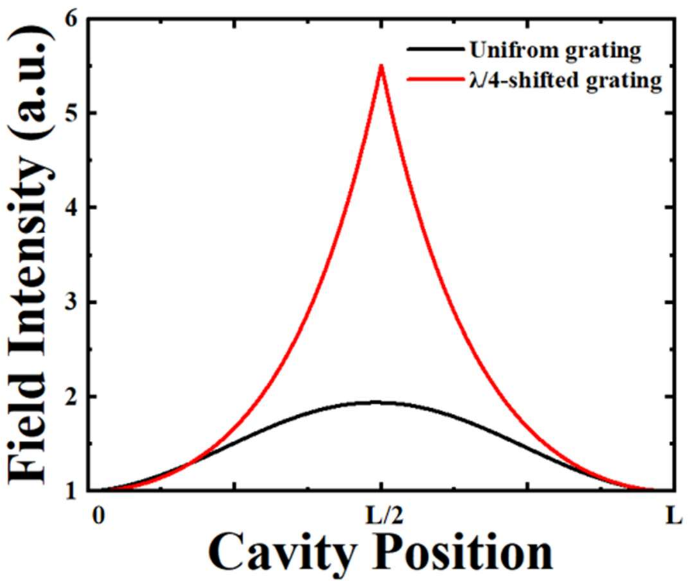

Figure 2.32: Field Intensity Distribution for Uniform (black line) and λ/4-Shifted Gratings (red line).

While high field intensity enhances output power, an excessively localised field distribution in the cavity transfers to the carrier density, refractive index, and Bragg conditions, exacerbating spatial inhomogeneities. This non-uniformity leads to linewidth broadening due to increased phase-noise and spectral instability [104].

Thus, reducing and flattening this peak field intensity has become a key focus in the development of narrow-linewidth DFB lasers. To mitigate the spatial-hole-burning effect and improve the stability of single-mode operation at high output powers, various grating optimisation techniques have been proposed.

2.2.6.3 Various Grating Optimisation Techniques

One notable method was introduced by Makoto Okai in 1989, which is known as the corrugation-pitch-modulated DFB (CPM-DFB) laser, which was designed to suppress field intensity peaks and achieve a more uniform optical field distribution [105]. The schematic structure of the CPM is illustrated in Figure 2.33. Unlike conventional π-phase shift gratings, CPM gratings incorporate a phase-arranging region where the grating period is varied from the rest of the structure. In the phase-arranging region, an additional phase shift is introduced by distributing a multiple *t* of half the grating period evenly across the grating periods within this region, where *t* is an odd integer that determines the magnitude of the introduced phase shift. The modified grating period in the phase-arranging region is determined by the total length of the region and the chosen value of *t*, ensuring a gradual phase transition rather than an abrupt π-phase shift.

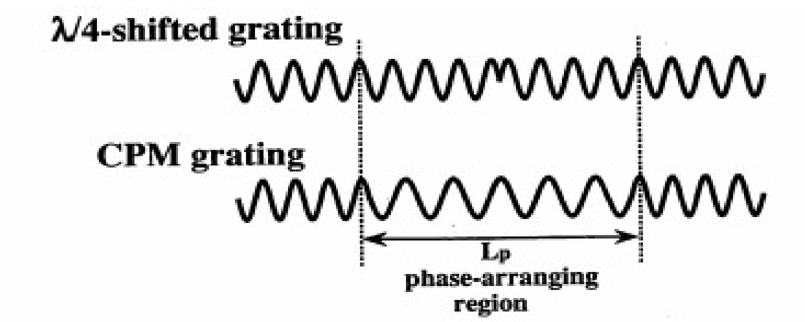

Figure 2.33: Schematic structure of a π-phase grating and a CPM grating [106].

This gradual phase shift redistributes the optical field and reduces localised intensity peaks. Figure 2.34(a) presents the simulated field intensity distribution along the cavity for different values of *t* (*t* = 1, 3, 5). As *t* increases, the optical field becomes more evenly distributed, effectively reducing localised light concentration and, consequently, narrowing the laser linewidth. This demonstrates the effectiveness of CPM-DFB structures in minimising spatial hole burning and improving laser coherence.

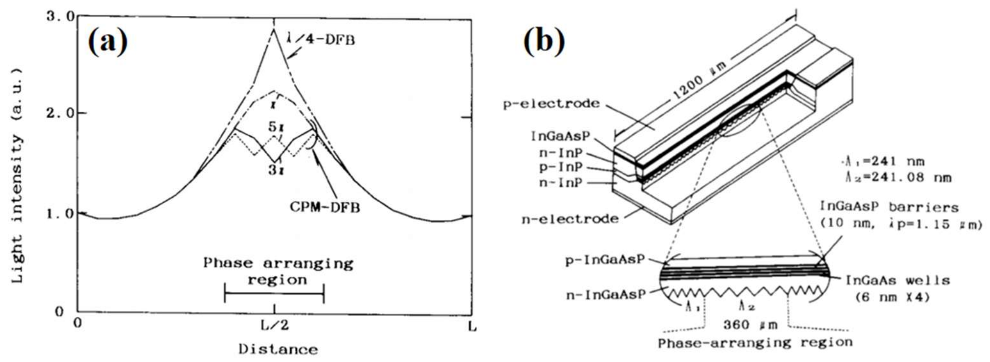

Figure 2.34: (a) The calculated results of light intensity along the laser cavity, and (b) fabricated CPM-DFB laser structure [105, 107].

However, this method presents a significant challenge. In 1990, M. Okai reported the fabricated CPM-DFB laser [107]. The study introduced a strained MQW-CPM-DFB laser with a 1200 μm long cavity and a 360 μm long phase-arranging region, as illustrated in Figure 2.34(b). By incorporating a strained MQW active layer, the fabricated CPM-DFB laser achieved a spectral linewidth of 170 kHz. Despite its effectiveness in linewidth reduction, the practical implementation of CPM gratings remains challenging. The grating period in the phase-arranging region differs by only 0.08 nm from that of the rest of the structure. Achieving such high precision in grating fabrication demands extremely tight control over EBL processing, which imposes stringent equipment requirements and limits scalability for mass production.

To address the precision challenges inherent in the CPM technique, a similar approach to SBGs was adopted, leading to the development of an equivalent CPM-based grating structure. In 2016, X. Tian reported an equivalent CPM-Apodised grating structure [108]. The new grating structure combines CPM, SBG and apodised grating using the reconstruction-equivalent-chirp (REC) technique, which can equivalently realise those complicated grating structures simply by designing a suitable sampling period [109]. The REC gratings are fabricated by conventional holograph exposure and photolithography, which reduces the difficulty of fabrication.

The schematic of the proposed equivalent CPM-apodised grating structure is shown in Figure 2.35. The total laser cavity length is 1 mm, with the CPM region centrally located and occupying approximately one-third of the cavity length. The equivalent π-phase-shift is introduced within this CPM region. Additionally, apodised grating regions are implemented symmetrically on both sides of the cavity, with the duty cycle gradually varying from 0.25 to 0.5. Figure 2.35(a) presents the seed grating with a uniform period, while Figure 2.35(b) illustrates the mask pattern used for fabrication. The equivalent CPM structure is achieved by modifying the sampling period within the phase-arranging region. Moreover, the introduction of apodised gratings further reduces light intensity concentration along the laser cavity, as demonstrated in Figure 2.35(c).

Through this approach, a narrow spectral linewidth DFB semiconductor laser with a linewidth of 224 kHz has been successfully achieved, demonstrating the effectiveness of the equivalent CPM-apodized grating in improving linewidth performance while easing fabrication constraints.

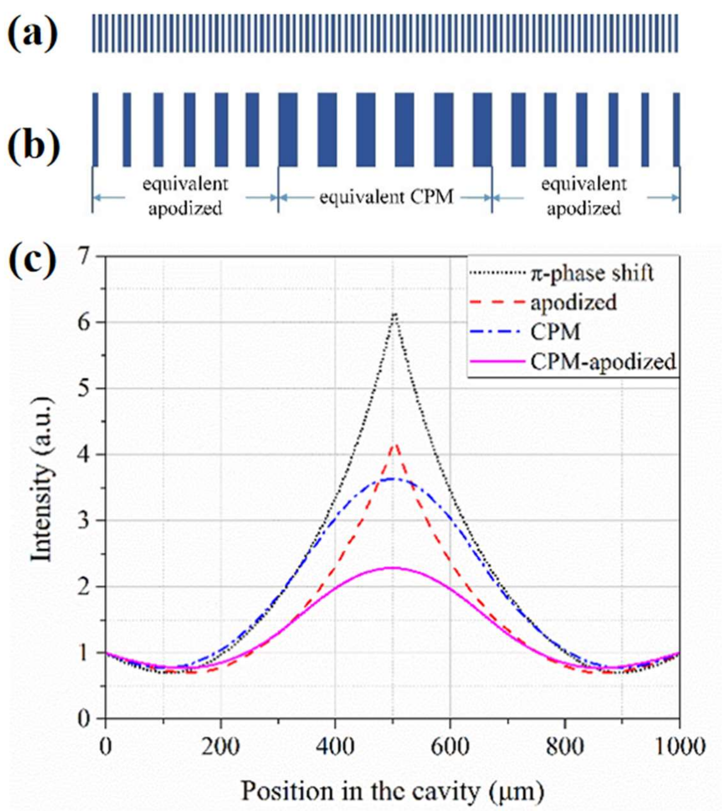

Figure 2.35: The schematics of grating profile (a) Seed grating, (b) Mask pattern. (c) The light intensity distribution @70mA [108].

Another approach to linewidth reduction through grating design is the introduction of multiple phase shifts along the laser cavity. In 1990, S. Ogita proposed a long-cavity multiple-phase-shift DFB (MPS-DFB) laser to enhance field distribution uniformity and suppress linewidth broadening [110]. As illustrated in Figure 2.36(a), instead of a single π-phase shift at the cavity centre, in MPS structures, multiple phase shifts are strategically introduced along the laser cavity at predefined intervals. This design effectively redistributes the optical field intensity, preventing excessive localisation of light and mitigating spatial hole burning. Figure 2.36(b) compares the field intensity distributions of a conventional π-phase shift DFB laser (dashed line) and an MPS-DFB laser (solid line) [111]. The MPS structure results in a significantly more uniform field distribution, reducing intensity peaks that contribute to linewidth broadening. This improvement enhances mode selectivity and spectral purity, making MPS-DFB lasers a promising solution for achieving narrow linewidth operation in high-performance optical communication systems.

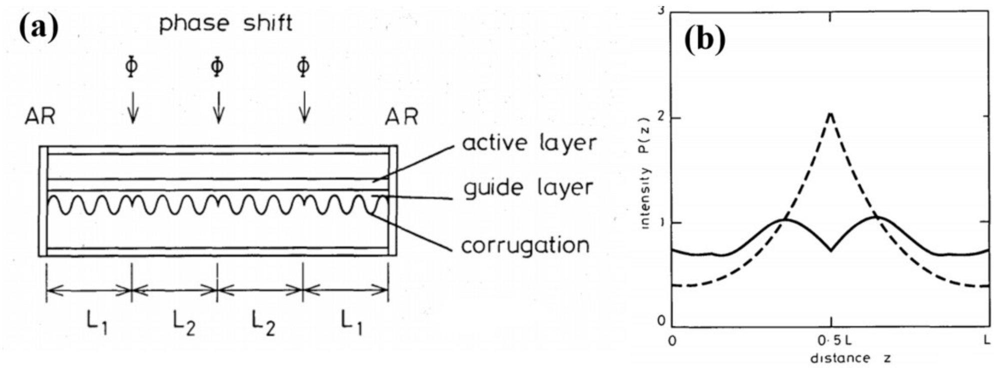

Figure 2.36: (a) Analyzed model and (b) Field distribution of MPS-DFB laser [110, 111].

A 1200 μm long MPS-DFB laser incorporating three phase shifts of 0.8π, -0.8π, and 0.8π was successfully fabricated, as shown in Figure 2.37, achieving a narrow linewidth of 830 kHz. Compared to conventional π-phase-shift DFB lasers, the MPS-DFB design redistributes the phase shifts along the cavity, leading to a more uniform field intensity and suppressing linewidth broadening. However, the incorporation of multiple phase shifts along the entire cavity significantly complicates the laser design. Extensive simulations and calculations are required to determine the optimal phase shift positions and magnitudes. Additionally, it needs precise phase control in fabrication to prevent the excitation of other modes, which could compromise single-mode stability and spectral purity.

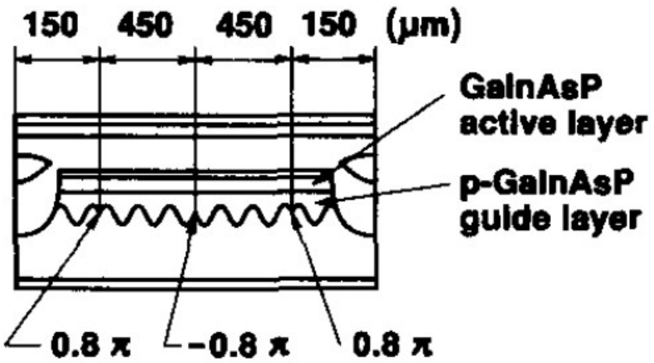

Figure 2.37: Fabricated MPS-DFB laser structure [110].

While both CPM and MPS approaches offer improvements over conventional π-phase-shift DFB lasers, their respective limitations highlight the need for alternative designs that combine the advantages of both methods. To address these issues, a novel grating structure is proposed in this work, integrating key elements from CPM and MPS techniques to further optimise field distribution, suppress linewidth broadening, and enhance manufacturability.

2.2.6.4 Design and Simulation Results of a Novel DPS Grating Structure for Narrow Linewidth DFB Lasers

As discussed in the previous section, in CPM-DFB lasers, the π-phase shift is evenly distributed within the phase-arranging region. While this method effectively makes the field distribution more uniform compared to a conventional π-phase shift design, the local variation in the grating period within the phase-arranging region alters the Bragg condition, potentially affecting the stability of the output wavelength. To address this issue, our research focuses on achieving the same field distribution effect while keeping the grating period unchanged.

A possible solution is inspired by MPS-DFB lasers, which suppress spatial hole burning by distributing multiple phase shifts along the cavity. Instead of modifying the grating period, traditional MPS-DFB lasers introduce several discrete phase shifts at optimised positions to redistribute the optical field and achieve better mode control. However, the effectiveness of this approach depends heavily on precise phase placement, and the need for multiple well-controlled phase shifts increases fabrication complexity.

Building on the concepts of both CPM and MPS designs, our proposed structure maintains the constant grating period while implementing a gradual phase shift transition rather than discrete phase shifts. Figure 2.38(a) illustrates a uniform grating structure along the cavity, where the cavity length is L and the grating period is Λ. Figure 2.38(b) depicts a conventional uniform grating with a discrete π-phase-shift at the cavity centre. Instead of introducing an abrupt π-phase shift at a single point, our proposed design distributes the phase shift gradually over a defined region, referred to as the distributed phase shift (DPS) region, with a length L_{DPS}, as shown in Figure 2.38(c). Within the DPS region, the phase shift is incrementally introduced, ensuring that the total phase difference between the two sections of the cavity remains π. The key advantage of this approach is that the phase shift occurs smoothly within the seed period, with each incremental phase shift in the DPS region given by $\pi/(L_{\mathrm{DPS}}/\Lambda)$.

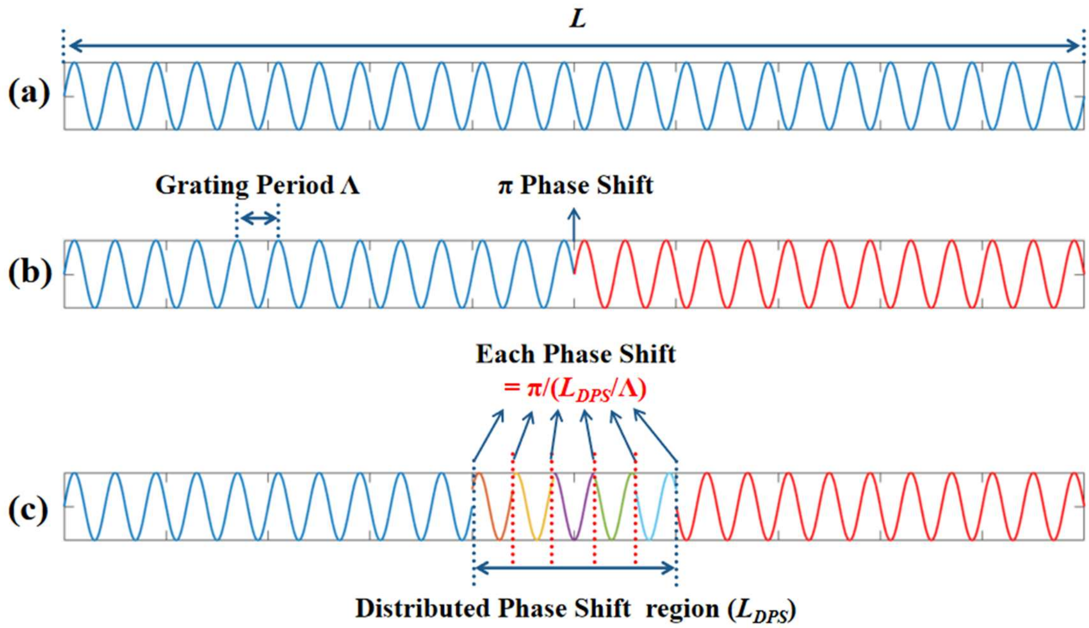

Figure 2.38: Index modulation of (a) a grating with a uniform period Λ. (b) a uniform grating with π-phase shift at the cavity centre. (c) a grating with DPS.

For a detailed comparison, Figure 2.39 illustrates the schematic structures of the various grating types discussed above, highlighting their differences in phase shift implementation. (I) is the uniform grating (UG) structure, which maintains a constant grating period throughout the cavity, providing no additional phase modifications. In contrast, the quarter-wavelength phase-shifted grating shown in (II), introduces a discrete π-phase shift at the cavity centre, which effectively achieves the SLM but also leads to strong SHB. (III) is the MPS grating, which distributes several discrete phase shifts along the cavity to improve field uniformity and suppress spatial hole burning. (IV) shows the CPM grating, mitigates spatial hole burning by smoothing the phase shift over the phase-arranging region L_p through slight variations in the grating period. (V) is the DPS grating, which combines the advantages of both CPM and MPS gratings. The DPS grating is similar to the CPM grating, featuring a specific region over which the π phase shift is distributed. However, its overall configuration closely resembles that of a uniform grating. This similarity is due to the unique grating design, which maintains the original grating period while gradually introducing phase shifts along the designated DPS region, with each phase shift occurring only at the beginning of each original grating period.

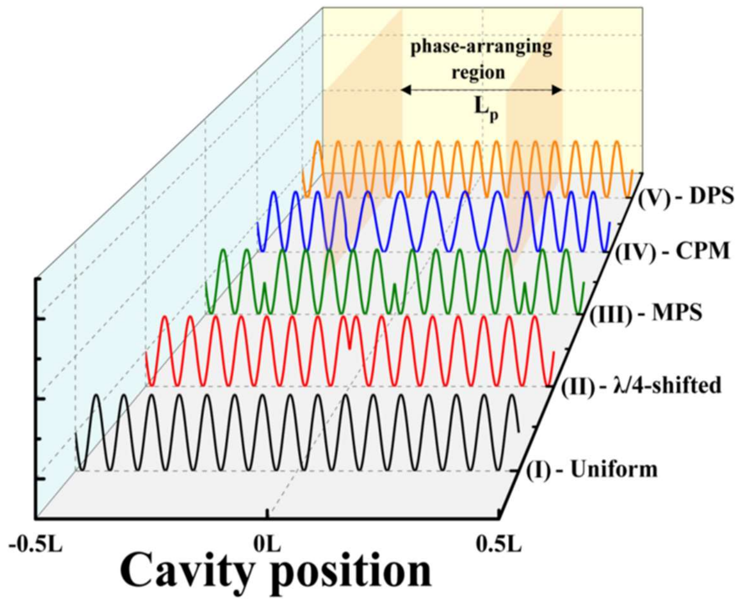

Figure 2.39: Schematic structure for: (I) uniform grating, (II) quarter-wavelength phase-shift grating, (III) MPS grating, (IV) CPM grating and (V) DPS grating.

To describe the physical structure of the DPS grating. Figure 2.40(a) presents a three-dimensional schematic of the DPS-DFB laser, where the total cavity length is L, and the DPS region occupies a section of the cavity with a length L_{DPS}. Figure 2.40(b) provides a cross-sectional view of the grating structure along the L_{DPS}. The grating period remains Λ throughout the structure, ensuring that the Bragg condition remains unchanged. In the DPS region, a small incremental phase shift is introduced at the beginning of each grating period, finally effectively distributing the π phase shift across the L_{DPS}. This gradual phase shift avoids abrupt discontinuities in the optical mode. Additionally, the modulation scenario of the DPS grating is shown in Figure 2.40(c).

The DPS grating maintains the same uniform grating period Λ across both DPS and non-DPS regions. The DPS region starts at the end of the previous grating period in the UG region, introducing the initial phase shift $\Delta\phi$, where $\Delta\phi = \pi/N$, with N representing the number of grating periods in the DPS region, calculated by $N = L_{DPS}/\Lambda$; it also signifies the total number of phase shifts applied in the DPS region, then, each phase shift is introduced at the commencement of each original grating period. Therefore, the total phase shift produced in the DPS region, π, replaces the single π phase shift found in traditional π phase shift gratings. The incremental phase shifts do not change the dimensions of the grating period; they only determine the position of the grating within each period. Furthermore, the total phase shift can be set to 3π, 5π, 7π, or 15π, with the phase shift increment defined as

$$\Delta\phi = \frac{n\pi}{N} = \frac{n\pi\Lambda}{L_{DPS}} \tag{2.45}$$

where n = 3, 5, 7, or 15, as illustrated in part (IV) of Figure 2.40 (c).

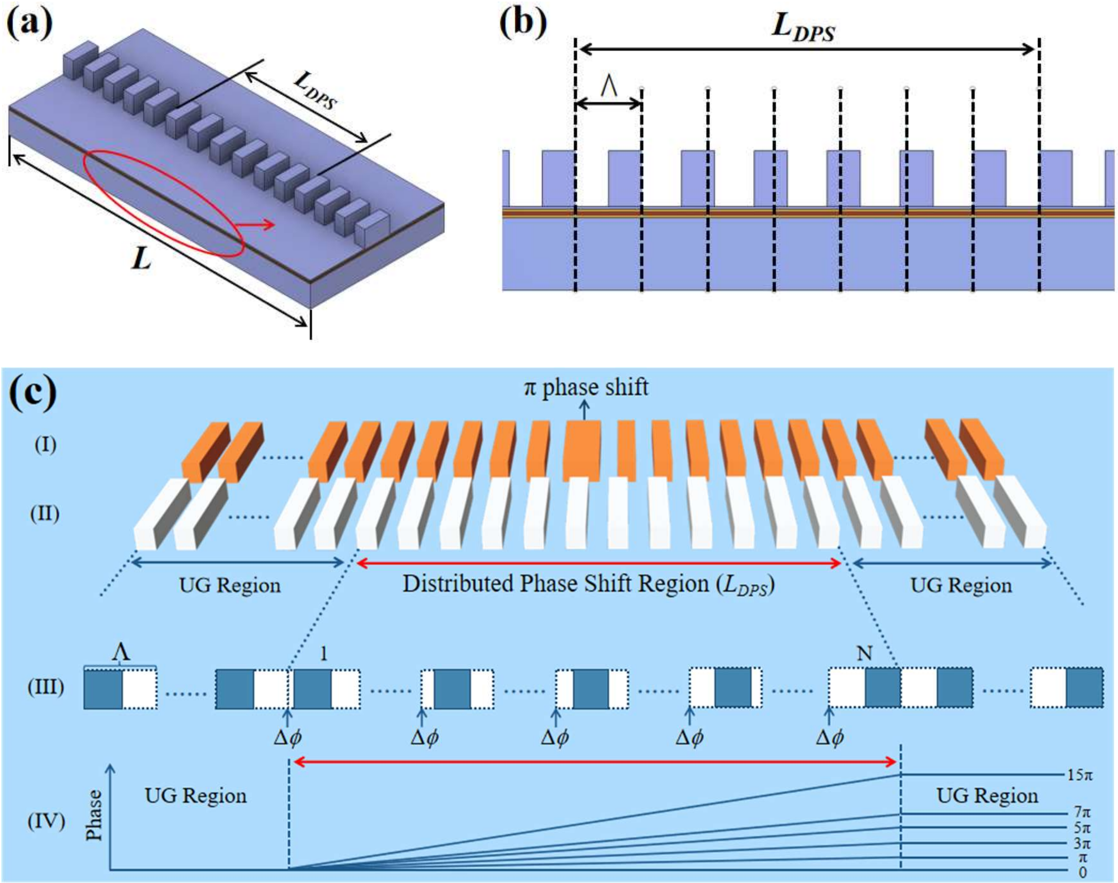

Figure 2.40: (a) The typical structure of DPS-DFB laser and (b) its cross-section. (c) Grating schematic of (I) quarter-wavelength phase-shift grating, (II) DPS grating, (III) the phase change within the DPS grating and (IV) designed total phase shift of π, 3π, 5π, 7π, and 15π in the DPS region.

Unlike the CPM structure, where an increase in phase shift leads to an enlargement of the grating period within the CPM region, ultimately reducing the side-mode suppression ratio (SMSR). This is because an increasing grating period makes the structure behave more like the parallel connection of two separate lasers, leading to multimode interference. In contrast, the multi-π DPS grating ensures that the primary lasing mode remains dominant over the side modes by introducing a uniformly distributed phase perturbation, resulting in stable single-longitudinal-mode (SLM) operation with a high SMSR.

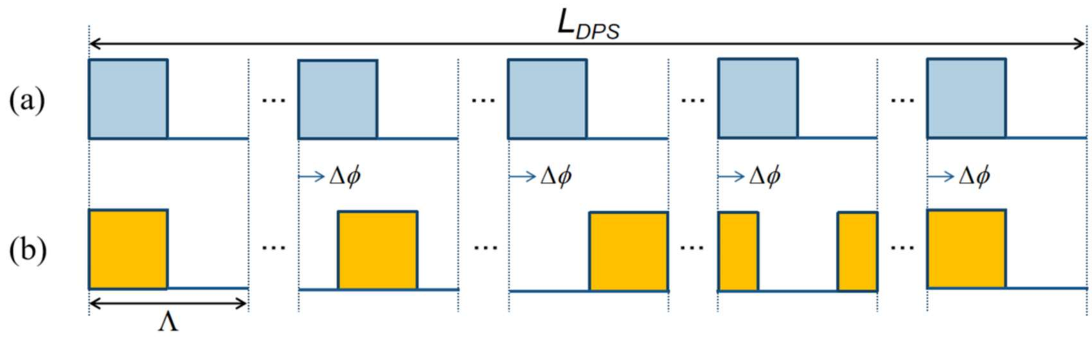

Figure 2.41: Schematic of the single period grating structure along the DPS region at positions 0, $L_{DPS}/4$, $L_{DPS}/2$, $3L_{DPS}/4$, and L_{DPS} for (a) uniform grating and (b) multi-phase shift structure within the DPS region.

To illustrate the multi-π DPS structure, Figure 2.41 (a) and (b) compare the uniform grating and 2π-DPS structure, both maintaining the same grating period within the DPS region. For uniform grating, no additional phase shift is introduced, meaning the fixed $\Delta\phi$ can be described using Equation 2.45 with $n = 0$, indicating zero phase shift. For 2π-DPS grating, $n = 2$, indicates that a total phase shift of 2π is evenly distributed along the L_{DPS}. Within the DPS region, when the grating is positioned at approximately one-quarter of the DPS region length ($L_{DPS}/4$), it is centred within the grating period with a phase shift of $\pi/2$. As the phase progresses to around the midpoint of the region ($L_{DPS}/2$), the phase shift reaches π, causing the grating to move toward the right within the period. With continued phase modulation, the grating shifts further to the right in each cycle. Any portion of the grating that exceeds the boundary of the grating period reappears on the left side, ensuring the continuity of the phase modulation. By the time the grating reaches the end of the DPS region length (L_{DPS}), it has fully shifted back to the left side, completing a total phase shift of 2π. It is worth noting that, in practical design implementations, n must be an odd integer to ensure stable SLM and effective mode discrimination. The 2π phase shift illustrated here serves as a conceptual simplification to demonstrate the phase shift distribution process.

The impact of the DPS structure on laser performance can be further analysed by examining the field intensity distribution within the cavity. Using the TMM, the field intensity distributions for various grating structures are illustrated in Figure 2.42. In the calculations, the effective index is set to 3.19 and the grating period to 243 nm, ensuring an output wavelength of 1550 nm. The cavity length L is set to 2 mm, providing a consistent basis for comparison.

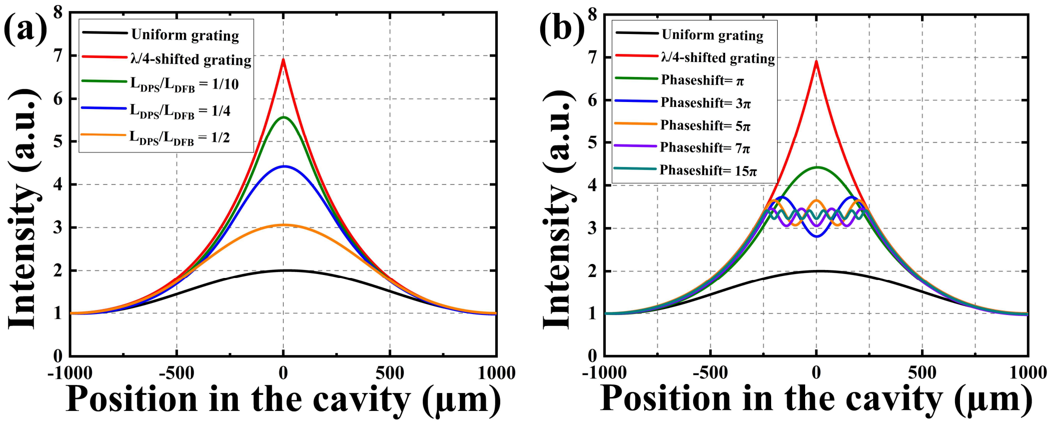

Figure 2.42: Calculated light field distribution along the cavity for different types of DPS gratings compared to uniform grating and traditional π phase shift grating: (a) different values of L_{DPS}/L_{DFB} with a fixed π phase shift, (b) different phase shifts with a fixed L_{DPS}/L_{DFB} = 1/4.

Figure 2.42(a) presents the simulated field intensity distribution for three types of structures: a uniform grating, a traditional π-phase-shifted grating, and DPS gratings with varying L_{DPS}/L_{DFB} ratios. Compared to the uniform grating, the traditional π-phase-shifted grating exhibits a strong intensity peak at the cavity centre. With the introduction of a DPS grating with a distributed π-phase shift, the peak intensity in the cavity centre is significantly reduced. When L_{DPS}/L_{DFB} = 1/10, a noticeable attenuation in the peak intensity can be observed. As the L_{DPS}/L_{DFB} ratio is further increased from 1/10 to 1/4, even to 1/2, the intensity distribution becomes more uniform and approaches the flatness level of a uniform grating. This demonstrates that the DPS structure with high L_{DPS}/L_{DFB} ratios can effectively mitigate localized intensity concentrations, ensuring a more balanced optical field, which can reduce linewidth broadening effects.

However, two key challenges must be addressed when implementing the DPS grating structure. The first challenge is the fabrication resolution constraint. Based on the above assumptions, when L_{DPS}/L_{DFB} = 1/4, each incremental phase shift corresponds to a grating displacement of only 0.06 nm, this level of precision exceeds the typical resolution limit of 0.5 nm achievable using EBL, making it difficult to reliably fabricate such structures with high accuracy. The second issue is the instability in the output spectrum caused by an overly extended DPS region. While distributing the phase shift helps mitigate spatial hole burning and improves field uniformity, excessively lengthening the DPS region can introduce mode competition and instability, particularly when only a single π-phase shift is applied across the DPS region. This instability arises because an extended phase-modulated region reduces the effective optical confinement of the primary lasing mode, leading to a higher likelihood of multi-mode operation or spectral wandering. To achieve an optimal ratio of L_{DPS}/L_{DFB}, a balance must be struck between flattening the field intensity and maintaining stable single-mode operation while staying within practical requirement limits.

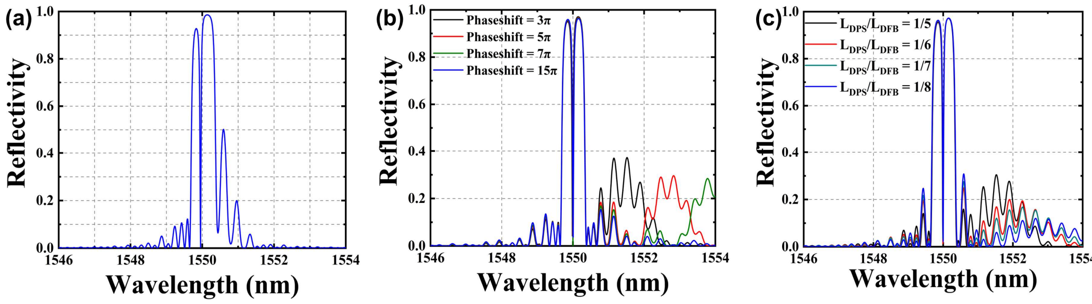

Figure 2.43: Calculated reflection spectra of (a) DPS grating with a π phase shift at the DPS region and L_{DPS}/L_{DFB}=1/4, (b) DPS grating with 3π, 5π,7π and 15π-phase shifts at the DPS region and L_{DPS}/L_{DFB}=1/4, (c) 3π-DPS grating with L_{DPS}/L_{DFB}=1/5, 1/6, 1/7 and 1/8.

Figure 2.43(a) shows the reflection spectra of a DPS grating with a single π phase shift at the DPS region and L_{DPS}/L_{DFB} = 1/4. The laser output is not centred at the main wavelength, and a significant side mode effect is also presented. This mode instability arises due to insufficient phase modulation, which fails to adequately suppress competing modes. To solve this problem, the multi-π phase shift has been introduced. While keeping L_{DPS}/L_{DFB} = 1/4, Figure 2.43(b) shows the reflection spectra of DPS gratings with 3π, 5π,7π and 15π phase shifts in the DPS region. As the value of phase shift increases, the extra side modes are suppressed and move away from the output central wavelength. Based on this, we simulated the light field distribution and found that as the phase shift value increases, the light field distribution in the DPS region becomes flatter, eventually approaching a smooth straight line, as shown in Figure 2.42 (b). Figure 2.43(c) illustrates the impact of DPS length on the reflection spectrum with a fixed 3π phase shift. As the ratio of the DPS region to the total cavity length decreases from 1/5 to 1/8, additional side modes are more effectively suppressed and move further away from the main lasing longitudinal mode.

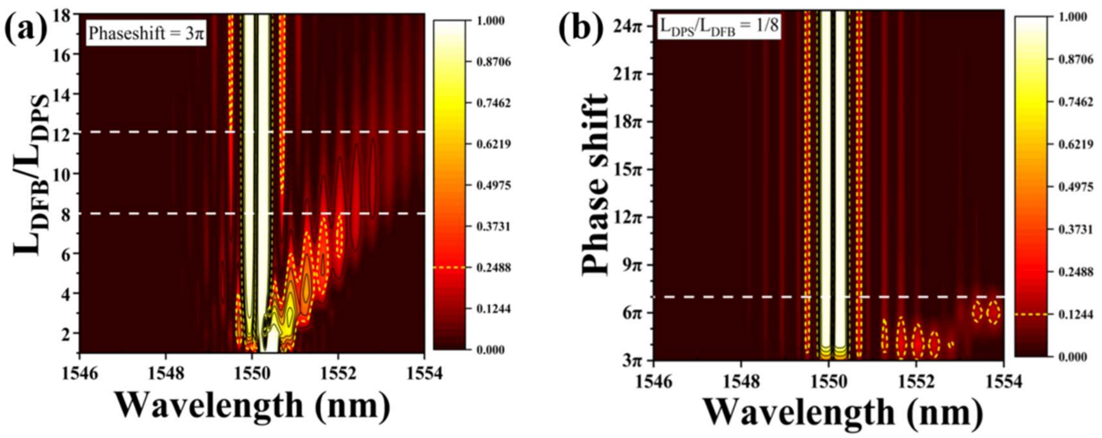

Figure 2.44: (a) Calculated 2D optical spectra vs L_{DFB}/L_{DPS} (1-18) with the phase shift fixed at π; (b) Calculated 2D optical spectra vs the phase shifts (3π-25π) with L_{DPS}/L_{DFB} = 1/8.

To systematically optimize the performance of DPS-DFB lasers, the appropriate DPS region length and phase shift size need to be adjusted. Figure 2.44(a) shows the simulated two-dimensional (2D) optical spectrum versus L_{DFB}/L_{DPS} (1-18) with phase shift fixed at 3π. It is found that, while L_{DFB}/L_{DPS} is larger than 8, the reflection intensities of other modes in the spectrum are much smaller than that of the first side lobe. Figure 2.44 (b) shows the simulated 2D optical spectrum versus the value of phase shift (ranging from 3π to 25π) with L_{DPS}/L_{DFB} = 1/8. As the phase shift increases, the reflectivity of other modes decreases further and, when the phase shift exceeds 7π, the reflectance spectrum closely resembles that of a traditional π-phase-shifted grating.

To further validate the effectiveness of the DPS grating, Figure 2.45 compares the simulated spectral of a traditional π phase shifted grating with a DPS grating incorporating a 15π phase shift and L_{DPS}/L_{DFB} = 1/8. The result demonstrates that the side modes in the DPS grating are effectively suppressed, ensuring improved spectral purity. This suppression is primarily attributed to the guided mode resonance between the DPS region and the two adjacent uniform grating sections, which enhances mode selectivity and stabilizes single-mode operation.

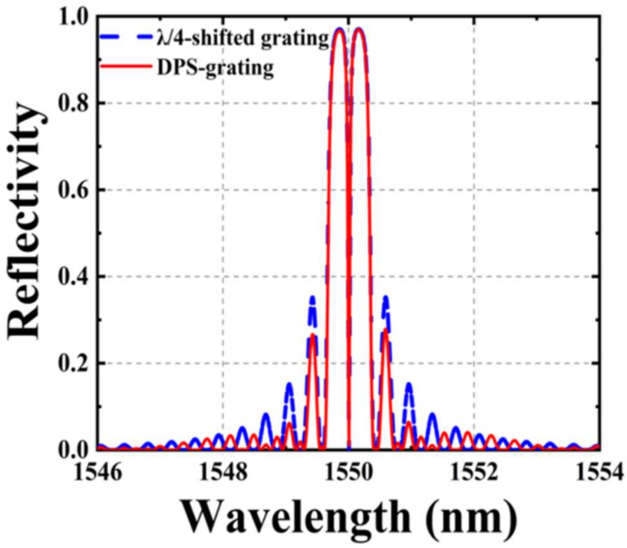

Figure 2.45: Calculated reflection spectra of 15π-DPS grating with L_{DPS}/L_{DFB} = 1/8 compared with traditional π phase shift grating.

More importantly, this optimised DPS design significantly relaxes the stringent fabrication constraints imposed by the resolution limits of EBL (0.5 nm). Compared to the initial DPS structure with L_{DPS}/L_{DFB} = 1/4 and a single π phase shift, where the required lithographic resolution was 0.06 nm, the refined design with L_{DPS}/L_{DFB} = 1/8 and a 15π phase shift achieves a fabrication tolerance of 1.77 nm. This enhancement in manufacturability makes DPS gratings more practical for real semiconductor laser fabrication while maintaining their good performance in linewidth narrowing and mode suppression.

2.2.7 Continuous Phase Modulation Technology Utilising DPS Grating

An interesting phenomenon emerges when the DPS region expands to cover the entire grating length, meaning when L_{DPS}/L_{DFB} = 1. Under this condition, as shown in Figure

2.46, a notable spectral shift is observed in the reflection spectrum, accompanied by the apparent disappearance of the stable SLM effect.

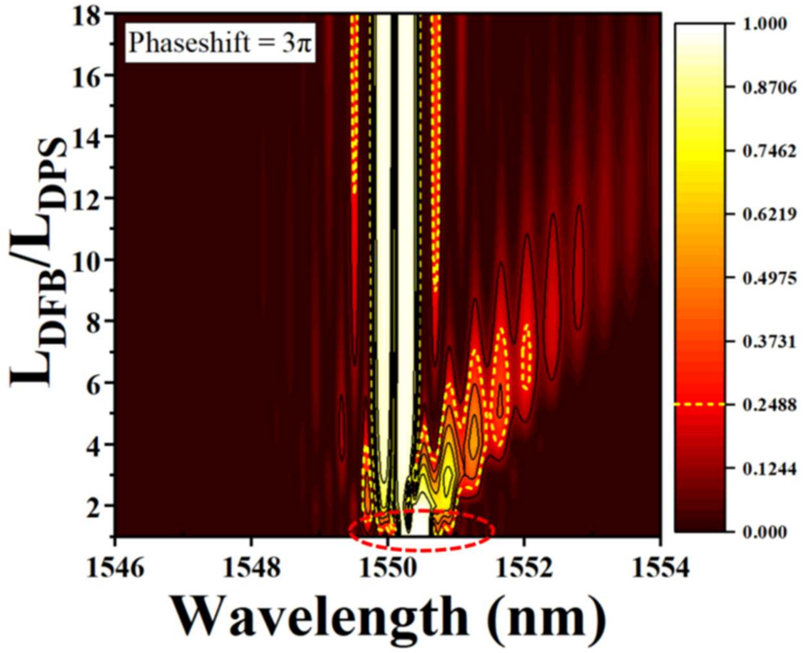

Figure 2.46: Calculated 2D optical spectra vs L_{DFB}/L_{DPS} (1-18) with the phase shift fixed at 3π; The position of the red dotted circle indicates L_{DFB}/L_{DPS} =1.

2.2.7.1 Possible Method of Controlling the Lasing Wavelength

To research this phenomenon, Figure 2.47 presents the reflection spectra for different grating configurations: a uniform grating, a uniform grating with a π-phase shift; and π-DPS gratings with varying L_{DPS}/L_{DFB} values of 1/8, 1/4, 1/2, and 1. The first two spectra, corresponding to a uniform grating and a π-phase-shifted grating, serve as a reference for comparison. For π-DPS gratings, with the L_{DPS}/L_{DFB} increases, a progressive transformation in the reflection spectra is observed. Specifically, the central dip of the reflection spectrum, which corresponds to the lowest reflectivity point, exhibits a continuous blue shift, while the central wavelength undergoes a redshift. When L_{DPS}/L_{DFB} =1, indicating that the phase shift is distributed across the entire cavity, the characteristic central dip vanishes. The spectral profile closely resembles that of a uniform grating, though the centre wavelength of the spectrum has redshifted.

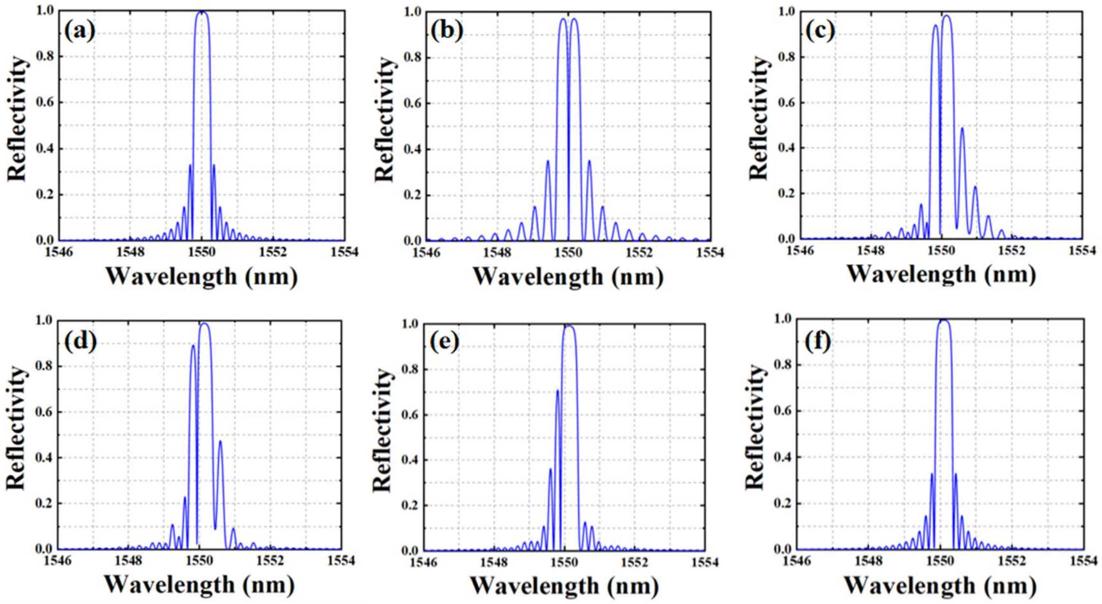

Figure 2.47: Calculated reflection spectra of (a) Uniform grating, (b) Uniform grating with π phase shift; π-DPS grating with (c) L_{DPS}/L_{DFB}=1/8, (d) L_{DPS}/L_{DFB}=1/4, (e) L_{DPS}/L_{DFB}=1/2, (f) L_{DPS}/L_{DFB}=1.

This trend indicates that when the phase shift distribution extends across the whole cavity, it modifies the modal properties of the lasing. The effective resonance conditions are altered, affecting how light interacts with the grating. The disappearance of SLM suggests that the uniform distribution of phase shifts changes the interference conditions within the cavity, potentially leading to new ways of controlling the lasing wavelength.

2.2.7.2 CPSG for Precise Wavelength Tuning

To further explore the observed spectral shift and its underlying mechanism, we propose a novel grating structure termed Continuous-Phase-Shift-Grating (CPSG). Figures 2.48(a) and 2.48(b) depict the schematic representation of the CPSG, where the total cavity length remains L and the grating period Λ is maintained uniformly. Unlike the DPS structure, where phase shifts are introduced within a limited region, the CPSG distributes the phase shift continuously throughout the whole grating. Figure 2.48(c) presents the phase distribution across a CPSG array, where the total phase shift varies from 2π to 16π in increments of 2π. By implementing this continuous phase modulation, we hypothesize that the CPSG structure can provide a novel approach to fine-tuning the lasing wavelength while maintaining spectral stability.

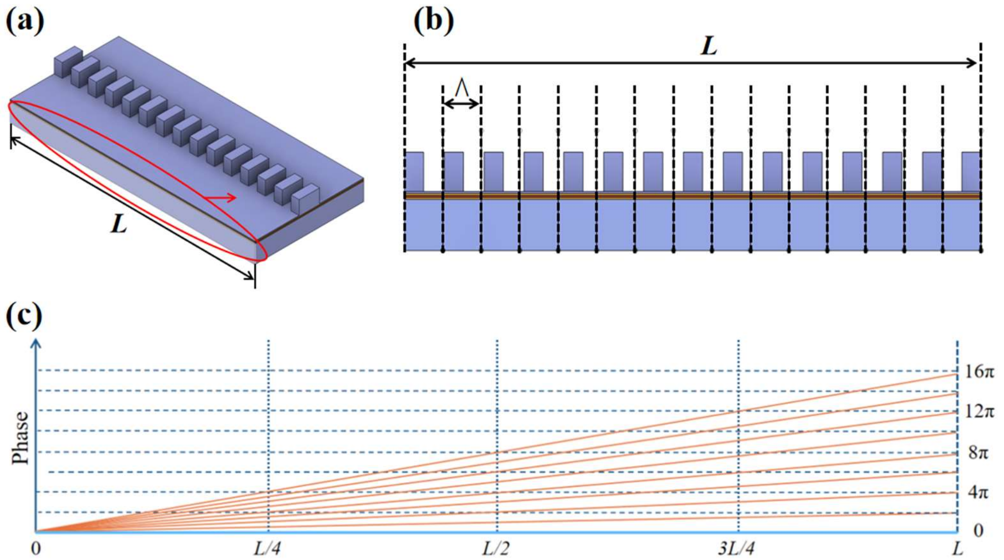

Figure 2.48: (a) The typical structure of CPSG-DFB laser and (b) its cross-section. (c) The phase increment for the DFB array is 2π, resulting in a phase shift ranging from 0 to 16π from CH1 to CH8.

To model the proposed continuous phase-shifted grating structure using the TMM, the grating region is divided into discrete segments, with the number of matrices corresponding to the number of grating periods. A phase matrix is inserted between each pair of adjacent coupling matrices to represent the gradual phase evolution. This segmentation approach approximates the continuous phase modulation as a sequence of discrete phase steps, enabling compatibility with the standard TMM framework. By appropriately adjusting the values of the inserted phase matrices, the model accurately captures the cumulative effect of the phase evolution along the cavity.

Figure 2.49 shows the simulated reflection spectrum of a uniform grating and 4π to 28π-CPSG, each with a grating period of 243 nm, a cavity length of 800 μm. As shown in the Figure, the central wavelength position of CPSG increases linearly with the total phase shift increases. The amount by which the wavelength shifts is directly proportional to the magnitude of the phase change, meaning that larger phase shifts result in greater wavelength movement. This linear relationship between phase shift and wavelength position ensures precise control over the lasing wavelength. Importantly, while the CPSG effectively modifies the central wavelength, other spectral characteristics, compared to a uniform grating, such as bandwidth and reflectivity, remain largely unchanged. This ensures that wavelength tuning can be achieved without introducing unwanted degradation in laser performance.

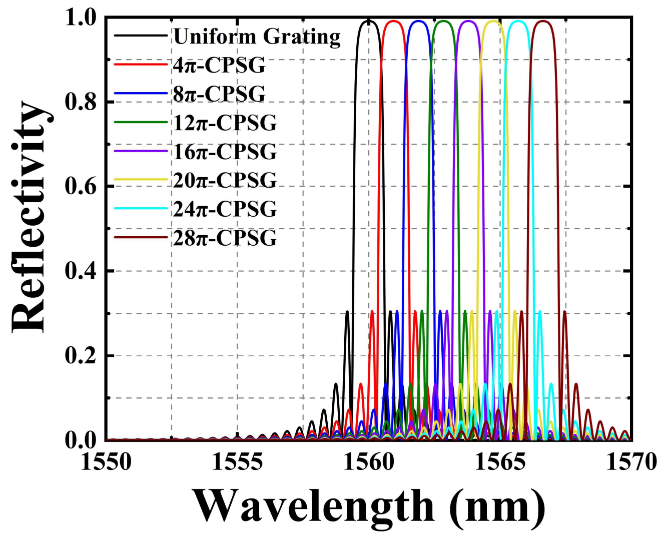

Figure 2.49: The reflection spectrum of uniform grating and 4π to 28π-CPSG, with the same grating period (243 nm) and cavity Length (800 µm).

Since the conversion relationship between phase and grating period is $\Delta\phi/\Delta\Lambda = 2\pi/\Lambda$. The wavelength difference between each CPSG can be expressed as:

$$\Delta\lambda = \frac{N \cdot n_{eff} \cdot \Lambda^2}{L} \tag{2.46}$$

where n_{eff} is the effective refractive index of the ridge waveguide; N is any real number, indicating that the total number of $N\pi$ is evenly distributed across each grating cavity length. This parameter serves as a critical tuning factor, allowing precise control over the lasing wavelength. For the designed and calculated parameters, n_{eff} is 3.21 and Λ is 243 nm, placing the lasing wavelength under uniform grating conditions (N=0) at 1560 nm. This wavelength aligns with the gain peak of another MQW material, which will be further discussed in the next chapter.

From Equation 2.46, the corresponding lasing wavelengths of CPSG for different values of L or N are presented in Table 2.2. Once the epilayer and grating structure are confirmed, we can accurately obtain $\Delta\lambda$ by adjusting N, Λ, and L, even for DWDM wavelength spacing of 0.8 nm or as narrow as 0.4 nm.

Table 2.2 The wavelength of CPSG under different conditions

Grating Type	Length of Cavity L	Wavelength
Uniform Grating	800 μm	1560.000 nm
2π-CPSG (N=2)	800 μm	1560.475 nm
4π-CPSG (N=4)	800 μm	1560.950 nm
4π-CPSG (N=4)	400 μm	1561.900 nm

2.2.7.3 Challenges and Possibilities

The primary challenge in CPSG structure is that its precise fabrication requirements exceed the resolution limits of current EBL techniques. For example, in a 4π-CPSG with a cavity length of 800 μm and a grating period of 243 nm, the required phase shift per grating corresponds to approximately 0.15 nm. This level of precision is beyond the typical resolution capability of 0.5 nm, making direct fabrication challenging.

However, the intrinsic nature of phase modulation in CPSG enhances its feasibility for successful fabrication, despite resolution limitations. Figure 2.50(a) illustrates the resolution constraints of uniform grating structures, where minor deviations in the grating period or refractive index can lead to substantial wavelength variations. Taking a nominal grating period of 243 nm as a reference, fabrication limitations prevent precise control over periods ranging between 242.5 nm and 243.5 nm, corresponding to a potential wavelength variation of approximately 6.4 nm.

In contrast to conventional uniform gratings, CPSG leverages a continuous phase modulation mechanism, as depicted in Figure 2.50(b). This approach shifts the primary focus from absolute grating period accuracy to maintaining a smooth and consistent phase evolution along the cavity. Due to the phase shift is not confined to a single abrupt transition but is instead spread across the entire grating length. While lithographic precision still influences the exact phase shift, the continuous nature of the CPSG phase evolution introduces a self-correcting effect, wherein minor phase deviations between intervals do not critically alter the overall resonance condition. As a result, minor phase errors introduced by fabrication imperfections have a negligible impact on the overall phase modulation trend.

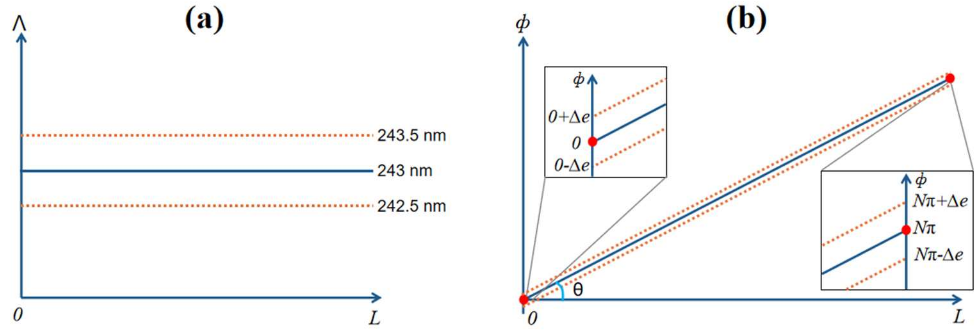

Figure 2.50: Fabrication Constraints in (a) Uniform grating and (b) CPSG.

To define the impact of unit phase error on the CPSG structure, the phase error Δe introduced by the resolution limitations of EBL can be described as,

$$\frac{\Delta e}{2\pi} = \frac{R}{\Lambda} \tag{2.47}$$

where R is the resolution of EBL and Λ is the grating period.

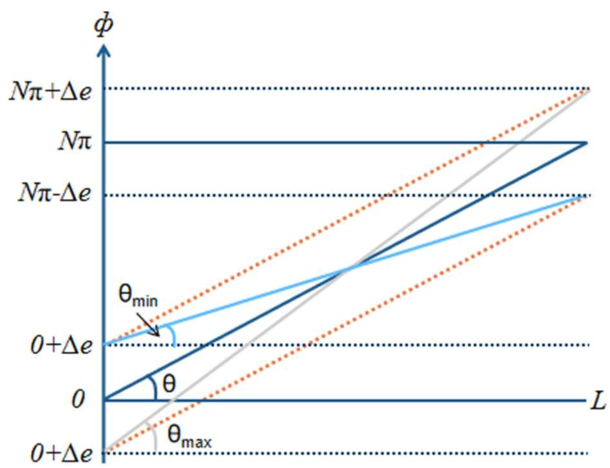

Figure 2.51: The phase evolution process within the $N\pi$-CPSG cavity.

Figure 2.51 illustrates the phase evolution process within the $N\pi$-CPSG cavity. Under ideal conditions, the phase shift progresses linearly from 0 to $N\pi$ along the cavity length L. However, in the presence of phase errors introduced at each grating period, the actual phase shift of each grating deviates by $\pm\Delta e$. Despite these local variations, the overall phase evolution remains confined within a specific range. To quantify this effect, we define the nominal phase change angle θ over the cavity length L as $\tan\theta = N\pi/L$, Similarly, considering the phase errors, the maximum and minimum phase change angles, θ_{max} and θ_{min}, can be determined by incorporating the error bounds $\pm\Delta e$,

$$\begin{cases} \tan\theta_{\max} = \dfrac{N\pi + 2\Delta e}{L} \\ \tan\theta = \dfrac{N\pi}{L} \\ \tan\theta_{\min} = \dfrac{N\pi - 2\Delta e}{L} \end{cases} \rightarrow \begin{cases} \theta_{\max} = \arctan(\dfrac{N\pi + 2\Delta e}{L}) \\ \theta = \arctan(\dfrac{N\pi}{L}) \\ \theta_{\min} = \arctan(\dfrac{N\pi - 2\Delta e}{L}) \end{cases} \tag{2.48}$$

Therefore, the actual wavelength difference $\Delta\lambda_{real}$ can be defined by the actual phase change angle θ_{real}, where $\theta_{real} \in [\theta_{min}, \theta_{max}]$:

$$\Delta\lambda_{\mathrm{real}} = \frac{\theta_{real}}{\theta}\Delta\lambda \tag{2.49}$$

Considering a typical resolution limit of 0.5 nm and a grating period of 243 nm, we apply the derived Equation 2.49 to numerically evaluate the wavelength range of CPSG under phase error conditions induced by EBL limitations. The calculated results are summarised in Table 2.3. The results clearly demonstrate that phase errors have a minimal impact on the lasing wavelength. Specifically, the error magnitude is inversely proportional to the cavity length L and directly proportional to N. Moreover, through careful design and optimisation of L and N, the wavelength difference can be reduced to below 0.1 nm for a laser array, ensuring compliance with the stringent wavelength stability requirements of DWDM systems.

Table 2.3 The wavelength range of CPSG under different conditions with Δe

Grating Type	L	Expect Wavelength	Wavelength Range
2π-CPSG (N=2)	800 μm	1560.475 nm	1560.475 ± 0.009 nm
4π-CPSG (N=4)	800 μm	1560.950 nm	1560.950 ± 0.018 nm
4π-CPSG (N=4)	400 μm	1561.900 nm	1561.900 ± 0.036 nm

To quantitatively assess the stability of the main mode under phase error conditions. Figure 2.52 shows the calculated 2D optical spectra with the effect of these tiny random phase errors ($<2N\pi R^2/\Lambda^2$, i.e., maximum phase error per grating period). Results from 30 repeated calculations indicate that small deviations primarily affect side modes, with negligible impact on the stable central wavelength. This highlights the CPSG design's robustness against phase errors.

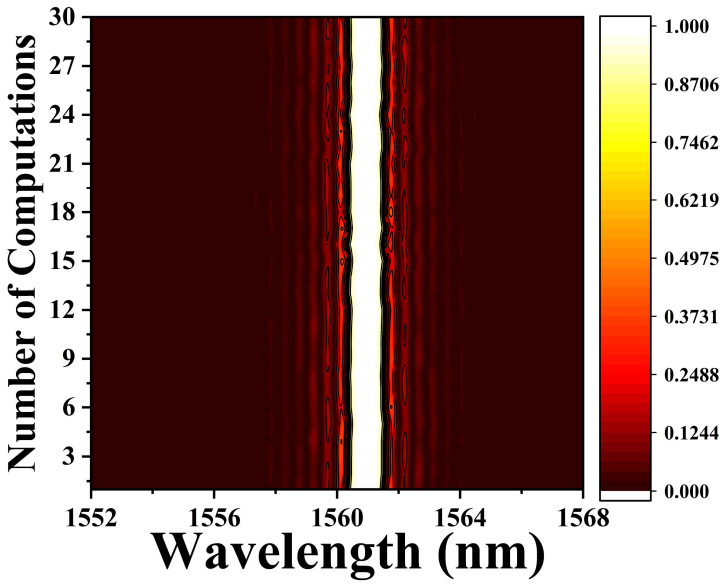

Figure 2.52: Calculated 2D spectra considering the effects of random phase errors.

As fabrication technologies continue to advance, particularly with the emergence of high-resolution EBL [112], nanoimprint lithography [113], and advanced photonic integration techniques, the practical realisation of CPSG structures with sub-nanometer precision will become increasingly feasible. Thus, while CPSG may not yet be fully implementable at the ultimate precision dictated by theory, its inherent tolerance to phase errors and its potential for fine-tuned wavelength control make it a promising direction for future semiconductor laser design. This makes the proposed method particularly promising for high-performance optical communication systems where wavelength stability and accuracy are essential.

2.3 Chapter Summary

This chapter systematically introduces the design of high-performance semiconductor lasers, starting from material selection and waveguide optimisation, and progressing to advanced grating engineering. The waveguide structure was carefully designed to ensure efficient mode confinement and minimal propagation loss, providing a stable foundation for high-quality lasing. Following the waveguide design, the chapter explores the theory and implementation of various grating configurations. Beginning with the fundamental FP laser, then discuss the uniform Bragg gratings and the Bragg condition. To accurately model and analyse these grating structures, the TMM is introduced in detail.

For precise wavelength control, some complex grating designs, such as SBG and *n*PS-SBG are discussed first. These structures enable finer spectral control, enhancing laser performance in applications requiring high spectral purity and stability. For narrow linewidth performance. The DPS structure was introduced as an innovative approach that combines the advantages of CPM and MPS structures to mitigate spatial hole burning, which demonstrates superior performance over conventional π-phase-shifted DFB designs. Building on this method, the research extended to CPSG arrays, which leverage phase-engineered gratings to achieve precise wavelength tuning and scalable multi-wavelength laser integration, offering a promising pathway for high-precision laser applications.

The methods presented in this chapter establish a foundational basis for the subsequent fabrication and experimental validation, which will be detailed in the following chapters.

Chapter 3

Device Fabrication and Test Results

With the theoretical designs established, the next step is to translate them into a real device through precise fabrication processes. The performance of the fabricated devices is then systematically tested to verify the effectiveness of the proposed design.

This chapter details the design and fabrication procedures used to realise the semiconductor laser structures, including wafer selection, structure design, fabrication process, and test results. By comparing experimental results with theoretical predictions, we can validate the effectiveness of the proposed modifications and identify potential areas for further optimisation.

3.1 4PS DFB-SOA Devices

3.1.1 Sidewall Gratings

While the theoretical analysis in Chapter 2 primarily considered a buried grating configuration for simplicity and ease of modelling, practical implementation requires a more comprehensive evaluation of fabrication constraints and integration challenges. As discussed earlier, Bragg gratings are created by introducing a periodic modulation of the refractive index experienced by the propagating mode. In conventional DFB laser designs, grating is typically achieved by etching the material on top of the active region, and then, by a regrowth process to build the waveguide, this grating is called a buried grating [114]. Although the buried grating approach ensures a strong coupling mode, it also introduces significant fabrication challenges. The regrowth process over a patterned grating complicates epitaxial growth, increases fabrication time, and adds to overall production costs [115].

Moreover, in DWDM laser sources, additional photonic components such as a multimode interferometer (MMI), SOA, and EAM should be integrated within the same platform. The inclusion of a regrowth-based buried grating further complicates this integration, limiting process scalability and yield. To address these challenges, an alternative approach using sidewall gratings is considered. Unlike buried gratings, sidewall gratings are fabricated adjacent to the waveguide, eliminating the need for regrowth while still providing strong optical feedback [116, 117]. This approach significantly simplifies fabrication while maintaining effective mode coupling.

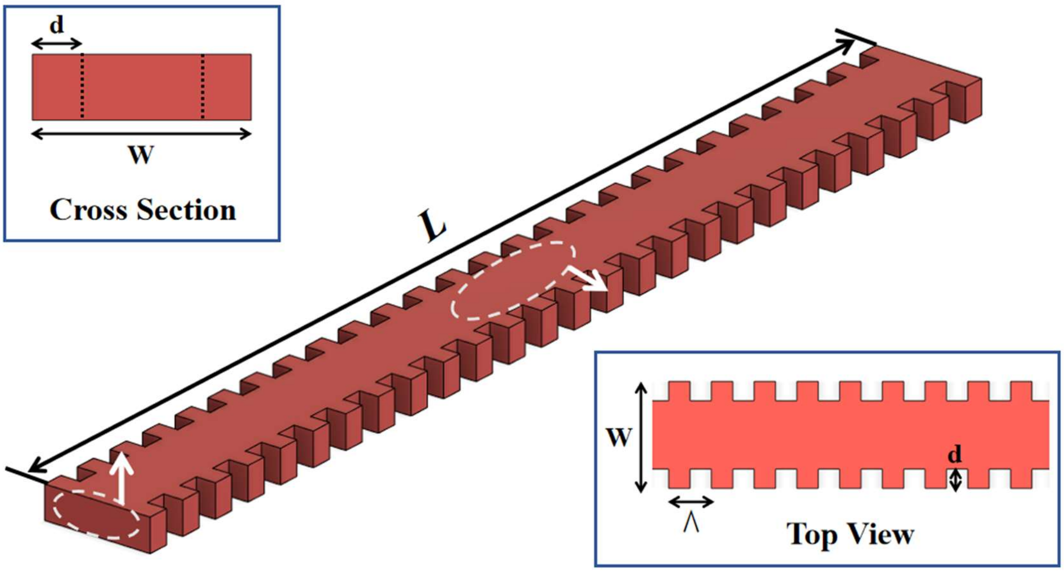

Figure 3.1: A 3D perspective of the sidewall grating along the waveguide, with its cross-section view (top left) and top view (bottom right).

As illustrated in Figure 3.1, sidewall grating can be fabricated by laterally etching the active waveguide, a technique first proposed in [116]. This structure integrates the lateral optical confinement of a ridge waveguide with DFB provided by gratings etched along the waveguide's sidewalls. The sidewall grating consists of a waveguide of width W, where periodic lateral recesses with a depth d and grating period Λ create a rectangular refractive index profile that facilitates distributed feedback, leading to reflection in accordance with the Bragg condition.

This design offers significant flexibility in controlling the coupling coefficient κ, as its value can be precisely adjusted by modifying either the recess depth d or the waveguide width W. Specifically, increasing the d/W ratio can enhance the coupling strength. Such tunability makes laterally coupled gratings highly advantageous for optimising laser performance. This type of grating can be fabricated using a fully post-growth process, facilitating seamless integration with other optical structures. The gratings are defined alongside the rest of the device in a single lithographic step using an EBL. This approach ensures precise control over the geometrical dimensions of the structures, leading to highly accurate optical characteristics.

To obtain the coupling efficiency of the sidewall grating under different conditions. There are two simulation methods utilised in the calculation of the coupling coefficient in a DFB laser. One is calculating the mode refractive index difference and getting the estimated coupling coefficient by $R_{max}=\tanh^2(\kappa L)$, which has been mentioned. However, this approach assumes a uniform coupling coefficient along the grating and does not fully account for the impact of localised variations in the refractive index or scattering losses, making it less precise for complex grating geometries. The second approach directly simulates the grating reflectance and extracts the coupling coefficient using the equation below [76].

$$\kappa \approx \frac{n_2^2 - n_1^2}{m n_{eff} \lambda} \sin(\frac{\pi m w}{\Lambda}) \tag{3.1}$$

where m is the order of Bragg diffraction, λ indicates the Bragg wavelength, Λ is the grating period, w is the duty cycle of the grating and n_1 and n_2 are the effective refractive indices corresponding to different waveguide widths. Considering that the Bragg grating has the maximum coupling efficiency at duty cycle w = 0.5, Equation 3.1 can be written as:

$$\kappa \approx \frac{n_2^2 - n_1^2}{m n_{eff} \lambda} \sin(\frac{\pi m w}{\Lambda}) \approx \frac{n_2^2 - n_1^2}{m n_{eff} \lambda} \approx \frac{(n_2 + n_1)(n_2 - n_1)}{m \frac{n_2 + n_1}{2} \lambda} \approx \frac{2(n_2 - n_1)}{m \lambda} \tag{3.2}$$

To ensure single-mode operation, the waveguide width W is maintained at 2.5 μm. Under this condition, the higher refractive index n_2 can be treated as a constant, this value can be accurately simulated using *Rsoft*. Additionally, *Rsoft* can also be used to obtain the refractive index n_1 under different recess depths d. Figure 3.2 illustrates the relationship between the coupling coefficient κ and the recess depth d for a first-order

DFB laser (m = 1). As shown in the figure, κ increases nonlinearly with d, indicating that deeper recesses lead to stronger mode coupling. When d is larger than 0.85 μm, no transverse modes are supported in the structure. This trend suggests that adjusting d provides an effective means of tuning the coupling strength in sidewall grating designs.

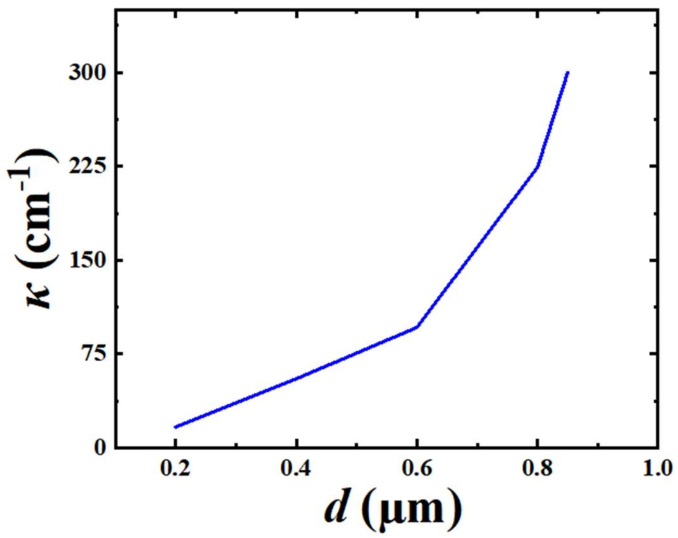

Figure 3.2: The relationship between coupling coefficient κ and recess depth d for sidewall gratings.

3.1.2 Sidewall Gratings with 4PS-SBG Devices

Sidewall gratings not only offer significant flexibility in tailoring the coupling coefficient but also enable precise control over the Bragg wavelength. According to the Bragg condition $\lambda_b = 2n_{eff}\Lambda$, both the effective refractive index n_{eff} and the grating period Λ can be adjusted in Sidewall gratings. Building upon the previously analysed sidewall grating characteristics, Figure 3.3(a) and (b) present the implementation of sidewall gratings in C-SBG and 4PS-SBG structures, respectively. In the C-SBG configuration, half of the sampling period lacks a grating, which inherently reduces the coupling strength and introduces sideband effects. In contrast, the 4PS-SBG design distributes the grating within each sampling period into four sections, each incorporating a π/2 phase shift. By integrating sidewall grating technology into 4PS-SBG designs, it becomes possible to achieve precise wavelength control while maintaining a fabrication-friendly approach without requiring regrowth processes.

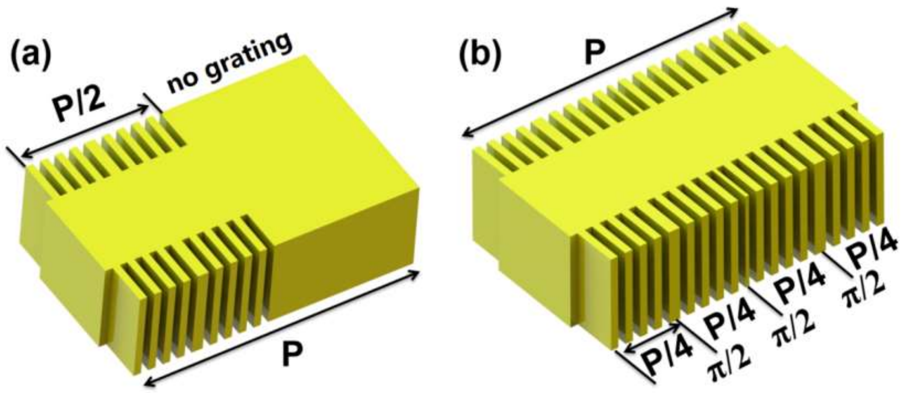

Figure 3.3: Grating structures of (a) C-SBG, (b) 4PS-SBG. *P* is the sampling period.

The wavelength spacing of the 4PS-SBG laser array is controlled by adjusting the sampling period *P*. By substituting Equation 2.35 into the Bragg condition, the wavelength of the -1st channel for 4PS-SBG can be expressed as,

$$\lambda_{+1} = 2n_{eff} \cdot \frac{P\Lambda_0}{P+\Lambda_0} \tag{3.3}$$

The next step involves optimising the device parameters for practical fabrication. In the final design and calculations, Λ_0 is selected to 257 nm, which locates the 0th channel at 1640 nm; the -1st channel, used as the output channel, is located at the gain peak of the MQW material, which is around 1560 nm; n_{eff} is 3.192 and the dispersion coefficient is considered of −0.00021/nm.

A four-channel SLM laser array (CH1 to CH4) has been designed. The sampling period *P* was varied from 4.867 µm to 5.037 µm across the four channels, ensuring precise wavelength tuning while maintaining single-mode operation. The detailed design values of *P* and their corresponding lasing wavelengths are summarised in Table 3.1.

Table 3.1. Sampling period *P* values for different wavelengths

Channel No.	**Sampling period *P***	**Wavelength**
CH1	4.867µm	1558.4 nm
CH2	4.923 µm	1559.2 nm
CH3	4.979 µm	1560.0 nm
CH4	5.037 µm	1560.8 nm

To validate the design of the 4PS-SBG structure, Figure. 3.4 (a) demonstrates the simulated reflectivity spectrum for C-SBGs and 4PS-SBGs. Compared with the C-SBG structure, in the 4PS-SBG structure, the 0th channel in 1640 nm disappears and the -1st channel is significantly enhanced. Additionally, by introducing a π phase shift within the seed grating period Λ_0 at the centre of the cavity, a resonance peak corresponding to the lasing mode appears at the centre of the stopband in the -1st channel, ensuring stable single-mode operation.

The time-delay spectrum for the designed sampling period P is illustrated in Figure 3.4(b). From Table 3.1 and Fig. 3.4(b), a difference in sampling period of 56 nm results in lasing wavelengths being separated by 0.8 nm. In this design, the sampling period difference is much larger than that of EBL's typical resolution of 0.5 nm, ensuring that the design is straightforward to fabricate with high precision.

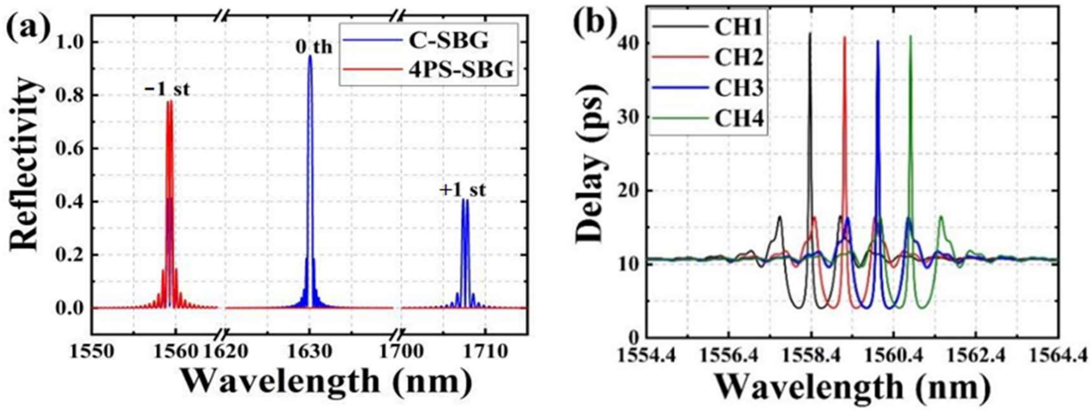

Figure 3.4: (a) Calculated reflection spectra of 4PS-SBG with a π phase-shift in the centre of the cavity (red curve) and compared with that of the C-SBG (blue curve), (b) The time-delay spectrum under different sampling periods.

3.1.3 SOA and Curved Ridge Waveguides Design

To achieve high output power in 4PS-SBG lasers, a straightforward approach is to integrate an SOA at the output facet. SOA operates based on the principle of stimulated emission, like a laser diode, but without a built-in resonant cavity. When an optical signal passes through the SOA, the injected carriers in the active region provide optical gain, amplifying the signal [118]. Ideally, a linear and time-independent SOA should simply amplify the input signal without altering its spectral characteristics. However, in practical fabrication, cleaved facets of a poorly designed SOA at the end of DFB diode lasers can lead to the formation of FP modes. These modes may disrupt single-longitudinal-mode (SLM) operation and degrade spectral purity.

One effective way to mitigate these effects is the application of antireflection (AR) coatings. This method involves depositing precisely controlled dielectric films on the facets to minimize unwanted reflections [119]. The effectiveness of AR coatings depends on the precise tuning of both the refractive index and the thickness of the deposited layers. However, the fabrication complexity and additional processing steps required for AR coatings can pose challenges in achieving consistent performance across multiple devices. Another approach to suppress facet reflections without relying on AR coatings is waveguide tilting [120]. Research has shown that introducing an angled waveguide relative to the cleavage plane provides an effective way to reduce back reflections while maintaining strong optical confinement [121]. For shallow-etched ridge waveguides, adopting a curved ridge configuration with a small radius of curvature can effectively suppress reflections while maintaining efficient light propagation.

To accurately evaluate the impact of ridge curvature on optical scattering losses, the Finite-Difference Time-Domain (FDTD) method has been employed. FDTD is a powerful numerical technique for solving Maxwell's equations in both time and space domains, making it highly effective for modelling light propagation in complex waveguide structures [122]. The model was implemented in *Lumerical*, as shown in Figure 3.5(a), and the corresponding device design is illustrated in Figure 3.5(b). The SOA consists of a 50 μm-long straight waveguide, followed by a 450 μm-long bent waveguide with a curvature radius R defined as R=450 μm/sinθ. The tilt angle of the curved ridge waveguide is denoted as θ, with a fixed ridge width of 2.5 μm. To analyse the impact of different waveguide angles on optical performance, FDTD simulations were conducted for θ values ranging from 0° to 12°.

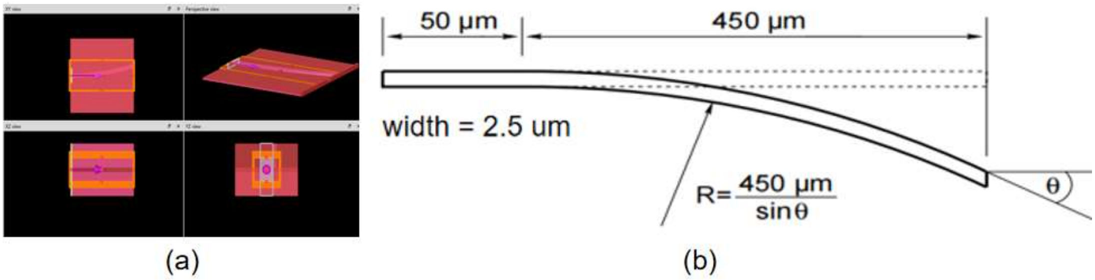

Figure 3.5: (a) Device simulation with FDTD in *Lumerical*. (b) Design of SOA with the curved ridge waveguides.

The results, shown in Figure 3.6, illustrate a significant reduction in reflectivity as θ increases. At $\theta = 0°$, the reflectivity of 0.27 corresponds to the Fresnel reflection due to the refractive index contrast between the laser crystal and air [123]. As θ increases, reflectivity decreases exponentially, reaching a minimum of 4×10^{-4} at θ = 12°, demonstrating the effectiveness of angled waveguides in minimizing unwanted feedback.

By introducing a curved ridge, the optical mode is gradually deviated from the facet normal, reducing the amount of light reflected directly back into the gain region. This spatial misalignment significantly increases return loss, thereby enhancing the stability of single-mode operation.

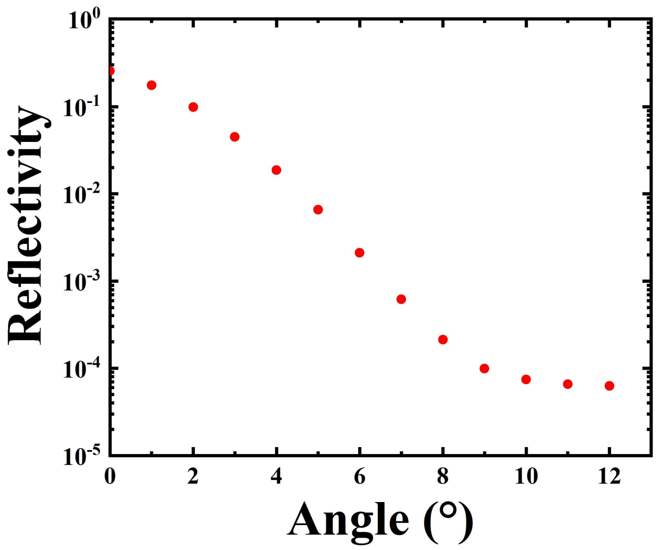

Figure 3.6: Simulated intensity reflectivity vs curved waveguide angles θ.

3.1.4 Pattern Design

To specific design considerations, each device has a similar structure with three sections: two curved waveguides located on the front and rear sides, respectively, to reduce facet reflections, with the 800/1000/1200 μm long DFB section in the middle. The front 450-μm-long curved waveguide acts as an SOA. For the cleaving process, a straight waveguide is generally added behind the SOA, which will cause the angle of the final device to be larger than the design; therefore, a designed tilt angle of 10° at the output facet results in an intensity reflectivity. The isolation gap between the DFB and SOA sections is 20 μm wide. On the back side of the DFB laser diode, a 125-μm-long waveguide with a radius of 233.3 μm and a tilt angle of 32° was applied. Figure 3.7 illustrates the layout of the DFB-SOA integrated device, featuring an 800 μm-long DFB section and a 450 μm-long SOA section.

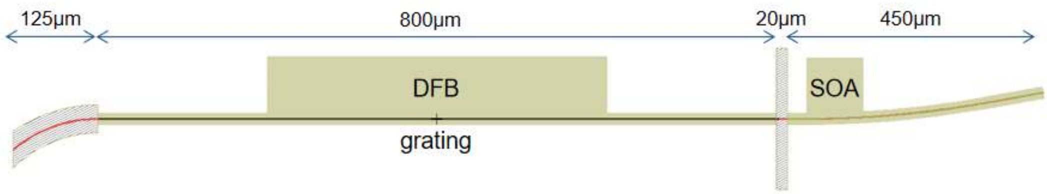

Figure 3.7: The pattern design of a SOA-DFB laser with bent ridge waveguides.

Before proceeding with fabrication, it is necessary to design different devices to compare their performance under different conditions. This step ensures that the optimal design can be selected based on experimental validation. The layout of the individual device above was created using *L-Edit*, a commercial computer-aided design (CAD) software widely used for semiconductor mask design. In semiconductor fabrication, precise lithography masks must be prepared for each process step, ensuring accurate pattern transfer onto the wafer.

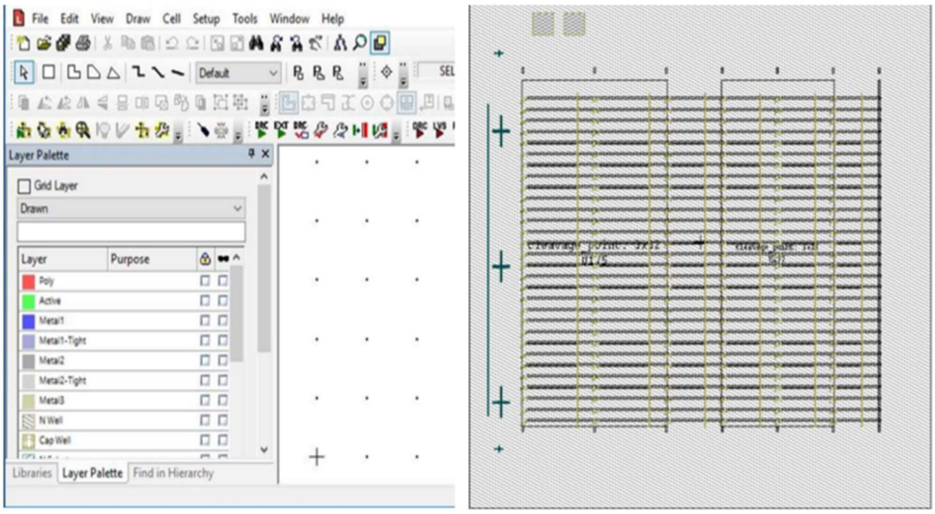

Figure 3.8: (a) The user interface of *L-Edit*. (b) The total pattern design view.

Figure 3.8(a) shows the user interface of *L-Edit*, where different layers are assigned to different lithography steps, allowing for seamless integration of various patterning processes. To achieve high precision in defining the grating structure and waveguide features, the grid resolution was manually set to 0.5 nm, which aligns with the resolution requirements of EBL. Figure 3.8(b) illustrates the complete pattern design used in this work. The structural parameters of the device were carefully selected based on simulation results to optimise performance.

To guarantee the proper functioning of the device, varying grating lengths have been developed and implemented, as depicted in Figure 4.3.2. The lengths of the gratings are 1200 µm, 1000 µm, and 800 µm, respectively. By fabricating devices with different grating lengths, it becomes possible to systematically evaluate their impact on key laser parameters, including SMSR, output power stability, and tuning characteristics. These experimental results will guide the selection of an optimal grating length for achieving high performance, narrow linewidth semiconductor lasers tailored for specific applications.

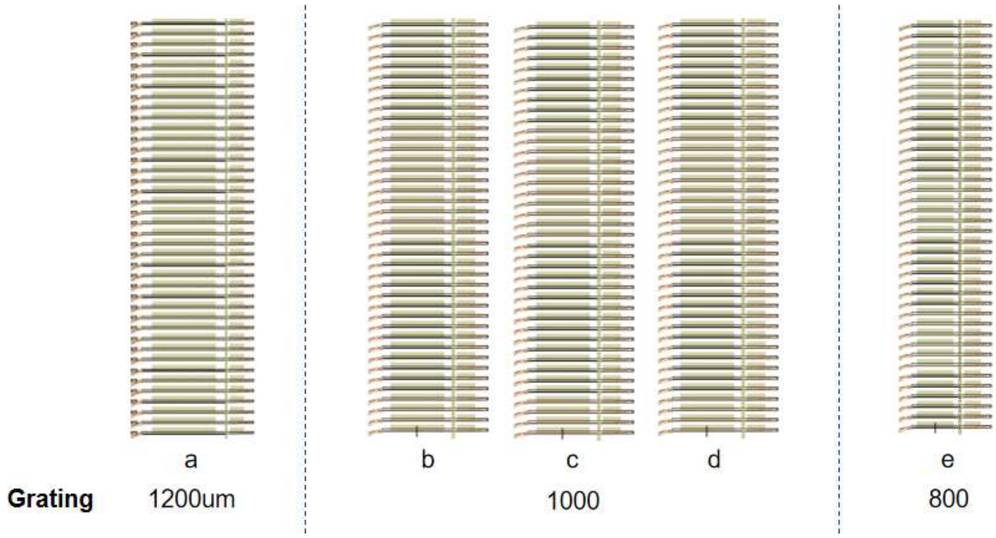

Figure 3.9: The design of a DFB laser diode with bend ridge waveguides on both sides.

3.1.6 Fabrication Process of 4PS-SBG Devices

The fabrication of the devices was completed in the James Watt Nanofabrication Centre (JWNC), which is one of the most sophisticated facilities in the United Kingdom and a member of the EPSRC National Centre for III-V Technologies. This centre provided the essential state-of-the-art equipment, including an Ultra-High resolution Electron beam lithography tool, dry etching and metal evaporation tools, and high-resolution scanning electron microscopes (SEM).

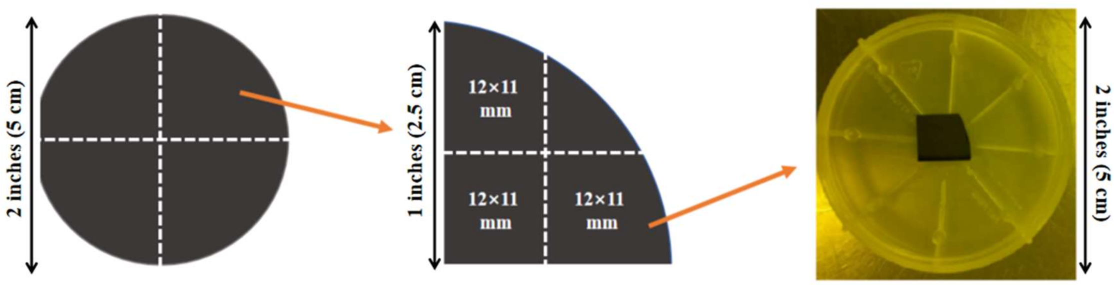

Figure 3.10: Cleaving and sample preparation from a 2-inch MQW wafer.

The semiconductor lasers fabricated in this thesis are all based on commercial MQW epitaxial wafers, and the wafers were bought from the IQE Company. The purchased MQW material is a 2-inch wafer. Due to the research-oriented nature of this project, only a certain number of devices need to be fabricated in each run. This required the use of small portions of the original wafer. Figure 3.10 illustrates how the wafer was initially cleaved from the 2-inch wafer and further divided into smaller samples, each measuring approximately 11 mm × 12 mm. The upper edge of the sample shown at this time appears curved because it was taken near the wafer's edge. To prevent contamination during fabrication, the samples were stored in 2-inch plastic boxes.

The fabrication process flow of this device can be divided into 8 key steps:

- Sample cleaning.
- Marker definition.
- Isolation definition.
- Waveguide definition.
- Contact Window Opening.
- P-contact metal deposition.
- InP substrate thinning and N-contact metal deposition.
- Rapid thermal annealing and device bar cleaving.

3.1.6.1 Sample Cleaning

Sample cleaning is essential before each fabrication step to remove both organic and inorganic contaminants. The standard cleaning process involves sequential immersion in acetone (CH_3COCH_3), isopropyl alcohol (IPA), and reverse osmosis (RO) water, with each step lasting five minutes in a water bath. Ultrasonic cleaning at room temperature can be introduced to enhance effectiveness. After RO water rinsing, the sample is dried using a nitrogen gun.

3.1.6.2 Marker Definition

For any multi-step lithography process, alignment markers are essential. Without well-defined markers, distortions, pattern shifts, or layer mismatches can occur, potentially rendering the device non-functional. In EBL, the alignment process is automated and depends on high-contrast markers to accurately identify reference points on the sample.

To meet this requirement, metallized markers were chosen and fabricated using the lift-off technique [124].

As shown in Figure 3.11, the metallized markers are small gold-covered squares, with 20x20 μm big, placed as a frame all around the central area where the devices pattern will lie. Each lithography step will refer to these small squares, ensuring the correct alignment of the different patterns; before each EBL writing, it should check the state of the markers, to avoid any edged defects that could disrupt proper alignment.

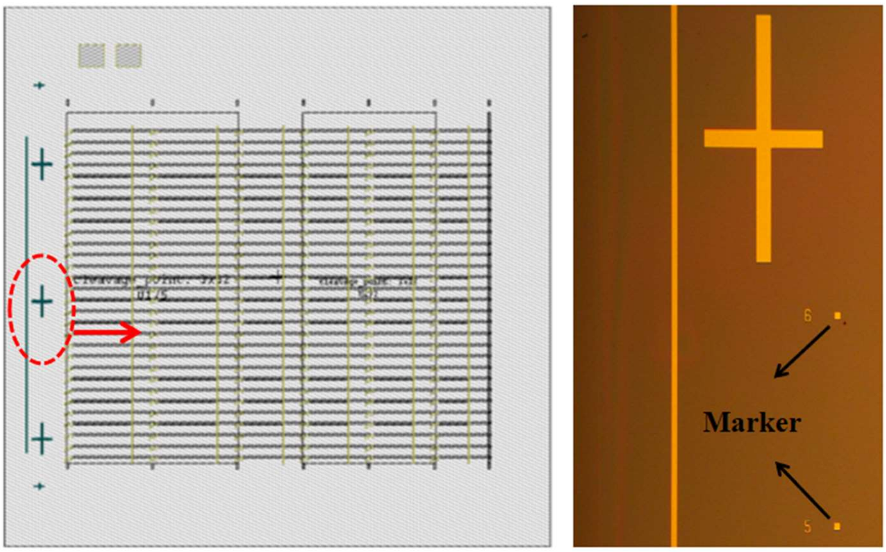

Figure 3.11: Alignment Markers for Multi-Step Lithography.

3.1.6.3 Isolation Definition

For semiconductor lasers with complex designs and multiple electrodes, electrical isolation is essential to ensure the independent operation of each device. In this part, SOA-DFB lasers were designed with two electrodes, allowing separate control of the SOA and DFB sections. An effective approach to achieving electrical isolation involves removing the highly doped contact layers at the top of the wafer structure, as shown in Figure 2.6. These layers consist of 200 nm of InGaAs and 50 nm of InGaAsP (1.3Q). Reactive Ion Etching (RIE) was utilised to selectively remove them, ensuring do not compromise the underlying structure. By removing highly doped contact layers, the electrical connection between the electrodes is effectively broken, preventing unwanted current flow [125]. Additionally, the remaining material underneath is 1600 nm of intrinsic InP, which is less conductive. This significantly increases the electrical resistance between adjacent devices, ensuring that each device can operate independently without interference.

3.1.6.4 Waveguide Definition

The fabrication of ridge waveguides is one of the most critical steps in semiconductor laser development, as it directly impacts grating performance. The waveguide definition process encompasses multiple fabrication steps, from pattern writing to material etching, which ultimately form the physical structures responsible for light generation and guidance. Any imperfections introduced during this stage, such as sidewall roughness, etch non-uniformities, or mask defects, can lead to scattering losses, mode distortion, and degraded device efficiency. Therefore, achieving high-quality waveguide fabrication is crucial for ensuring stable laser operation.

A lithography mask is typically used to define waveguide structures. The most common approach involves either silica (SiO_2) deposition or the use of hydrogen silsesquioxane (HSQ) as a masking material. HSQ offers a significant advantage; once developed, it transforms into a SiO_2-like structure, which can serve as a direct hard mask for etching. This reduction in processing steps not only lowers fabrication complexity but also enhances pattern fidelity by minimising potential alignment errors and resist-related defects [126]. Due to these advantages, HSQ was chosen as the lithography mask in this study. Figure 3.12(a) displays an SEM image of the defined HSQ mask, showcasing its high resolution in accurately defining waveguide structures and sidewall gratings.

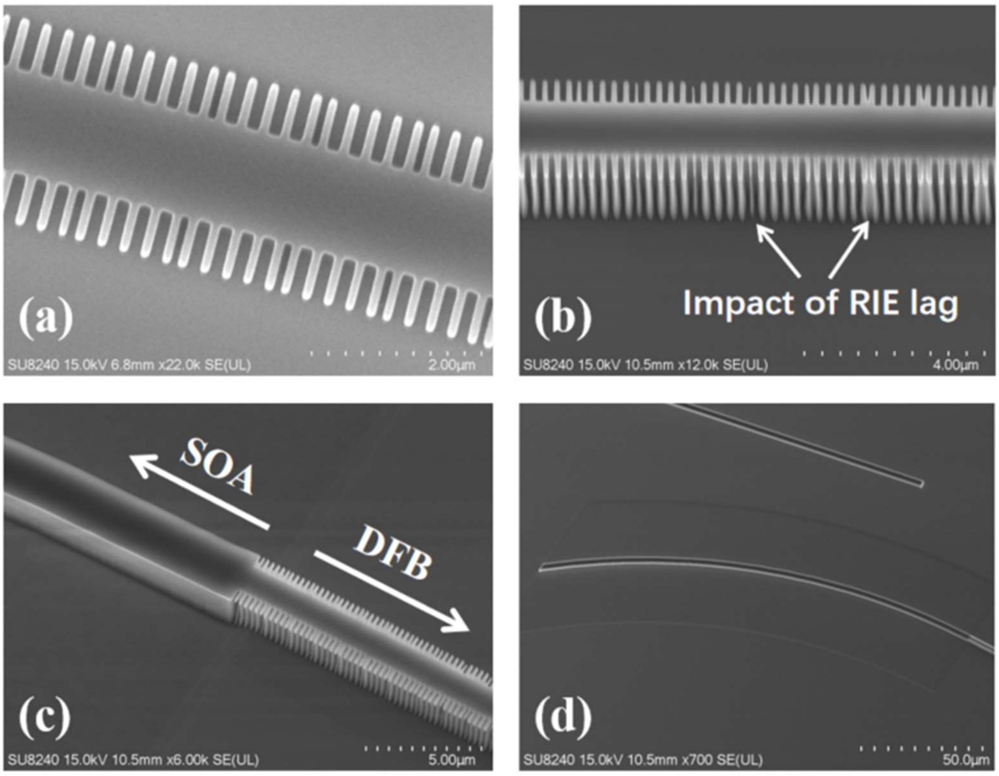

Figure 3.12: SEM images of fabricated (a) waveguide mask, (b) etched 4PS-SBG grating, (c) the junction of DFB and SOA and (d) etched rear short curved waveguide.

Once the ridge waveguide pattern was defined, inductively coupled plasma (ICP) dry etching was employed to transfer the pattern into the semiconductor material. The ICP380 system was used for this process, following an established $Cl/CH_4/H_2/Ar$ (16/10/12/5 sccm) etching recipe, which has been previously optimised for precise pattern transfer [127]. Figure 3.12(b) provides an SEM image of an etched 4PS-SBG grating, confirming the etching accuracy required for efficient optical feedback.

However, a common etching challenge encountered during the process of nPS-SBG structure was "reactive ion etching lag (RIE lag)". This phenomenon occurs due to the etch rate dependency on slot width and aspect ratio, where narrow trenches experience lower etching rates compared to wider openings [128]. Compared to uniform gratings, narrower gratings can be formed in a 4PS-SBG structure, where a $\pi/2$ phase difference exists between each pair of adjacent sections. This will make the RIE lag effect more pronounced, which may cause the grating to be over-etched and thus affect κ. This impact can be reflected in subsequent tests.

Overall, the waveguide etching is very well done. The etching results of the junction of DFB and SOA and the curved waveguide are shown in Figure 3.12 (c) and (d), respectively. These results demonstrate the feasibility of using HSQ-based lithography and ICP dry etching for producing high-quality waveguides.

Figure 3.13 illustrates a side view of an etched 4PS-SBG grating under SEM. From this figure, we can see that the side-wall gratings were defined and the 4PS-Bragg grating structures are very clear, with a ridge waveguide width of 2.5 μm and a grating recess depth of 0.6 μm on each side of the ridge. Each sampling period contains four sections, and there is a π/2 phase difference between adjacent sections. Meanwhile, a π phase shift of the seed grating period Λ_0 was inserted into the centre of the cavity of the 800-μm-long DFB laser to ensure the SLM operation of the device.

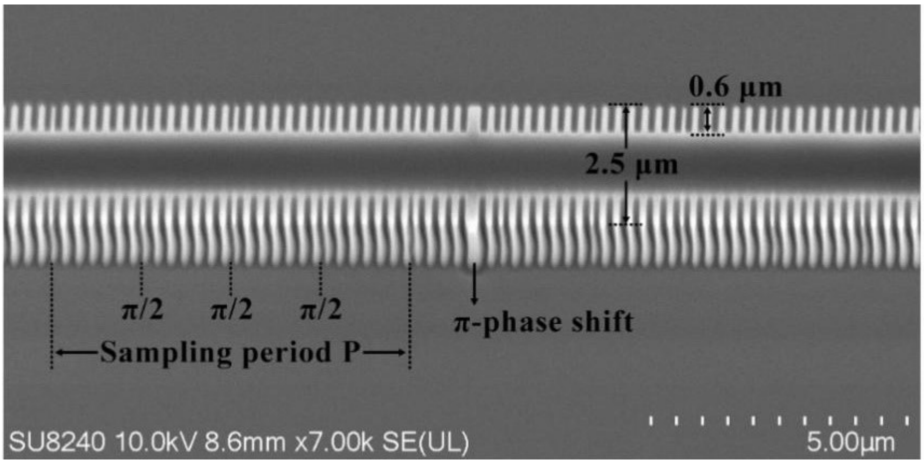

Figure 3.13: SEM picture of 4PS-SBG sidewall grating

3.1.6.5 Contact Window Opening

After defining the ridge waveguides, a 200 nm SiO_2 layer was deposited by PECVD, followed by a 400 nm HSQ spin-coating for surface smoothing. The sample was then baked at 180°C for 2 hours, solidifying the HSQ into liquid glass. Finally, a 100 nm PECVD SiO_2 layer was added for insulation. Contact windows were then opened on top of the ridge waveguides by selectively etching the SiO_2, followed by metal deposition to form p-contact electrodes. This process ensured that electric currents were injected only into the top area of the ridge waveguides, preventing unwanted leakage [129].

3.1.6.6 P-contact Metal Deposition

After the contact window opening, a resist of polymethyl methacrylate (PMMA) was spin-coated and patterned to define the p-contact shape. After development, metal deposition was carried out on top of the sample to form the anode electrodes (p-contact). The Ti/Pt/Au metal stack with thicknesses of 33/33/240 nm, respectively, was deposited as the p-contact. Titanium (Ti) was used as an adhesion layer, as it is a reactive metal that readily forms oxides, improving metal-to-semiconductor bonding. Platinum (Pt) acted as a diffusion barrier, preventing gold from migrating into the semiconductor. Since Titanium has lower conductivity than gold, a 240 nm Au layer was deposited to ensure high electrical conductivity. The top 200 nm InGaAs layer in the wafer structure was highly doped with Zn (1.5×10^{19} cm^{-3}), ensuring the formation of a low-resistance p-type ohmic contact with the Ti/Pt/Au stack.

3.1.6.7 InP Substrate Thinning and N-contact Metal Deposition

The initial sample thickness was approximately 370 μm. To facilitate cleaving and improve heat dissipation, the n-type substrate was thinned down to approximately 180 μm. The thinning and polishing process was carried out using Chemical Mechanical Polishing (CMP) with an Al_2O_3 (alumina) dispersoid in water. After thinning and polishing, n-type metallisation was deposited on the backside of the sample. The InP substrate was Si-doped to a concentration of 3×10^{18} cm^{-3}, ensuring good electrical contact. The n-contact metal stack, consisting of Au/Ge/Au/Ni/Au with thicknesses of 14/14/14/11/240 nm, was also deposited via metal evaporation.

3.1.6.8 Rapid Thermal Annealing and Device Bar Cleaving

To enhance the ohmic contact quality for both the p-contact and n-contact, annealing was performed using a Rapid Thermal Annealing (RTA) system. The process was carried out at 380°C for 60 seconds, allowing Ge atoms to diffuse into the semiconductor material beneath the n-contact [130]. This diffusion results in degenerating n-type doping of the InP substrate, significantly reducing contact resistance and improving carrier injection efficiency.

With the annealing completed, the fabrication of the diode lasers was finalized, marking the completion of the full device processing sequence. The final device structure is shown in Figure 3.14(a). To get the lasers for characterization test, the fabricated sample was then cleaved into individual laser bars, as depicted in Figure 3.14(b).

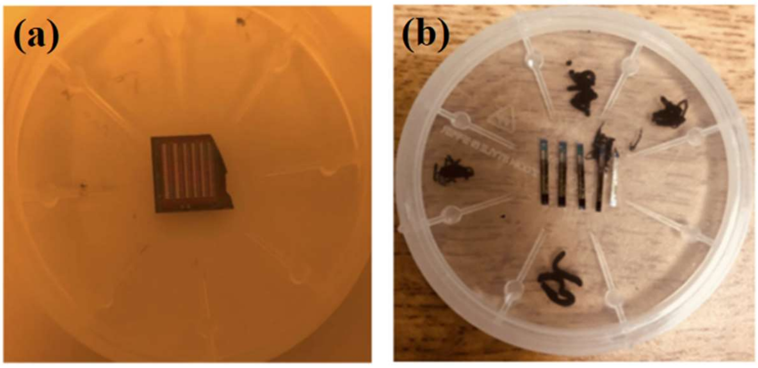

Figure 3.14: (a) Completed sample. (b) Cleaved laser bars.

3.1.7 Test Result

3.1.7.1 Measurement Platform Set-up

Figure 3.15 shows the schematic of the set-up to measure the DFB laser diode integrated with an SOA. A fabricated 4PS-SBG DFB laser array has been mounted on a copper sheet, under which there is a thermoelectric cooler (TEC) used for temperature control (set at 20 °C). The measured device needs two probes to apply current, one for the DFB section and the other for the SOA section. A current driver is used to control the injection currents and the TEC at the same time. The output light is coupled into a lensed fibre and then detected by an optical power meter or an optical spectrum analyzer. The optical power meter is used to measure the output optical power, and the optical spectrum analyzer is used to measure the optical spectrum. Utilizing the General-Purpose Interface Bus (GPIB) interface, automated control can be realized by *Labview*. The current driver is controlled automatically by a computer and generated data can be collected and saved automatically, reducing the measuring time dramatically. All measurements are conducted under continuous-wave (CW) conditions.

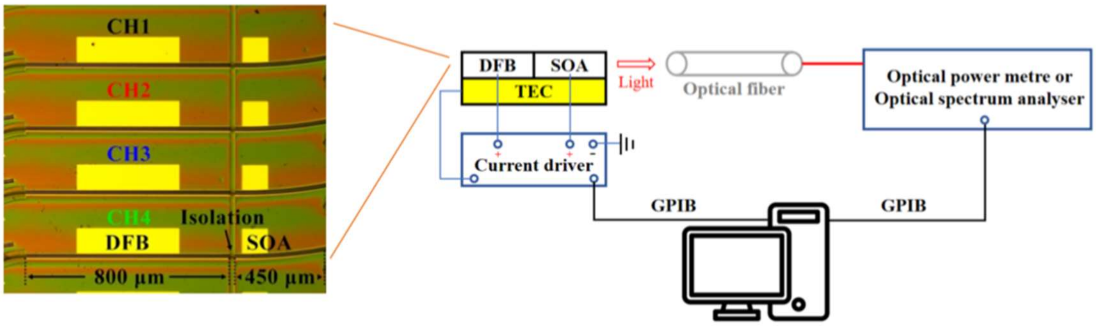

Figure 3.15: Schematic of the Measurement platform set-up for SOA-DFB device test.

Figure 3.16(a) presents a photograph of the experimental setup. Two independent probes were employed for separate current injections, while a lensed fibre was mounted on a three-dimensional translation stage to precisely adjust its position for optimal light coupling. A microscope positioned above the system allowed for real-time alignment verification, with the live feed displayed on a screen to ensure precise probe and fibre positioning. Figure 3.16(b) provides a photograph of the two probe tips in contact with the device and the lensed fibre positioned for light collection. Due to the curved ridge waveguide design, the lensed fibre was tilted at a specific angle of 32°, aligning it with the emission direction to maximize coupling efficiency.

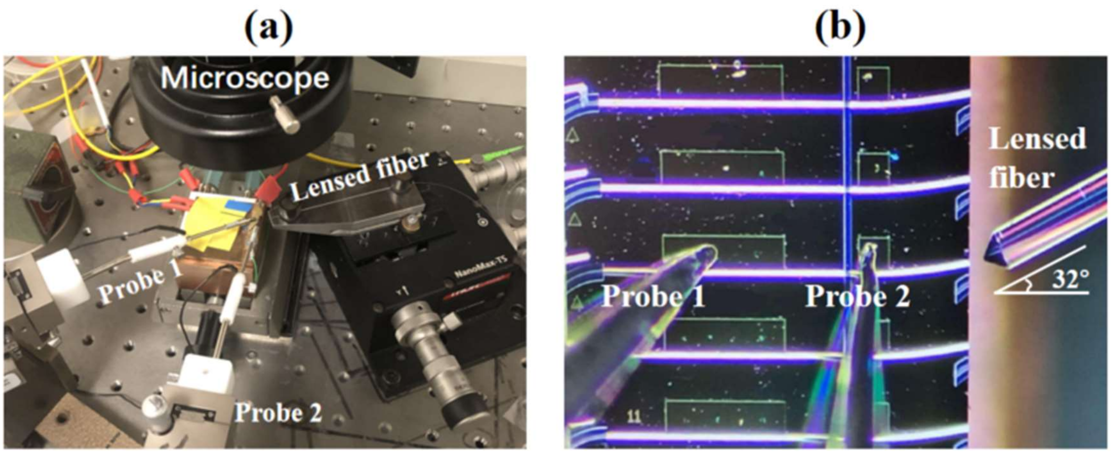

Figure 3.16: The photograph of (a) the experimental set-up, and (b) two probe tips in contact with the device.

3.1.7.2 Output Power Measurement and Coupling Coefficients Calculation

Before analysing spectral properties or other dynamic performance, measuring the output power first can find fundamental characteristics of devices like threshold current, device efficiency and potential nonlinear effects, which can be directly used for later spectral analysis. Additionally, understanding the interaction between the DFB laser and the SOA helps in optimising operating conditions for stable single mode lasing and high-power output.

Figure 3.17 shows typical output power versus DFB current (I_{DFB}) (L-I_{DFB}) characteristics for CH1 under different SOA currents (I_{SOA}). The threshold current of the DFB laser is 37 mA. When fixing I_{DFB} and increasing I_{SOA}, the output power from the SOA side is increased. When I_{DFB}=206 mA and I_{SOA} = 120 mA, the output power reaches its maximum value of 33 mW. For all the L-I_{DFB} curves, a relatively larger slope efficiency is between 37 mA and 50 mA. This is because the SOA has a larger amplification for the relatively lower optical power from the DFB part. As I_{DFB} >50 mA, the optical power from the DFB part becomes larger, resulting in a decrease in SOA amplification and a relatively lower slope efficiency [131]. As for I_{DFB} >175 mA, several kinks observed in all the P-I curves' characteristics indicate that the DFB laser is disturbed by the amplified back reflection from the SOA facet.

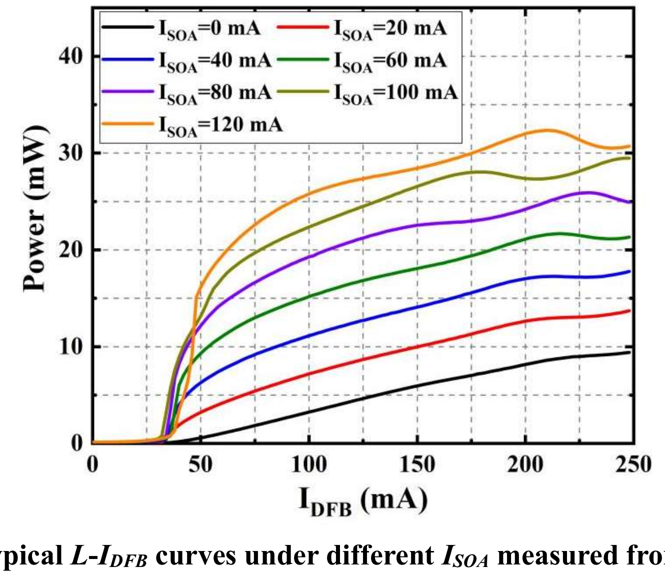

Figure 3.17: Typical L-I_{DFB} curves under different I_{SOA} measured from the SOA side.

The coupling efficiency κ of the uniform grating and 4PS-SBG devices can be evaluated by analysing their spectra at the threshold current. DFB lasers with a uniform grating (other than a π-phase shift section inserted at the centre of the DFB laser cavity) and the 4PS structure were fabricated on the same wafer. The measured spectra with

I_{DFB}=34 mA and I_{SOA}= 30 mA are shown in Fig. 3.18. From coupled mode theory, the κ can be calculated from $\Delta\lambda_s$ and λ_B using the following formula [132].

$$\kappa = n_{eff} \cdot \frac{\Delta\lambda_s}{\lambda_B^2} \tag{3.4}$$

where n_{eff} is the effective index; $\Delta\lambda_s$ is the stopband width; λ_B is the Bragg wavelength of the grating. Fig. 3.18(a) and (b) show the measured optical spectrum for 800-μm-long DFB lasers with a uniform grating and 4PS-SBG, respectively. For the uniform grating, the stopband width $\Delta\lambda_s$ is 1.378 nm and the Bragg wavelength λ_B is 1550.9 nm. For 4PS-SBG, the stopband width $\Delta\lambda_s$ is about 1.15 nm, and the Bragg wavelength λ_B is about 1558.3 nm. Therefore, the κ values of the uniform grating and 4PS-SBG devices are calculated as 18.28 cm^{-1} and 15.12 cm^{-1}, respectively. The ratio of the effective κ of the 4PS-SBG to that of the uniform grating is about 0.83, lower than the theoretical value of 0.9, which is probably due to the RIE lag effect during the sidewall grating fabrication, which has been mentioned in the last section [133]. However, the results still show that the κ is significantly enhanced using the 4PS-SBG structure.

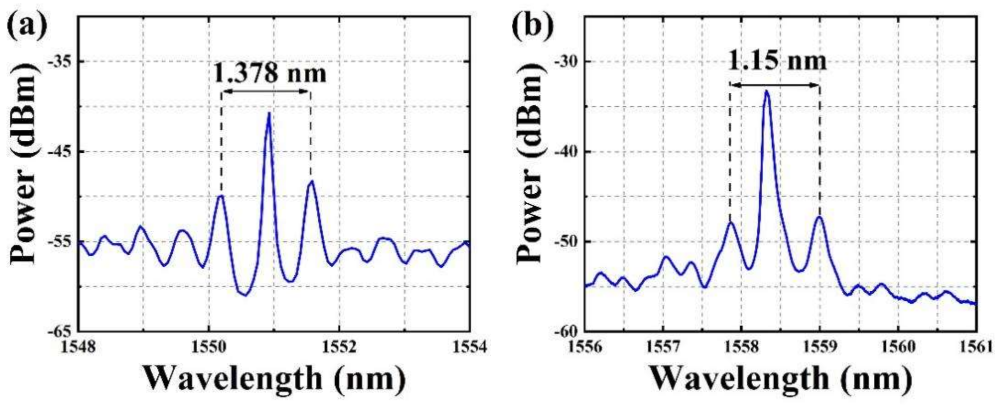

Figure 3.18: Optical spectrum at threshold current of (a) uniform grating with a π-phase shift section inserted at the centre of the DFB laser cavity, and (b) 4PS-SBG structure.

3.1.7.3 Single Mode Performance and Wavelength Spacing Control

Ensuring mode stability is a prerequisite for achieving precise wavelength spacing in laser arrays. Any instability in the lasing mode, such as mode hopping or spectral broadening, can introduce uncertainties in the emitted wavelength, making it difficult to maintain the desired channel spacing. Fig. 3.19(a) shows a 2D optical spectrum versus I_{DFB} (0-300 mA) with I_{SOA} = 30 mA for CH1. Very stable SLM operation is observed from the threshold current (37 mA) up to 300 mA, with no mode-hopping. The average current-induced wavelength redshift coefficient is around 0.023 nm/mA, which is much smaller than that of an FP laser and allows for fine-tuning of wavelengths across the DWDM laser array. It is worth noting that the nonlinear wavelength shift with increasing current is mainly attributed to thermal and carrier-induced refractive index changes; these effects lead to a nonlinear redshift in the emission wavelength with increasing power, especially in the high-current regime.

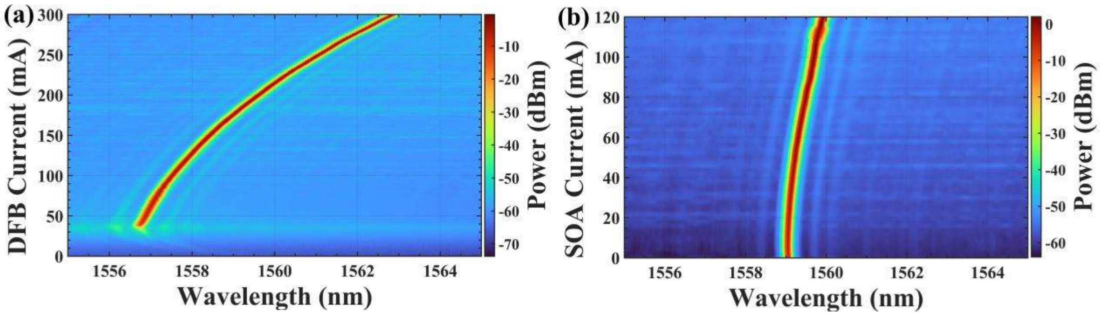

Figure 3.19: (a) 2D optical spectra vs I_{DFB} of CH1 with I_{SOA} = 30 mA, (b) 2D optical spectra vs I_{SOA} with I_{DFB} = 180 mA.

Fig. 3.19(b) presents a two-dimensional optical spectrum versus injection current of the semiconductor optical amplifier (I_{SOA}), ranging from 0 to 120 mA while maintaining the DFB laser current (I_{DFB}) at 180 mA. Stable SLM operation is maintained, with a current-induced redshift of approximately 0.0075 nm/mA. These results indicate that varying the I_{SOA} current has a minimal impact on the DFB lasing wavelength, demonstrating that the SOA effectively boosts output power without significantly altering the wavelength.

Once mode stability is established, the next crucial step is to precisely control the wavelength spacing of the laser array to ensure uniformity across all channels. Lasers in the array were measured sequentially, not simultaneously, to avoid thermal interference. Fig. 3.20(a) shows the optical spectra for each channel with I_{SOA} =30 mA and I_{DFB} = 180 mA. The spectrum was measured using an optical spectrum analyser (OSA) with a resolution bandwidth of 0.06 nm. The lasing wavelengths are 1559.64

nm, 1560.44 nm, 1561.22 nm, and 1561.96 nm from CH1 to CH4. These measured lasing wavelengths are nearly the same as the designed ones (shown in Table 3.1).

Fig. 3.20(b) shows the corresponding linear fit to the lasing wavelengths of the four channels, and the slope of the line is 0.774 nm, with an error of 0.026 nm compared with the designed wavelength spacing of 0.8 nm. The value of this error is less than the resolution of the OSA, which demonstrates the excellent wavelength precision that can be achieved by the 4PS-SBG structure.

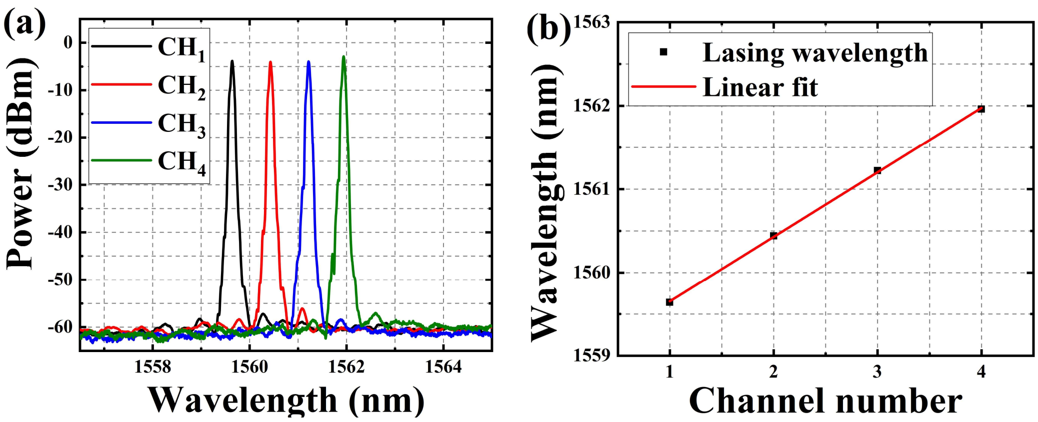

Figure 3.20: (a) Measured optical spectrum of the devices for different periods, *P*, when I_{DFB} = 180 mA, I_{SOA} = 30 mA, (b) lasing wavelengths and linear fit to the four points.

The SMSR of the four devices versus I_{DFB} is shown in Fig. 3.21. The SMSRs of all four channels are larger than 50 dB when I_{DFB} >100 mA and the maximum SMSR value can reach 55 dB when I_{DFB}=250 mA.

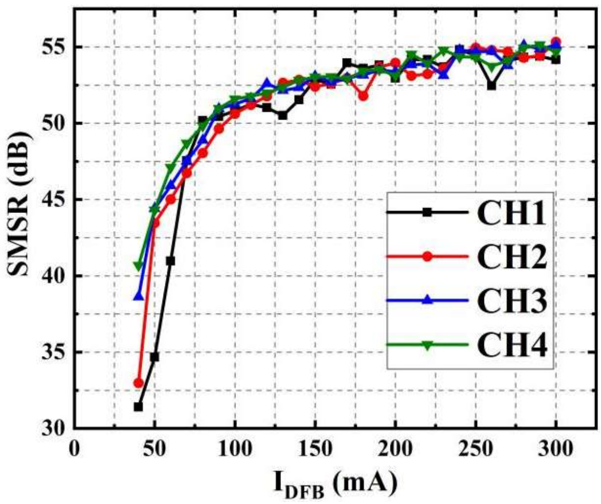

Figure 3.21: SMSRs of four lasers versus I_{DFB} when I_{SOA} is 30 mA.

The measurement results confirm that the 4PS-SBG structure enables precise control over individual DFB laser lasing wavelengths while achieving a high coupling coefficient. SLM operation was maintained across a wide range of drive currents for both the DFB and SOA, with a maximum output power of approximately 33 mW and an SMSR exceeding 55 dB. The successful implementation of sidewall grating 4PS-SBG DFB laser arrays demonstrates a significant advantage in fabrication, requiring only a single MOVPE step and one dry etch process of the III-V material. This streamlined fabrication approach makes the technology highly attractive for DWDM applications.

Beyond confirming the effectiveness of the 4PS-SBG design, these experimental results offer valuable insights into optimising DFB laser structures based on AlGaInAs material. The data highlight key areas for refinement in future designs, such as optimising the interplay between cavity length and grating recess depth to enhance mode stability and suppress the SHB effect. These findings provide a strong foundation for the next generation of devices, enabling further improvement of the required device performance.

3.2 DPS-DFB Device

As previously discussed, the design of devices is closely linked to the choice of wafer structures, as different layer compositions exhibit distinct electrical and optical properties, such as refractive index, bandgap energy, and carrier mobility.

For narrow-linewidth lasers, minimising internal optical loss is essential, as it directly reduces the influence of spontaneous emission noise and enhances temporal coherence. One effective approach to achieving lower internal loss is to reduce the number of quantum wells, given that increasing the number of quantum wells generally leads to higher absorption and scattering losses. Based on these considerations, a 3QW wafer was selected instead of a 5QW structure to achieve optimal performance for narrow-linewidth operation [134].

3.2.1 Wafer Structure and Device Design

3.2.1.1 Wafer Structure and Comparison

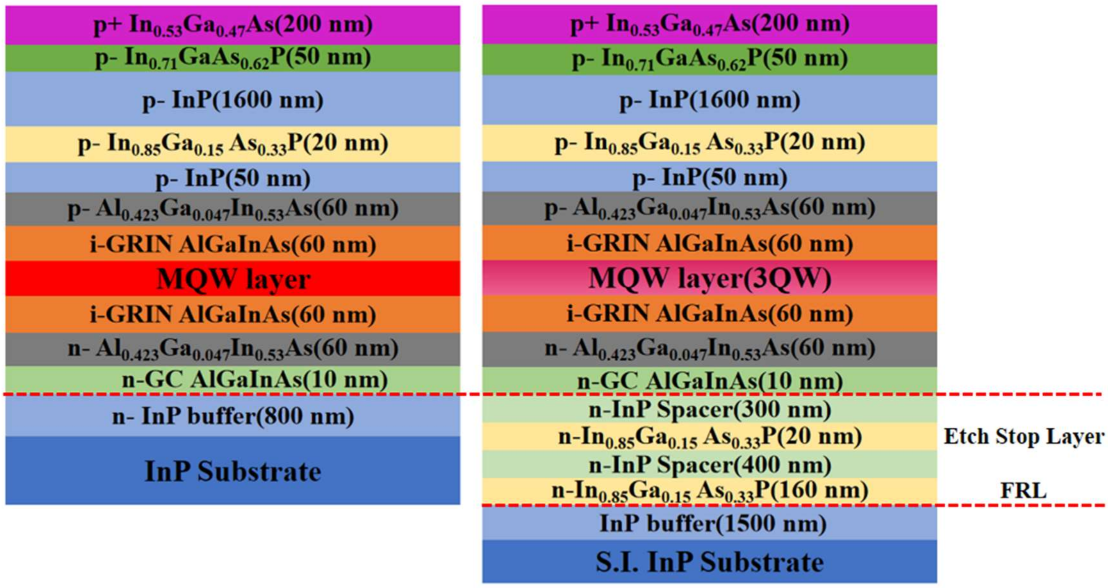

Figure 3.22: Comparison between 3QW structure and 5QW structure.

The wafer used for fabricating the CPM devices incorporates several optimisations over the standard MQW structure to better accommodate the specific requirements of narrow-linewidth operation. Figure 3.22 illustrates the comparison between the basic 5QW structure and the newly designed 3QW structure, respectively. Both structures utilise a 1.55 μm AlGaInAs/InP SC-MQW design, which balances compressive-strained and tensile-strained layers to improve carrier confinement and optical performance.

In both wafers, the SC-MQW active region consists of compressively strained (+1.2%) AlGaInAs quantum wells (6 nm thick) and tensile-strained (−0.3%) AlGaInAs barriers (10 nm thick) [135]. The 5QW structure comprises five quantum wells and six quantum barriers, whereas the 3QW structure contains three quantum wells and four quantum barriers. The active region is symmetrically sandwiched between two 60 nm GRINSCH layers, along with a 60 nm p-AlGaInAs layer on the p-side and an n-AlGaInAs cladding layer on the n-side.

The most significant difference between the two wafer structures lies in the layers beneath the MQW region. The 3QW structure incorporates an optimised 160 nm thick far-field reduction layer (FRL) composed of $In_{0.85}Ga_{0.15}As_{0.33}P$, along with a 0.7 μm InP spacer layer [136]. Additionally, a 20 nm wet etch-stop layer is embedded within the spacer layer to facilitate precise fabrication. These modifications were strategically implemented to maximise the optical mode size while maintaining a single fundamental transverse mode operation. The FRL layer functions as a secondary waveguide, featuring a refractive index that is lower than that of the active region but higher than that of InP. This configuration effectively extends the optical near-field distribution toward the n-cladding. This mode engineering approach minimises optical loss in the heavily doped p-cladding layer, suppresses higher-order transverse modes, and reduces the optical confinement factor, contributing to narrower linewidth operation [137]. Another key distinction lies in the choice of substrate. The 5QW structure utilises a standard n-doped InP substrate, whereas the 3QW structure is grown on a semi-insulating (SI) InP substrate. This alteration prevents the direct deposition of the n-electrode on the backside, necessitating modifications in the device layout and fabrication process.

3.2.1.2 Device Design

A fundamental approach to achieving a narrower linewidth in semiconductor lasers is to extend the cavity length. This is based on the established Schawlow-Townes linewidth equation, which indicates that the laser linewidth is inversely proportional to both the cavity length and the output power. By increasing the cavity length, the photon lifetime within the cavity is extended, effectively reducing phase noise and broadening spectra. Considering this, a 2000 μm cavity length was chosen for the DFB laser design, as shown in Figure 3.23.

Unlike previous designs that integrated an SOA at the output facet to boost power, this structure excludes the SOA section. The primary motivation for this decision is to eliminate potential crosstalk between adjacent devices in the laser array. A 40 μm-long straight waveguide is added at the output side of the device, serving as a cleaving region.

Similarly, to minimise end-facet reflections and FP effects, a 125 μm unpumped curved waveguide with a 233.3 μm radius and 32° angle is added at one laser output facet. Since this wafer is an SI substrate, the P-contact and N-contact need to be designed on the same side, ensuring uniform current injection across the active region.

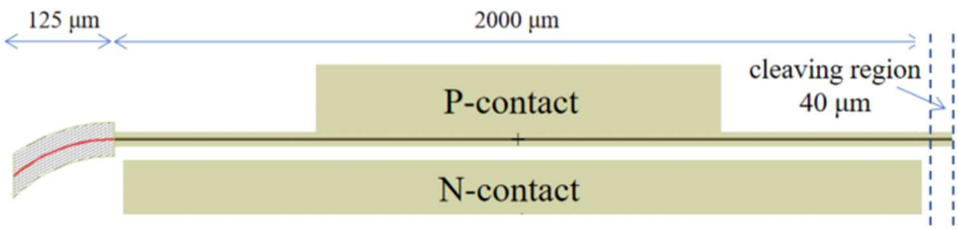

Figure 3.23: The pattern design of a CPM grating DFB laser.

With the cavity design established, the next crucial step is the optimisation of the grating parameters to ensure the desired coupling coefficient κ is achieved. Since the cavity length has been extended to 2000 μm, it is necessary to adjust the grating recess depth accordingly to optimise the κL product for stable single-mode operation.

Given that DPS gratings resemble uniform gratings in their structure properties, the required κ value can be estimated using the uniform grating model. In previous designs with an 800 μm-long cavity, the theoretical coupling coefficient was determined to be $\kappa = 100$ cm^{-1}. For the 2000 μm-long cavity in the current design, the required coupling coefficient of DPS grating is calculated as $\kappa_{DPS} = (100\times800)/(0.83\times2000) = 48.2$ cm^{-1}.

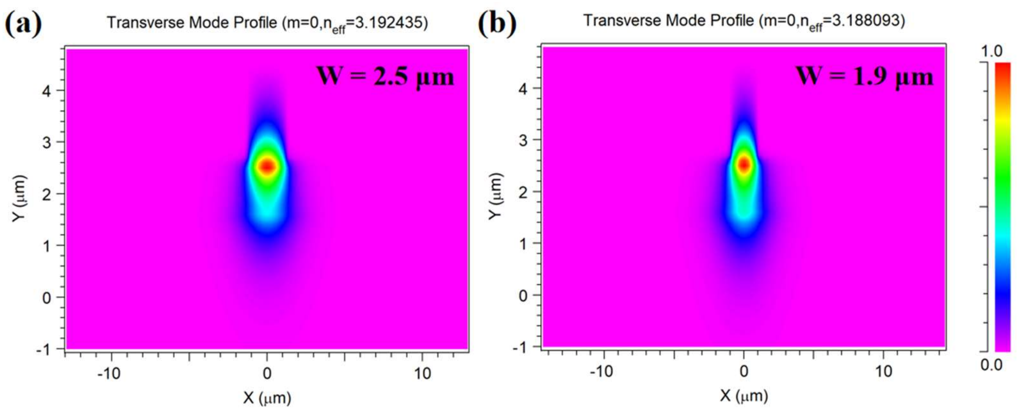

Figure 3.24: Transverse mode profile for different waveguide widths (a) Mode profile for W = 2.5 μm with an effective refractive index of n_{eff} = 3.192; (b) Mode profile for W = 1.9 μm with an effective refractive index of n_{eff} = 3.188.

Since the grating recess depth d directly influences κ. To determine the appropriate recess depth, *RSoft* simulations were performed to obtain the effective refractive index corresponding to different recess depths. The waveguide width W remains set at 2.5 μm, while the d is varied to achieve the target κ value. As shown in Figure 3.24, through simulation for 3QW wafer structure, while the waveguide width W = 2.5 μm with an effective refractive index of n_{eff} = 3.192, and W = 1.9 μm (recess depth d is of 0.3 μm) with an effective refractive index of n_{eff} = 3.188, the calculated κ value from Equation 3.2 is 50 com^{-1}, which aligns with the requirement. Additionally, the n_{eff} of grating waveguide can be estimated as (3.192+3.188)/2 = 3.19, therefore, to meet the laser emission at the gain centre (1550 nm), the grating period is set to 243 nm.

At this point, the design of the overall device has been completed. Figure 3.25 illustrates a sidewall grating DFB laser featuring a DPS grating structure. This DFB laser utilises a 3QW AlGaInAs active layer, complemented by an FRL situated beneath the active layer on an S.I. InP substrate. The top ridge waveguide is 2.5 μm wide and 1.92 μm high, with a grating recess depth of 0.3 μm, and the grating period is 243 nm. The second ridge, incorporating the active layer, is 20 μm wide and 608 nm high, and is designated for n-contact deposition. The total cavity length of the DFB laser (L_{DFB}) is 2 mm, with the DPS region centred in the cavity length. A 125 μm unpumped curved waveguide with a 233.3 μm radius and 32° angle is added at one laser output facet.

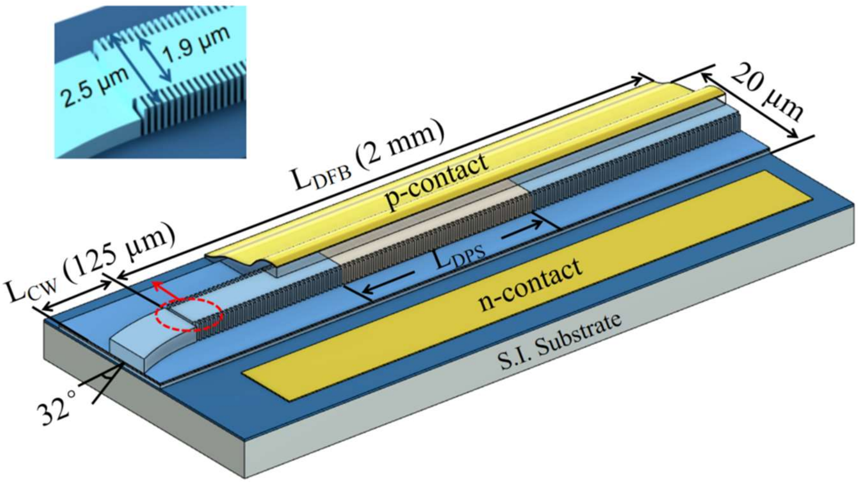

Figure 3.25: Schematic of the DFB structure based on the DPS grating, with the inset showing the dimensions of the ridge waveguide featuring sidewall gratings.

3.2.2 Fabrication Process of DPS Devices

The fabrication process of this DPS device closely follows the steps used for the 4PS-SBG device. And there are three key differences in the fabrication steps. Firstly, an additional step is required to define the N-contact region. Secondly, during the contact window opening process, both the P-contact and N-contact windows must be opened simultaneously. Finally, in the metal deposition step, both the P-contact and N-contact are deposited in a single fabrication step. Therefore, the fabrication process flow of this device can be divided into 9 key steps:

- Sample cleaning.
- Marker definition.
- Isolation definition.
- Waveguide definition (first etch).
- N-contact region definition (second etch).
- P- and N-Contact Window Opening.
- P-contact and N-contact metal deposition.
- InP substrate thinning.
- RTA and device bar cleaving.

3.2.2.1 Waveguide and N-Contact Region Definition

As shown in Figure 3.26, after the first etching for the waveguide definition, the remaining surface is still covered by the p-doped layers. Thence, to define the N-contact region, two-step etching is necessary, consisting of the first etching to define the waveguide and a second etching step to expose the n-doping layer. This process must be carefully executed to ensure that the waveguide structure remains intact while selectively removing the surrounding material. To protect the waveguide during this deep etching process, a 20 μm-wide rectangular region is covered with PMMA as a protective mask. This ensures that the ridge waveguide remains unaffected while the second etching. The second etching is still using ICP380 dry etching, to precise control over the etch depth. The process continues until the etch fully penetrates through the MQW layer and reaches the n-doped region.

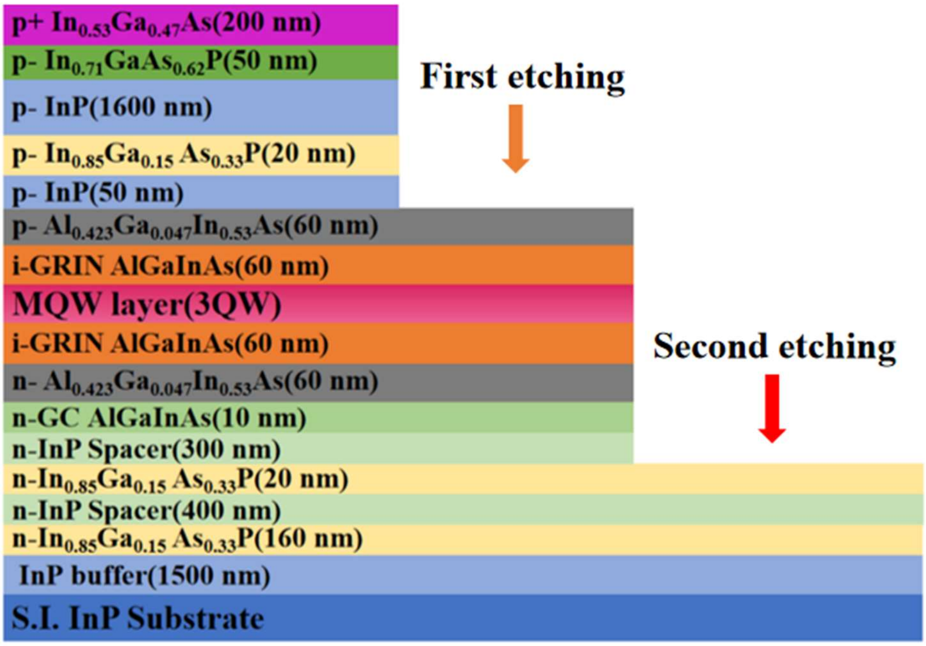

Figure 3.26: Two-step etching process for exposing the n-doping layer in the 3QW Wafer Structure.

Figure 3.27(a) presents an SEM image of the entire device layout after etching. Each fabricated device features a 2000 µm-long grating section, a 40 µm-long straight waveguide for cleaving, and a curved waveguide on the left side. A magnified view of one of the devices is shown in Figure 3.27(b), where the structural differentiation between the p-doped and n-doped layers can be observed. The grating structure is clearly defined atop a 20 µm-wide platform corresponding to the p-doped region, while the n-doped layer lies beneath this etched platform, confirming the effectiveness of the two-step etching process in selectively exposing the desired regions without compromising waveguide integrity.

Figure 3.27(c) provides a detailed SEM cross-section of the sidewall grating structure. The well-defined grating features exhibit a period of 243 nm and a recess depth of 0.3 µm on each side of the ridge.

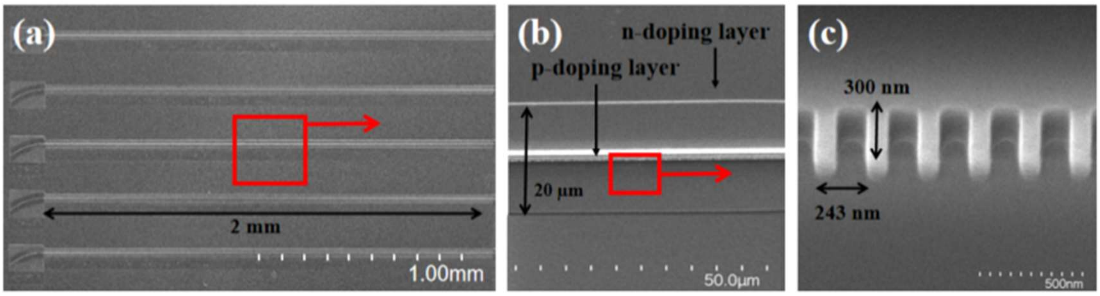

Figure 3.27: SEM image of (a) the entire device structure; (b) Magnified view the grating structure on a 20 μm-wide p-doped platform, (c) Cross-sectional of the sidewall grating.

3.2.2.2 Contact Window Opening and Metal Deposition.

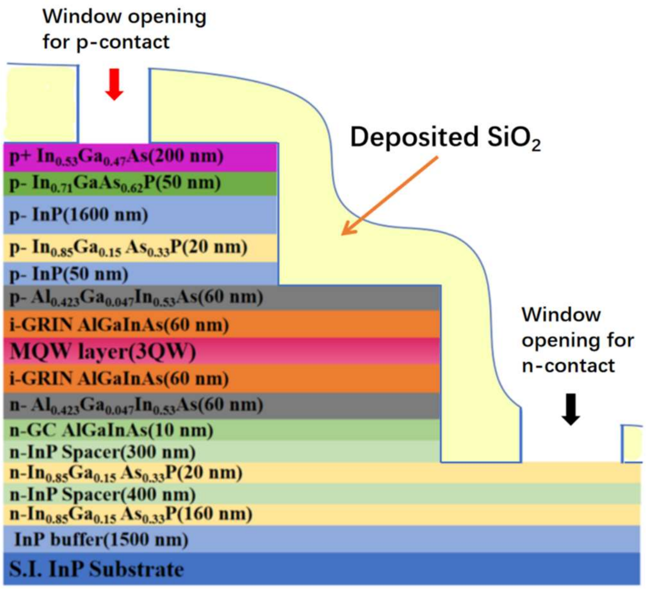

Figure 3.28: Schematic of SiO_2 deposition and window opening for p- and n-contact.

After defining the ridge waveguides, an insulation layer (200 nm SiO_2, 400 nm HSQ, 100 nm SiO_2) was deposited onto the sample. Unlike the fabrication process of 4PS devices, where the p- and n-contacts are defined in separate steps, the DPS device requires both contacts to be opened simultaneously in different regions. Shown in Figure 3.28, this is achieved by selectively etching the SiO_2 layer to expose the underlying p- and n-doped layers, ensuring proper electrical connectivity. Following this step, a single process of metal deposition is performed to define both the p-contact and n-contact electrodes. This approach not only streamlines fabrication by reducing the number of processing steps but also ensures uniform contact formation, improving device reliability and performance.

The remaining fabrication steps follow the same process as the 4PS device. After electrode formation, the samples undergo InP substrate thinning to improve heat dissipation, ensuring better thermal management during operation. Once thinned, the samples are annealed using RTA to optimise contact performance and material properties. Finally, the completed devices are cleaved into individual laser bars, preparing them for subsequent testing and characterisation.

3.2.3 Test Results

3.2.3.1 Measurement Platform Set-up

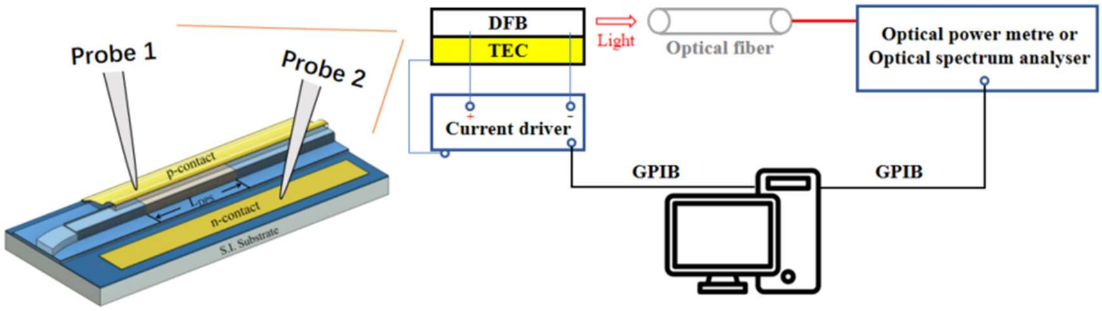

Figure 3.29: Schematic of the measurement platform setup for DPS-DFB device test.

Figure 3.29 shows the schematic of the setup to measure the DPS DFB laser. Each laser bar was mounted onto a copper heat sink, which was placed on a Peltier cooler. The heat sink temperature was set to 20 °C. Two probes are used to apply current; one is connected to the p-contact, and another is connected to the n-contact. The output light emitted from the straight facet of the DFB laser is directly coupled into a lensed fibre and subsequently measured using either an optical power meter or an optical spectrum analyser. Utilising the GPIB interface, automated control can be realised by *LabVIEW*. All measurements are conducted under CW conditions.

3.2.3.2 Output Power Measurement and SMSR

The power-current (*L-I*) characteristics of different types of grating devices are presented in Figure 3.30(a). The threshold current is 122 mA for the traditional π phase-shifted laser and approximately 85 mA for DPS grating devices. The results showed a significant threshold current reduction in DPS grating devices, due to a uniform light field distribution that enhances the optical field and gain medium overlap [138]. For traditional phase-shifted lasers, the maximum output power reaches 13 mW at a DFB current (I_{DFB}) of 400 mA. In contrast, all DPS grating devices demonstrate higher output power at the same drive current. A kink at I_{DFB} =184 mA is observed in the 3π DPS grating device due to mode hopping. However, excluding the effects of mode hopping, increasing the phase shift value leads to a rise in output power, with the highest output of 15.5 mW achieved by the 15π DPS grating device at I_{DFB} = 400 mA. This is because a larger DPS phase shift improves optical field uniformity, reduces phase noise, and enhances laser feedback, resulting in lower threshold current and higher slope efficiency than conventional π-phase-shift DFB lasers.

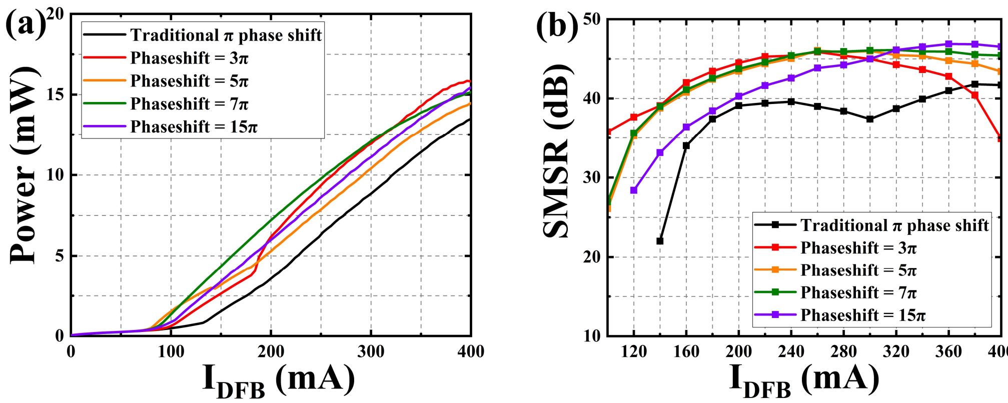

Figure 3.30: (a) Typical *L*-I_{DFB} curves of traditional π phase shift grating and 3π, 5π, 7π and 15π phase shifted DPS gratings with L_{DPS}/L_{DFB} = 1/8, (b) SMSRs versus I_{DFB} for traditional π phase shift grating and DPS gratings with 3π, 5π, 7π, and 15π phase shifts, with L_{DPS}/L_{DFB} = 1/8.

The SMSRs of traditional π phase-shifted and DPS grating devices with 3π, 5π, 7π and 15π versus I_{DFB} are shown in Fig. 3.30(b). For the traditional π phase-shifted device, the SMSRs fluctuate around I_{DFB} = 290 mA due to mode-hopping, with the maximum SMSR value reaching 41 dB at I_{DFB} = 380 mA. By contrast, multi-π phase shift DPS grating devices exhibit more stable and higher SMSRs. The highest SMSR value achieved is 47 dB for the 15π phase shift DPS grating device, which operates in a stable SLM across I_{DFB} range from 200 mA to 400 mA with an SMSR consistently above 40 dB.

These results further confirm the advantages of DPS grating designs. The uniform optical field distribution enabled by DPS structures not only reduces the threshold current and enhances output power but also effectively suppresses side modes, leading to improved spectral purity. Suitable phase shift value enhances the feedback mechanism, suppresses mode competition, and establishes a solid foundation for stable SLM operation.

3.2.3.3 Output Mode Characteristics

For ease of comparison, Figure 3.31 shows a 2D optical spectrum versus I_{DFB} for different types of lasers. The spectrum of the traditional π phase-shifted grating is shown in Fig. 3.31 (a). As the injection current is increased, there is a stable SLM output, and a mode hop appears at I_{DFB}=280 mA. Fig. 3.31 (b) shows the optical spectrum of a DPS grating with 3π and $L_{\mathrm{DPS}}/L_{\mathrm{DFB}}$ =1/5; it shows that when I_{DFB}>280mA, the output exhibits serious mode hopping and multi-mode phenomena, consistent with the simulation results in Fig. 2.43 (c). This is because, at low π values of DPS devices, the single-mode operation is less stable, and as the injection current increases, the gain peak redshifts, allowing side modes to reach threshold and cause mode hopping or multimode behaviour.

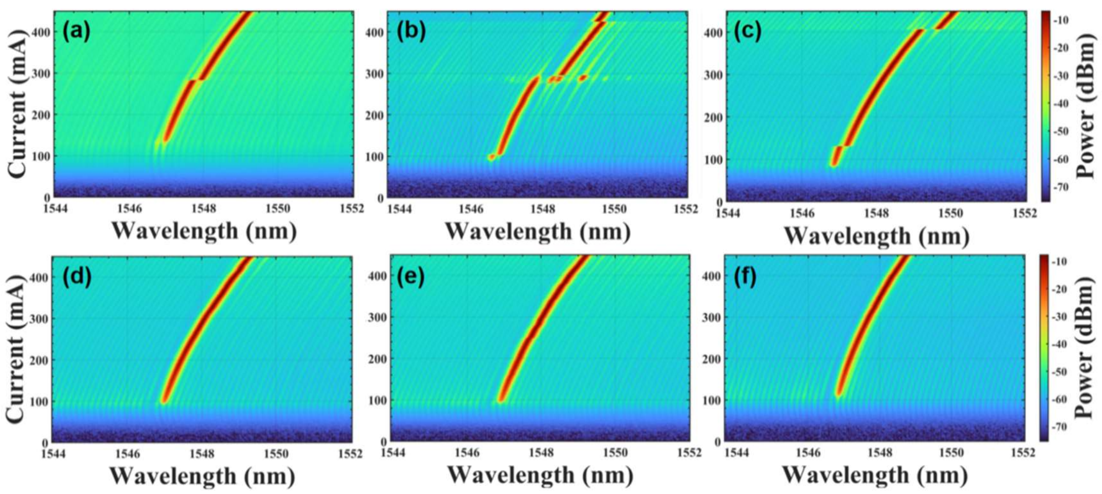

Figure 3.31: 2D optical spectra vs I_{DFB} for (a) traditional π phase shift grating, (b) 3π DPS grating with $L_{\mathrm{DPS}}/L_{\mathrm{DFB}}$ = 1/5, (c) 3π, (d) 5π, (e) 7π, and (f) 15π DPS grating with $L_{\mathrm{DPS}}/L_{\mathrm{DFB}}$ = 1/8.

Fig. 3.31 (c) shows the optical spectrum of a DPS grating with 3π and $L_{\mathrm{DPS}}/L_{\mathrm{DFB}}$ = 1/8, where SLM characteristics are notably enhanced. Fig. 3.31 (d), (e), and (f) show the spectra for DPS gratings with $L_{\mathrm{DPS}}/L_{\mathrm{DFB}}$ = 1/8 and phase shifts of 5π, 7π and 15π, respectively. As the number of π increases, the fundamental mode becomes more dominant while side modes are more strongly suppressed. This enhanced mode selectivity leads to a more stable lasing spectrum, effectively limiting mode hopping. Very stable SLM operation is observed from the threshold current (85 mA) up to 450 mA, without any mode-hopping. The average current-induced wavelength redshift coefficient is around 0.0075 nm/mA.

By optimising the DPS region length and phase shift value, mode competition is effectively suppressed, ensuring stable SLM operation over a wide injection current range. Such stability is critical for achieving narrow linewidth characteristics, as it directly enhances the laser's coherence and spectral purity.

3.2.3.4 Linewidth Measurement Platform Set-up

Since the linewidths of the fabricated lasers are much narrower than the resolution limit of conventional optical spectrum analysers, phase noise characterisation was performed using a more precise and stable radio frequency (RF) -based interferometric measurement system. The interferometric delayed self-heterodyne setup, shown in Figure 3.32, was employed to accurately determine the linewidth of the DFB lasers [139].

To minimise feedback-induced linewidth broadening, the laser output first passes through an optical isolator (ISO), effectively reducing the influence of reflections. After the ISO, an optical coupler (OC) splits the signal into two paths. One portion is directed through a 12.5 km delay fibre to introduce a sufficiently long optical path difference, which corresponds to a delay time of approximately 61.5 μs, which ensures sufficient separation between the delayed and undelayed signals, allowing accurate resolution of laser linewidths down to ~5 kHz [140]. This delayed signal is then attenuated using an adjustable optical attenuator (ATT) to optimise the power level for detection. The second portion of the split optical signal is directed through an 80 MHz acousto-optic modulator (AOM), which applies a frequency shift to the signal prior to recombination. A polarisation controller (PC) is employed in this path to ensure proper polarisation alignment between the two arms, preventing interference degradation due to polarisation mismatches. The two optical signals are then coherently combined. The recombined signal is further split into two outputs: one directed to a photodetector (PD) and analysed directly using an electrical spectrum analyser (ESA) to extract the linewidth information, and the other sent to an OSA for spectral observation, following the procedure described in [141]. This technique allows the extraction of the Lorentzian linewidth by fitting the beat spectrum obtained from the optical signal mixed with its delayed copy.

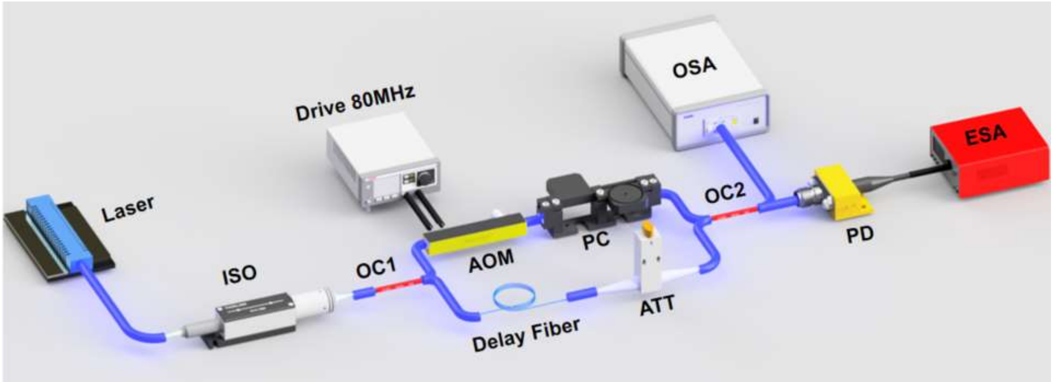

Figure 3.32: Schematic of the delayed self-heterodyne interferometric setup for laser linewidth measurement.

During measurement, the ESA settings were configured with a resolution bandwidth (RBW) of 20 kHz, a video bandwidth (VBW) of 20 kHz, and a sweep time of 0.09047 seconds. The measured RF spectra were fitted to Lorentz and Voigt profiles to calculate the −3 dB linewidth of the DFB laser, which is the typical line shape expected from DFB lasers [142].

3.2.3.5 Linewidth Measurement Results

In the previous performance evaluations, DPS devices with L_{DPS}/L_{DFB} = 1/8 exhibited good characteristics in terms of SLM stability, SMSR, and output power. Therefore, for the linewidth measurement, we selected devices with L_{DPS}/L_{DFB} = 1/8 to further investigate the impact of the phase shift value in the DPS region on linewidth performance. The measured linewidth as a function of I_{DFB} is shown in Fig. 3.33(a). The traditional π phase-shifted devices exhibit typical linewidth-current characteristics: as I_{DFB} increases from 120 mA to 160 mA, the spectral linewidth narrows from 4.6 MHz to 1.45 MHz, before broadening again at approximately 280 mA. In contrast, the DPS grating devices with L_{DPS}/L_{DFB} = 1/8 achieve narrow linewidth characteristics. As the equivalent phase shift in the DPS region increases, linewidth broadening is effectively suppressed. When the phase shift is set to 15π, no evident linewidth broadening is observed within the I_{DFB} range of 120 mA to 400 mA. This is because, as the phase shift further increases, the light field distribution in the DPS region tends to flatten into a straight line.

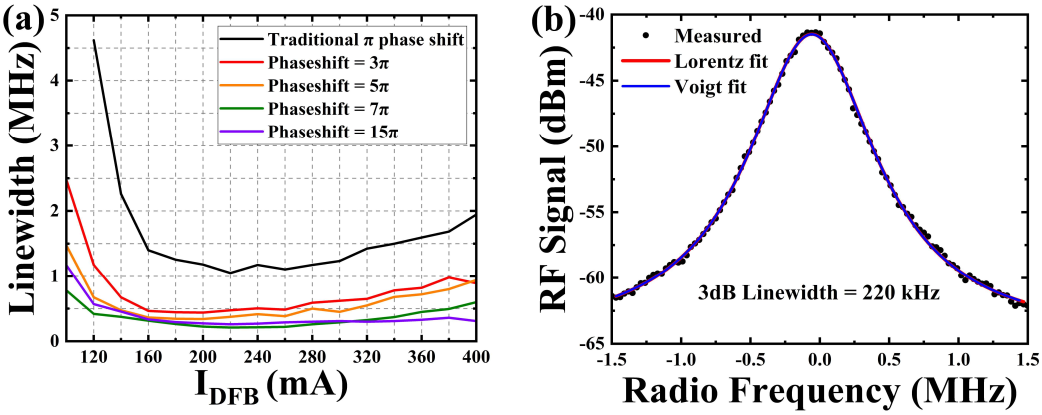

Figure 3.33: Measured optical linewidth versus I_{DFB} for traditional π phase shift grating and DPS gratings with 3π, 5π, 7π, and 15π phase shifts, with L_{DPS}/L_{DFB} = 1/8, (b) RF beat note signal fitted to Lorentzian (red dot) and Voigt (blue dot) profiles for the narrowest achieved linewidth, with a FWHM of 220 kHz, with the 7π DPS grating device at I_{DFB} = 260 mA.

In the analysis of the beat spectrum, both Lorentzian and Voigt profiles were used for fitting. The Lorentzian fit reflects the intrinsic linewidth of the laser, which is mainly caused by spontaneous emission and carrier-induced phase noise. The Voigt profile, being a convolution of Lorentzian and Gaussian components, accounts for both intrinsic and extrinsic noise sources. The Gaussian part typically arises from external factors such as current source fluctuations or temperature instability. Using the Voigt fit allows for more accurate linewidth estimation when external noise is non-negligible. Fig. 3.33(b) shows the RF beat note signal fitted to the Lorentz (red dot) and Voigt (blue dot) profiles for the narrowest achieved linewidth signal (220 kHz) with the 7π DPS grating device at I_{DFB} = 260 mA. It is worth noting that the measured linewidth may exhibit irregular fluctuations at certain bias currents. This behaviour can be attributed to extrinsic factors such as current source noise, temperature instability, mechanical vibrations, or residual optical feedback, which are not intrinsic to the laser itself but can influence the observed linewidth during measurement.

In conclusion, the experimental results demonstrate that DPS grating devices offer significant advantages, including reduced threshold current, stable SLM operation, improved side-mode suppression, and robust narrow-linewidth performance. By carefully designing the phase distribution in the DPS region, spatial hole burning can be effectively mitigated, and the linewidth can be further reduced, resulting in excellent spectral purity and stability across a wide current range. These attributes position DPS DFB lasers as strong candidates for high-coherence applications that demand high power and narrow linewidths.

3.3 CPSG DFB Device

The successful implementation of DPS structures has demonstrated the feasibility of phase distribution modulation in enhancing laser performance. Building upon this concept, the next step is to extend phase distribution across the entire grating structure, leading to the development of CPSG devices. By incorporating a smoothly varying phase shift throughout the grating, CPSG aims to further refine spectral control, improve wavelength stability, and explore new possibilities in grating engineering.

3.3.1 Device Design

The wafer used for fabricating the CPSG devices is identical to that of the 4PS devices. However, due to inherent variations in industrial manufacturing, wafer parameters may exhibit slight differences across production batches. In this case, the effective refractive index of the wafer was experimentally determined through sample testing, yielding a value of 3.21, which was not derived from direct index measurement but was inferred from spectral shifts observed in devices fabricated from the same wafer, approximately 0.56% higher than the theoretical expectation. Based on this measured refractive index, the grating period was set to 243 nm to ensure laser emission within the wavelength range around 1560 nm.

To validate the feasibility of the proposed CPSG design, laser arrays with different grating lengths (800 μm and 400 μm) and total phase distributions (2π and 4π) were fabricated, corresponding to the simulated parameters in Table 2.2. In each array, the first laser served as a control reference, utilising a uniform grating with a π phase shift at the centre of the cavity. The subsequent lasers, however, incorporated phase modulation, with a total phase difference of either 2π or 4π between adjacent devices. Additionally, to simplify the testing process and eliminate potential crosstalk effects, the design does not include an SOA. Figure 3.34 illustrates the schematic layout of the CPSG DFB device

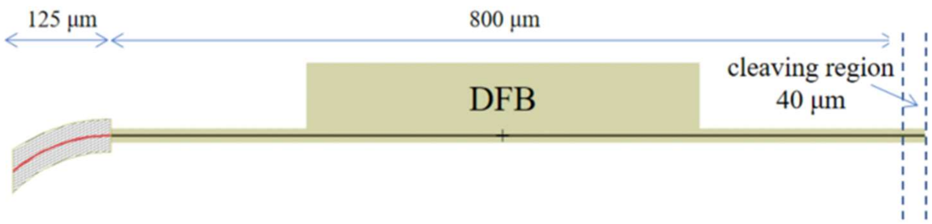

Figure 3.34: The layout of the CPSG DFB device.

3.3.2 Fabrication Results

The fabrication process of the CPSG device follows the same steps as that of the 4PS device. However, due to improvements in the etching process and the absence of abrupt phase shifts in CPSG, unlike in 4PS devices, the grating etching results are significantly improved. Figure 3.35(a) presents an SEM image of a CPSG sidewall grating structure, featuring a ridge waveguide width of 2.5 µm and a grating recess depth of 0.6 µm on each side of the ridge. Given that the phase changes in CPSG are introduced incrementally, the structural differences between CPSG and a uniform grating are difficult to distinguish under an electron microscope. This subtle phase modulation not only simplifies the etching process compared to other phase modulation schemes but also ensures that the coupling coefficient remains consistent with that of a uniform grating. Additionally, to maintain stable SLM operation, a π phase shift corresponding to the seed grating period Λ was introduced at the centre of the cavity.

Fig. 3.35(b) shows an optical microscopy image of the fabricated DFB laser array (without cleaving), composed of three main sections: a central grating region (800 µm or 400 µm), a cleave section, and a back end designed to suppress reflections. The central grating (uniform or CPSG) provides wavelength selection and modulation. A 40 µm straight waveguide on the output side enables clean cleavage for efficient emission, while a 125 µm curved waveguide at 33° on the back end minimises back reflections for improved stability. Finally, the sample was cleaved and tested.

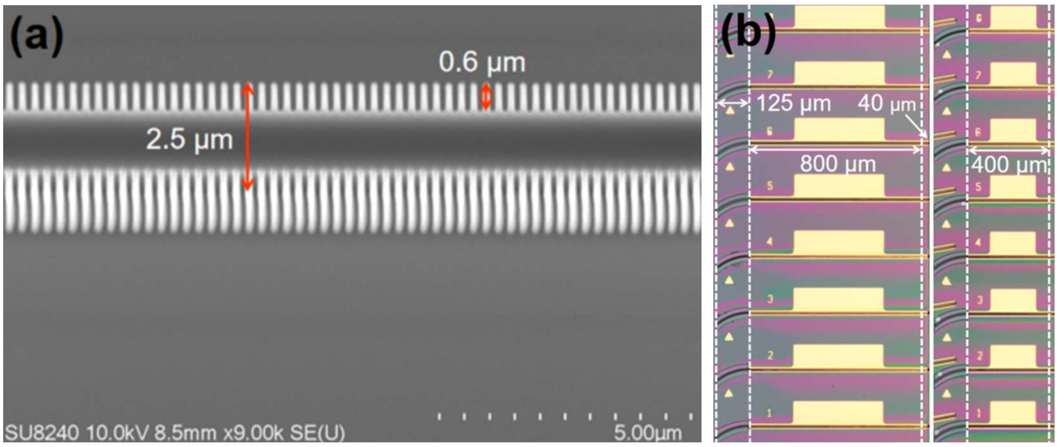

Figure 3.35: (a) SEM picture of CPSG sidewall grating with ridge waveguide width of 2.5 µm and a recess depth of 0.6 µm, (b) Optical microscope image of the fabricated DFB laser array featuring different lengths (800 µm and 400 µm).

3.3.3 Test Results

The measurement setup remains identical to that of the 4PS device. Since the CPSG device does not include an integrated SOA, only a single probe is required to supply current to the DFB section. The cleaved laser bar is securely mounted on a copper heat sink equipped with a Peltier cooler, maintaining a stable operating temperature of 20°C. All measurements are conducted under CW conditions.

3.3.3.1 Output Power Measurement

To compare the power of devices with different cavity lengths, multiple laser arrays with different structures were tested for their power characteristics. The results indicate that devices with the same cavity length exhibit nearly identical P-I characteristics. Therefore, for clarity and efficiency in analysis, the comparison of different cavity lengths, 800 µm and 400 µm, a single CPSG device and a single uniform grating device were selected.

Figure 3.36 shows the P-I characteristics with different cavity lengths for CPSG and uniform grating devices. At the same cavity length, the power curves for the two structures are nearly identical. The threshold currents for the 800 µm and 400 µm devices are approximately 45 mA and 50 mA, respectively. For the 800 µm cavity devices, the maximum output power reaches 14.8 mW at an I_{DFB} of 250 mA. In contrast, for the 400 µm cavity devices, the maximum output power is approximately 4.5 mW at I_{DFB} = 154 mA. The reduced output power in the 400 µm devices can be attributed to several factors like reduced gain, higher threshold current, increased mirror loss, lower differential gain, and greater heat density, all of which affect the overall device performance. Moreover, the CPSG structure demonstrates stable operation over a 400 µm cavity length, underscoring its high grating coupling efficiency κ, which is nearly identical to that of uniform gratings.

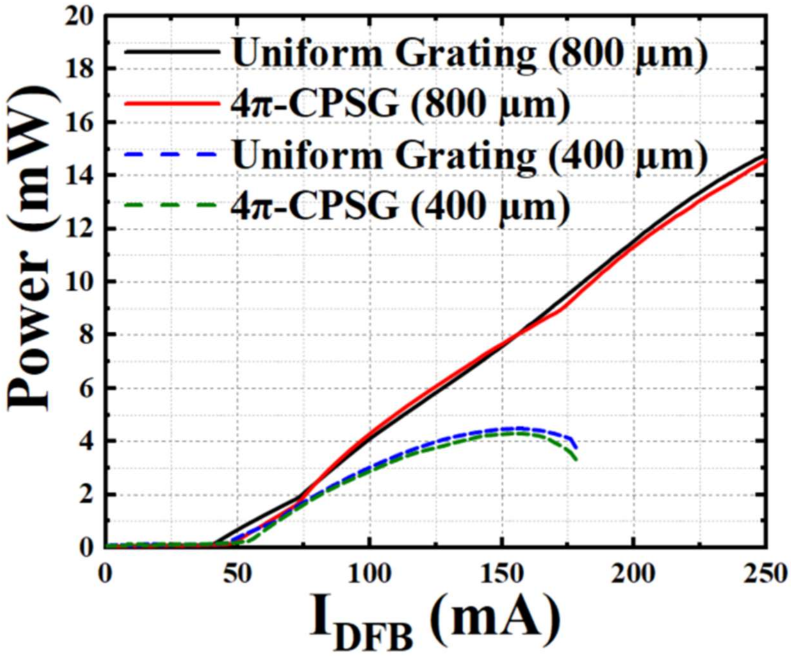

Figure 3.36: Typical P-I_{DFB} curves for different kinds of DFB lasers.

3.3.3.2 Optical Spectrum and SMSR Measurement of Different Arrays

For all array measurements presented in this work, each laser was characterised individually in a sequential manner to prevent thermal crosstalk between adjacent devices. The spectrum was measured using an OSA with a resolution bandwidth of 0.06 nm. With I_{DFB} = 200 mA, the lasing wavelengths are 1564.75 nm, 1565.70 nm, 1566.66 nm, 1567.64 nm, 1568.54 nm, 1569.50 nm, 1570.50 nm and 1571.37 nm from CH1 to CH8. Figure 3.37 (b) shows the SMSR and corresponding linear fit of the lasing wavelengths across the eight channels.

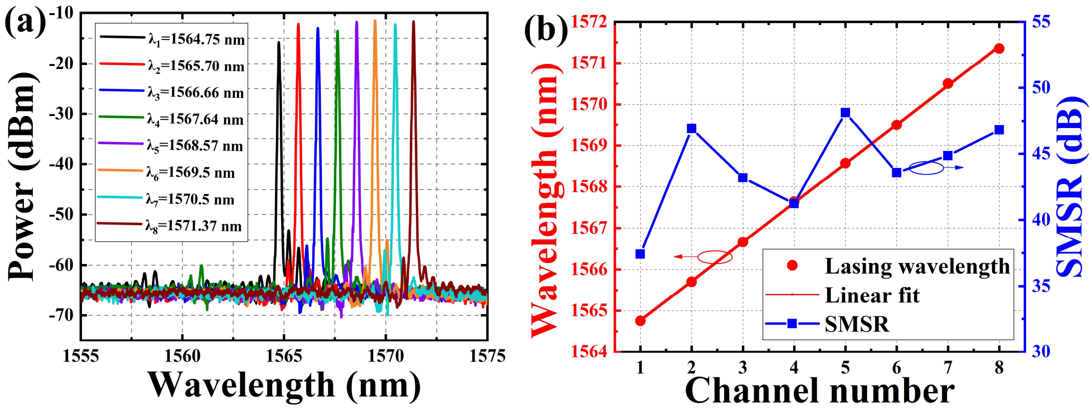

Figure 3.37: (a) Measured optical spectrum of the devices for laser array with a total phase difference of 4π between each consecutive channel and a grating cavity length of 800 μm at I_{DFB} = 200 mA, (b) SMSRs and lasing wavelengths for eight channels, with a linear fit applied to the wavelengths.

The maximum SMSR reaches 48.14 dB, with a fitted line slope of 0.949 nm, closely matching the simulated value of 0.95 nm (as shown in Table 2.2). The excellent agreement between experimental and theoretical results demonstrates the high spectral purity and precise wavelength control of the CPSG design.

Fig. 3.38 shows a 2D optical spectrum versus I_{DFB} (0-270 mA) for CH1 to CH8 with a grating cavity length of 800 μm. The threshold current for all devices is approximately 50 mA. At low current levels, side modes exhibit lower threshold conditions, which dominate the lasing behaviour initially. Notably, the current range of side mode lasing in CPSG may be larger than that of uniform grating (CH1). This may be due to process errors, which are consistent with the characteristics in Figure 2.52. As the current increases, the gain in the main mode surpasses that of the side modes, leading to the main mode lasing.

Very stable SLM operation of the laser array is observed from 100 mA to 270 mA, with no mode-hopping. The average current-induced wavelength redshift coefficient of all devices is around 0.025 nm/mA, indicating a predictable and consistent current-induced wavelength shift across all channels.

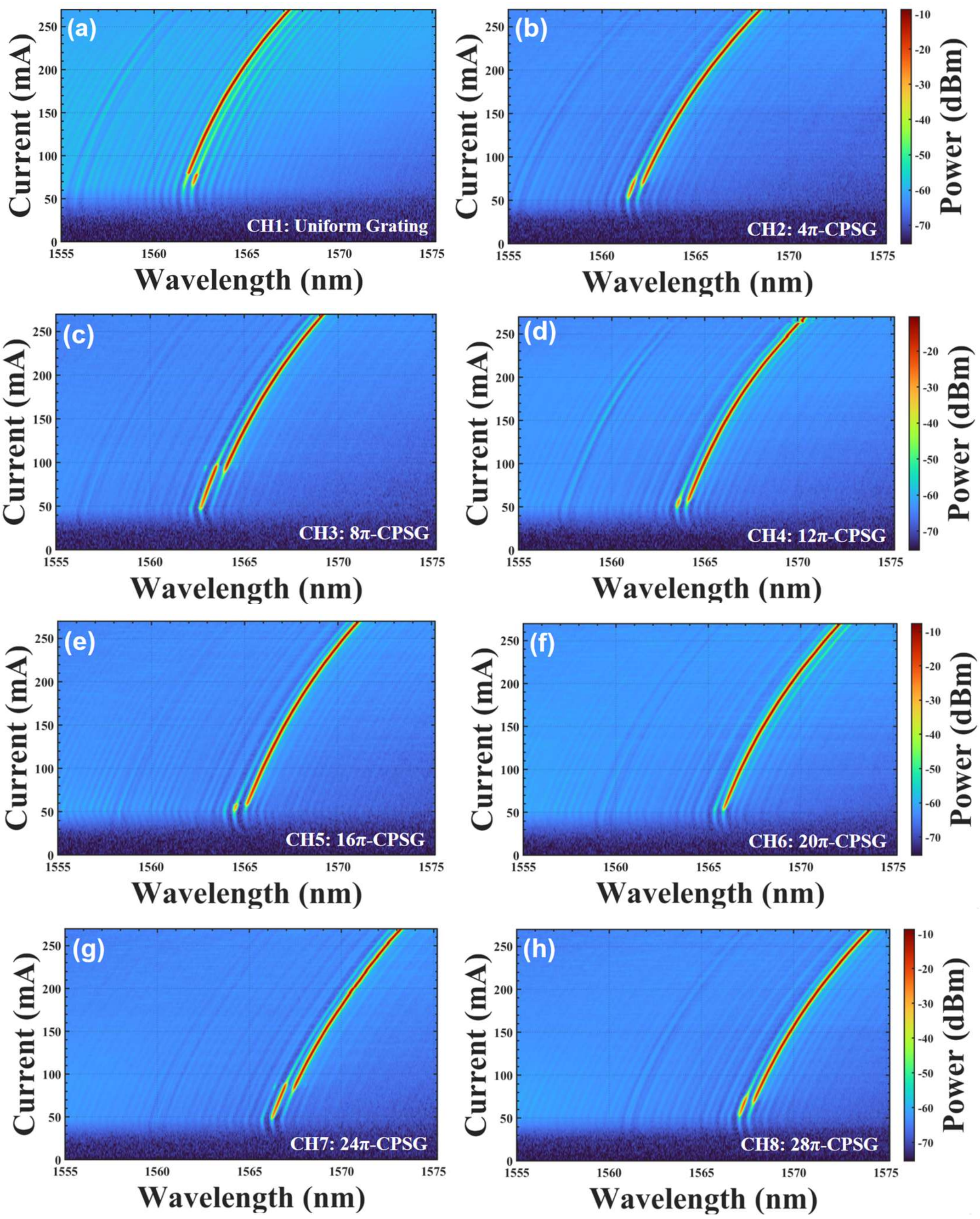

Figure 3.38: 2D optical spectra vs I_{DFB} for (a) uniform grating; (b) 4π, (c) 8π, (d) 12π, (e) 16π, (f) 20π, (g) 24π, and (h) 28π-CPSG, each with a grating length of 800 μm and a 4π phase interval between adjacent lasers.

Fig. 3.39(a) shows the optical spectra for the total phase difference of 2π between each consecutive channel with a grating cavity length of 800 μm. During cleaving, the scribe knife damaged some waveguides, leaving only 4 of 8 lasers functional. With I_{DFB} = 200 mA, the lasing wavelengths are 1566.80 nm, 1567.28 nm, 1567.77 nm and 1568.23 nm from CH5 to CH8 (corresponding to 8π to 14π-CPSG).

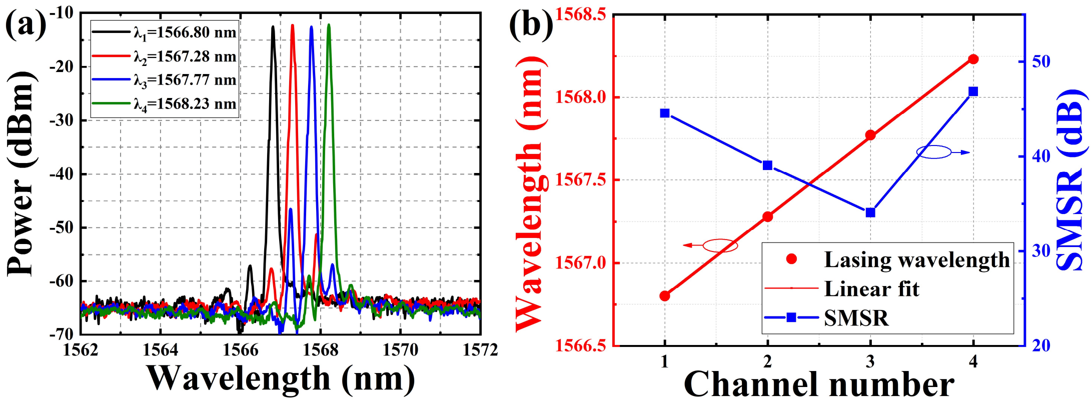

Figure 3.39: (a) Measured optical spectrum of the devices for laser array with a total phase difference of 2π between each consecutive channel and a grating cavity length of 800 µm at I_{DFB} = 200 mA, (b) SMSRs and lasing wavelengths for four channels, with a linear fit applied to the wavelengths.

Figure 3.39(b) presents the SMSR and the corresponding linear fit of the lasing wavelengths for the four channels, with a maximum SMSR of 46.85 dB and a fitted line slope of 0.493 nm. This result confirms the expected wavelength spacing between channels (0.475 nm). The value of this error (0.02 nm) is less than the OSA resolution (0.06 nm), validating the universality of the designed phase shift modulation. Although only half of the array operated as intended, the successful channels demonstrate the feasibility and wavelength tunability of the phase-modulated laser design.

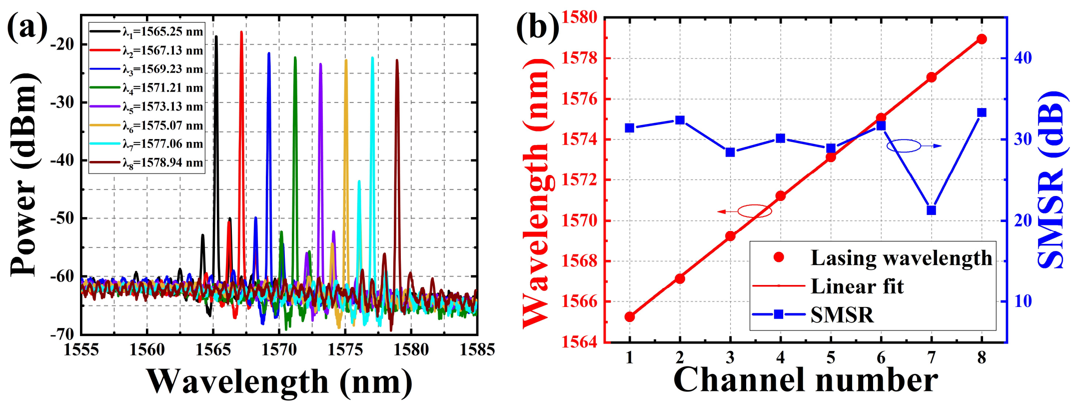

Figure 3.40: (a) Measured optical spectrum of the devices for laser array with a total phase difference of 4π between each consecutive channel and a grating cavity length of 400 µm at I_{DFB} = 140 mA, (b) SMSRs and lasing wavelengths for eight channels, with a linear fit applied to the wavelengths.

To verify the effect of grating length on the wavelength in Equation 2.46, a laser array was fabricated with a grating length of 400 µm. Similarly, the first laser features a uniform grating, while the remaining lasers have a total phase interval of 4π between consecutive channels. Fig. 3.40(a) shows the optical spectra for each channel with I_{DFB} = 140 mA. The lasing wavelengths are 1565.25 nm, 1567.13 nm, 1569.23 nm, 1571.21 nm, 1573.13 nm, 1575.07 nm, 1577.06 nm, and 1578.94 nm from CH1 to CH8.

Figure 3.40(b) shows the SMSR and corresponding linear fit of the lasing wavelengths for the eight channels, with a maximum SMSR of 33.32 dB and a fitted line slope of 1.956 nm, exhibiting a 0.056 nm deviation from the designed wavelength spacing of 1.9 nm. This error value is also below the resolution of the OSA, demonstrating the exceptional wavelength precision achievable with the CPSG structure.

The operation of the short cavity length device demonstrates that the CPSG structure exhibits a κ comparable to that of traditional grating designs. From coupled mode theory, the κ can be calculated from $\Delta\lambda_s$ and λ_B using Equation 3.4. Figures 41(a) to (h) show the measured optical spectrum at I_{DFB}= 50 mA for 400-μm-long DFB lasers with a uniform grating and 4π-to 28π-CPSG. For the uniform grating, the stop bandwidth $\Delta\lambda_s$ is 2 nm and the Bragg wavelength λ_B is 1562.79 nm. For 4π-CPSG, the stop bandwidth $\Delta\lambda_s$ is also 2 nm, and the Bragg wavelength λ_B is approximately 1564.09 nm. Therefore, the κ values of the uniform grating and CPSG devices are calculated as 26.29 cm^{-1} and 26.24 cm^{-1}, respectively. Moreover, according to the Figures, the stop bandwidths $\Delta\lambda_s$ of each CPSG device are very close, indicating that they all have similar κ, and κ should decrease due to the increasing lasing wavelength as the phase shift increases. Nonetheless, this demonstrates that continuous phase modulation has minimal impact on the coupling coefficient, maintaining performance comparable to traditional uniform grating structures. This makes CPSG a highly effective alternative for laser arrays and integrated photonic devices.

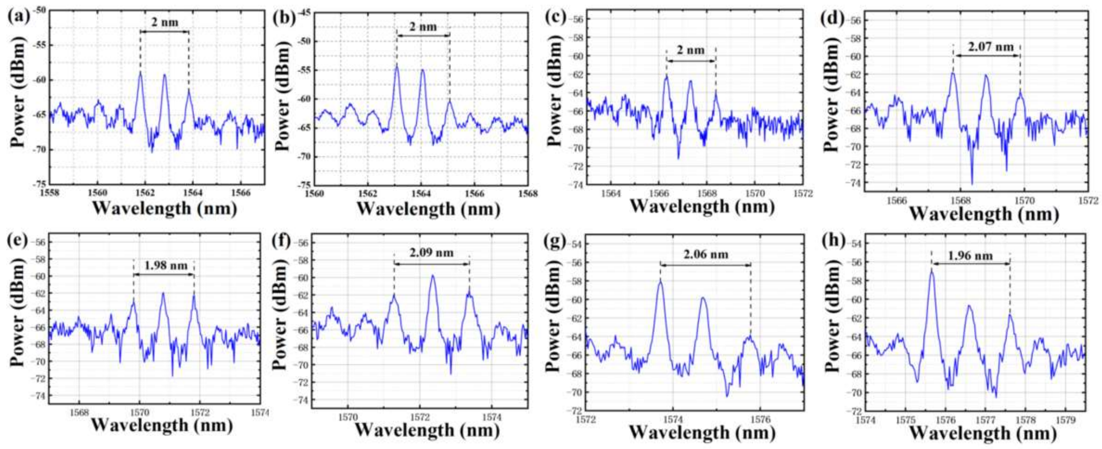

Figure 3.41: Measured optical spectrum near the threshold current for (a) the uniform grating and (b) 4π, (c) 8π, (d) 12π, (e) 16π, (f) 20π, (g) 24π, and (h) 28π CPSG structures, each with a cavity length of 400 µm.

In conclusion, CPSG devices demonstrate significant advantages in terms of stability, robustness, and performance. Despite the introduction of continuous phase modulation, the coupling coefficient of CPSG remains consistent with that of uniform gratings, ensuring efficient optical interaction and light coupling. The phase modulation technique allows for precise wavelength control and reduced sensitivity to fabrication errors, making CPSG devices highly reliable for multi-channel laser arrays. Furthermore, CPSG designs can maintain strong lasing performance even in short-cavity configurations, making them suitable for compact, high-density integrated photonic applications. Overall, the CPSG approach offers a promising solution for advanced optical communication systems and photonic integration, where precision and robustness are paramount.

3.4 Chapter Summary

This chapter presented the design, fabrication, and measurement of novel narrow-linewidth DFB semiconductor lasers and laser arrays. Compared to conventional buried grating waveguides, sidewall grating waveguides were introduced to simplify fabrication and improve scalability. Three advanced grating structures (4PS-SBG, DPS, and CPSG) were developed, and their manufacturing process is described in detail. The experimental setup for laser characterisation was also described, incorporating automated *LabVIEW*-based measurements for enhanced precision.

The 4PS-SBG laser achieved excellent SLM operation and high SMSR, with a four-wavelength DFB laser array demonstrating precise 100 GHz channel spacing, overcoming EBL resolution limitations. The 4PS-SBG structure's effectiveness was confirmed by comparing the stopbands of DFB lasers near the threshold, showing an effective coupling coefficient of 0.83 times that of uniform gratings. With an integrated SOA, the output power reached 33 mW.

The DPS structure was optimised through cavity field intensity modelling. Compared to traditional π-phase-shifted DFB lasers, DPS devices with optimised DPS region lengths and larger phase shifts exhibited stable SLM operation over a broader current range, with lower threshold currents, higher slope efficiency, and better SMSR. The minimum optical linewidth was significantly reduced from 1.3 MHz to 220 kHz, demonstrating the advantages of distributed phase modulation.

By extending the DPS region across the entire cavity, CPSG devices were introduced and experimentally validated. This approach applied continuous phase modulation, with total phase shifts increasing in arithmetic progression. The resulting laser arrays achieved precise channel spacings of 0.493 nm, 0.949 nm, and 1.956 nm. CPSG structures maintained a coupling coefficient comparable to uniform gratings, ensuring stable lasing characteristics while enhancing wavelength stability and reducing fabrication sensitivity. This increased tolerance to manufacturing variations represents a significant advancement, making CPSG a promising solution for precise and stable wavelength control.

Overall, this chapter demonstrated the successful realisation of high-performance DFB diode lasers. These lasers and laser arrays hold strong potential for WDM systems and other applications requiring high spectral stability, narrow linewidth, and precise wavelength control.

Chapter 4

Monolithic Integrated DFB Laser Array Design

A PIC is a device that integrates multiple optical components onto a single chip to enable various photonic functions. Unlike discrete optical components that require complex fibre interconnections, PICs provide a scalable and compact solution for advanced optical systems. In the previous chapter, we demonstrated the integration of 4PS-DFB lasers with SOA, achieving power amplification through a straightforward integration approach. However, as photonic systems evolve, a more sophisticated monolithic integration platform is required, one that should incorporate both active (e.g., lasers, detectors, modulators) and passive (e.g., waveguides, couplers, filters) components on a single substrate [143].

This chapter first explores several common active/passive integration solutions, analysing their respective advantages and limitations. By considering factors such as fabrication feasibility, material compatibility, and performance requirements, a suitable integration strategy is identified. This selected approach is then applied to achieve the integration of the novel laser devices developed in the previous chapter, followed by experimental evaluation and performance verification.

4.1 Active/Passive Integration

Integrating active and passive components on the same chip is crucial because active photonic devices inherently introduce significant optical losses. For example, when integrating a laser with a waveguide coupler that directs light to another device, the waveguide losses within the coupler can be excessively high due to direct band-gap absorption in the active material. This absorption can severely degrade the performance of the photonic circuit, preventing efficient light propagation [144, 145].

To minimise optical losses, an ideal integration strategy would involve using a waveguide material with a higher bandgap than that of the laser. This bandgap engineering reduces absorption losses in the coupler section, leading to lower waveguide losses, ideally below 1 dB/cm, though in some cases, losses up to 10 dB/cm may still be acceptable for practical applications [146]. However, achieving this bandgap contrast while maintaining efficient optical coupling between active and passive components presents a significant challenge. This is because active and passive materials inherently have different structural and electronic properties, making it difficult to integrate them seamlessly on a single substrate without compromising individual device performance.

To address this challenge, several integration techniques have been developed, allowing active and passive structures to be combined shown in Figure 4.1, including Butt-Joint growth, quantum well intermixing (QWI), selective area growth (SAG), and asymmetric twin waveguide (ATG) [147].

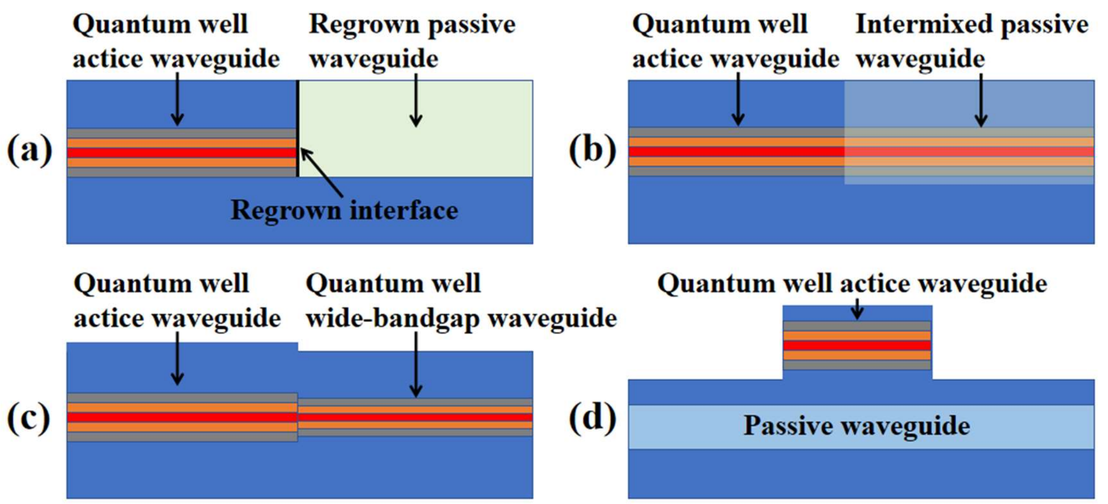

Figure 4.1: Several methods of active/passive integration: (a) Butt-Joint growth, (b) QWI, (c) SAG, and (d) ATG technology.

4.1.1 Butt-Joint Regrowth

The butt-joint regrowth technique enables the integration of different semiconductor materials within a device by growing an initial material, selectively etching a portion, and regrowing another material [148]. This approach allows independent optimisation of material composition, thickness, and doping profiles for each section. Kobayashi et al. successfully demonstrated high-speed electro-absorption modulated lasers (EMLs) using this method [149].

Despite its advantages, butt-joint regrowth imposes strict fabrication requirements, particularly in etching precision and interface quality, as defects or misalignment at the regrowth boundary can introduce optical losses. This challenge becomes more pronounced in multi-section structures requiring different bandgaps. Additionally, the multiple epitaxial growth steps increase fabrication complexity and cost.

4.1.2 Selective Area Growth

SAG is an epitaxial technique that uses a patterned dielectric mask to control material deposition. In masked areas, growth is suppressed, while in unmasked regions, the local concentration of precursors increases, leading to faster growth and changes in material composition. For quantum well structures, this variation in growth rate causes a bandgap shift, as the thickness of the grown layers is altered [150]. Takahashi et al. demonstrated the integration of a DFB laser and an EAM using this method [151].

SAG enables bandgap engineering across different regions, making it useful for multi-wavelength integration. However, it does not allow full customisation of material properties in each region, and the extent of bandgap tuning is limited, which constrains its flexibility in photonic integration.

4.1.3 Quantum Well Intermixing

QWI is a post-growth technique that modifies the bandgap energy of a quantum well without requiring additional epitaxial regrowth. This process allows for selective bandgap tuning across a wafer, making it a valuable method for photonic integration, particularly in reducing fabrication complexity and cost [152]. During the QWI process, high-temperature annealing induces defects in the quantum well, which facilitates the diffusion of atoms into the well, altering its composition. This typically results in a bandgap increase (blue shift), affecting both the refractive index and the emission wavelength [153]. L. Hou et al. demonstrated a CWDM laser array source using this method, QWI was employed to selectively increase the bandgap of passive sections such as S-bends, MMI couplers, and isolation slots, while maintaining the original bandgap of the active DFB, SOA, and EAM sections [154].

QWI enables post-growth bandgap engineering, simplifying fabrication by eliminating the need for epitaxial regrowth. However, it lacks precise control over bandgap modification, as the intermixing process is diffusion-based and challenging to localise with high accuracy, it should take a long time to adjust the recipe to get the best effect.

4.1.4 Asymmetric Twin Waveguide

ATG technique enables the integration of active and passive waveguides by sequentially growing different material layers. The upper layer typically consists of an active gain medium, while the lower layer forms a passive waveguide with a lower refractive index, allowing efficient optical mode coupling through lateral taper structures [155-157]. Gradually narrowing taper waveguides facilitate low-loss optical coupling between the active and passive layers. This design enables monolithic integration of photonic devices while maintaining high coupling efficiency. ATG does not require regrowth steps, making it a cost-effective and scalable approach for photonic integration. ATG technology has been successfully demonstrated in various photonic devices. S. Ye et al. reported a 1.55-μm DFB laser monolithically integrated with a passive waveguide crossing, using the ATG technology [158].

ATG simplifies fabrication and enhances design flexibility, but it also presents challenges. The mode coupling efficiency is highly dependent on the precise etching process, and any deviation can lead to device damage. Additionally, the taper structures must be carefully engineered to minimise transmission loss, which can affect overall device performance.

4.1.5 Approach Selection and Design Strategy

In recent years, the integration of III-V materials on silicon (Si) has emerged as a key research direction for photonic integration, offering a potential pathway toward large-scale, high-performance photonic integrated circuits [159]. This approach combines the superior optoelectronic properties of III-V materials with the scalability and manufacturability of Si-based platforms [160]. However, III-V/Si integration remains a significant challenge due to the lattice mismatch between the two materials, which leads to high defect densities and limits device performance. Despite these challenges, the top-down optical transmission scheme, where light generated in the III-V material needs to be coupled downward into the Si-based waveguide platform, remains a major focus of research [161-163].

The ATG technique follows a similar top-down optical transmission principle, making its signal transmission method like III-V/Si integration. In ATG-based integration, an upper III-V active waveguide emits light that is efficiently coupled into a lower passive waveguide through lateral taper structures. This approach enables monolithic integration without requiring complex regrowth or heterogeneous bonding processes, simplifying fabrication while maintaining high coupling efficiency.

The feasibility of ATG integration has been demonstrated in DFB lasers monolithically integrated with passive waveguide crossings [158]. The success of ATG-based photonic integration not only validates its potential for III-V platforms but also provides valuable insights and a technological foundation for advancing Si/III-V hybrid integration schemes in the future. Therefore, in this project, ATG technology has been used for active/passive integration.

The previous work from our group demonstrated monolithically integrated DFB laser arrays with precise channel spacing [154]; a similar design concept is applied in the present ATG structure. The design concept is illustrated in Figure 4.2. The optical signal is initially generated by the DFB laser in the active region. This light is then efficiently coupled into the passive waveguide through a taper structure. After propagation through the passive waveguide, another taper is used to couple the light back into the active region, where it undergoes amplification and modulation before being output. By leveraging ATG's advantages, this design offers an efficient and scalable solution for multi-functional photonic integration, balancing performance, manufacturability, and cost-effectiveness.

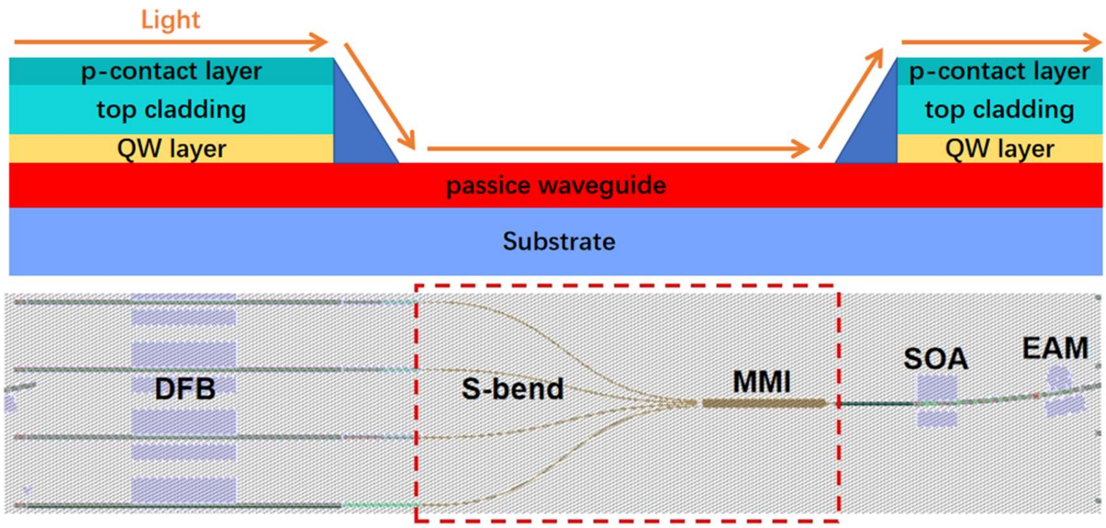

Figure 4.2: Schematic of overall design strategy based on ATG technology.

For a 4-channel DFB laser array, once the light is coupled into the passive region, it first passes through an S-bend waveguide, which aligns and routes the optical signals from multiple DFB lasers into the MMI coupler. The MMI functions as an optical combiner, merging the individual laser outputs into a single optical waveguide. This combined signal is then transmitted via a taper back into the active region, where an SOA and an EAM further amplify and modulate the signal before the final output.

4.2 DWDM PIC Device Design Based on ATG Technology

This section begins with the selection of a suitable wafer, as the epitaxial structure plays a critical role in determining device performance, integration feasibility, and fabrication complexity. Once an appropriate wafer structure is determined, the next step is to design individual photonic components, ensuring good integration within the PIC framework. This includes defining the devices in the active region, which includes the

DFB laser, EAM and SOA, and that in the passive waveguide region, which includes the S-bend waveguides and MMI to combine multiple optical signals with minimal propagation loss.

4.2.1 Materials Selection

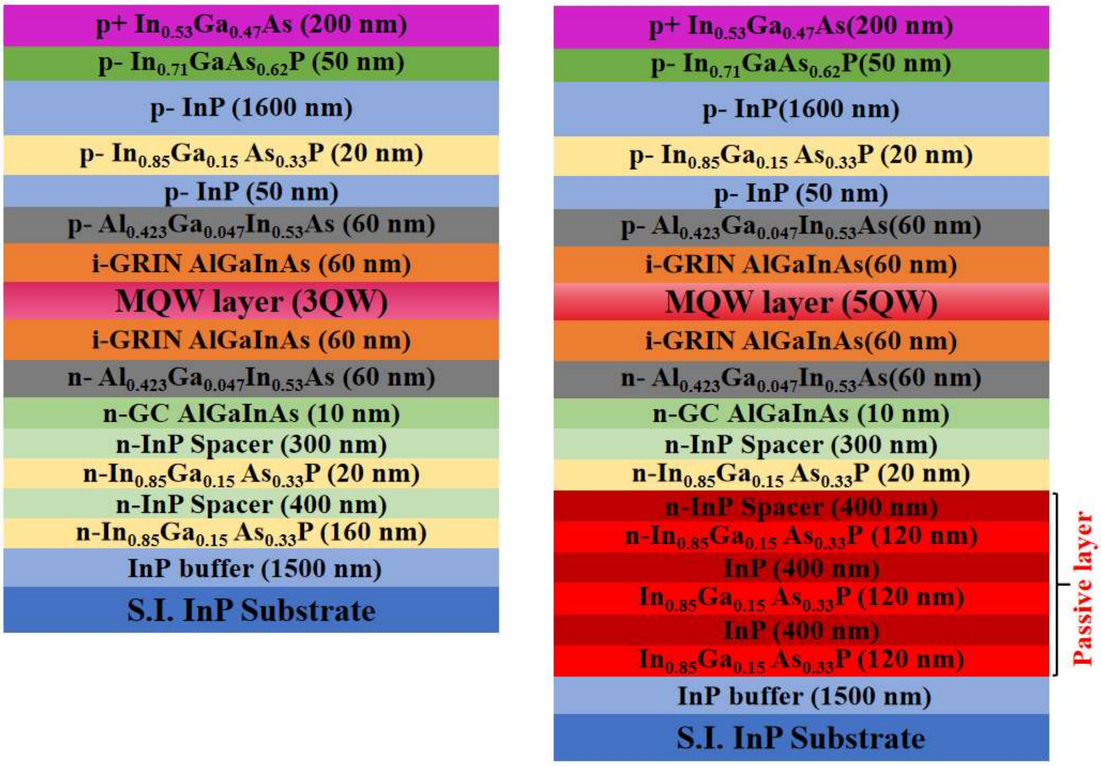

Figure 4.3: The comparison between 3QW wafer structure and ATG wafer structure.

The design of an ATG wafer requires the simultaneous definition of both the active and passive layers during the epitaxial growth process. Consequently, the wafer structure is quite different from the structure introduced earlier. Figure 4.3 illustrates a comparison between the S.I. 3QW wafer and the ATG wafer, highlighting the structural modifications necessary for integrating active and passive waveguides within a monolithic platform. Both wafers are grown on an S.I. InP substrate and employ a 1.55 µm AlGaInAs/InP MQW design. However, to enhance carrier confinement and improve high-speed modulation performance, the ATG wafer adopts a 5QW structure instead of the 3QW.

The most significant structural difference lies in the layers beneath the FRL region. In the 3QW wafer, the region below the FRL consists solely of an InP buffer layer followed by the S.I. InP substrate. In contrast, the ATG wafer incorporates a well-defined passive waveguide layer beneath the FRL region. This passive layer consists of three alternating periods of 0.12-µm-thick InGaAsP and 0.4-µm-thick InP stacks, forming a low-loss optical waveguide. This design significantly reduces absorption loss, measured at approximately 2.8 dB/cm at a wavelength of 1.55 µm [164].

For simplicity, the ATG wafer can be described as a six-layer structure, consisting of the p-contact layer, top cladding layer, 5QW active layer (AlGaInAs MQW), n-contact separation layer, passive waveguide layer (InGaAsP/InP), and the S.I. InP substrate. Similar to the 3QW wafer, the n-contact must be defined on the same side as the p-contact. Due to the integration of both active and passive layers, a three-step etching process is required to accurately define different device regions.

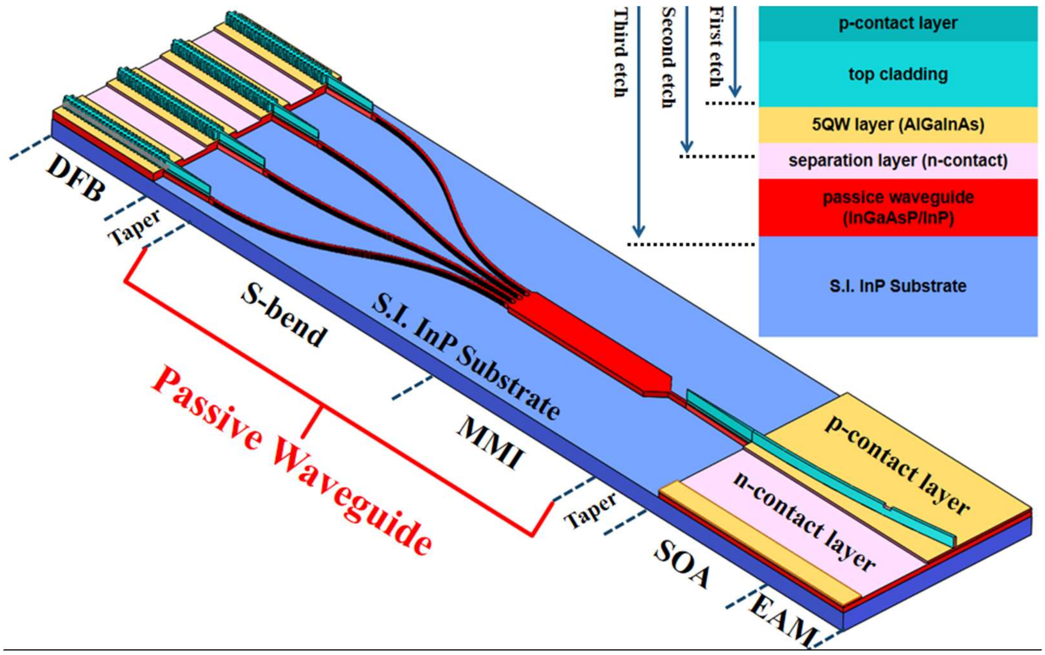

Figure 4.4: 3D view of DWDM source integrated with active/passive devices using the ATG technique and its Simplified wafer structure.

As shown in Figure 4.4, the overall device fabrication begins with the first etching step, which defines the DFB laser, SOA, EAM, and taper structures, ensuring proper electrical and optical confinement within the active layers. The second etching step is then performed to expose the n-contact separation layer, allowing for the formation of electrical contacts. Finally, the third etching step is used to define the passive waveguide region, which includes key optical routing structures such as the S-bend waveguides and the MMI coupler, ensuring efficient optical signal transfer between different functional sections of the device.

By integrating both active and passive waveguides within a single wafer, the ATG structure enables efficient light coupling between different regions, eliminating the need for regrowth while ensuring low-loss, high-speed photonic integration. This makes it particularly well-suited for DWDM applications where compact, high-performance photonic circuits are required.

4.2.2 Taper Design and Simulation

With the overall device design finalised, the next step is to optimise the individual device structures, beginning with the design of the taper coupler, which plays a crucial role in facilitating efficient optical mode transfer between the active and passive waveguides. The inherently asymmetric nature of the ATG wafer structure poses a challenge in achieving high coupling efficiency. In the untapered regions, the dominant optical mode remains largely confined within the upper active waveguide, resulting in poor overlap with the lower passive waveguide section [165-167]. Consequently, an efficient mode transformation mechanism is required to ensure low-loss optical coupling while leveraging the high optical gain provided by the strong ATG structure.

To address this, a waveguide taper coupler has been proposed and successfully demonstrated by P.V. Studenkov et al [155]. The structure consists of an initial untapered section, where the active waveguide maintains a higher effective refractive index than the passive waveguide, preventing direct coupling. As the taper narrows, the width of the active waveguide gradually decreases, leading to a progressive transfer of optical power into the passive waveguide [168].

These tapers function as mode transformers, leveraging the refractive index contrast between the layers to adiabatically guide the optical mode into the desired waveguide with minimal loss. A schematic of the improved taper structure is shown in Figure 4.5.

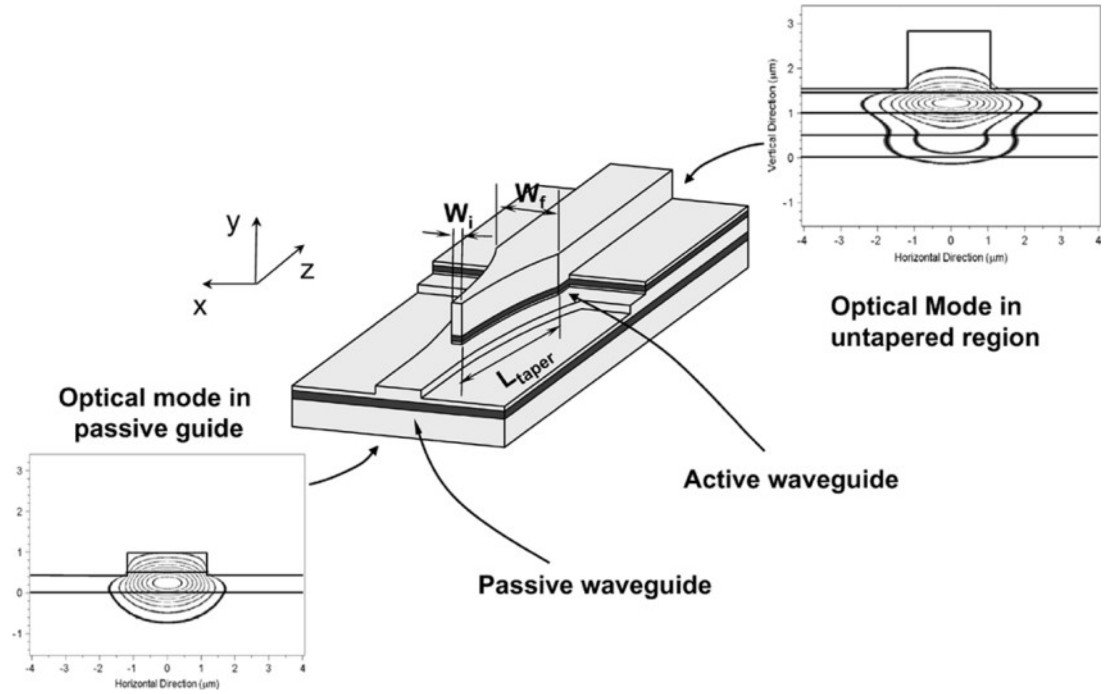

Figure 4.5: Schematic of an ATG laser with taper coupler. Left: optical mode in the passive waveguide. Right: optical mode in the active waveguide. W_i/W_f is the tip/base width of the taper coupler, and L_{taper} is the length of the taper coupler [147].

The schematic structure of an adiabatic taper coupler is shown in Figure 4.5. The term "adiabatic" refers to a design in which optical power remains confined within the fundamental mode, minimising coupling to higher-order modes and ensuring efficient power transfer between the active and passive waveguides [169]. Consider an output optical field in the active waveguide, which is then gradually transferred to the passive waveguide through the taper coupler. To ensure adiabatic coupling, the tip width of the taper W_i should be sufficiently small to prevent disruption of the fundamental mode in the passive waveguide. Conversely, the base width of the taper W_f should be large enough to ensure that the majority of the optical power is efficiently transferred to the active waveguide at the output [147]. The goal of the taper design is to achieve a compact and efficient coupler that minimises scattering losses and prevents mode conversion into higher-order modes during the transition.

One approach to ensuring adiabatic power transfer is to use a long and gradually varying taper profile, where the width variation rate is sufficiently small to suppress scattering into unwanted modes. However, for high-density PICs, maintaining a short taper length is essential for reducing the overall device footprint while preserving high coupling efficiency. To address this trade-off, an exponential taper profile has been proposed, which provides an optimised balance between coupling efficiency and compactness [170].

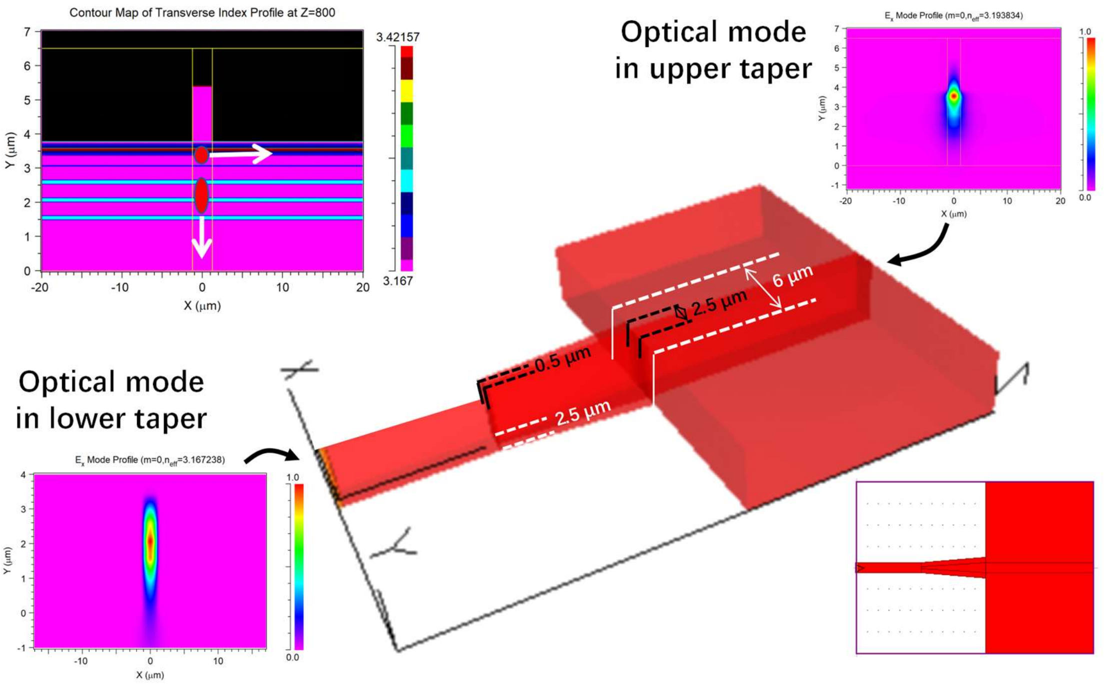

Figure 4.6: 3D layout design of taper coupler in *Rsoft* and simulation results of optical mode in the upper/lower taper.

To ensure efficient mode transfer between the active and passive waveguides, the taper structure was optimised using BPM simulations in *Rsoft*. The taper structure was carefully designed to support stable single-mode propagation, minimising higher-order mode excitation and ensuring low-loss adiabatic coupling. The taper design employed in this work is based on the concept first proposed by S. Ye in our group [158], as shown in Figure 4.6. The taper was designed with an exponential profile over a length of 300 µm to facilitate smooth mode transformation. The upper taper is defined with a width reduction from 2.5 µm to 0.5 µm (W_i = 0.5 µm) to effectively guide the optical mode into the passive layer. Beneath this, the lower taper, also 300 µm in length, features a width transition from 6 µm to 2.5 µm (W_f = 2.5 µm). The simulation results show that the light can gradually shift from the upper taper to the lower taper with minimal loss. To analyse the power transfer characteristics, two path monitors were set up in the simulation: one positioned in the upper taper and another in the lower taper. As shown in Figure 4.7, the power distribution profile indicates a smooth transition, as the light propagates through the taper, a gradual and efficient power transfer occurs, shifting the optical mode into the passive region, and achieving an 89% power transfer efficiency. This high coupling efficiency highlights this taper design to facilitate optical mode conversion, making it a good solution in ATG technology.

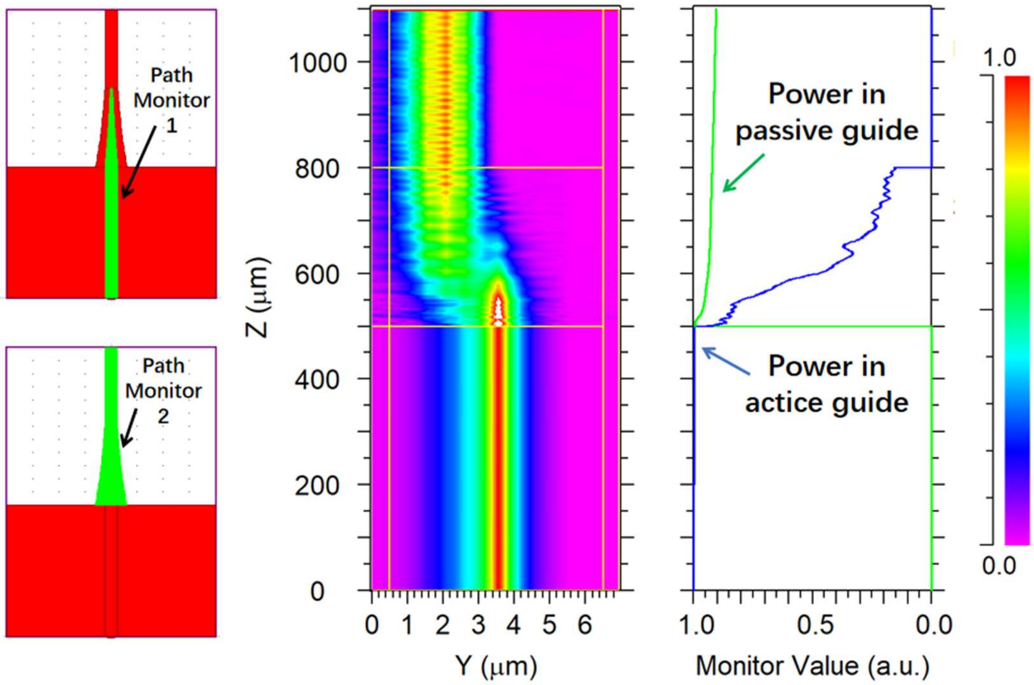

Figure 4.7: Simulation of light propagation from a passive to an active and back to a passive waveguide. Here, Z corresponds to the propagation direction and Y to the height of the waveguide. The monitor values correspond to the optical power in the upper/lower taper section.

4.2.3 MMI Design and Simulation

After the light is coupled into the passive waveguide through the taper structure, a raised cosine S-bend waveguide is designed to smoothly guide the optical signal from the taper output to the MMI input while minimising bending loss[171]. The MMI coupler plays a crucial role in channel splitting and combining, to efficiently distribute optical signals among multiple waveguide ports [172]. By leveraging interference effects within a multimode waveguide section, the MMI ensures uniform power distribution and low-loss signal routing, making it an essential component for highly integrated photonic circuits [173, 174].

MMI couplers operate based on the self-imaging principle in multimode waveguides. This phenomenon allows an input optical field to be reproduced periodically along the propagation direction, forming either single or multiple images depending on the waveguide dimensions and operating conditions [175]. By carefully designing the multimode waveguide geometry, MMI couplers can be tailored to perform various optical functions, including power splitting, combining, and mode conversion.

Depending on the application, MMI couplers can be configured with multiple input and output ports, enabling their use in complex photonic circuits [176]. Figure 4.8 illustrates a 1×N MMI coupler with a length of L and a width of W, which evenly distributes optical power from a single input waveguide into N output waveguides, ensuring efficient optical signal processing in dense photonic integration.

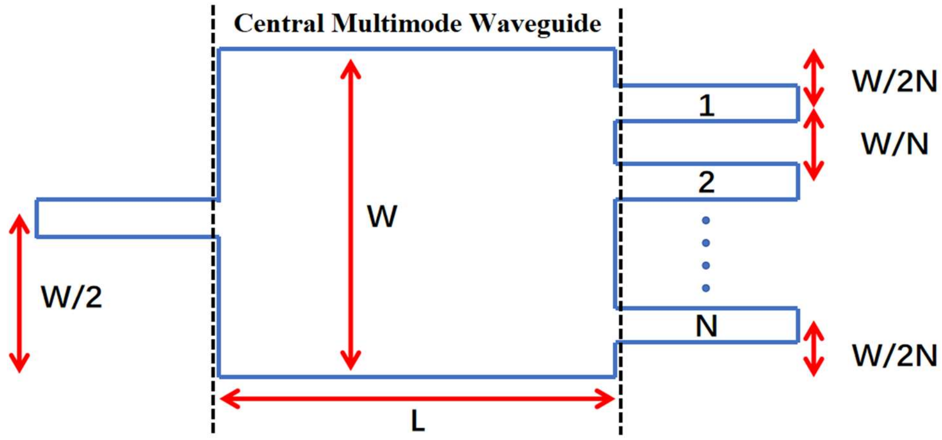

Figure 4.8: 1xN Multi-Mode Interference coupler.

The central multimode waveguide in an MMI coupler is designed to support multiple lateral modes, typically more than three, allowing for effective multimode interference. The self-imaging effect in the MMI section is determined by the ratio of L/W^2, as well as the positions of the input and output waveguides. By carefully adjusting these parameters, different self-imaging configurations can be achieved, enabling precise control over the power distribution. Since self-imaging relies on the interference of multiple guided modes, a key characteristic parameter for MMI design is the coupling length L_c, which represents the beat length between the two lowest-order modes. This length serves as a fundamental design factor in determining the periodicity and efficiency of the self-imaging process [175]:

$$L_c \equiv \frac{4n_{eff}W_{eq}^2}{3\lambda} \tag{4.1}$$

where n_{eff} and W_{eq} represent the effective refractive index and the equivalent width of the multimode waveguide, respectively. The equivalent width W_{eq} accounts for the lateral penetration depth of the optical modes, which becomes significant in low-refractive-index-contrast waveguides [177]. This correction ensures a more accurate representation of the waveguide's optical properties, particularly when designing MMI couplers for optimised self-imaging performance. The value of W_{eq} can be determined using the following expression:

$$W_{eq} = W + (\frac{\lambda}{\pi})(n_{eff}^2 - n_c^2)^{(-1/2)} \tag{4.2}$$

where n_c represents the effective refractive index of the cladding. When the input waveguide is positioned at the centre of the multimode waveguide, as illustrated in Figure 4.7, the self-imaging effect is governed by the linear combination of symmetric modes. This ensures that the reproduced field profiles maintain symmetry relative to the waveguide axis, and the self-images appear at:

$$L = \frac{M}{N} \cdot \frac{3L_c}{a} \tag{4.3}$$

where N represents the number of self-images, and M is an integer that has no common divisors with N. Together, they define the specific distances at which the N self-images appear. The parameter a characterises the MMI coupler, influencing the self-imaging conditions, in the case of a 1xN coupler, a = 4 [175]. To maintain a compact coupler footprint, W should be chosen as small as possible while still supporting the required number of lateral modes for effective multimode interference. This ensures an efficient, space-saving MMI design while preserving high optical coupling efficiency and low insertion loss.

The 1×4 MMI coupler was designed with a width of 30 μm to allow for sufficient waveguide separation at the MMI entrance to prevent coupling between adjacent waveguides. The effective refractive indices used in the design were n_c = 3.166 (cladding) and n_{eff} = 3.168 (effective index in the passive layer). Based on these parameters, through Equations 4.1 to 4.3, the coupler length L was initially calculated to be 461 μm to achieve 1×4 MMI self-imaging.

To verify this theoretical prediction, a BPM simulation by *Rsoft* was conducted. Figure 4.9(a) illustrates the 3D layout of the 1×4 MMI coupler in *Rsoft*, which was modelled with a width of 30 μm and a total length of 1000 μm to ensure adequate propagation distance and mode evolution. For an ideal 1×4 power splitting, the output power at each branch should be 1/4 of the total input power. Fig. 4.9(b) shows the simulated optical intensity distribution in the X–Z plane of the MMI coupler. The colour map represents normalised optical power, with red indicating high intensity and purple indicating low intensity. The simulation results closely matched the theoretical predictions. When the coupler length was set around 460 μm, four self-images were observed, confirming effective multimodal interference. Only a minor optimisation of the coupler length was required to further enhance power uniformity and maximise output efficiency.

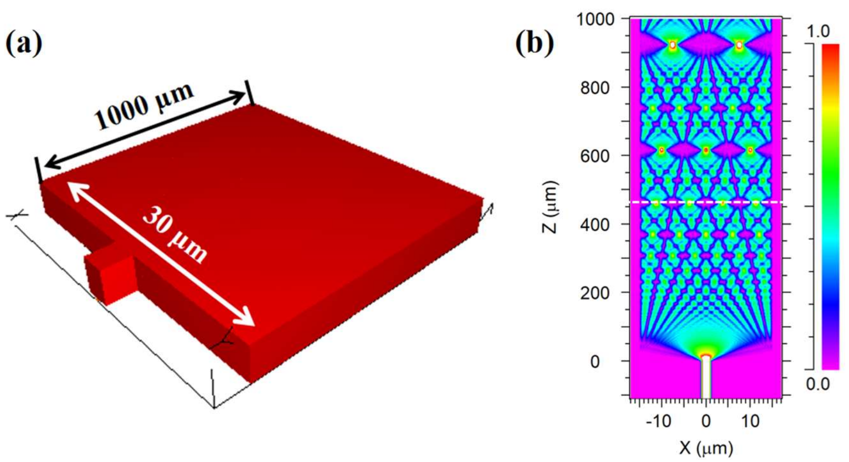

Figure 4.9: (a) 3D layout design of MMI in *Rsoft*. (b) Simulation of light propagation through the MMI with a length of 1000 μm.

Through a two-step verification process combining analytical modelling and numerical simulations, the finalised MMI coupler design is presented in Figure 4.10. As shown in Figure 4.10(a), the MMI structure has a width of 30 μm and a length of 461 μm, ensuring optimal multimode interference and self-imaging performance. To evaluate the power distribution across the four output channels, optical power was monitored along each waveguide path. As illustrated in Figure 4.10(b), the simulation confirms that the output power at each channel is uniformly distributed, with each port receiving approximately 1/4 of the total input power, making it well-suited for the required 4-channel design.

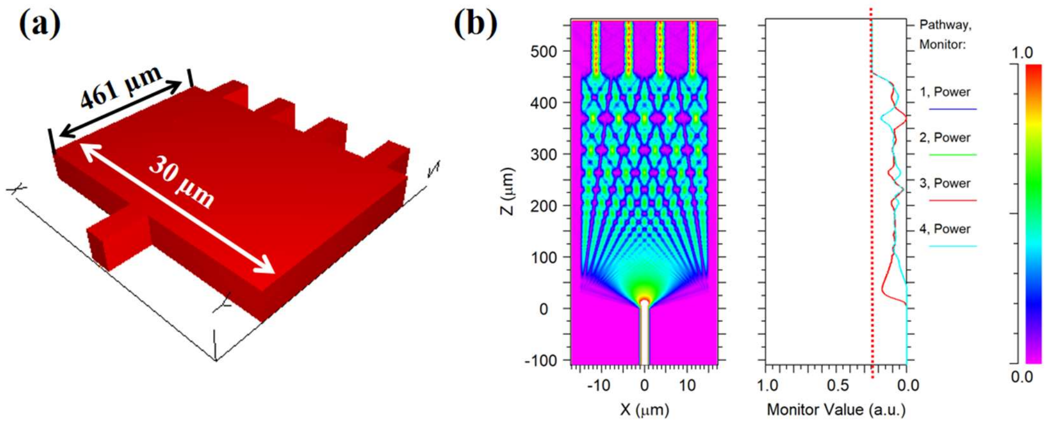

Figure 4.10: (a) 3D layout design of MMI in *Rsoft*. (b) Simulation of light propagation through the MMI with a length of 461 μm.

4.2.4 EAM Design and Simulation

After the light is coupled by the MMI, it needs to be efficiently transferred into another active region for further processing. To achieve this, the light is first coupled from the passive waveguide to the active waveguide through a taper. Once in the active region, the signal undergoes optical amplification in the SOA, which enhances the power level to compensate for any propagation losses from the S-bend and MMI and improve the signal-to-noise ratio. Finally, the amplified optical signal is directed into the EAM, where it is modulated at high speed, enabling precise control over the output optical intensity [178].

EAMs play a crucial role in high-speed optical communication systems, leveraging the quantum-confined Stark effect (QCSE) to modulate the intensity of light by applying an external electric field [179-181]. Compared with conventional external modulators, EAMs offer several advantages, including compact size, low power consumption, high-speed operation, and ease of integration into PICs. These benefits make EAMs particularly suitable for DWDM systems and other high-speed optical interconnects. To evaluate the modulation characteristics, X. Sun and I reported a simulation method to analyse the absorption spectrum of the AlGaInAs EAM under different bias voltages [182]. The results indicate a significant shift in the absorption edge with increasing reverse bias, confirming strong QCSE-induced modulation in AlGaInAs materials. For a 100-μm-long EAM, an eight-channel EML array was simulated to analyse its modulation characteristics under varying reverse bias voltages. As shown in Figure 4.11, the extinction ratio increases with an increasing reverse bias, reaching a maximum of approximately 23 dB at −3.2 V. As the voltage increases beyond −3.2 V, the extinction ratio gradually declines. This phenomenon occurs because the QCSE-induced redshift moves the absorption edge further away from the operating wavelength of the laser, thereby weakening the modulation effect. Additionally, the extinction ratio exhibits wavelength-dependent variations across the eight channels. Channels operating at longer wavelengths experience a weaker extinction effect because the QCSE-induced bandgap shift is less effective at higher wavelengths [183].

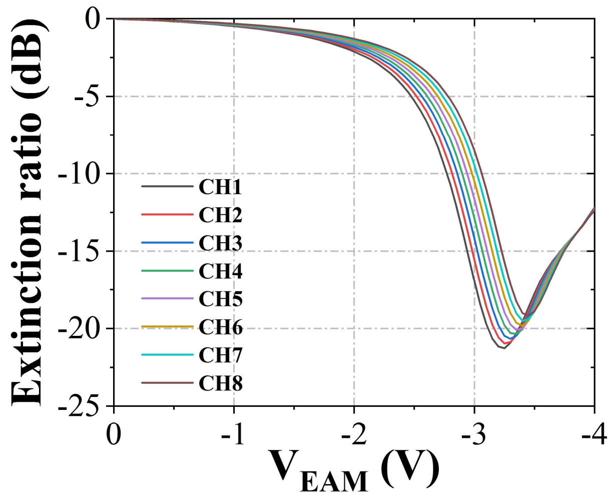

Figure 4.11: Simulated extinction ratio of the eight-channel AlGaInAs EML as a function of reverse bias voltage [182].

To validate this theory, we fabricated and characterised an eight-channel 4PS EML device [184]. As shown in Figure 4.12 (a), the device consists of an 800-µm-long sidewall grating DFB laser monolithically integrated with a 100-µm-long EAM. The structure was fabricated using a ridge waveguide with a width of 2.5 µm, ensuring effective optical confinement. Figure 4.12(b) shows the measured extinction ratios of eight integrated EMLs. The extinction ratio was calculated as the ratio (in dB) between the optical power at each bias point and the power measured at zero bias (V = 0 V). Measurements were conducted sequentially for each channel under identical conditions using a calibrated power meter, a high extinction ratio of 20 dB at −3.6 V bias, validating the efficiency of the AlGaInAs EAM. The device exhibited exceptionally high-speed performance, achieving modulation bandwidths of up to 25 GHz, which confirms its suitability for DWDM PICs.

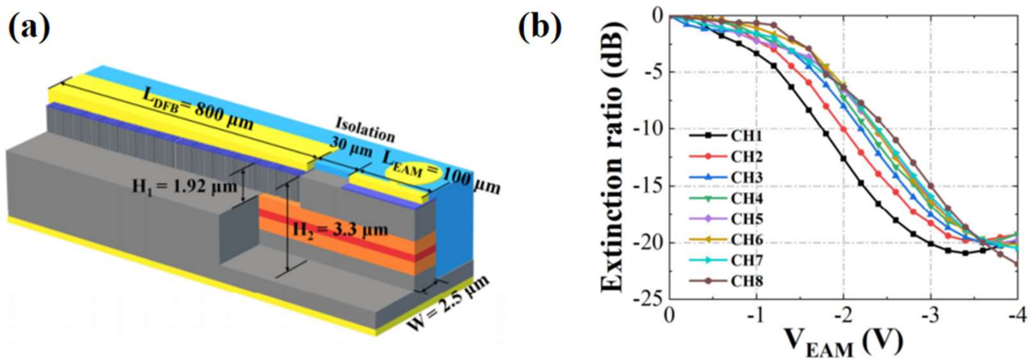

Figure 4.12: (a) Schematic structure of the 4PS-SBG EML. (b) Measured extinction ratios of the eight EMLs [184].

Since the active region structure of the ATG wafer is identical to the one reported by X. Sun et al., both utilising a 5QW wafer, the modulation characteristics observed in the reported study can be directly applied to our integration approach. Given this structural consistency, we adopt a 150-µm-long EAM in the ATG-integrated design to achieve a better balance between extinction ratio, insertion loss, and fabrication tolerances.

4.2.5 Overall Device Design

After finalising the Taper, MMI, and EAM structures, the complete design of the DWDM source using the ATG integration technique is established. The structure of the

ATG-based device is shown in Figure 4.13. To accommodate the electrical contacts while maintaining compact integration, the separation between adjacent DFB lasers was set at 250 μm, ensuring sufficient space for both p- and n-contact metallisation. The active and passive sections are interconnected by a 300-μm-long exponential taper, enabling low-loss mode conversion.

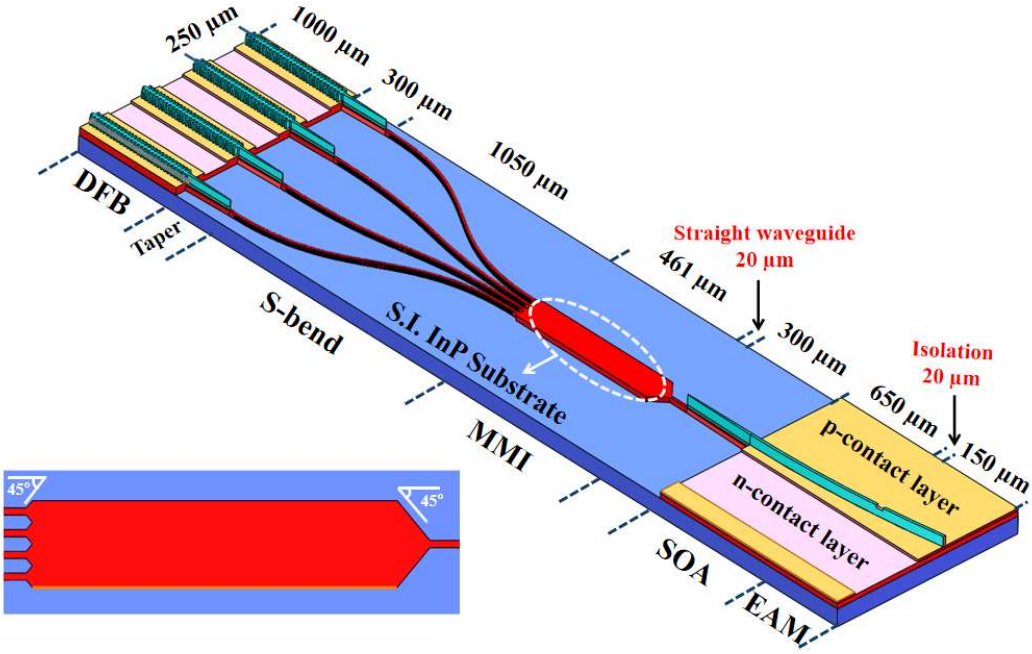

Figure 4.13: The overall design of the DWDM source using the ATG technique.

The passive section comprises the S-bends and the MMI coupler. The S-bends were designed with a raised cosine profile and a total length of 1050 μm, carefully avoiding discontinuities in the radius of curvature to minimise mode mismatch losses [185]. The MMI coupler was 30 μm in width and 461 μm in length. To suppress reflections at the input and output waveguides, a 45° tilt was introduced at each corner, reducing back reflections at the input by at least 10 dB [186]. Additionally, a 20 μm-long straight waveguide was incorporated at the MMI output to facilitate smooth optical coupling into the subsequent output taper, ensuring a stable and efficient transition between the passive and active regions.

After the optical signal is decoupled from the passive region back to the active region. A 650-μm-long curved SOA is designed to amplify the signal, which was designed as a curved waveguide terminating at an angle of 10° relative to the normal direction of the facet. The final modulation stage consists of a 150 μm-long EAM, ensuring efficient signal modulation while balancing extinction ratio and insertion loss, and it has a 20 μm length isolation between the SOA to prevent crosstalk.

Each of the four-channel DFB lasers was designed using 4PS-SBG technology, with a cavity length of 1000 μm. The grating period Λ was set at 257 nm, ensuring a zero-order wavelength at 1640 nm. This wavelength was deliberately detuned from the quantum well gain peak (~1.55 μm) to mitigate mode competition. The sampled grating periods were selected from 4.418 μm to 4.545 μm, resulting in lasing wavelengths from 1550 nm to 1552.4 nm, yielding a wavelength spacing of 0.8 nm between adjacent channels. The grating was fabricated with a 50% duty cycle, formed by etching 0.6-μm-deep recesses into the sidewalls of the 2.5 μm ridge waveguide.

4.3 Fabrication Process

The fabrication process for the ATG device follows a similar approach to that used for 3QW devices, with the key difference being the necessity of the third etching step to define structures in the passive region. As shown in Figure 4.14, the ATG device was fabricated using a three-step etching process to precisely form the required structures.

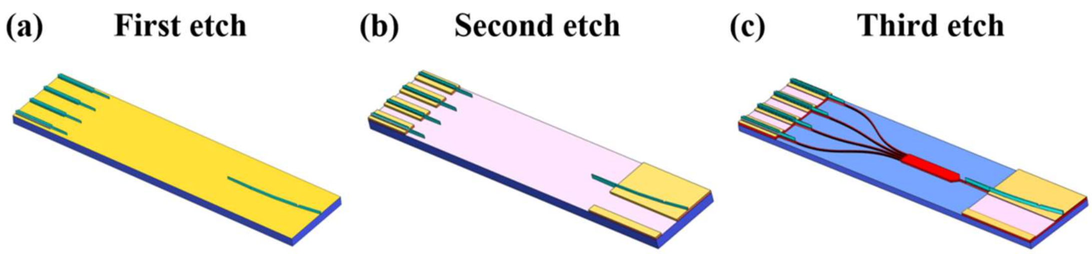

Figure 4.14: 3-step etch processes: (a) Form the grating of the DFB laser section, upper taper structure, SOA and EAM. (b). Etched down to the n-contact separation layer. (c) From the lower taper structure, MMI and S-bend in the passive waveguide.

In the first etching step, the p-contact and top cladding layers were selectively etched to define the grating, the upper taper structure, as well as the EAM and SOA sections. Following this, in the second etching step, the grating region, EAM and SOA were protected, and the etching area was extended to the n-contact separation layer. Finally, in the third etching step, after protecting the active device region, the passive structures, including the S-bend, MMI, and lower taper, were defined by etching through the separation layer and passive layer. The etching process reached a depth of 1.5 μm into the InP buffer layer, forming passive waveguides with a total height of approximately 3.5 μm, ensuring efficient optical confinement and low-loss light propagation.

Therefore, the fabrication process flow of this device can be divided into 10 key steps:

- Sample cleaning.
- Marker definition.
- Isolation definition.
- Active devices definition (first etch).
- N-contact region definition (second etch).
- Passive devices definition (third etch).
- Contact Window Opening.
- P-contact and N-contact metal deposition.
- InP substrate thinning.
- RTA process and device bar cleaving.

4.4 Dry Etching Process and Fabrication Results

Since the other fabrication steps are identical to those used in previous device manufacturing processes, they will not be discussed in detail here. Instead, the focus is on the three-step dry etching process and results, which is the most critical and technically demanding aspect of ATG device fabrication. This process requires high precision, process stability, and advanced etching control to ensure accurate waveguide definition and efficient active-passive integration, both of which are essential for achieving optimal device performance.

4.4.1 First Etching Step

Figure 4.15(a) presents an SEM image of the fabricated device after completing the three-step dry etching process, showing the successfully defined active and passive devices. Among that, the first etching step is crucial for accurately defining the grating structure, upper taper, SOA, and EAM. This process must be performed with high precision to ensure the performance of the active devices, especially the correct period and depth of the gratings. Fig. 4.15(b) shows SEM images of the fabricated 4PS-SBG grating on a 2.5 μm wide ridge waveguide, with a 0.6 μm recess depth on each side through the first etching step. Each sampling period consists of four sections with a π/2 phase shift between them.

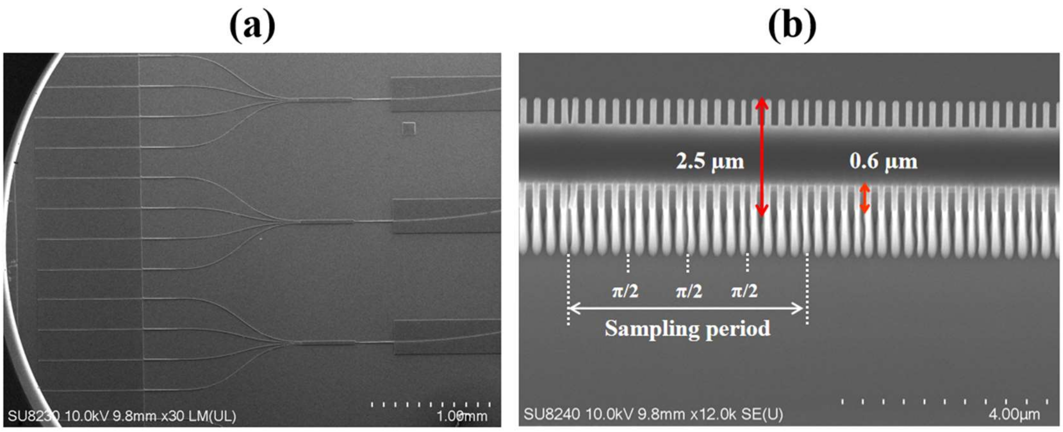

Figure 4.15: SEM images of (a) the overall view after the three-step etching process; (b) sidewall gratings of the 4PS-SBG structure after the first etching step.

4.4.2 Second/Third Etch Step and Its Problems

The second etching step involves the selective removal of material down to the n-contact separation layer. Precise etch depth and uniformity need to be maintained at this stage to achieve low contact resistance and efficient current injection. The third etching step presents the greatest challenge, as it requires precisely defining the passive waveguide region by etching 3.5 μm deep while ensuring that previously fabricated structures remain intact. This process demands a mask with sufficient etch resistance to provide adequate protection throughout the extended etching duration. Additionally, the selection of the etch recipe is critical, as it must achieve high etch selectivity between different material layers while simultaneously ensuring smooth sidewalls and precise feature definition.

Any deviation in etching conditions may result in rough waveguide sidewalls or even device damage, which can severely degrade optical coupling efficiency and overall device performance. Figure 4.16(a) presents an example of a failed three-step etching process, highlighting the impact of insufficient protection during etching. The image distinctly shows the grating and upper taper structures formed during the first etching step, the n-contact region defined in the second etching step, and the passive waveguide and lower taper structures created during the third etching step.

To facilitate analysis, we define Etch Region 1 (left of the dotted line) and Etch Region 2 (right of the dotted line). A clear discrepancy is observed between the two regions: the sidewall height of the active area in the protected area of Etch Region 1 is significantly lower than that in Etch Region 2, indicating etch-induced damage in the first region. Figure 4.16(b) provides a magnified SEM view of the grating section in Etch Region 1. Compared to the successfully fabricated grating in Figure 4.15(b), the grating height is visibly reduced, suggesting that the protective layer on the grating was insufficient to withstand the subsequent etching steps. As a result, the grating structure was partially etched away, leading to significant structural damage.

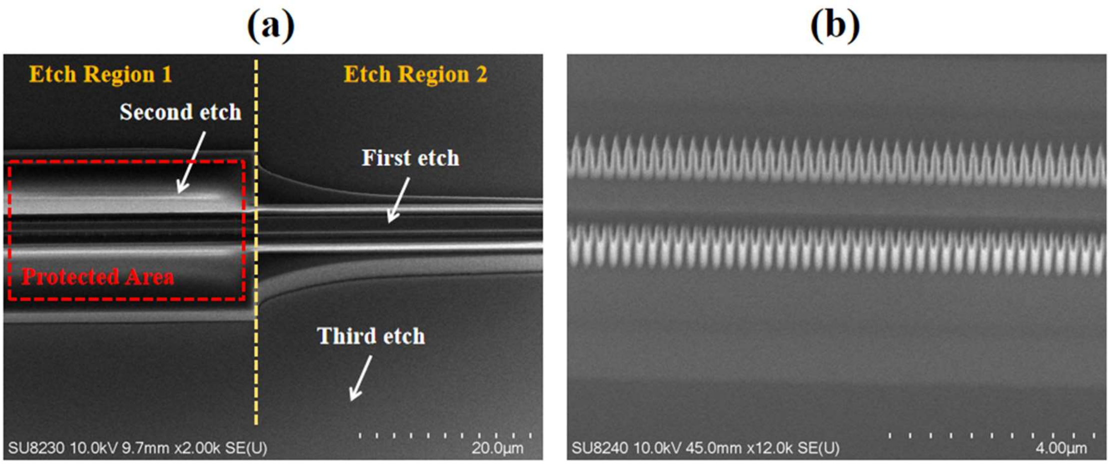

Figure 4.16: SEM images of (a) a failed three-step etching process. (b) the grating erosion results in Etch Region 1.

Therefore, this process must be carefully optimised and controlled to minimise structural defects. To address the etch-induced damage observed in the failed fabrication attempt, two possible solutions were explored: (1) increasing the etching resistance of the protective mask and (2) optimising the etching process to enhance etch selectivity.

For the first approach, we aimed to improve the coverage and thickness of the protective mask. As shown in Figure 4.17(a), in the initial etching attempt, only HSQ resist was applied to the protected area shown in Figure 4.16(a) to act as a protective mask. However, the HSQ layer above the ridge waveguide was significantly thinner than expected. This issue arose because the ridge waveguide width was too narrow, preventing HSQ from forming a uniform and adequately thick layer on top of the structure. As a result, the insufficient HSQ thickness led to partial erosion of the ridge waveguide during the third etching, causing structure destruction. To resolve this, we implemented an improved mask strategy, as illustrated in Figure 4.17(b). In this approach, we extended the HSQ coverage to the entire Etch Region 1 to ensure a more uniform protective layer. Additionally, two layers of PMMA were deposited on top of the HSQ, further enhancing the etching resistance.

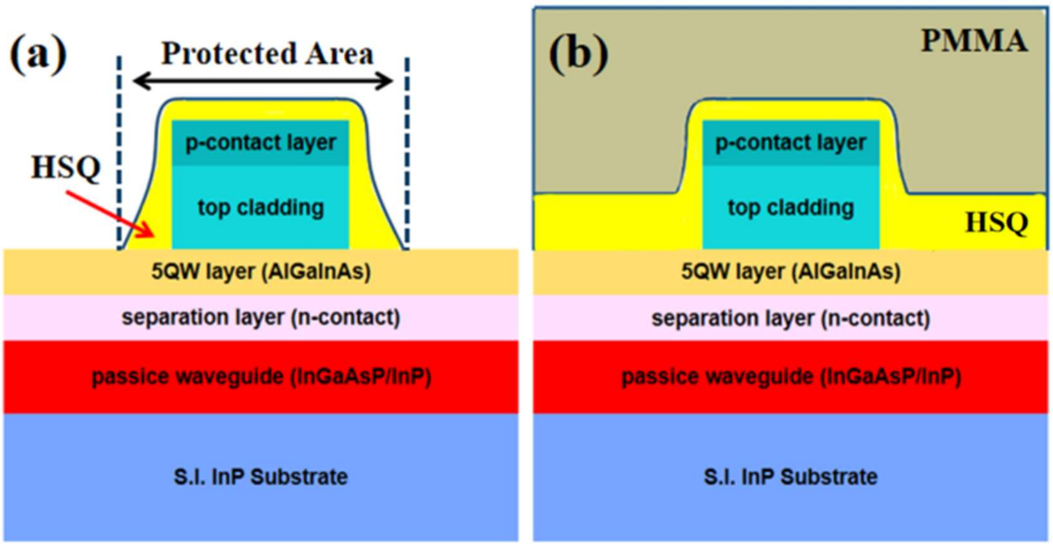

Figure 4.17: (a) Initial protection method using HSQ only over the ridge waveguide in Etch Region 1. (b) Enhanced protection method covering the entire Etch Region 1 with HSQ, supplemented by two additional PMMA layers.

Simultaneously, we refined the etching process. For both the first and second etching steps, we also followed a standard $Cl/CH_4/H_2/Ar$ (16/10/12/5 sccm) recipe that had been previously optimised for accurate pattern transfer. For the third etch, the gas composition was adjusted to $Cl/CH_4/H_2/Ar$ = 12/10/15/0 sccm to enhance etch selectivity between the target material and the mask. By carefully adjusting the gas composition, etching power, and pressure, for more efficient etching while maintaining effective pattern transfer [187, 188].

4.4.3 Final Etch Results

Figure 4.17 shows SEM images of the fabricated grating and taper section by the improved 3-step dry etch processes. For clarity and comparison, in Figure 4.18(a), the SEM image after the optimised process is still divided into Etch Region 1 and Etch Region 2. The image clearly shows that Etch Region 1 now exhibits a smooth surface with a well-defined etching height difference relative to the passive layer, indicating that the active device area was effectively protected during processing. Minor shape variations are observed near the dotted line, likely due to incomplete development of the multi-layer resist. However, these variations do not significantly affect device performance, as they are outside the critical optical path. Figure 4.18(b) shows a well-defined oblique SEM view of the connection between the DFB section and the taper section after completing the three-step etching process. The image demonstrates a clean and precisely etched transition, ensuring smooth light coupling and verifying the effectiveness of the optimised fabrication process.

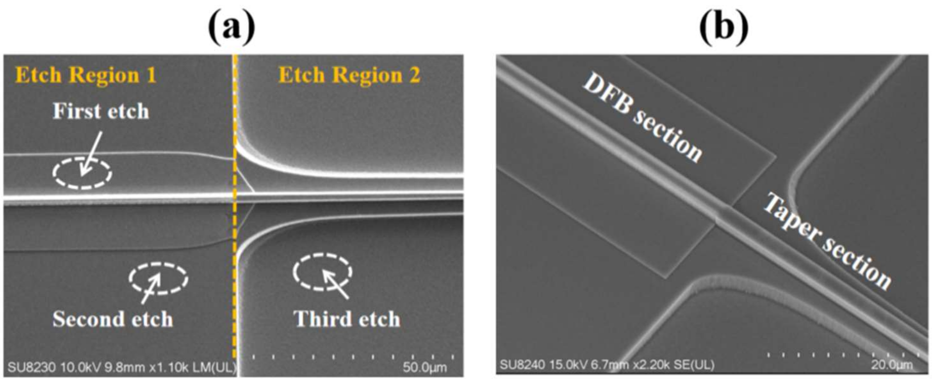

Figure 4.18: SEM images of (a) an improved three-step etching process. (b) Oblique view of the connection between the DFB section and taper section after three-step etching.

The overall taper structure is also fabricated using a three-step etching process. The upper taper is first defined during the first etching step and maintains its shape through the second etching step, as shown in Figure 4.19(a). The lower taper structure is then formed during the third etching step, ensuring that the previously fabricated upper taper remains intact and undisturbed.

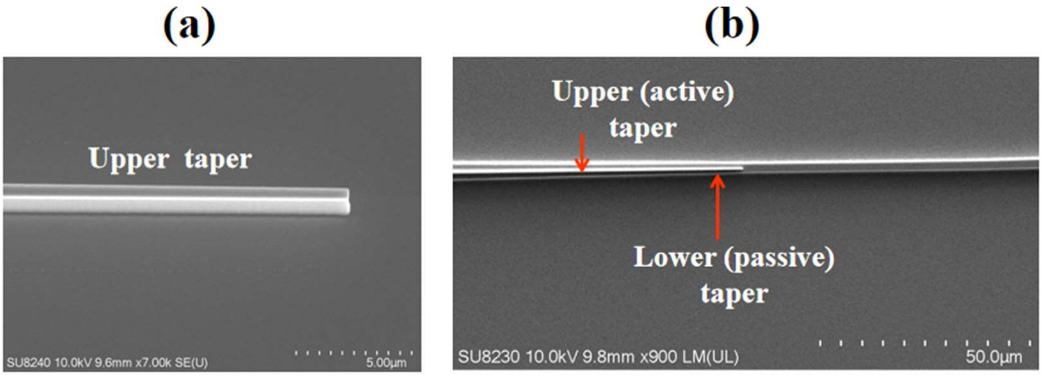

Figure 4.19: SEM images of (a) the upper taper structure formed in the first etching step and the second etching step. (b) Final taper structure, showing both the upper (active) taper and lower (passive) taper.

As illustrated in Figure 4.19(b), the final taper structure after the three-step etching process is well-defined. The upper taper is 300 µm long, with its width gradually tapering from 2.5 µm to 0.5 µm within the active layer. Directly beneath it, the lower taper, also 300 µm long, is defined in the passive waveguide, tapering from 6 µm to 2.5 µm. This structure ensures efficient optical mode transfer between the active and passive regions, minimising coupling loss and mode mismatch.

The raised cosine S-bends and the MMI coupler were defined in the passive layer in the third etching process. The MMI coupler measured 30 µm in width and 461 µm in length. To suppress reflections at the input and output waveguides, a 45° tilt was introduced at each corner shown in Fig. 4.20(a) and (b). The MMI output is connected to a taper structure identical to that at the DFB laser output, designed to transfer light from the passive layer to the SOA and EAM in the active layer.

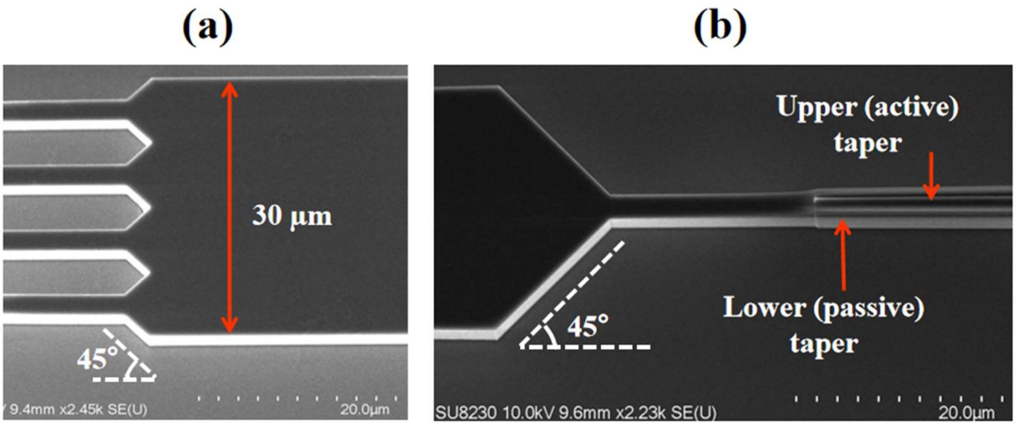

Figure 4.20: SEM images of (a) the input section of the 4×1 MMI coupler; (b) the output section of the 4×1 MMI coupler and the coupling taper from the underlying passive waveguide to the SOA.

4.4.4 Fabricated ATG Device

Figure 4.21(a) shows the device under a microscope after the 3-step etching, with residual photoresist still present on the surface, indicating that the designed resist layers effectively protect the active device during the etching process. After photoresist removal, a clean and well-defined surface is observed, as shown in Figure 4.21(b), taken under a 5× objective.

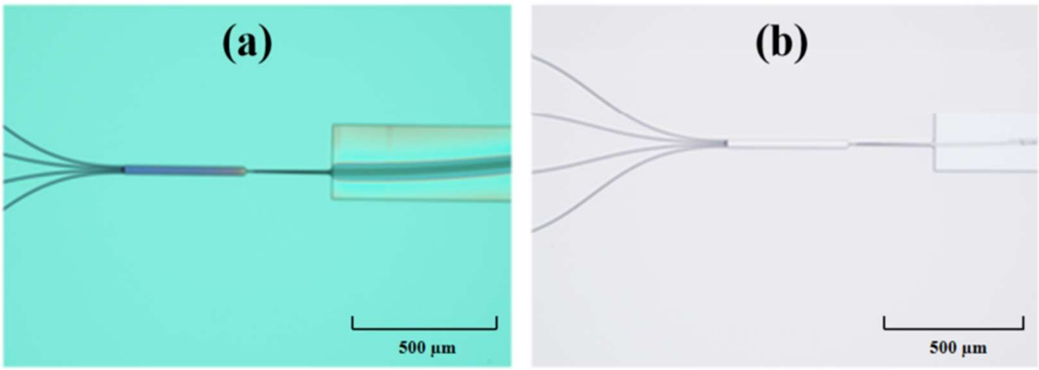

Figure 4.21: Optical micrograph of (a) the sample surface still has photoresists after three-step etching. (b) The sample surface after removing the photoresist.

In the following process, a 700-µm-thick insulation layer (200 nm PECVD SiO_2, 400 nm HSQ, 100 nm PECVD SiO_2) is deposited over the entire sample for electrical isolation and surface protection. The p- and n-contacts are then formed by opening contact windows in the SiO_2 layer and subsequently depositing and patterning metal electrodes.

To enhance thermal management and device performance, the substrate is thinned to 180 μm, improving heat dissipation. Finally, an RTA process is carried out to optimize the metal contacts and activate dopants, thereby completing the fabrication of the ATG device.

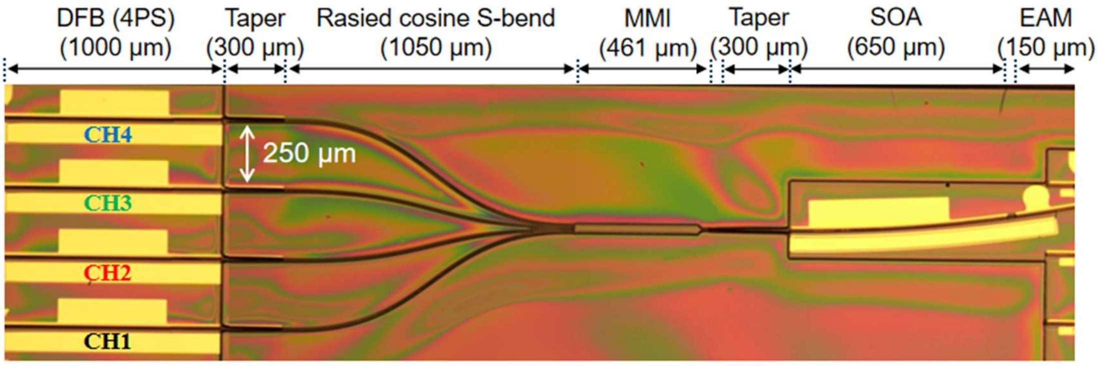

Figure 4.22: The optical micrograph of the overall ATG device.

Figure 4.22 presents an optical micrograph of the fabricated ATG device, which closely follows the intended design. It consists of four DFB lasers, with the separation between adjacent lasers set at 250 μm. Each laser is coupled through a taper to an S-bend waveguide, which connects to a 4×1 MMI coupler. Another taper is used after the MMI to efficiently transfer light to the active region, where an SOA and an EAM are integrated along the output side. The 650 μm-long SOA was connected to a 150 μm-long EAM section, both designed as curved waveguides terminating at a 10° angle to the facet normal. A 30 μm-long isolation section separates the SOA and EAM, preventing electrical crosstalk and ensuring independent functionality. The next step is to conduct optical performance tests to validate the device's operation and efficiency.

4.5 Device Performance

4.5.1 Measurement Platform Set-up

Figure 4.23 illustrates the experimental setup for measuring the ATG-integrated device. The fabricated devices were mounted on a copper sheet and placed on a TEC set at 20°C for temperature stabilisation. Unlike non-integrated devices, ATG-integrated devices require independent electrical probes for each active device. Specifically, the

DFB laser and SOA each require two probes for current injection, while the EAM requires two probes for voltage application, making a total of at least six probes necessary for complete device characterisation. A current driver supplies the injection currents, and a power source applies the required bias voltages.

The output light is collected using a lensed fibre and directed to either an optical power meter or an OSA. The power meter measures output optical power, while the OSA analyses the spectral characteristics of the emitted light. To improve measurement efficiency, the setup is automated using *LabVIEW* via a GPIB interface. All measurements are conducted under CW conditions.

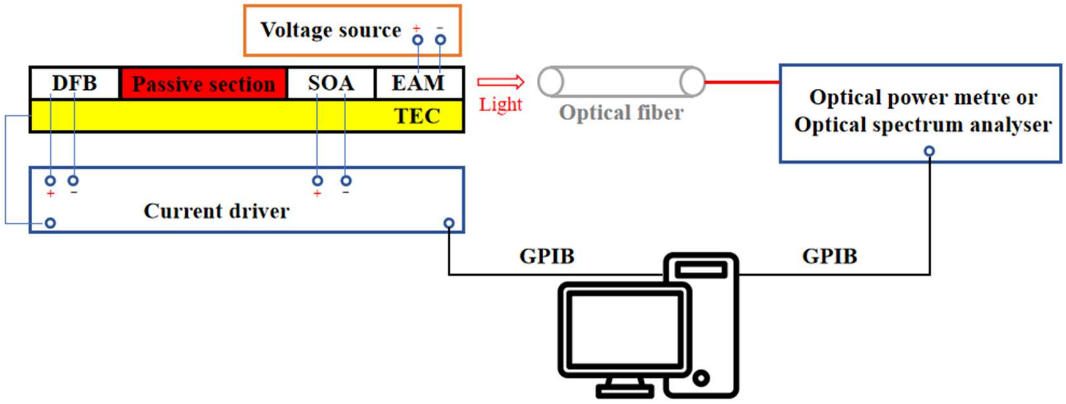

Figure 4.23: Schematic of the measurement platform set-up for ATG device test.

4.5.2 Output Power Measurement

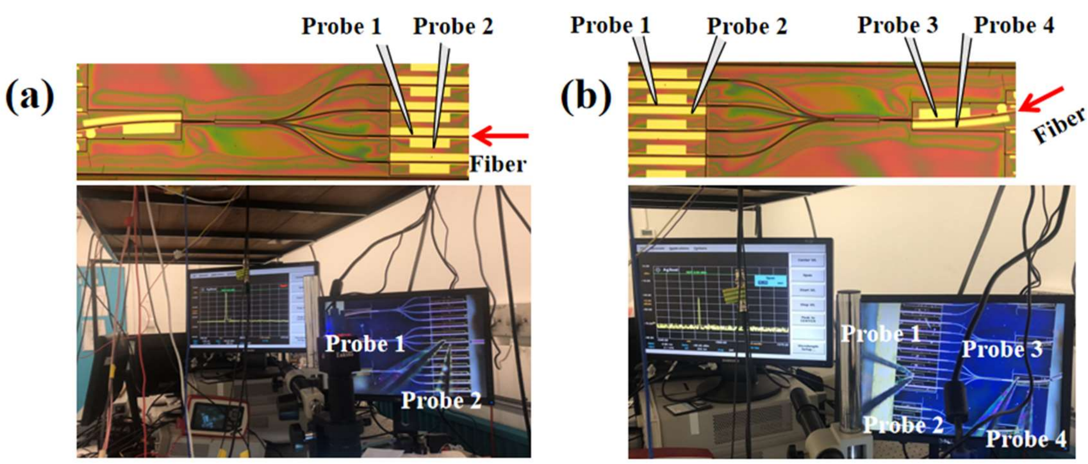

Figure 4.24: Schematic diagram of the measurement platform setup for testing the ATG device.

To accurately measure both the DFB side output power and the integrated device output power, two testing methods were implemented, as shown in Figure 4.24. Figure 4.24(a) illustrates the power measurement setup at the DFB end, where the device is rotated 180 degrees, enabling direct measurement of the DFB laser output power from the opposite facet before it enters the integrated optical circuit. Figure 4.24(b) shows the power measurement setup at the EAM end, where the optical signal propagates through the integrated photonic components, including the first taper, S-bend, MMI coupler, second taper, SOA, and EAM, before being collected at the output. During this process, optical losses occur at various stages, resulting in a reduction of the final measured output power.

Figure 4.25 is the power coupled into an SMF as a function of DFB current I_{DFB} for the CH2 under different SOA current I_{SOA}, and EAM bias voltage V_{EAM} is set at 0 V. The threshold current of the DFB laser is 65 mA. At I_{SOA} = 0 mA, the output power peaks at 0.77 mW. As I_{SOA} increases, the output power from the EAM side also increases. When I_{DFB} = 160 mA and I_{SOA} = 160 mA, the output power reaches its maximum value of 4.3 mW. The dotted line in Fig. 4.24 shows the typical output power as a function of I_{DFB} for CH2 from the DFB side, achieving 9.7 mW at I_{DFB}=160 mA.

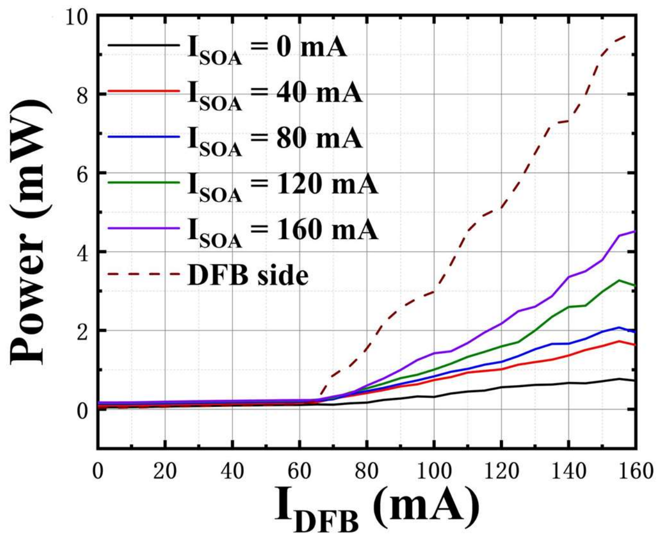

Figure 4.25: CH2 coupled power of the SMF versus I_{DFB} under different I_{SOA} (solid lines) measured from the EAM side, with the dotted line representing the L-I_{DFB} curve measured from the DFB side.

4.5.3 Optical Spectra Measurement and Wavelength Spacing Control

Lasers within the device were tested individually and sequentially. Figure 4.26(a) shows the measured optical spectra at the EAM end for four channels measured at the output of the EAM side with I_{DFB} = 100 mA, I_{SOA}=120 mA and V_{EAM} = 0 V, using an OSA with a resolution bandwidth of 0.06 nm. The emission wavelengths of the DFB lasers from CH1 to CH4 are 1553.06 nm, 1553.93 nm, 1554.83 nm, and 1555.67 nm, respectively, each achieving an SMSR greater than 45 dB.

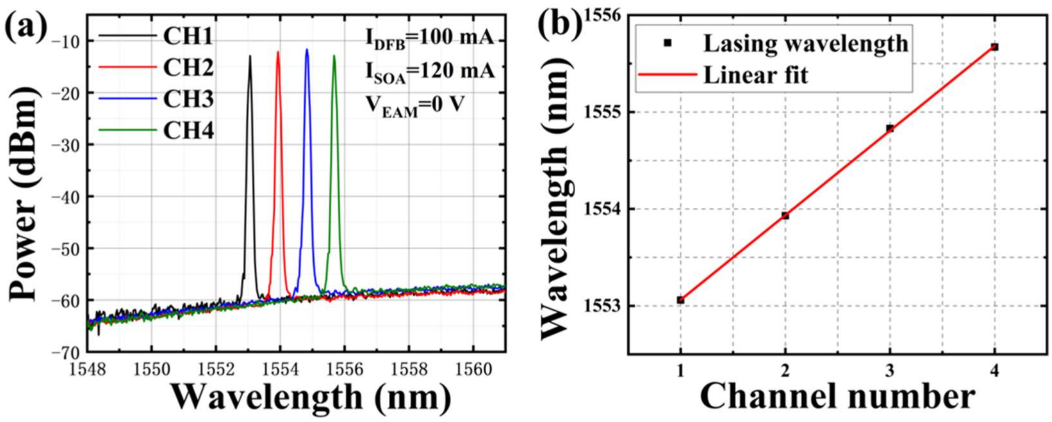

Figure 4.26: (a) Measured optical spectrum of the 4-channel DFB array at I_{DFB} = 100 mA, I_{SOA} = 120 mA, and V_{EAM} = 0 V; (b) linear fit to the lasing wavelength.

Figure 4.26(b) shows the linear fit to the lasing wavelengths of the four channels, with a slope of 0.873 nm and an error of 0.073 nm compared to the designed wavelength spacing of 0.8 nm.

Figure 4.27 presents the 2D optical spectra for each of the four channels (CH1–CH4) over a range of I_{DFB} from 0 mA to 150 mA, with I_{SOA} =120 mA and V_{EAM} =0 V. The threshold currents for CH3 and CH4 are approximately 60 mA, while CH1 exhibits a higher threshold of around 90 mA. This variation in threshold current may be caused by the fabrication error in the grating or cavity loss. For all channels, a single strong DFB lasing peak is observed, maintaining an SMSR greater than 40 dB in the operating range of I_{DFB} =100 to 150 mA, indicating stable single-mode operation. The wavelength shift due to current-induced heating is measured to be less than 0.02 nm/mA, which is relatively low, demonstrating good thermal stability of the device.

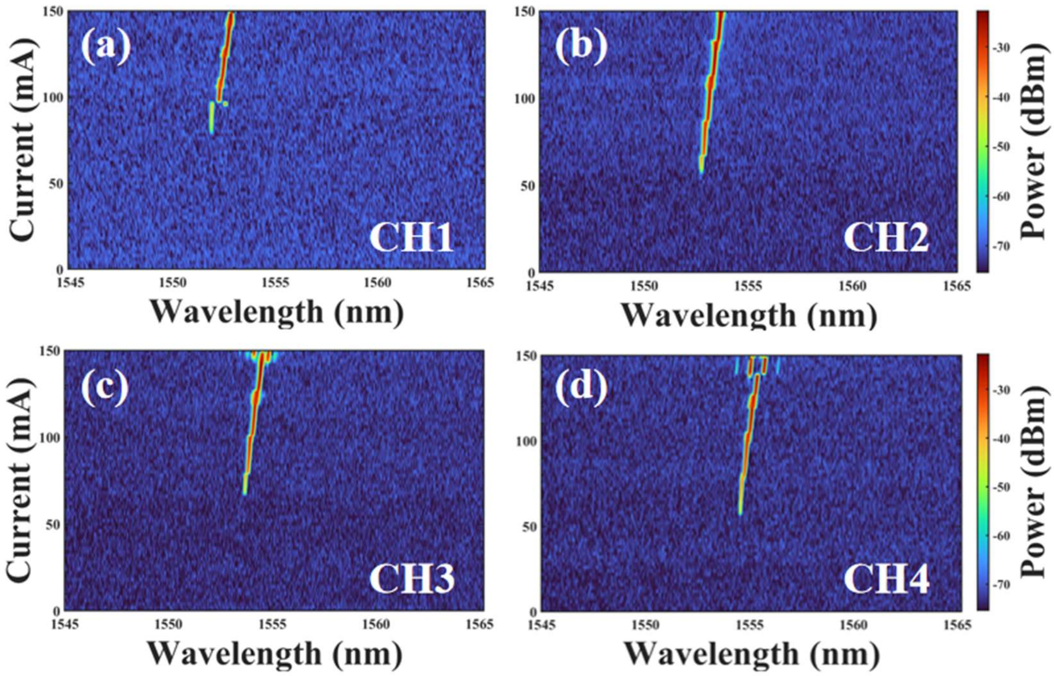

Figure 4.27: Measured optical spectrum of the 4-channel DFB array at I_{DFB} = 100 mA, I_{SOA} = 120 mA, and V_{EAM} = 0 V.

4.5.4 EAM DC Extinction Ratio (ER) Measurement

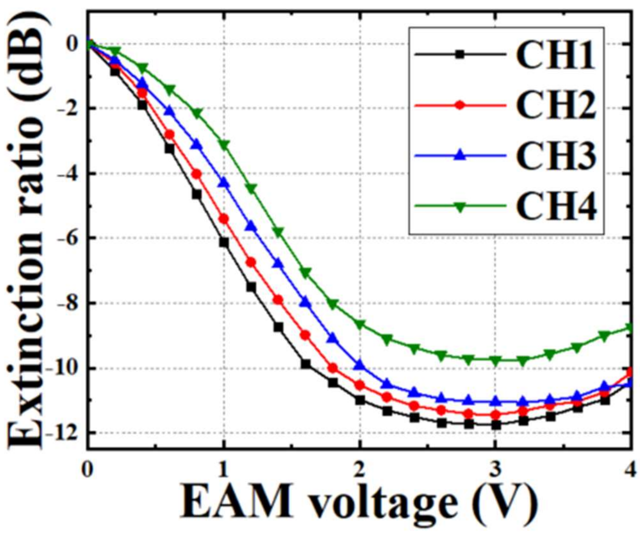

Figure 4.28: EAM DC extinction behaviours of the four channels with I_{DFB} = 150 mA and I_{SOA} = 80 mA.

The performance of the EAM is evaluated by measuring its extinction ratio (ER) as a function of applied voltage, as shown in Figure 4.28 with I_{DFB} = 150 mA and I_{SOA} = 80 mA. For all four channels (CH1–CH4), the extinction ratio reaches a maximum of approximately -12 dB at $V_{EAM} \approx$ 3V. As shown in the simulated results in Fig. 4.10, the extinction ratio (ER) decreases as the wavelength increases. This is because longer-wavelength channels typically experience reduced bandgap absorption, resulting in lower modulation efficiency.

In a previously reported 100-μm-long EML, a deep etching process was employed in EAM to reduce the P-I-N junction capacitance and enhance modulation efficiency [184]. This approach helps to achieve a higher modulation bandwidth in a shorter EAM device. However, in the ATG device design, deep etching was not applied to the EAM section due to the complexity of the fabrication process. Additionally, the EAM length was set to 150 μm, which could result in a lower -3-dB bandwidth of approximately 10 GHz, as indicated in[189]. To further optimise the EAM performance, future designs should explore the trade-off between device length, etching depth, and optical confinement, aiming for an optimal balance between extinction ratio, insertion loss, and modulation efficiency. And the EAM's static electro-optic (EO) response and dynamic performance will be tested soon, including eye diagrams, for all channels.

Overall, the combination of 4PS-SBG and ATG technology presents a highly scalable, regrowth-free approach for photonic integration, offering a promising path for the development of next-generation DWDM PICs with high manufacturing efficiency, wavelength precision, and integration flexibility.

4.6 Chapter Summary

In this chapter, we first emphasised the importance of photonic integration in achieving compact, high-performance, and scalable PICs. To explore different integration approaches, we introduced and analysed four major integration techniques (Butt-joint regrowth, SAG, QWI and ATG). Considering practical application requirements, ATG technology is selected for integration design. Following this decision, it is necessary to conduct comprehensive simulations to design and optimise for each integrated component, including the taper, S-bend waveguide, MMI coupler, SOA, and EAM, to ensure low-loss optical transitions and efficient performance. Finally, A DWDM source with a wavelength spacing of 0.8 nm was designed using a combination of 4PS-SBG and ATG technologies.

During fabrication, we optimised the three-step dry etching process, which is the most critical step in ATG device fabrication. Process refinements were made to improve and maintain precise etching depths and enhance active region protection, ensuring the successful definition of both active and passive regions. The final ATG-integrated DWDM source was fabricated and tested.

The experimental results confirm the reliability and scalability of this technique, with the fabricated device exhibiting stable single-mode operation, an SMSR > 40 dB, and a low wavelength shift of <0.02 nm/mA, demonstrating excellent thermal stability. Achieving the wavelength spacing of 0.873 nm, the error is less than 0.1 nm, making it suitable for DWDM applications. The integration of a 150-μm-long EAM provides efficient electro-absorption modulation, though further optimisations in etching depth, device length, and coupling efficiency could further enhance performance. These results validate the ATG technique as a promising alternative for monolithic photonic integration for future high-density PICs.

Chapter 5

Conclusions and Future Work

5.1 Research Summary

In this research, the novel Bragg grating designs and their applications in narrow-linewidth lasers and precise wavelength-controlled lasers were systematically investigated. By using ATG technology, we successfully integrated active and passive photonic components, enabling the development of a DWDM source with a wavelength spacing of 0.8 nm through the combined use of 4PS-SBG and ATG techniques. Each research was structured into three main phases: device design, fabrication and measurement.

To design Bragg gratings with specific functionalities, the TMM was employed to simulate the reflectivity spectra of various grating structures. TMM is well-suited for analysing complex Bragg gratings, including those with non-uniform or phase-shifted parts. Starting from the fundamental theory of uniform gratings, the concept of SBGs and phase-shift was introduced. By incorporating phase-shifted sections within the sampling periods, nPS-SBG structures were developed, offering higher effective coupling coefficients and precise wavelength control.

Building upon 4PS-SBG technology, a DFB semiconductor laser array was designed and fabricated, achieving precise wavelength selection with an enhanced coupling coefficient compared to DFB lasers with uniform gratings. This advancement enables greater spectral stability and improved manufacturing scalability, making it highly suitable for DWDM applications. The findings were reported in [190].

To further achieve narrow linewidth, the DPS structure was proposed. By introducing phase shifts into the DPS region, the field distribution within the laser cavity was flattened, mitigating the SHB effect. By optimizing the DPS region length and phase shift size, DPS lasers were designed and fabricated. Compared to traditional DFB lasers with uniform gratings, DPS lasers demonstrated a significant linewidth reduction, achieving higher SMSR, lower threshold current, and improved output stability. The related results were published in [191].

In subsequent research, the DPS concept was extended to the entire grating structure, leading to the first proposal of the CPSG structure based on uniform gratings. By gradually varying the initial phase within each grating period, the output wavelength exhibited a linear relationship with the total phase shift, enabling precise spectral tuning. Utilising this novel structure, we successfully fabricated laser devices with wavelength intervals of 0.493 nm, 0.949 nm, and 1.956 nm, while maintaining a strong coupling coefficient. This breakthrough effectively overcomes the resolution limitations of traditional manufacturing techniques by introducing the concept of total phase change trends, paving the way for the next generation of high-precision lasers. The findings were published in [192].

To achieve monolithic photonic integration, we adopted ATG technology, enabling the integration of active and passive components. Using vertical mode coupling, light was efficiently transferred between the active and passive regions. Each functional component was designed and optimised through extensive simulations to ensure low-loss optical transitions and efficient device operation. The final ATG-integrated DWDM source was fabricated using a three-step dry etching process. The fabricated device was experimentally validated, demonstrating stable single-mode lasing, high SMSR, efficient optical power transfer, and reliable electro-absorption modulation. The successful implementation of ATG technology not only eliminates the limitations of regrowth-based integration but also offers a scalable, high-yield solution for next-generation PICs, enabling high-density and cost-effective DWDM photonic circuits. The experimental results will be reported at CLEO 2025.

5.2 Future Work

The phase-controlled Bragg grating structure remains a promising area for further optimisation and exploration. While this research has introduced several novel grating designs, there is still significant potential for enhancing their performance and expanding their applications in PICs. Based on these considerations, my suggestions for future research are as follows:

1. Non-Uniform Phase Shifts for Longitudinal Mode Separation and Multi-Longitudinal Mode Lasers

In this study, phase shifts were inserted at fixed values. However, introducing non-uniform phase shifts could enable mode separation, leading to the design of multi-mode lasers with precisely engineered mode distributions. This approach could be particularly useful for multi-wavelength and mode-locked laser applications.

2. Non-Uniform Phase Shift Spacing for Reflection Peak Engineering

The phase shifts in this study were inserted at equal intervals, resulting in a predictable but rigid reflection profile. By introducing variable spacing between phase shifts, the intensity and distribution of the reflection peaks can be tailored, allowing for customised spectral shaping. This method could be useful in specialised optical filters, multi-wavelength lasers, and mode-selective devices.

3. Combining DPS and CPSG for Wavelength Control and Narrow Linewidth

The CPSG structure enables precise wavelength spacing, while the DPS structure is effective in narrowing the laser linewidth. Since phase shifts can be superimposed, which could facilitate the design of narrow-linewidth laser arrays with highly controlled channel spacing. This hybrid approach would enhance laser stability and spectral precision, making it highly suitable for coherent communication and sensing applications.

4. Heterogeneous Integration for III-V/Si Photonic Devices

Currently, all fabricated devices rely on III-V materials, which, while offering excellent performance, are not easily scalable for industrial production. Exploring III-V/Si heterogeneous integration would allow the development of cost-effective and CMOS-compatible photonic devices, to enable the monolithic integration of III-V active devices with Si-based photonic platforms.

5. Parallel Optical Coupling for Loss Reduction (QWI technology)

The current ATG integration strategy follows a top-down optical coupling approach, where light is transferred from the upper active waveguide to the lower passive waveguide. While effective, this process inherently introduces coupling losses. Exploring parallel light transmission structures, such as QWI-based integration, could reduce optical losses and improve device efficiency, making integrated photonic devices more practical for real-world applications.

6. Multi-Segment CPSG for Injection-Locked Multi-Channel Lasers

In most conventional laser structures, the output wavelength is independent of cavity length. However, in the CPSG structure, the wavelength is inversely related to cavity length. By employing mutually injection-locked multi-segment CPSG lasers, it may be possible to generate evenly spaced multi-channel outputs, creating a new class of highly stable DWDM laser arrays. This concept could be further explored for multi-wavelength coherent sources, high-speed optical communication, and frequency-comb generation.

This thesis explored novel semiconductor diode lasers, including laser arrays, narrow-linewidth lasers, and ATG-based integrated devices, demonstrating advancements in precision wavelength control, linewidth reduction, and monolithic integration. As research continues to evolve, next-generation semiconductor lasers with diverse functionalities will emerge, further expanding the capabilities and applications of optoelectronic devices, and shaping the future of high-speed communication, sensing, and integrated photonics.

Bibliography

[1] F. Tariq, M. Khandaker, K.-K. Wong, M. Imran, M. Bennis, and m. Debbah, *A Speculative Study on 6G*. 2019, doi: 10.48550/arXiv.1902.06700.

[2] Y. Li, Y. Yan, W. Chen, S. K. Bose, and G. Shen, "Strategies and benefits of deploying ultralow-loss fiber links in an elastic optical network," *Journal of Optical Communications and Networking,* vol. 11, no. 5, pp. 238-249, 2019, doi: 10.1364/JOCN.11.000238.

[3] B. O. hAnnaidh *et al.*, "Devices and Sensors Applicable to 5G System Implementations," in *2018 IEEE MTT-S International Microwave Workshop Series on 5G Hardware and System Technologies (IMWS-5G)*, pp. 1-3, 2018, doi: 10.1109/IMWS-5G.2018.8484316.

[4] S. Chaudhary, R. Johari, R. Bhatia, K. Gupta, and A. Bhatnagar, "CRAIoT: Concept, Review and Application(s) of IoT," in *2019 4th International Conference on Internet of Things: Smart Innovation and Usages (IoT-SIU)*, pp. 1-4, 2019, doi: 10.1109/IoT-SIU.2019.8777467.

[5] T. Kato *et al.*, "Field-Deployed Fiber Transmission of DWDM Signal in S+C+L-Band Co-Propagating With 400GBASE-LR8," *IEEE Photonics Technology Letters,* vol. 36, no. 1, pp. 16-19, 2024, doi: 10.1109/LPT.2023.3331765.

[6] E. Chen and J. M. Kahn, "Comparison of Discrete-Laser and Comb-Based DWDM Analog Coherent Links in the Presence of Fiber Kerr Nonlinearity," *Journal of Lightwave Technology,* vol. 43, no. 7, pp. 3070-3077, 2025, doi: 10.1109/JLT.2024.3519252.

[7] J. Peng, H. Yu, J. Liu, Y. Cao, Z. Zhang, and L. Sun, "Principles, Measurements and Suppressions of Semiconductor Laser Noise—A Review," *IEEE Journal of Quantum Electronics,* vol. 57, no. 5, pp. 1-15, 2021, doi: 10.1109/JQE.2021.3093885.

[8] A. B. Petrov *et al.*, "High Power Ultranarrow Linewidth Picosecond Laser System Based on Tapered Fiber Amplifier and Gain-Switched DFB Laser Diode," *Journal of Lightwave Technology,* vol. 40, no. 12, pp. 3930-3934, 2022, doi: 10.1109/JLT.2022.3149350.

[9] H. Shi *et al.*, "Timing Jitter of the Dual-Comb Mode-Locked Laser: A Quantum Origin and the Ultimate Effect on High-Speed Time- and Frequency-Domain Metrology," *IEEE Journal of Selected Topics in Quantum Electronics,* vol. 24, no. 5, pp. 1-10, 2018, doi: 10.1109/JSTQE.2018.2810381.

[10] A. Liu, B. Yang, and W. Zheng, "Cryogenic High-Speed Vertical-Cavity Surface-Emitting Lasers for Quantum Computing: A Review," *IEEE Journal of Selected Topics in Quantum Electronics,* vol. 31, no. 5: Quantum Materials and Quantum Devices, pp. 1-12, 2025, doi: 10.1109/JSTQE.2025.3558915.

[11] C. Xu *et al.*, "A DFB Laser With Integrated Passive Region Suitable for PAM-4 Modulation Signal," *IEEE Photonics Journal,* vol. 14, no. 4, pp. 1-6, 2022, doi: 10.1109/JPHOT.2022.3189525.

[12] P. A. Verrinder *et al.*, "Gallium Arsenide Photonic Integrated Circuit Platform for Tunable Laser Applications," *IEEE Journal of Selected Topics in Quantum Electronics,* vol. 28, no. 1, pp. 1-9, 2022, doi: 10.1109/JSTQE.2021.3086074.

[13] J. E. Midwinter, "Optical fiber systems: Low-loss links: Long-wavelength intercity telecommunications increase repeater spacing and promise low cost," *IEEE Spectrum,* vol. 17, no. 3, pp. 45-47, 1980, doi: 10.1109/MSPEC.1980.6330325.

[14] K. Nakagawa, "Advanced very high-speed optical fiber transmission systems," in *IEEE International Conference on Communications, Including Supercomm Technical Sessions*, vol. 1, pp. 172-176, 1990, doi: 10.1109/ICC.1990.117072.

[15] L. Gilli, G. Cossu, and E. Ciaramella, "New Prospects of Optical Wireless Communication Systems Exploiting VCSEL-Based Transmitters," *Journal of Lightwave Technology,* vol. 43, no. 4, pp. 1615-1624, 2025, doi: 10.1109/JLT.2025.3530819.

[16] B. Han, Y. Ma, Y. Zhao, and H. Wu, "The Applications of Random Fiber Lasers in Optical Fiber Communication and Sensing Systems: A Review," *IEEE Transactions on Instrumentation and Measurement,* vol. 73, pp. 1-17, 2024, doi: 10.1109/TIM.2023.3335534.

[17] D. Uzunidis, M. Presi, A. Sgambelluri, F. Paolucci, A. Stavdas, and F. Cugini, "Bidirectional single-fiber filterless optical networks: modeling and experimental assessment," *Journal of Optical Communications and Networking,* vol. 13, no. 6, pp. C1-C9, 2021, doi: 10.1364/JOCN.411637.

[18] M. R. Kadhum and H. Haboobi, "Advanced Optical Waveform With Single Mode Fiber Optic for Developing Upcoming Networks of Mobile Communications," *IEEE Access,* vol. 13, pp. 6413-6421, 2025, doi: 10.1109/ACCESS.2024.3523818.

[19] J. Viheriälä, K. Haring, S. Suomalainen, R. Koskinen, T. Niemi, and M. Guina, "High Spectral Purity High-Power GaSb-Based DFB Laser Fabricated by Nanoimprint Lithography," *IEEE Photonics Technology Letters,* vol. 28, no. 11, pp. 1233-1236, 2016, doi: 10.1109/LPT.2016.2519044.

[20] W. Du, D. Cote, C. Barber, and Y. Liu, "Forecasting loss of signal in optical networks with machine learning," *Journal of Optical Communications and Networking,* vol. 13, no. 10, pp. E109-E121, 2021, doi: 10.1364/JOCN.423667.

[21] Z. Chen, X. Dong, J. Gao, Z. Yu, and K. Xu, "Performance Investigation of Low-Resolution Coherent Optical Communication System with Low-Complexity Adaptive Equalizer," *IEEE Photonics Journal,* vol. 17, no. 2, pp. 1-6, 2025, doi: 10.1109/JPHOT.2025.3555482.

[22] D. E. Ceballos-Herrera, M. López-Coyote, and R. Gutiérrez-Castrejón, "Crosstalk Characteristics of WDM Channels in Quasi-Homogeneous Multicore Fibers," *IEEE Photonics Technology Letters,* vol. 32, no. 13, pp. 759-762, 2020, doi: 10.1109/LPT.2020.2995144.

[23] M. Pelusi, T. Kurosu, and S. Namiki, "Brillouin Amplifier Noise Limiting With a Semiconductor Optical Amplifier for Coherent Communication Applications," *Journal of Lightwave Technology,* vol. 41, no. 5, pp. 1375-1388,

2023, doi: 10.1109/JLT.2022.3222010.
[24] H. Dang *et al.*, "Spectral Purity Improvement by Combining Self-Injection Locking and Stimulated Thermal Rayleigh Scattering in Fiber Lasers," *IEEE Photonics Journal,* vol. 10, no. 2, pp. 1-9, 2018, doi: 10.1109/JPHOT.2018.2803144.
[25] F. Hamaoka *et al.*, "Long-Haul >100-Tb/s Transmission Over >1000 km With High-Symbol-Rate Triple-Band WDM Signals," *Journal of Lightwave Technology,* vol. 43, no. 4, pp. 1987-1994, 2025, doi: 10.1109/JLT.2024.3463670.
[26] N. Deng, L. Zong, H. Jiang, Y. Duan, and K. Zhang, "Challenges and Enabling Technologies for Multi-Band WDM Optical Networks," *Journal of Lightwave Technology,* vol. 40, no. 11, pp. 3385-3394, 2022, doi: 10.1109/JLT.2022.3162725.
[27] F. Pittalà *et al.*, "1.71 Tb/s Single-Channel and 56.51 Tb/s DWDM Transmission Over 96.5 km Field-Deployed SSMF," *IEEE Photonics Technology Letters,* vol. 34, no. 3, pp. 157-160, 2022, doi: 10.1109/LPT.2022.3142538.
[28] Y. Zhang, Z. Zhou, S. Xiao, and M. Bi, "12.5-GHz Spaced Downstream Transmitter for Long Reach DWDM-PON," in *2014 Asia Communications and Photonics Conference (ACP)*, pp. 1-3, 2014.
[29] "IEEE/ISO/IEC International Standard -Telecommunications and exchange between information technology systems--Requirements for local and metropolitan area networks--Part 3: Standard for Ethernet AMENDMENT 13: Physical layers and management parameters for 100 Gb/s operation over DWDM systems," *ISO/IEC/IEEE 8802-3:2021/Amd.13:2022(E),* pp. 1-136, 2022, doi: 10.1109/IEEESTD.2022.9921258.
[30] V. K. Stamatios, "DWDM Current Issues and Research," in *Introduction to DWDM Technology: Data in a Rainbow*: IEEE, pp. 209-209, 2000.
[31] J. Cho *et al.*, "Trans-Atlantic Field Trial Using High Spectral Efficiency Probabilistically Shaped 64-QAM and Single-Carrier Real-Time 250-Gb/s 16-QAM," *Journal of Lightwave Technology,* vol. 36, no. 1, pp. 103-113, 2018, doi: 10.1109/JLT.2017.2776840.
[32] T. Zami *et al.*, "31.2-Tb/s Real Time Bidirectional Transmission of 78×400 Gb/s Interleaved Channels over C Band of One 90-km SMF Span," in *2018 Optical Fiber Communications Conference and Exposition (OFC)*, pp. 1-3, 2018.
[33] B. J. Puttnam *et al.*, "402 Tb/s GMI Data-Rate OESCLU-Band Transmission," in *Optical Fiber Communication Conference (OFC) 2024*, San Diego California, 2024/03/24 2024: Optica Publishing Group, in Technical Digest Series, doi: 10.1364/OFC.2024.Th4A.3.
[34] T. Septon *et al.*, "Large linewidth reduction in semiconductor lasers based on atom-like gain material," *Optica,* vol. 6, no. 8, pp. 1071-1077, 2019/08/20 2019, doi: 10.1364/OPTICA.6.001071.
[35] M. Buyalo, A. Gubenko, S. Mikhrin, V. Mikhrin, A. R. Kovsh, and A. V. Krishnamoorthy, "Efficient, high-power, narrow-linewidth, continuous-wave quantum-dot semiconductor comb laser," *Scientific Reports,* vol. 14, no. 1, p.

4197, 2024, doi: 10.1038/s41598-024-53609-9.
[36] A. L. Schawlow and C. H. Townes, "Infrared and Optical Masers," *Physical Review,* vol. 112, no. 6, pp. 1940-1949, 1958, doi: 10.1103/PhysRev.112.1940.
[37] T. H. Maiman, "Stimulated Optical Radiation in Ruby," *Nature,* vol. 187, no. 4736, pp. 493-494, 1960, doi: 10.1038/187493a0.
[38] M. Malinauskas *et al.*, "Ultrafast laser processing of materials: from science to industry," *Light: Science & Applications,* vol. 5, no. 8, pp. e16133-e16133, 2016, doi: 10.1038/lsa.2016.133.
[39] D. Pérez-López *et al.*, "General-purpose programmable photonic processor for advanced radiofrequency applications," *Nature Communications,* vol. 15, no. 1, p. 1563, 2024, doi: 10.1038/s41467-024-45888-7.
[40] B. Chichkov, "Laser printing: trends and perspectives," *Applied Physics A,* vol. 128, no. 11, p. 1015, 2022, doi: 10.1007/s00339-022-06158-9.
[41] A. Marcu *et al.*, "Photon energy transfer on titanium targets for laser thrusters," *High Power Laser Science and Engineering,* vol. 10, p. e27, 2022, doi: 10.1017/hpl.2022.23.
[42] M. Virte, E. Mercier, H. Thienpont, K. Panajotov, and M. Sciamanna, "Physical random bit generation from chaotic solitary laser diode," *Opt. Express,* vol. 22, no. 14, pp. 17271-17280, 2014, doi: 10.1364/OE.22.017271.
[43] Z. Gao, X. Wang, and Y. Wang, "High speed secure optical communication based on optical code processing (Invited paper)," in *2019 18th International Conference on Optical Communications and Networks (ICOCN)*, 2019, pp. 1-3, doi: 10.1109/ICOCN.2019.8934755.
[44] https://en.wikipedia.org/wiki/Photonic_integrated_circuit (accessed.
[45] C. Porzi *et al.*, "Spectrally Pure W-Band RF Carrier Generation With Packaged Silicon Photonics Circuit," *IEEE Journal of Quantum Electronics,* vol. 60, no. 6, pp. 1-9, 2024, doi: 10.1109/JQE.2024.3380552.
[46] D. Coenen, H. Oprins, P. D. Heyn, J. V. Campenhout, and I. D. Wolf, "Analysis of Thermal Crosstalk in Photonic Integrated Circuit Using Dynamic Compact Models," *IEEE Transactions on Components, Packaging and Manufacturing Technology,* vol. 12, no. 8, pp. 1350-1357, 2022, doi: 10.1109/TCPMT.2022.3195699.
[47] C. Besancon *et al.*, "Comparison of AlGaInAs-Based Laser Behavior Grown on Hybrid InP-SiO_2/Si and InP Substrates," *IEEE Photonics Technology Letters,* vol. 32, no. 8, pp. 469-472, 2020, doi: 10.1109/LPT.2020.2979254.
[48] E. Selcuk, "Guided and deterministic self organization of quantum dots," *Nano Letters - NANO LETT,* 01/01 2009.
[49] A. Morana *et al.*, "Extreme Radiation Sensitivity of Ultra-Low Loss Pure-Silica-Core Optical Fibers at Low Dose Levels and Infrared Wavelengths," *Sensors,* vol. 20, p. 7254, 2020, doi: 10.3390/s20247254.
[50] B. Zhu *et al.*, "3.08 Tb/s (77/spl times/42.7 Gb/s) transmission over 1200 km of non-zero dispersion-shifted fiber with 100-km spans using C and L-band distributed Raman amplification," in *OFC 2001. Optical Fiber Communication Conference and Exhibit. Technical Digest Postconference Edition (IEEE Cat.*

01CH37171), 2001, vol. 4, pp. PD23-PD23.

[51] H. Jaw, "Phase diagram for LPE growth of GaInAsP layers lattice matched to InP substrates," *IEEE Journal of Quantum Electronics,* vol. 17, no. 2, pp. 118-122, 1981, doi: 10.1109/JQE.1981.1071083.

[52] R. F. Kazarinov and G. L. Belenky, "Novel design of AlGaInAs-InP lasers operating at 1.3 /spl mu/m," *IEEE Journal of Quantum Electronics,* vol. 31, no. 3, pp. 423-426, 1995, doi: 10.1109/3.364396.

[53] J. J. Hsieh, "Room-Temperature Operation of GaInAsp/Inp Double-Heterostructure Diode Lasers Emitting at 1.1 µm*," in *Integrated Optics*, Salt Lake City, Utah, 1976: Optica Publishing Group, in Technical Digest Series, p. MB2, doi: 10.1364/IOPT.1976.MB2.

[54] J. C. L. Yong, J. M. Rorison, and I. H. White, "1.3-µm quantum-well InGaAsP, AlGaInAs, and InGaAsN laser material gain: a theoretical study," *Quantum Electronics, IEEE Journal of,* vol. 38, pp. 1553-1564, 2003, doi: 10.1109/JQE.2002.805100.

[55] S. Adachi, "Refractive indices of III–V compounds: Key properties of InGaAsP relevant to device design," *Journal of Applied Physics,* vol. 53, no. 8, pp. 5863-5869, 1982, doi: 10.1063/1.331425.

[56] M. J. Mondry, D. Babic, J. Bowers, and L. A. Coldren, "Refractive Indexes of (Al, Ga, In)As Epilayers on InP for Optoelectronic Applications," *Photonics Technology Letters, IEEE,* vol. 4, pp. 627-630, 1992, doi: 10.1109/68.141990.

[57] N. Nishiyama *et al.*, "Long-Wavelength Vertical-Cavity Surface-Emitting Lasers on InP With Lattice Matched AlGaInAs–InP DBR Grown by MOCVD," *IEEE Journal of Selected Topics in Quantum Electronics,* vol. 11, no. 5, pp. 990-998, 2005, doi: 10.1109/JSTQE.2005.853841.

[58] S. Kawakami and S. Nishida, "Characteristics of a doubly clad optical fiber with a low-index inner cladding," *IEEE Journal of Quantum Electronics,* vol. 10, no. 12, pp. 879-887, 1974, doi: 10.1109/JQE.1974.1068118.

[59] C. Hwang, "Densities of states and properties of spontaneous and stimulated emission in semiconductor lasers," *IEEE Journal of Quantum Electronics,* vol. 6, no. 6, pp. 310-310, 1970, doi: 10.1109/JQE.1970.1076471.

[60] D. Schicketanz and G. Zeidler, "GaAs-double-heterostructure lasers as optical amplifiers," *IEEE Journal of Quantum Electronics,* vol. 11, no. 2, pp. 65-69, 1975, doi: 10.1109/JQE.1975.1068560.

[61] A. Valster and C. J. v. d. Poel, "High temperature and high power operation of dual strained layer QW visible laser diodes," in *Proceedings of IEEE 14th International Semiconductor Laser Conference*, 1994, pp. 197-198, doi: 10.1109/ISLC.1994.519332.

[62] T. H. Wood, "Multiple quantum well devices for optoelectronics," in *1985 International Electron Devices Meeting*, 1985, pp. 458-461, doi: 10.1109/IEDM.1985.191001.

[63] K. Otsuka and K. Kubodera, "Effects of auger recombination process on laser dynamics," *IEEE Journal of Quantum Electronics,* vol. 16, no. 5, pp. 538-541, 1980, doi: 10.1109/JQE.1980.1070510.

[64] W. Chen *et al.*, "1.47 μm high characteristic temperature InGaAsP/InP MQW laser," in *2012 International Conference on Optoelectronics and Microelectronics*, 2012, pp. 115-118, doi: 10.1109/ICoOM.2012.6316230.
[65] N. Takenaka *et al.*, "151-channel AM-FDM transmission using 1.3 /spl mu/m strained-layer MQW-DFB laser with high optical output power operation," in *Proceedings of 1994 IEEE International Electron Devices Meeting*, 11-14 Dec. 1994 1994, pp. 773-776, doi: 10.1109/IEDM.1994.383309.
[66] J. Hecht, "Short history of Laser development," *Applied optics,* vol. 49, pp. F99-122, 2010, doi: 10.1117/1.3483597.
[67] L. Ka-Suen and C. Shu, "Generation of optical millimeter-wave with a widely tunable carrier using Fabry-Perot grating-lens external cavity laser," *IEEE Microwave and Guided Wave Letters,* vol. 9, no. 5, pp. 192-194, 1999, doi: 10.1109/75.766761.
[68] M. Asada, A. Kameyama, and Y. Suematsu, "Gain and intervalence band absorption in quantum-well lasers," *IEEE Journal of Quantum Electronics,* vol. 20, no. 7, pp. 745-753, 1984, doi: 10.1109/JQE.1984.1072464.
[69] S. Seki, K. Yokoyama, and P. Sotirelis, "Theoretical analysis of high-temperature characteristics of 1.3-/spl mu/m InP-based quantum-well lasers," *IEEE Journal of Selected Topics in Quantum Electronics,* vol. 1, no. 2, pp. 264-274, 1995, doi: 10.1109/2944.401205.
[70] L. M. Augustin *et al.*, "InP-Based Generic Foundry Platform for Photonic Integrated Circuits," *IEEE Journal of Selected Topics in Quantum Electronics,* vol. 24, no. 1, pp. 1-10, 2018, doi: 10.1109/JSTQE.2017.2720967.
[71] R. Paoletti *et al.*, "Highly reliable and high-yield 1300-nm InGaAlAs directly modulated ridge fabry-Perot lasers, operating at 10-gb/s, up to 110/spl deg/C, with constant current swing," *Journal of Lightwave Technology,* vol. 24, no. 1, pp. 143-149, 2006, doi: 10.1109/JLT.2005.861128.
[72] S. Foster and A. Tikhomirov, "Experimental and theoretical characterization of the mode profile of single-mode DFB fiber lasers," *IEEE Journal of Quantum Electronics,* vol. 41, no. 6, pp. 762-766, 2005, doi: 10.1109/JQE.2005.846684.
[73] H. Kogelnik and C. V. Shank, "Coupled-Wave Theory of Distributed Feedback Lasers," *Journal of Applied Physics,* vol. 43, pp. 2327-2335, 1972, doi: 10.1063/1.1661499.
[74] M. Nakamura, K. Aiki, J. Umeda, and A. Yariv, "cw operation of distributed-feedback GaAs-GaAlAs diode lasers at temperatures up to 300 K," *Applied Physics Letters,* vol. 27, p. 403, 1975, doi: 10.1063/1.88492.
[75] L. A. Coldren and S. W. Corzine, *Diode lasers and photonic integrated circuits*. New York (N.Y.) : Wiley (in eng), 1995.
[76] B. Jens, A. Markus-Christian, and J. B. Daniel, "SingleMode Laser Diodes," in *Tunable Laser Diodes and Related Optical Sources*: IEEE, 2005, pp. 43-78.
[77] T. Erdogan, "Fiber grating spectra," *Journal of Lightwave Technology,* vol. 15, no. 8, pp. 1277-1294, 1997, doi: 10.1109/50.618322.
[78] J. Hong, W. Huang, and T. Makino, "On the transfer matrix method for distributed-feedback waveguide devices," *Journal of Lightwave Technology,*

vol. 10, no. 12, pp. 1860-1868, 1992, doi: 10.1109/50.202840.

[79] J. Seufert *et al.*, "DFB laser diodes in the wavelength range from 760 nm to 2.5 µm," *Spectrochimica Acta Part A: Molecular and Biomolecular Spectroscopy,* vol. 60, no. 14, pp. 3243-3247, 2004, doi: https://doi.org/10.1016/j.saa.2003.11.043.

[80] F. Ouellette, P. A. Krug, T. Stephens, G. Dhosi, and B. Eggleton, "Broadband and WDM dispersion compensation using chirped sampled fibre Bragg gratings," *Electronics Letters,* vol. 31, no. 11, pp. 899-901, 1995, doi: 10.1049/el:19950586.

[81] H. Haus and C. Shank, "Antisymmetric taper of distributed feedback lasers," *IEEE Journal of Quantum Electronics,* vol. 12, no. 9, pp. 532-539, 1976, doi: 10.1109/JQE.1976.1069214.

[82] Y. Nakano, Y. Luo, and K. Tada, "Facet reflection independent, single longitudinal mode oscillation in a GaAlAs/GaAs distributed feedback laser equipped with a gain-coupling mechanism," *Applied Physics Letters,* vol. 55, pp. 1606-1608, 1989.

[83] H. Soda, Y. Kotaki, H. Sudo, H. Ishikawa, S. Yamakoshi, and H. Imai, "Stability in single longitudinal mode operation in GaInAsP/InP phase-adjusted DFB lasers," *IEEE Journal of Quantum Electronics,* vol. 23, no. 6, pp. 804-814, 1987, doi: 10.1109/JQE.1987.1073454.

[84] K. Utaka, S. Akiba, K. Sakai, and Y. Matsushima, "λ/4-shifted InGaAsP/InP DFB lasers," *IEEE Journal of Quantum Electronics,* vol. 22, no. 7, pp. 1042-1051, 1986, doi: 10.1109/JQE.1986.1073089.

[85] B. Yan *et al.*, "Fabrication of sub-10 nm Gap by using Electron Beam Lithography," in *2023 24th International Vacuum Electronics Conference (IVEC)*, 2023, pp. 1-2, doi: 10.1109/IVEC56627.2023.10156935.

[86] G. P. Li, T. Makino, and C. M. Wu, "Multi-/spl lambda/ ridge waveguide gain-coupled DFB laser array," *Journal of Lightwave Technology,* vol. 13, no. 2, pp. 196-199, 1995, doi: 10.1109/50.365206.

[87] G. P. Li, T. Makino, A. Sarangan, and W. Huang, "16-wavelength gain-coupled DFB laser array with fine tunability," *IEEE Photonics Technology Letters,* vol. 8, no. 1, pp. 22-24, 1996, doi: 10.1109/68.475765.

[88] K. Kudo *et al.*, "1.55-µm wavelength-selectable microarray DFB-LD's with monolithically integrated MMI combiner, SOA, and EA-modulator," *IEEE Photonics Technology Letters,* vol. 12, no. 3, pp. 242-244, 2000, doi: 10.1109/68.826901.

[89] Y. Shi, L. Li, J. Zheng, Y. Zhang, B. Qiu, and X. Chen, "16-Wavelength DFB Laser Array With High Channel-Spacing Uniformity Based on Equivalent Phase-Shift Technique," *IEEE Photonics Journal,* vol. 6, pp. 1-9, 2014, doi: 10.1109/JPHOT.2014.2374610.

[90] C. Ting, Q. Yajuan, S. Yuechun, X. Rulei, and C. Xiangfei, "Widely tunable semiconductor laser based on step-chirped sampled Bragg grating," in *2015 14th International Conference on Optical Communications and Networks (ICOCN)*, 2015, pp. 1-3, doi: 10.1109/ICOCN.2015.7203777.

[91] L. San-Liang, J. Ing-Fa, P. Ching-Tang, W. Chi-Yu, and S. Tien-Tsong, "Sampled grating DBR laser arrays with adjustable 0.8/1.6 nm wavelength spacing," *IEEE Photonics Technology Letters,* vol. 11, no. 8, pp. 955-957, 1999, doi: 10.1109/68.775311.

[92] J. Li *et al.*, "A Multiexposure Technology for Sampled Bragg Gratings and its Applications in Dual-Wavelength Lasing Generation and OCDMA En/Decoding," *IEEE Photonics Technology Letters,* vol. 21, no. 21, pp. 1639-1641, 2009, doi: 10.1109/LPT.2009.2030877.

[93] B. Wu, Y. Liu, and Z. Dai, "Narrow Linewidth Fiber Grating F-P Cavity Laser and Application," in *2006 International Conference on Communications, Circuits and Systems*, 2006, vol. 3, pp. 1971-1974, doi: 10.1109/ICCCAS.2006.285060.

[94] M. Ramakrishnan, G. Rajan, Y. Semenova, and G. Farrell, "Overview of Fiber Optic Sensor Technologies for Strain/Temperature Sensing Applications in Composite Materials," *Sensors,* vol. 16, no. 1, p. 99, 2016.

[95] B. H. Lee *et al.*, "Interferometric Fiber Optic Sensors," *Sensors,* vol. 12, no. 3, pp. 2467-2486, 2012.

[96] S. Ismail and E. Browell, "Differential Absorption Lidar," pp. 277-288, 2015.

[97] S. Abdelazim, D. Santoro, M. Arend, F. Moshary, and S. Ahmed, "Coherent Doppler Lidar for Wind Sensing," 2020.

[98] T. Udem, R. Holzwarth, and T. W. Hänsch, "Optical frequency metrology," *Nature,* vol. 416, no. 6877, pp. 233-237, 2002, doi: 10.1038/416233a.

[99] J.-Q. Chen *et al.*, "Linewidth Measurement of a Narrow-Linewidth Laser: Principles, Methods, and Systems," *Sensors,* vol. 24, no. 11, p. 3656, 2024.

[100] T. Okoshi, K. Kikuchi, and A. Nakayama, "Novel method for high resolution measurement of laser output spectrum," *Electronics Letters,* vol. 16, no. 16, pp. 630-631, 1980, doi:10.1049/el:19800437.

[101] C. Henry, "Theory of the linewidth of semiconductor lasers," *IEEE Journal of Quantum Electronics,* vol. 18, no. 2, pp. 259-264, 1982, doi: 10.1109/JQE.1982.1071522.

[102] H. Debrégeas, "Widely Tunable Laser Diodes," vol. 161, 2017, pp. 209-248.

[103] J. Buus, "Dynamic single-mode operation of DFB lasers with phase shifted gratings and reflecting mirrors," *IEE Proceedings J (Optoelectronics),* vol. 133, no. 2, pp. 163-163, 1986, doi: doi:10.1049/ip-j.1986.0027.

[104] H. J. Wunsche, U. Bandelow, and H. Wenzel, "Calculation of combined lateral and longitudinal spatial hole burning in lambda /4 shifted DFB lasers," *IEEE Journal of Quantum Electronics,* vol. 29, no. 6, pp. 1751-1760, 1993, doi: 10.1109/3.234431.

[105] M. Okai, N. Chinone, H. Taira, and T. Harada, "Corrugation-pitch-modulated phase-shifted DFB laser," *IEEE Photonics Technology Letters,* vol. 1, no. 8, pp. 200-201, 1989, doi: 10.1109/68.36041.

[106] M. Okai, M. Suzuki, T. T. Tuyoshi Taniwatari, and N. C. Naoki Chinone, "Corrugation-Pitch-Modulated Distributed Feedback Lasers with Ultranarrow Spectral Linewidth," *Japanese Journal of Applied Physics,* vol. 33, no. 5R, p.

2563, 1994/05/01 1994, doi: 10.1143/JJAP.33.2563.
[107] M. Okai, T. Tsuchiya, K. Uomi, N. Chinone, and T. Harada, "Corrugation-pitch-modulated MQW-DFB laser with narrow spectral linewidth (170 kHz)," *IEEE Photonics Technology Letters,* vol. 2, no. 8, pp. 529-530, 1990, doi: 10.1109/68.58038.
[108] T. Xiang *et al.*, "Theoretical and experimental demonstration on narrow-linewidth DFB laser utilizing equivalent CPM-apodized grating," in *2016 15th International Conference on Optical Communications and Networks (ICOCN)*, 2016, pp. 1-3, doi: 10.1109/ICOCN.2016.7875784.
[109] J. Li *et al.*, "Experimental demonstration of distributed feedback semiconductor lasers based on reconstruction-equivalent-chirp technology," *Opt. Express,* vol. 17, no. 7, pp. 5240-5245, 2009, doi: 10.1364/OE.17.005240.
[110] S. Ogita, Y. Kotaki, M. Matsuda, Y. Kuwahara, and H. Ishikawa, "Long-cavity multiple-phase-shift distributed feedback laser diode for linewidth narrowing," *Journal of Lightwave Technology,* vol. 8, no. 10, pp. 1596-1604, 1990, doi: 10.1109/50.59202.
[111] S. Ogita, Y. Kotaki, H. Ishikawa, and H. Imai, "OPTIMUM DESIGN POR MULTIPLE-PHASE-SHIFT DISTRIBUTED FEEDBACK LASER," in *International Conference on Quantum Electronics*, Tokyo, H. Y. T. Inaba and T. Ikegami, Eds., 1988.
[112] H. Zhao *et al.*, "Accurate and Efficient Proximity Effect Correction for Electron Beam Lithography Based on Distributed Parallel Computing," in *2022 International Workshop on Advanced Patterning Solutions (IWAPS)*, 2022, pp. 1-4, doi: 10.1109/IWAPS57146.2022.9972245.
[113] V. S. Tumashev, V. A. Seleznev, A. I. Komonov, and S. V. Mutilin, "Nanoimprint Lithography Technique for the Planarized SU-8 Nanogratings Formation on Microstructured Surfaces," in *2024 IEEE 25th International Conference of Young Professionals in Electron Devices and Materials (EDM)*, 2024, pp. 310-314, doi: 10.1109/EDM61683.2024.10614986.
[114] H. Yu *et al.*, "1550-nm Evanescent Hybrid InGaAsP–Si Laser With Buried Ridge Stripe Structure," *IEEE Photonics Technology Letters,* vol. 28, no. 10, pp. 1146-1149, 2016, doi: 10.1109/LPT.2016.2532926.
[115] L. Quan, W. Jianhong, and G. Peiliang, "Fabrication of the buried grating," in *2017 Conference on Lasers and Electro-Optics Pacific Rim (CLEO-PR)*, pp. 1-2, 2017, doi: 10.1109/CLEOPR.2017.8119103.
[116] L. M. Miller *et al.*, "A distributed feedback ridge waveguide quantum well heterostructure laser," *IEEE Photonics Technology Letters,* vol. 3, no. 1, pp. 6-8, 1991, doi: 10.1109/68.68030.
[117] L. Hou, M. Haji, R. Dylewicz, B. Qiu, and A. C. Bryce, "10-GHz Mode-Locked Extended Cavity Laser Integrated With Surface-Etched DBR Fabricated by Quantum-Well Intermixing," *IEEE Photonics Technology Letters,* vol. 23, no. 2, pp. 82-84, 2011, doi: 10.1109/LPT.2010.2091121.
[118] J. Guo *et al.*, "Up to 25 Gb/s direct modulation of high power SOA integrated with a 1.5 μm InGaAlAs/InP DFB laser," in *49th European Conference on*

Optical Communications (ECOC 2023), 2023, vol. 2023, pp. 424-427, doi: 10.1049/icp.2023.2096.
[119] R. H. Clarke, "Theory of reflection from antireflection coatings," *The Bell System Technical Journal,* vol. 62, no. 10, pp. 2885-2891, 1983, doi: 10.1002/j.1538-7305.1983.tb03458.x.
[120] D. Marcuse, "Reflection loss of laser mode from tilted end mirror," *Journal of Lightwave Technology,* vol. 7, no. 2, pp. 336-339, 1989, doi: 10.1109/50.17776.
[121] V. Subramaniam, G. N. D. Brabander, D. H. Naghski, and J. T. Boyd, "Measurement of mode field profiles and bending and transition losses in curved optical channel waveguides," *Journal of Lightwave Technology,* vol. 15, no. 6, pp. 990-997, 1997, doi: 10.1109/50.588672.
[122] H. Ihsudha, Y. Aska, and M. A. Sulthoni, "Photonic Simulation of Al2O3-coated and Au Nanorod using Lumerical FDTD," in *2021 International Symposium on Electronics and Smart Devices (ISESD)*, pp. 1-6, 2021, doi: 10.1109/ISESD53023.2021.9501779.
[123] W. Yang, "Modal analysis of slab optical waveguides: Fresnel equations v.s. wave equations," in *IEEE SOUTHEASTCON 2014*, pp. 1-5, 2014, doi: 10.1109/SECON.2014.6950733.
[124] L. Hongyu *et al.*, "Research on metal lift-off in fabrication of a vertical cavity surface emitting laser," in *2015 International Conference on Optoelectronics and Microelectronics (ICOM)*, pp. 379-382, 2015, doi: 10.1109/ICoOM.2015.7398847.
[125] A. Joo-Heon *et al.*, "Successful utilization of CH/sub 4//H/sub 2/ RIE for the fabrication of 1.3 /spl mu/m InGaAsP/InP integrated laser with butt-coupled passive waveguides," in *Proceedings of 8th International Conference on Indium Phosphide and Related Materials*, pp. 121-124, 1996, doi: 10.1109/ICIPRM.1996.491950.
[126] Z. Min, C. Baoqin, X. Changqing, L. Ming, and N. Jiebing, "Study of process of HSQ in electron beam lithography," in *2010 IEEE 5th International Conference on Nano/Micro Engineered and Molecular Systems*, pp. 1021-1024, 2010, doi: 10.1109/NEMS.2010.5592584.
[127] P. Strasser, R. Wuest, F. Robin, D. Erni, and H. Jackel, "Process optimization for dry etching of InP-InGaAsP-based photonic crystals with a Cl/sub 2//CH/sub 4//H/sub 2/ mixture on an ICP-RIE," in *16th IPRM. 2004 International Conference on Indium Phosphide and Related Materials,* pp. 175-178, 2004, doi: 10.1109/ICIPRM.2004.1442639.
[128] H. Jansen *et al.*, "BSM 7: RIE lag in high aspect ratio trench etching of silicon," *Microelectronic Engineering,* vol. 35, no. 1, pp. 45-50, 1997, doi: https://doi.org/10.1016/S0167-9317(96)00142-6.
[129] S. Vaidya and A. K. Sinha, "Electromigration Induced Leakage at Shallow Junction Contacts Metallized with Aluminum/Poly-Silicon," in *20th International Reliability Physics Symposium*, pp. 50-54, 1982, doi: 10.1109/IRPS.1982.363022.
[130] Z. Weifeng, K. Seiyon, Z. Jian, and I. Adesida, "Thermally stable Ge/Ag/Ni

Ohmic contact for InAlAs/InGaAs/InP HEMTs," *IEEE Electron Device Letters,* vol. 27, no. 1, pp. 4-6, 2006, doi: 10.1109/LED.2005.860381.

[131] P. W. Juodawlkis, J. J. Plant, W. Loh, L. J. Missaggia, K. E. Jensen, and F. J. O. Donnell, "Packaged 1.5-μm Quantum-Well SOA With 0.8-W Output Power and 5.5-dB Noise Figure," *IEEE Photonics Technology Letters,* vol. 21, no. 17, pp. 1208-1210, 2009, doi: 10.1109/LPT.2009.2023332.

[132] M. Razeghi *et al.*, "Low-threshold distributed feedback lasers fabricated on material grown completely by LP-MOCVD," *IEEE Journal of Quantum Electronics,* vol. 21, no. 6, pp. 507-511, 1985, doi: 10.1109/JQE.1985.1072707.

[133] S. Guilet, S. Bouchoule, C. Jany, C. S. Corr, and P. Chabert, "ICP Etching Process Development based on Cl2/H2 Chemistry and Adapted to Non-Thermalized InP Wafers for the Realization of High Aspect Ratio and Vertical Sidewall Deep Ridge Waveguides and Buried Heterostructures," in *2006 International Conference on Indium Phosphide and Related Materials Conference Proceedings*, pp. 262-265, 2006, doi: 10.1109/ICIPRM.2006.1634164.

[134] H. Yamazaki, T. Sasaki, N. Kida, M. Kitamura, and I. Mito, "250kHz Linewidth Operation in Long Cavity 1.5μm Multiple Quantum Well DFB-LDs with Reduced Linewidth Enhancement Factor," in *Optical Fiber Communication*, San Francisco, California, p. PD33, 1990, doi: 10.1364/OFC.1990.

[135] L. Hou *et al.*, "Subpicosecond Pulse Generation at Quasi-40-GHz Using a Passively Mode-Locked AlGaInAs–InP 1.55-μm Strained Quantum-Well Laser," *IEEE Photonics Technology Letters,* vol. 21, no. 23, pp. 1731-1733, 2009, doi: 10.1109/LPT.2009.2031088.

[136] L. Hou, M. Haji, J. Akbar, J. H. Marsh, and A. C. Bryce, "AlGaInAs/InP Monolithically Integrated DFB Laser Array," *IEEE Journal of Quantum Electronics,* vol. 48, no. 2, pp. 137-143, 2012, doi: 10.1109/JQE.2011.2174455.

[137] K. Kojima, K. Kyuma, and T. Nakayama, "Analysis of the spectral linewidth of distributed feedback laser diodes," *Journal of Lightwave Technology,* vol. 3, no. 5, pp. 1048-1055, 1985, doi: 10.1109/JLT.1985.1074295.

[138] B. Hakki and T. Paoli, "cw degradation at 300°K of GaAs double-heterostructure junction lasers. II Electronic gain," *Journal of Applied Physics,* vol. 44, pp. 4113-4119, 1973, doi: 10.1063/1.1662905.

[139] T. N. Huynh, L. Nguyen, and L. P. Barry, "Delayed Self-Heterodyne Phase Noise Measurements With Coherent Phase Modulation Detection," *IEEE Photonics Technology Letters,* vol. 24, no. 4, pp. 249-251, 2012, doi: 10.1109/LPT.2011.2174216.

[140] J. W. Dong, B. Wang, C. Gao, Y. C. Guo, and L. J. Wang, "Highly accurate fiber transfer delay measurement with large dynamic range," *Opt. Express,* vol. 24, no. 2, pp. 1368-1375, 2016, doi: 10.1364/OE.24.001368.

[141] D. J. Derickson, "Fiber optic test and measurement," 1998.

[142] H. G. Zhang *et al.*, "Narrow-Linewidth Microwave Generation Using a Self-Injected DBR Laser Diode," *IEEE Photonics Technology Letters,* vol. 21, no. 15, pp. 1045-1047, 2009, doi: 10.1109/LPT.2009.2022176.

[143] C. H. Joyner *et al.*, "Large-scale DWDM photonic integrated circuits: a manufacturable and scalable integration platform," in *2005 IEEE LEOS Annual Meeting Conference Proceedings*, pp. 344-345, 2005, doi: 10.1109/LEOS.2005.1548019.

[144] L. A. Coldren *et al.*, "Photonic Integrated Circuits," in *Diode Lasers and Photonic Integrated Circuits*, pp. 451-507, 2012.

[145] E. Bigan, A. Ougazzaden, F. Huet, M. Carré, A. Carenco, and A. Mircea, "Efficient electroabsorption in InGaAsP/InGaAsP MQW optical waveguide," *Electronics Letters,* vol. 27, no. 18, pp. 1607-1609, 1991, doi: doi:10.1049/el:19911006.

[146] S. Roy, "Silicon Photonics: Foundation, Recent Application and Challenges," in book: Reference Module in Materials Science and Materials Engineeringm 2022, DOI:10.1016/B978-0-12-819728-8.00037-1.

[147] X. Fengnian, V. M. Menon, and S. R. Forrest, "Photonic integration using asymmetric twin-waveguide (ATG) technology: part I-concepts and theory," *IEEE Journal of Selected Topics in Quantum Electronics,* vol. 11, no. 1, pp. 17-29, 2005, doi: 10.1109/JSTQE.2004.841466.

[148] Y. Barbarin, E. A. J. M. Bente, C. Marquet, E. J. S. Leclere, J. J. M. Binsma, and M. K. Smit, "Measurement of reflectivity of butt-joint active-passive interfaces in integrated extended cavity lasers," *IEEE Photonics Technology Letters,* vol. 17, no. 11, pp. 2265-2267, 2005, doi: 10.1109/LPT.2005.857597.

[149] W. Kobayashi *et al.*, "Design and Fabrication of 10-/40-Gb/s, Uncooled Electroabsorption Modulator Integrated DFB Laser With Butt-Joint Structure," *Journal of Lightwave Technology,* vol. 28, no. 1, pp. 164-171, 2010, doi: 10.1109/JLT.2009.2036865.

[150] T. Van Caenegem, I. Moerman, and P. Demeester, "Selective area growth on planar masked InP substrates by metal organic vapour phase epitaxy (MOVPE)," *Progress in Crystal Growth and Characterization of Materials,* vol. 35, no. 2, pp. 263-288, 1997, doi: https://doi.org/10.1016/S0960-8974(98)00003-5.

[151] M. Takahashi, M. Suzuki, M. Aoki, K. Uomi, and T. Kawano, "In-plane quantum energy control of InGaAs/InGaAsP MQW structure by MOCVD selective area growth," in *LEOS 1992 Summer Topical Meeting Digest on Broadband Analog and Digital Optoelectronics, Optical Multiple Access Networks, Integrated Optoelectronics, and Smart Pixels*, pp. 206-209, 1992, doi: 10.1109/ICIPRM.1992.235603.

[152] J. H. Marsh, "Quantum well intermixing," *Semiconductor Science and Technology,* vol. 8, no. 6, p. 1136, 1993, doi: 10.1088/0268-1242/8/6/022.

[153] L. Hou and J. H. Marsh, "Photonic Integrated Circuits Based on Quantum well Intermixing Techniques," *Procedia Engineering,* vol. 140, pp. 107-114, 2016, doi: https://doi.org/10.1016/j.proeng.2015.10.152.

[154] L. Hou, M. Haji, J. Akbar, J. H. Marsh, and A. C. Bryce, "CWDM source based on AlGaInAs/InP monolithically integrated DFB laser array," *Opt. Lett.,* vol. 36, no. 21, pp. 4188-4190, 2011, doi: 10.1364/OL.36.004188.

[155] P. V. Studenkov, M. R. Gokhale, and S. R. Forrest, "Efficient coupling in integrated twin-waveguide lasers using waveguide tapers," *IEEE Photonics Technology Letters,* vol. 11, no. 9, pp. 1096-1098, 1999, doi: 10.1109/68.784167.

[156] X. Fengnian *et al.*, "An asymmetric twin-waveguide high-bandwidth photodiode using a lateral taper coupler," *IEEE Photonics Technology Letters,* vol. 13, no. 8, pp. 845-847, 2001, doi: 10.1109/68.935823.

[157] X. Fengnian, W. Jian, V. Menon, and S. R. Forrest, "Monolithic integration of a semiconductor optical amplifier and a high bandwidth p-i-n photodiode using asymmetric twin-waveguide technology," *IEEE Photonics Technology Letters,* vol. 15, no. 3, pp. 452-454, 2003, doi: 10.1109/LPT.2002.807930.

[158] S. Ye *et al.*, "1.55-μm Sidewall Grating DFB Lasers Integrated With a Waveguide Crossing for an Optical Beam Forming Network," *IEEE Photonics Technology Letters,* vol. 35, no. 14, pp. 785-788, 2023, doi: 10.1109/LPT.2023.3278880.

[159] Y. De Koninck *et al.*, "GaAs nano-ridge laser diodes fully fabricated in a 300-mm CMOS pilot line," *Nature,* vol. 637, no. 8044, pp. 63-69, 2025/01/01 2025, doi: 10.1038/s41586-024-08364-2.

[160] A. Georgakilas *et al.*, "III-V material and device aspects for the monolithic integration of GaAs devices on Si using GaAs/Si low temperature wafer bonding," in *2001 International Semiconductor Conference. CAS 2001 Proceedings (Cat. No.01TH8547)*, vol. 1, pp. 239-244, 2001, doi: 10.1109/SMICND.2001.967455.

[161] B. Kunert, K. Volz, and W. Stolz, "Advances in the growth of lattice-matched III-V compounds on Si for optoelectronics," in *2010 22nd International Conference on Indium Phosphide and Related Materials (IPRM)*, pp. 1-4, 2010, doi: 10.1109/ICIPRM.2010.5516285.

[162] L. C. Chuang, M. Moewe, S. Crankshaw, C. Chase, and C. Chang-Hasnain, "Epitaxial III-V Nanowires on Lattice-Mismatched Substrates by MOCVD," in *2007 International Nano-Optoelectronics Workshop*, pp. 94-95, 2007, doi: 10.1109/INOW.2007.4302899.

[163] D. K. Sadana, C. W. Cheng, B. Wacaser, W. Spratt, K. T. Shiu, and S. W. Bedell, "Materials challenges for III-V/Si co-integrated CMOS," in *2015 IEEE Custom Integrated Circuits Conference (CICC)*, pp. 1-6, 2015, doi: 10.1109/CICC.2015.7338398.

[164] S. Taebi, M. Khorasaninejad, and S. S. Saini, "Modified Fabry-Perot interferometric method for waveguide loss measurement," *Applied Optics,* vol. 47, no. 35, pp. 6625-6630, 2008, doi: 10.1364/AO.47.006625.

[165] S. S. Saini, V. Vusirikala, R. Whaley, F. G. Johnson, D. Stone, and M. Dagenais, "Compact mode expanded lasers using resonant coupling between a 1.55-μm InGaAsP tapered active region and an underlying coupling waveguide," *IEEE Photonics Technology Letters,* vol. 10, no. 9, pp. 1232-1234, 1998, doi: 10.1109/68.705600.

[166] W. Tong, V. M. Menon, X. Fengnian, and S. R. Forrest, "An asymmetric twin waveguide eight-channel polarization-independent arrayed waveguide grating

with an integrated photodiode array," *IEEE Photonics Technology Letters,* vol. 16, no. 4, pp. 1170-1172, 2004, doi: 10.1109/LPT.2004.824923.
[167] L. Hou, Z. Ren, Y. Shu, and S. Yu, "Angled-Facet Spot-Size-Converter Integrated Semiconductor Optical Amplifiers Using Asymmetric Twin Waveguide Technology," *IEEE Photonics Technology Letters,* vol. 20, no. 8, pp. 563-565, 2008, doi: 10.1109/LPT.2008.918860.
[168] J. Yuan *et al.*, "Mid-infrared self-similar compression of picosecond pulse in an inversely tapered silicon ridge waveguide," *Opt. Express,* vol. 25, no. 26, pp. 33439-33450, 2017, doi: 10.1364/OE.25.033439.
[169] E. Rouvalis, C. C. Renaud, D. G. Moodie, M. J. Robertson, and A. J. Seeds, "Traveling-wave Uni-Traveling Carrier Photodiodes for continuous wave THz generation," *Opt. Express,* vol. 18, no. 11, pp. 11105-11110, 2010, doi: 10.1364/OE.18.011105.
[170] V. M. Menon, X. Fengnian, and S. R. Forrest, "Photonic integration using asymmetric twin-waveguide (ATG) technology: part II-devices," *IEEE Journal of Selected Topics in Quantum Electronics,* vol. 11, no. 1, pp. 30-42, 2005, doi: 10.1109/JSTQE.2004.841465.
[171] T. Rasmussen, J. K. Rasmussen, and J. H. Povlsen, "Design and performance evaluation of 1-by-64 multimode interference power splitter for optical communications," *Journal of Lightwave Technology,* vol. 13, no. 10, pp. 2069-2074, 1995, doi: 10.1109/50.469726.
[172] L. Cahill, "The Modelling of MMI Devices," in *2006 International Conference on Transparent Optical Networks*, 2006, vol. 2, pp. 138-141, doi: 10.1109/ICTON.2006.248357.
[173] H. Yang *et al.*, "Monolithic Integration of Single Facet Slotted Laser, SOA, and MMI Coupler," *IEEE Photonics Technology Letters,* vol. 25, no. 3, pp. 257-260, 2013, doi: 10.1109/LPT.2012.2233197.
[174] T. Morgado *et al.*, "InP MMI based polarization splitter for Photonic Integrated Circuits," in *2017 19th International Conference on Transparent Optical Networks (ICTON)*, 2017, pp. 1-4, doi: 10.1109/ICTON.2017.8024841.
[175] L. B. Soldano and E. C. M. Pennings, "Optical multi-mode interference devices based on self-imaging: principles and applications," *Journal of Lightwave Technology,* vol. 13, no. 4, pp. 615-627, 1995, doi: 10.1109/50.372474.
[176] M. Bachmann, P. A. Besse, and H. Melchior, "General self-imaging properties in N × N multimode interference couplers including phase relations," *Applied Optics,* vol. 33, no. 18, pp. 3905-3911, 1994, doi: 10.1364/AO.33.003905.
[177] B. R. West and S. Honkanen, "MMI devices with weak guiding designed in three dimensions using a genetic algorithm," *Opt. Express,* vol. 12, no. 12, pp. 2716-2722, 2004, doi: 10.1364/OPEX.12.002716.
[178] J. Xu, S. Liang, Z. Zhang, J. An, H. Zhu, and W. Wang, "EML Array fabricated by SAG technique monolithically integrated with a buried ridge AWG multiplexer," *Optics & Laser Technology,* vol. 91, pp. 46-50, 2017, doi: https://doi.org/10.1016/j.optlastec.2016.12.010.
[179] M. Sugawara, T. Fujii, S. Yamazaki, and K. Nakajima, "Theoretical and

experimental study of the optical-absorption spectrum of exciton resonance in ${\mathrm{In}}_{0.53}$${\mathrm{Ga}}_{0.47}$As/InP quantum wells," *Physical Review B,* vol. 42, no. 15, pp. 9587-9597, 1990, doi: 10.1103/PhysRevB.42.9587.
[180] S. D. Kim, J. A. Trezza, and J. S. Harris, Jr., "Observation of 1.5 µm quantum confined Stark effect in InGaAs/AlGaAs multiple quantum wells on GaAs substrates," *Journal of Vacuum Science & Technology B: Microelectronics and Nanometer Structures Processing, Measurement, and Phenomena,* vol. 13, no. 4, pp. 1526-1528, 1995, doi: 10.1116/1.588181.
[181] D.-b. Zhou *et al.*, "Analysis and optimization of 1.5-µm InGaAsP/InP MQWs electroabsorption modulator," *Optik,* vol. 182, pp. 1088-1092, 2019, doi: https://doi.org/10.1016/j.ijleo.2019.02.011.
[182] X. Sun *et al.*, "Simulation of an AlGaInAs/InP Electro-Absorption Modulator Monolithically Integrated with Sidewall Grating Distributed Feedback Laser by Quantum Well Intermixing," *Photonics,* vol. 9, no. 8, p. 564, 2022.
[183] P. Matin, J. Wu, H. Liu, J. Seddon, and A. Seeds, "Modeling of Ultrafast Waveguided Electro-Absorption Modulator at Telecommunication Wavelength (λ = 1.55 µm) Based on Intersubband Transition in an InGaAs/AlAs/AlAsSb Asymmetric Coupled Double Quantum Well Lattice-Matched to InP," *IEEE Journal of Quantum Electronics,* vol. 57, no. 4, pp. 1-10, 2021, doi: 10.1109/JQE.2021.3087327.
[184] X. Sun *et al.*, "Eight-channel EML array based on four phase-shifted sampled Bragg gratings," in *CLEO 2023*, San Jose, CA, 2023/05/07 2023: Optica Publishing Group, in Technical Digest Series, p. SF2Q.3, doi: 10.1364/CLEO_SI.2023.SF2Q.3.
[185] W. Minford, S. Korotky, and R. Alferness, "Low-loss Ti:LiNbO3waveguide bends at λ = 1.3 µm," *IEEE Journal of Quantum Electronics,* vol. 18, no. 10, pp. 1802-1806, 1982, doi: 10.1109/JQE.1982.1071389.
[186] R. Hanfoug *et al.*, "Reduced reflections from multimode interference couplers," *Electronics Letters,* vol. 42, no. 8, pp. 465-466, 2006, doi: doi:10.1049/el:20064422.
[187] F. Karouta *et al.*, "Influence of ICP etching on surface morphology of InP substrates," in *16th IPRM. 2004 International Conference on Indium Phosphide and Related Materials,* pp. 322-325, 2004, doi: 10.1109/ICIPRM.2004.1442720.
[188] R. Dylewicz, A. C. Bryce, M. Sorel, and R. M. D. L. Rue, "High aspect ratio inductively coupled plasma (ICP) etching of InP/InGaAsP/AlGaInAs using Cl2/Ar/N2 gas mixture," in *CLEO/Europe - EQEC 2009 - European Conference on Lasers and Electro-Optics and the European Quantum Electronics Conference*, pp. 1-1, 2009, doi: 10.1109/CLEOE-EQEC.2009.5196446.
[189] L. Hou, M. Tan, M. Haji, I. Eddie, and J. H. Marsh, "EML Based on Side-Wall Grating and Identical Epitaxial Layer Scheme," *IEEE Photonics Technology Letters,* vol. 25, no. 12, pp. 1169-1172, 2013, doi: 10.1109/LPT.2013.2261809.
[190] Y. Sun *et al.*, "DFB laser array based on four phase-shifted sampled Bragg gratings with precise wavelength control," *Opt. Lett.,* vol. 47, no. 23, pp. 6237-

6240, 2022, doi: 10.1364/OL.475909.
[191] Y. Sun *et al.*, "Narrow linewidth distributed feedback lasers utilizing distributed phase shift," *Opt. Lett.,* vol. 50, no. 2, pp. 471-474, 2025, doi: 10.1364/OL.541027.
[192] Y. Sun *et al.*, "Continuous phase modulation technology based on grating period interval for high grating coupling coefficient and precise wavelength control," *Opt. Lett.,* vol. 50, no. 3, pp. 750-753, 2025, doi: 10.1364/OL.543872.